

UNIVERSITY OF BREMEN

DOCTORAL THESIS

**Analysis of Recent Dynamic Changes
of Jakobshavn Isbræ, West
Greenland, using a
Thermomechanical Model**

Author:
Johannes Heinrich
BONDZIO

Supervisor:
Prof. Dr. Angelika
HUMBERT

*A thesis submitted in fulfilment of the requirements
for the degree of Doctor of Natural Sciences*

in the

Department of Geosciences (FB5)

June 19, 2017



Declaration of Authorship

Name: Johannes Heinrich BONDZIO
Anschrift: 72 Rockview Drive, 92612 Irvine, CA, U.S.A.

Der Autor, Johannes Heinrich BONDZIO, erklärt hiermit, dass er

- die Arbeit ohne unerlaubte fremde Hilfe angefertigt hat,
- keine anderen als die von ihm angegebenen Quellen und Hilfsmittel benutzt hat und
- die den benutzten Werken wörtlich oder inhaltlich entnommenen Stellen als solche kenntlich gemacht hat.

Gezeichnet:

Datum, Ort:

UNIVERSITY OF BREMEN

Abstract

Department of Geosciences (FB5)

Doctor of Natural Sciences

Analysis of Recent Dynamic Changes of Jakobshavn Isbræ, West Greenland, using a Thermomechanical Model

by Johannes Heinrich BONDZIO

Jakobshavn Isbræ is a major marine terminating outlet glacier of the western Greenland Ice Sheet, which has been undergoing widespread acceleration and strong mass loss since the disintegration of its floating ice tongue in the late 1990s. The underlying mechanisms are poorly understood despite a wealth in observational and modelling studies. This doctoral thesis analyses the dynamic changes of Jakobshavn Isbræ using the Ice Sheet System Model (ISSM), a state-of-the-art finite-element ice flow model. Two missing model features for 1) the modelling the polythermal regime of glaciers and ice sheets, and 2) the dynamic evolution of its horizontal calving front position are designed and implemented into ISSM. A three-dimensional, thermodynamically coupled model of Jakobshavn Isbræ is set up and calibrated using modern observational data products. Low basal drag in the trough under the ice stream requires that its high driving stress is balanced by lateral drag in the shear margins, which allows for high flow velocities, as the ice viscosity is strain-rate-dependent. The developed modules are applied to the glacier model, which captures 90% of the observed changes from 1985 to 2015. Analysis of the model results reveals that calving front retreat is able to trigger widespread inland acceleration due to a rheological ice viscosity drop in the shear margins. Thermal feedbacks contribute 5 to 10% to the total acceleration. The study shows that Jakobshavn Isbræ will continue to contribute to eustatic sea level rise for at least the next century due to ongoing geometry adjustment to the new calving front position. Future fields of research include deriving a suitable calving rate parametrisation for large-scale ice flow models, a material law for temperate ice with a microscopic water content larger than 1%, and technical refinements of the modules developed for this thesis.

UNIVERSITÄT BREMEN

Zusammenfassung

Fachbereich Geowissenschaften (FB5)

Doktor der Naturwissenschaften

Analysis of Recent Dynamic Changes of Jakobshavn Isbræ, West Greenland, using a Thermomechanical Model

von Johannes Heinrich BONDZIO

Jakobshavn Isbræ ist ein wichtiger Auslassgletscher des westgrönländischen Eisschildes, der seit dem Aufbruch seiner schwimmenden Eiszunge von 1998 bis 2004 sein Fließen weit beschleunigt und stark an Masse verloren hat. Die Mechanismen, die die Beschleunigung erzeugen, sind unklar trotz einer großen Zahl an Beobachtungen und Modellstudien. Diese Doktorarbeit analysiert die dynamischen Veränderungen des Gletschers mittels eines modernen Finite-Elemente Eismodells, des Ice Sheet System Models (ISSM). Zwei fehlende Module werden entworfen und in ISSM implementiert: 1. ein Modul zum Abbilden des polythermalen Regimes von Gletschern und Eisschilden, und 2. ein Modul, das die dynamische Evolution der horizontalen Kalbungsfrontposition im Modell erlaubt. Ein dreidimensionales, thermodynamisch gekoppeltes Fließmodell des Jakobshavn Isbræ wird erstellt, und mittels moderner Datensätze kalibriert. Niedrige basale Scherspannung im Graben unter dem Eisstrom bedingt, dass dessen hohe Triebspannung durch lateralen Spannungstransfer in den Scherrändern ausgeglichen wird. Dies ermöglicht die hohen Fließgeschwindigkeiten des Gletschers, da die Eisviskosität eine Funktion der Verformungsgeschwindigkeit ist. Durch Anwendung der entwickelten Module im Fließmodell werden 90% der beobachteten Veränderungen des Jakobshavn Isbræ im Zeitraum von 1985 bis 2015 nachgebildet. Eine Analyse des Modells ergibt, dass der Rückzug der Kalbungsfront die weite Fließbeschleunigung durch einen rheologiebedingten Abfall der Eisviskosität in den Scherrändern ermöglicht. Thermische Feedbackmechanismen steuern 5 bis 10% zur Gesamtbeschleunigung bei. Diese Studie zeigt, dass Jakobshavn Isbræ aufgrund der fortlaufenden Anpassung der Gletschergeometrie an die neue Kalbungsfrontposition auch im kommenden Jahrhundert zum Meeresspiegelanstieg beitragen wird. Zukünftige Forschungsfelder beinhalten die Entwicklung einer Kalbungsratenparametrisierung für großskalige Eismodelle, einem Materialgesetz für temperiertes Eis mit mikroskopischem Wassergehalt größer als 1%, und technische Verbesserungen der Module, die im Laufe dieser Doktorarbeit entwickelt worden sind.

For the benefit of all beings.

Contents

Title Page	i
Declaration of Authorship	iii
Abstract	v
Zusammenfassung	vi
Contents	ix
List of Abbreviations	xiii
List of Symbols	xv
1 Introduction	1
1.1 Climate change	1
1.2 The Greenland Ice Sheet	1
2 Jakobshavn Isbræ, West Greenland	5
2.1 Introduction	5
2.2 Observations	7
2.2.1 Early records	7
2.2.2 Recent Changes	9
Phase I (until 1998)	11
Phase II (1998 until fall 2003)	13
Phase III (late 2003 trough today)	14
2.3 Modelling Studies	15
2.4 Synopsis	19
2.5 Open Questions	20
2.6 Model Requirements	20
2.6.1 Feature Requirements	20
2.6.2 Technical Requirements	21
2.6.3 Model Choice	21
2.7 Objectives of this Thesis	21
3 Modelling Glaciers and Ice Sheets	23
3.1 On the Use of Models	23
3.2 Elements of Level-Set Methods	24
3.3 Large-scale Ice Sheet Thermodynamics	25
3.3.1 Mass Balance of Ice Sheets	25
Ice and Incompressibility	25
Continuity Equation	26
Kinematic Boundary Conditions	26
Ice Thickness Equation	27
3.3.2 Momentum Balance of Ice Sheets	27

	Quasi-Static Flow	28
	Boundary Conditions	29
	Glen's Flow Law	30
	Controls on the Rate Factor	31
	The Higher-Order Model (HOM)	32
	The Shelfy-Stream Approximation (SSA)	34
3.3.3	Energy Balance of Ice Sheets	34
	The Enthalpy Method	34
	Boundary Conditions	36
3.4	The Finite-Element Method (FEM)	39
3.5	The Ice Sheet System Model (ISSM)	41
4	Enthalpy Benchmark Experiments	43
4.1	Introduction	45
4.2	Theory	46
	4.2.1 Governing Equations	46
	4.2.2 Boundary Conditions	48
4.3	Numerical Models	49
	4.3.1 TIM-FD ³	50
	4.3.2 ISSM	50
	4.3.3 COMice	50
4.4	Experiment Description	51
	4.4.1 Experiment A: Parallel Sided Slab (Transient)	51
	4.4.2 Experiment B: Polythermal Parallel Sided Slab (Steady State)	52
4.5	Results	53
	4.5.1 Experiment A	53
	4.5.2 Experiment B	55
4.6	Discussion	58
4.7	Conclusions	60
4.8	Appendix: Analytical Solutions	60
	4.8.1 Basal Melt Rate in Experiment A	60
	4.8.2 Analytical Solution Experiment B	62
5	A Level-Set Method for Dynamic Calving Front Modelling	65
5.1	Introduction	67
5.2	Theory	70
	5.2.1 Ice Flow Model	70
	5.2.2 Level-Set Method	71
	5.2.3 Implementation	73
5.3	Data and Model Setup	75
	5.3.1 Jakobshavn Isbræ Model Setup	75
	5.3.2 Description of Experiments	76
5.4	Results	77
5.5	Discussion	82
5.6	Conclusions	83
5.7	Appendix: Validation of the Level-Set Method	84
	5.7.1 Advection	84
	5.7.2 Volume Conservation	85
5.8	Acknowledgements	86

6	The Mechanisms behind Jakobshavn Isbræ's Acceleration	87
6.1	Introduction	89
6.2	Ice Flow Model	91
6.3	Model and Experiment Setup	92
6.4	Results	92
6.5	Discussion	95
6.6	Conclusions	99
6.7	Supplementary Online Material	100
6.7.1	Text S1: Jakobshavn Isbræ Model Setup	100
6.7.2	Figures S1	103
7	Jakobshavn Isbræ's Thermodynamic Regime	115
7.1	Additional Results	115
7.1.1	Stress Regime	116
7.1.2	Thermal Regime	121
7.1.3	Geometry	125
7.1.4	Mass Balance	128
7.2	Limitations	131
7.3	Jakobshavn Isbræ's Future Evolution	132
7.3.1	A Hypothesis	133
7.4	Future Work	134
7.4.1	Closing the Gap to Observations	134
7.4.2	Creating Reliable Projections	135
8	Conclusions	137
8.1	Achievements	137
8.2	Thermodynamics of Jakobshavn Isbræ	138
8.2.1	Overview	138
8.2.2	After the Ice Tongue's Disintegration	139
8.3	Outlook	140
8.3.1	Jakobshavn Isbræ's Future Evolution	140
8.3.2	Fields of Further Study	140
	Acknowledgements	143
	Bibliography	145

List of Abbreviations

2D	two-dimensional
3D	three-dimensional
CTS	cold-temperate transition surface
e.s.l.r.	eustatic sea level rise
FEM	finite element method
GrIS	Greenland Ice Sheet
HOM	higher-order model
ISSM	Ice Sheet System Model
KCFC	Kinematic Calving Front Condition
LSE	Level-Set Equation
LSF	Level-Set Function
LSM	Level-Set Method
PDE	partial differential equation
SIA	shallow-ice approximation
SMB	surface mass balance
SSA	shelfy-stream approximation
w.e.	water equivalent
XFEM	extended finite element method

List of Symbols

σ	Cauchy stress tensor	Pa
σ'	deviatoric stress tensor	Pa
σ'_e	effective deviatoric stress	Pa
p	pressure	Pa
$\dot{\epsilon}$	strain rate	s ⁻¹
$\dot{\epsilon}_e$	effective strain rate	s ⁻¹
$\mathbf{v} = (v_x, v_y, v_z)$	velocity	m s ⁻¹
Ω	angular velocity	rad
g	Earth gravity constant	m s ⁻²
\mathbf{g}	Earth gravity acceleration	m s ⁻²
s	ice surface	m
b	ice base	m
$H = s - b$	ice thickness	m
z_{sl}	sea level elevation	m
M	mass	kg
ρ	(ice) density	kg m ⁻³
ρ_m	ice-water mixture density	kg m ⁻³
ρ_w	(sea) water density	kg m ⁻³
p_a	atmospheric pressure	Pa
p_w	water pressure	Pa
a_s	surface accumulation-ablation function	m s ⁻¹ ice equiv.
a_b	basal accumulation-ablation function	m s ⁻¹ ice equiv.
\mathbf{a}	accumulation-ablation flux	m s ⁻¹ ice equiv.
M_b	basal mass balance	kg s ⁻¹
Q	volume flux	m ² s ⁻¹
p', q', r', s'	basal friction law exponents	1
N_{eff}	basal effective pressure	Pa
k	basal friction parameter	Pa ^{(1-r')/2} s ^{s'/2} m ^{-s'/2}
α	basal friction parameter	kg ^{1/2} m ^{-1/2} s ⁻¹
τ_b	stress vector along basal tangential plane	Pa
\mathbf{v}_b	velocity in the basal tangential plane	m s ⁻¹
n	stress exponent	1
A	rate factor	Pa ⁻ⁿ s ⁻¹
B	ice viscosity parameter	Pa s ^{1/n}
μ	viscosity	Pa s
D	ice damage parameter	1
Q	activation energy	J
R	universal gas constant	J mol ⁻¹ K ⁻¹
T	temperature	K / °C
T_{pmp}	pressure melting point temperature	K
T^*	temperature relative to pressure melting point	K

T_{hom}	temperature relative to pressure melting point	°C
T_0	reference temperature	K
W	microscopic water content in temperate ice	1
β	Clausius-Clapeyron constant	K Pa ⁻¹
C_i	heat capacity of ice	J kg ⁻¹ K ⁻¹
E	specific inner energy ("enthalpy")	J kg ⁻¹
E_{pmp}	enthalpy of ice at pressure melting point	J kg ⁻¹
q	heat flux	J m ⁻² s ⁻¹
q_l	latent heat flux	J m ⁻² s ⁻¹
q_s	sensible heat flux	J m ⁻² s ⁻¹
Φ	heat production density	J m ⁻³ s ⁻¹
K_i	enthalpy heat conductivity (cold ice)	kg m ⁻¹ s ⁻¹
K_0	moisture diffusion coefficient	kg m ⁻¹ s ⁻¹
κ	thermal heat conductivity of ice-water mixture	J m ⁻¹ K ⁻¹ s ⁻¹
L	latent heat of fusion	J kg ⁻¹
F_b	basal friction heat production	J m ⁻² s ⁻¹
η_b	basal water layer thickness	m
Q_{cf}	calving flux	m ³ s ⁻¹
\mathbb{R}	space of real numbers	
\mathbb{R}_+^*	space of strictly positive real numbers	
\mathcal{M}^n	tensor-space of order n	
\mathcal{H}^1	Sobolev space	
Ω	subdomain in 2D/3D space	
x	position vector in 2D/3D space	

1 Introduction

1.1 Climate change

Warming of all components of the Earth climate system over the past hundred years is unequivocal. Since the 1950s, many of the observed changes are unprecedented over decades to millennia. Rising temperatures lead to increased melt of all components of the cryosphere, e.g. glaciers and ice sheets, and therefore eustatic sea level rise (e.s.l.r.). The largest contribution to the warming is caused by the uptake of energy of the climate system through the increase in the atmospheric concentration of carbon dioxide (CO₂) (Pachauri *et al.*, 2014).

Continued emissions of greenhouse gases will cause further warming and changes in all components of the climate system in a regionally non-uniform fashion. The global surface temperature increase for the end of the 21st century is likely to exceed 1.5 °C relative to 1850 to 1900 for all but one Representative Concentration Pathway scenario (IPCC-AR5, 2013). Warming of the Earth climate system will cause further shrinking of the cryosphere's components. Consequently, eustatic sea level will continue to rise during the 21st century at a rate which will very likely exceed the one which has been observed during 1971 to 2010 due to increased ocean warming and increased mass loss from glaciers and ice sheets. Most aspects of climate change will persist for many centuries even if emissions of CO₂ are stopped today. This represents a substantial multi-century climate change commitment created by past, present and future emissions of CO₂. Risks of harmful impacts on ecosystems and human systems increase with the rates and magnitudes of warming, ocean acidification, sea level rise and other dimensions of climate change. Efficient risk management requires thorough understanding of the climate system in all its components, like the cryosphere (Pachauri *et al.*, 2014).

1.2 The Greenland Ice Sheet

The Greenland Ice Sheet (GrIS) is the second-largest body of ice on Earth after the Antarctic Ice Sheet. Its total ice volume corresponds to 7.36 m of e.s.l.r. (Pachauri *et al.*, 2014). It is an important component of the Earth climate system and it interacts with the other components in a multitude of ways.

The GrIS is located between 60°N to 82°N (Fig. 1.1), which are latitudes of dominant westerly winds. Its average surface elevation of about 2130 m (Howat *et al.*, 2014) makes it a major orographic obstacle to atmosphere flow. Moreover, the high albedo of the ice sheet cools the surface air layers and creates a stationary high pressure system over the ice sheet. The ice sheet thus influences the atmospheric circulation, which in turn affects the patterns and magnitude of precipitation in its vicinity.

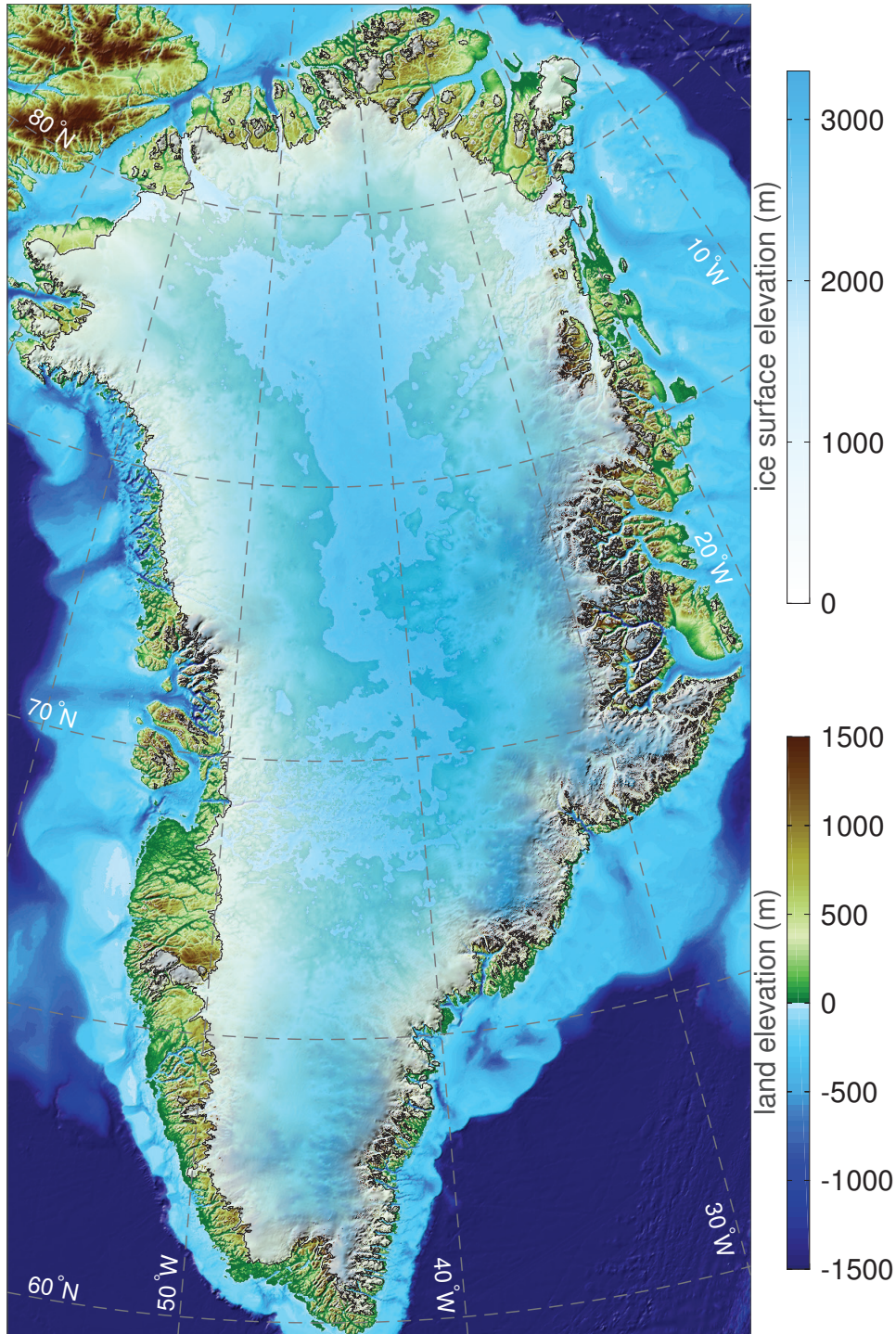


FIGURE 1.1: Land elevation of Greenland and surface elevation of its current ice sheet (M. Morlighem, pers. comm.). The ice surface is made transparent to show the underlying bedrock.

Greenland is surrounded by oceans. Ocean currents are efficient agents for heat transport and they circumnavigate Greenland's coastline in a roughly clockwise fashion (Straneo & Heimbach, 2013). Warm subsurface ocean waters are able to reach the base of Greenland's marine-terminating glaciers through valleys ("troughs") in the substrate of the continental shelf, and drive significant melt at the ice-ocean interface (Straneo & Heimbach, 2013).

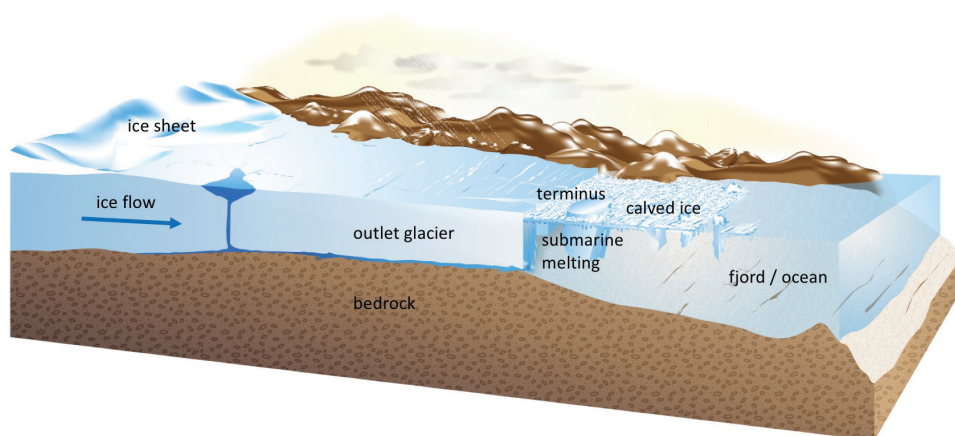


FIGURE 1.2: Sketch of a tidewater glacier of the Greenland ice sheet. Ice forms inland and moves towards the ocean. On its way it is lost through melting at the ice surface and base, as well as through calving and submarine melting at the terminus. Figure adapted from Straneo & Heimbach (2013).

The release of cold, fresh meltwater in turn affects the buoyancy-driven ocean circulation as well as the formation of sea ice at the ocean surface, which influences the exchange of moisture and heat between atmosphere and ocean (Cuffey & Paterson, 2010, p.553).

During the last two decades, the average contribution to e.s.l.r. from the GrIS has substantially increased from $0.09 [-0.02 \text{ to } 0.20] \text{ mm a}^{-1}$ (1992 to 2001) to $0.59 [0.43 \text{ to } 0.76] \text{ mm a}^{-1}$ (2002 to 2011) (average of 18 studies, brackets show value range, IPCC-AR5, 2013, p.320). Recent studies suggest that this trend continues and accelerates (Helm *et al.*, 2014). The ice loss from Greenland is partitioned in approximately similar amounts between surface melt and outlet glacier discharge, and both components have increased. The surface mass balance has become progressively more negative as a result of an increase in surface melt and runoff (van den Broeke *et al.*, 2016), and ice discharge has also increased due to the acceleration of some outlet glaciers (Moon *et al.*, 2012).

The IPCC-AR5 (2013) concludes that “changes in ice sheet mass balance are the result of an integrated response to climate, and it is imperative that we understand the context of current change within the framework of past changes and natural variability”. The projections of sea level rise based on numerical models and presented in the IPCC-AR4 (2007) explicitly excluded future rapid dynamical changes in ice flow, and it stated that “understanding of these processes is limited and there is no consensus on their magnitude”. Substantial efforts have been made since IPCC-AR4 (2007) to fill the knowledge gap (e.g. Nowicki *et al.*, 2013a; Nowicki *et al.*, 2013b; Pattyn *et al.*, 2013). However, considerable uncertainties in projections of e.s.l.r. remain, and require further dedicated work.

Greenland’s ice reaches the ocean by means of outlet glaciers, which often move through troughs (Fig. 1.2). The total width of the GrIS’s outlet glaciers is only 8% of the total Greenland coast line length, yet they discharge 88% of Greenland’s ice (Morlighem *et al.*, 2014a). Estimates of future ice discharge of the GrIS thus require understanding of the outlet glaciers’ dynamics.

This cumulative doctoral thesis aims to contribute to the understanding of the dynamics of outlet glaciers by means of a numerical study of a major marine-terminating outlet glacier of the western GrIS, Jakobshavn Isbræ. The following two chapters provide an overview over the current scientific understanding of Jakobshavn Isbræ (Chap. 2), and state the necessary fundamentals for numerical ice sheet modelling (Chap. 3), respectively. Chapters 4, 5, and 6 are three publications that address the aim of the study. Chapter 7 presents additional model results that were omitted from the preceding publication due to space limitations of the journal the manuscript was submitted to. Chapter 8 summarizes the conclusions of the thesis. For consistency reasons, the author modestly adopts the first-person plural narrator perspective for the remainder of the text.

2 Jakobshavn Isbræ, West Greenland

2.1 Introduction

In this section, we present an overview over current state of scientific understanding of Jakobshavn Isbræ: we give the glacier's general setting, and a short summary of the observational and modelling studies on Jakobshavn Isbræ made during the last decades. After a synopsis, we identify open questions about Jakobshavn Isbræ, and state the objectives of this thesis. For the terminology used in this chapter, we refer to the common glaciological literature, e.g. Hooke (2005) and Cuffey & Paterson (2010).

Jakobshavn Isbræ is a major marine-terminating outlet glacier of the Greenland Ice Sheet (GrIS, Figs. 2.1 and 2.2). Its drainage basin stretches from the western ice margin to the GrIS's central ice divide, and covers 90.135 km^2 , about 6.5% of the total surface area of the GrIS (Rignot & Kanagaratnam, 2006; Rignot & Mouginot, 2012). The glacier has become a major contributor to e.s.l.r. since the late 1990s.

The ice surface elevation is highest at the ice divide (about 3180 m), and slopes down westward to sea level at the ice margin (Fig. 2.3 a). The average ice surface elevation is about 2470 m (Howat *et al.*, 2014). The surface slope is rather steep compared to e.g. ice streams in West Antarctica: surface gradients range from 0.003 in the interior up to 0.48 in an ice fall near the calving front. The bedrock topography underneath the inland ice is to a large extent at or below sea level (Fig. 2.3 b). Moving along-flow towards the coast, the bedrock slopes upward, terminating in a mountain range of about 500 m altitude at the coast. A network of troughs develops near the ice divide, which becomes deeper relative to the surrounding bedrock the further one moves towards the coast. Along their path, the troughs merge several times, ultimately forming a single, deep, U-shaped trough, which terminates into the "Kangia", the deep fjord which connects Jakobshavn Isbræ to Disko Bugt (Fig. 2.1). The trough reaches depths of up to 1700 m below sea level and is about 6 km wide, with steep walls to either side (Bamber *et al.*, 2013; Gogineni *et al.*, 2014; Morlighem *et al.*, 2014a). The ice thickness is largest at the ice divide (up to about 3460 m) and in the deep trough (up to about 2500 m).

Jakobshavn Isbræ's ice flows westward from the ice divide to the coast in a converging pattern. Flow velocities range from a few meters per year at the ice divide to several kilometres per year in two branches, which merge and flow into the Kangia (Fig. 2.2). Both internal deformation and basal sliding contribute to Jakobshavn Isbræ's ice motion (Lüthi *et al.*, 2002). The faster branch, commonly referred to as "ice stream" (e.g. Cuffey & Paterson, 2010) is located in the deep trough mentioned above. The combination of thick ice and steep surface slopes creates average driving stresses of 360

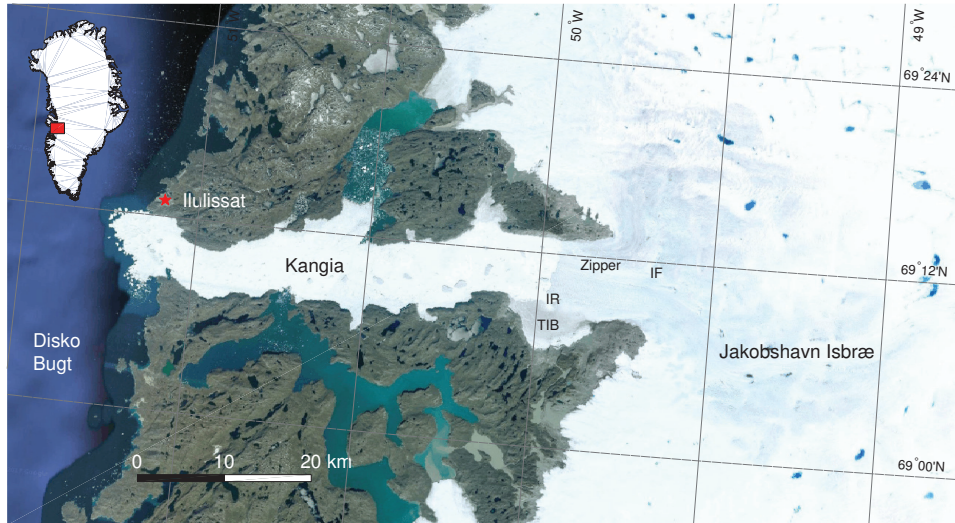


FIGURE 2.1: Overview map of the region around the Kangia and Jakobshavn Isbræ's terminus. Location abbreviations: TIB - Tissarissaq Ice Bay, IR - Ice Rump, IF - ice fall (cf. Echelmeyer & Harrison, 1990; Csatho *et al.*, 2008). Background image © Google Earth.

to 410 kPa, which are an order of magnitude higher than the driving stress of most ice streams in West Antarctica (about 20 kPa Cuffey & Paterson, 2010). Ice rapidly accelerates over just a few ice thicknesses width when it approaches the branches. The heavily crevassed ice surface in this area documents the large strain rates that characterize the shear margins on either side of the ice stream (Echelmeyer *et al.*, 1991). The ice flow pattern allows us to crudely subdivide the drainage basin of Jakobshavn Isbræ into two regions:

1. The “ice stream”, which includes the fast-flowing regions of the faster branch and its shear margins, and
2. the “ice sheet”, which includes the surrounding regions of slow ice flow.

Jakobshavn Isbræ's terminus is characterized by a vertical ice cliff, which rises 50 to 90 m over the water surface, and spans the entire width of the Kangia (Fig. 2.4). Calving, the separation of ice blocks from the terminus, occurs frequently and is a major means of ice discharge for Jakobshavn Isbræ (Echelmeyer *et al.*, 1992). The mixture of sea ice and calved icebergs forms a dense “ice mélange”, whose rigidity influences the glacier's calving rate (Amundson *et al.*, 2010). Moreover, observations show a strong correlation between the calving rate and surface air temperatures (Sohn *et al.*, 1998; Joughin *et al.*, 2004; Joughin *et al.*, 2008; Cassotto *et al.*, 2015), which presumably weaken the ice mélange and facilitate hydro-fracturing of meltwater-filled surface crevasses. These processes are poorly understood (Benn *et al.*, 2007). Calved icebergs, some with a draft of up to 600 m, slowly drift down the Kangia and may become stranded on a shallow submarine shoal at its mouth (Echelmeyer *et al.*, 1992). Only after the icebergs melt, break apart and are lifted during high tides do they float free and move on into the Disko Bugt and Davis Strait.

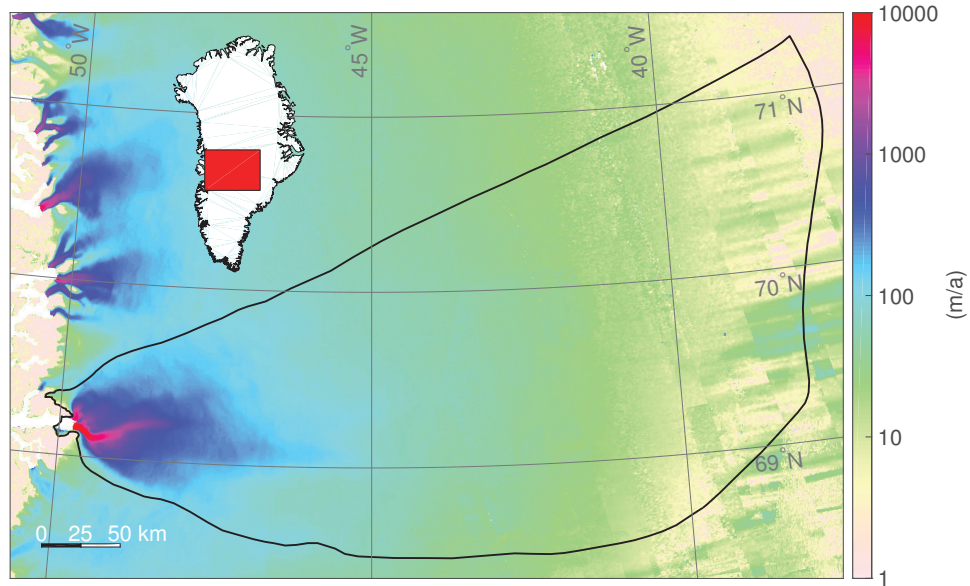


FIGURE 2.2: Ice surface velocity of Jakobshavn Isbræ during 2008/2009 (Rignot & Mouginot, 2012). The black contour denotes Jakobshavn Isbræ's drainage basin.

The Kangia connects the glacier to the Disko Bugt (Fig. 2.1), which in turn is a wide south-eastern inlet of the Baffin Bay. Its bathymetry is poorly known due to the year-round presence of a dense ice mélange, but it is estimated to be between 800 and 1500 m deep (Echelmeyer *et al.*, 1991; Gladish *et al.*, 2015). The water in the Kangia is a stratified mixture of cold, fresh water at the surface and warm, saline waters at depth. Basin waters at depth flow towards the glacier, entrained by a buoyancy-driven upwelling plume at ice-ocean interface. This pattern of fjord circulation drives comparatively high submarine melting rates ($228 \pm 49 \text{ m a}^{-1}$, with higher melting rates at depth, Motyka *et al.*, 2011) and has been observed at some other marine terminating glaciers in Alaska and Greenland (Motyka *et al.*, 2003; Rignot *et al.*, 2010; Straneo *et al.*, 2011).

Annual average air temperatures at 2 m above the ice surface range from -30°C at the ice divide to -7°C near the terminus (Fig. 2.3c). Summer air temperatures well above 0°C allow substantial surface melt at lower ice surface elevations. Figure 2.3d shows the surface mass balance (SMB) of Jakobshavn Isbræ averaged from 1957 to 2007. Its values are on the order of several centimetres water equivalent (w.e.) per year over wide areas of the ice sheet interior and rapidly decrease to negative values of several meters w.e. per year towards the margin of the ice sheet. The equilibrium line – the region where accumulation and ablation balance each other – is located at about 20 to 100 km from the ice margin.

2.2 Observations

2.2.1 Early records

Paleo-records show that the terminus position of Jakobshavn Isbræ has been ever-changing: at the end of the last ice age, ice retreated from a position near the west end of Disko Island to the mouth of the Kangia near the

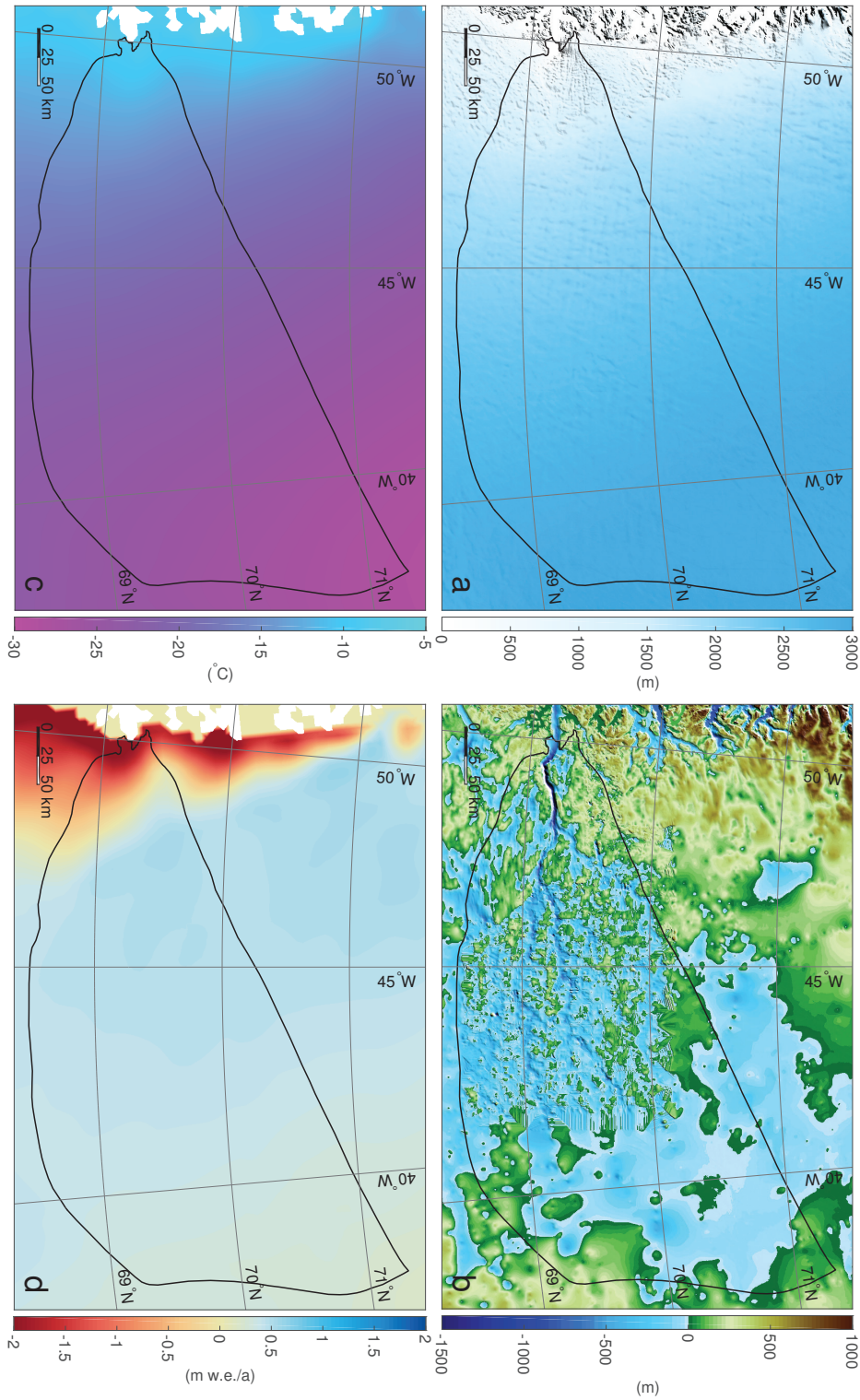


FIGURE 2.3: Jakobshavn Isbræ's geometry and surface forcings: a) ice surface elevation (Howat *et al.*, 2014), b) bedrock elevation (Bamber *et al.*, 2013; Gogineni *et al.*, 2014; Morlighem *et al.*, 2014a), c) annual average surface temperature (1958 - 2007) and d) annual surface mass balance (SMB) (1958 - 2007), both Ettema *et al.* (2009). The black line outlines Jakobshavn Isbræ's drainage basin (Rignot & Mouginot, 2012).



FIGURE 2.4: The calving front of Jakobshavn Isbræ's ice stream, as seen from NASA's P-3B aircraft on April 21, 2012. The ice cliff is up to 90 m high. An ice mélange covers the ocean in front of the glacier. View direction is approximately towards the South. Photo by: NASA/GSFC/Jefferson Beck, (Creative Commons licence BY 2.0). The photo has been cropped.

village of Ilulissat. Here, the shallow moraine shoal of 200 to 300 m depth marks a quasi-stationary terminus position at around 8000 BP. The ice then retreated to a minimum extent in this region, inland of its present position, until about 5000 BP. Following this retreat, the glacier advanced until it reached a position about halfway along the present fjord in 1850 (Bauer, 1968; Weidick, 1968; Echelmeyer *et al.*, 1991).

Georgi (1959) compiled a record of observed calving front positions from year 1850 until 1942, which shows gradual retreat over 25 km (Fig. 2.5). It is not possible to tell from this record whether calving front retreat occurred in a continuous or rather abrupt fashion. However, field observations show that the glacier during this period underwent various phases of intermittent strong thinning from 1902 to 1913 and from 1930 to 1959 (Csatho *et al.*, 2008). From the 1960s until the 1990s, the calving front position stabilized and fluctuated around an annual average position at the western head of Tissarissuq Ice Bay (Fig. 2.1) by about 2.5 km (Sohn *et al.*, 1998). The "Ice Rumples" (cf. Fig. 2.1), an ice rise in the Tissarissuq Ice Bay, presumably stabilized the Jakobshavn Isbræ's floating ice tongue (Joughin *et al.*, 2008).

2.2.2 Recent Changes

During the late 1990s and early 2000s, Jakobshavn Isbræ's floating ice tongue disintegrated, which triggered ongoing widespread flow acceleration, mass loss and calving front retreat. Since a comprehensive review of corresponding observations in the literature is lacking, we present here a summary of the observed changes. For reasons of clarity, we subdivide the continuous chain of events into three phases:

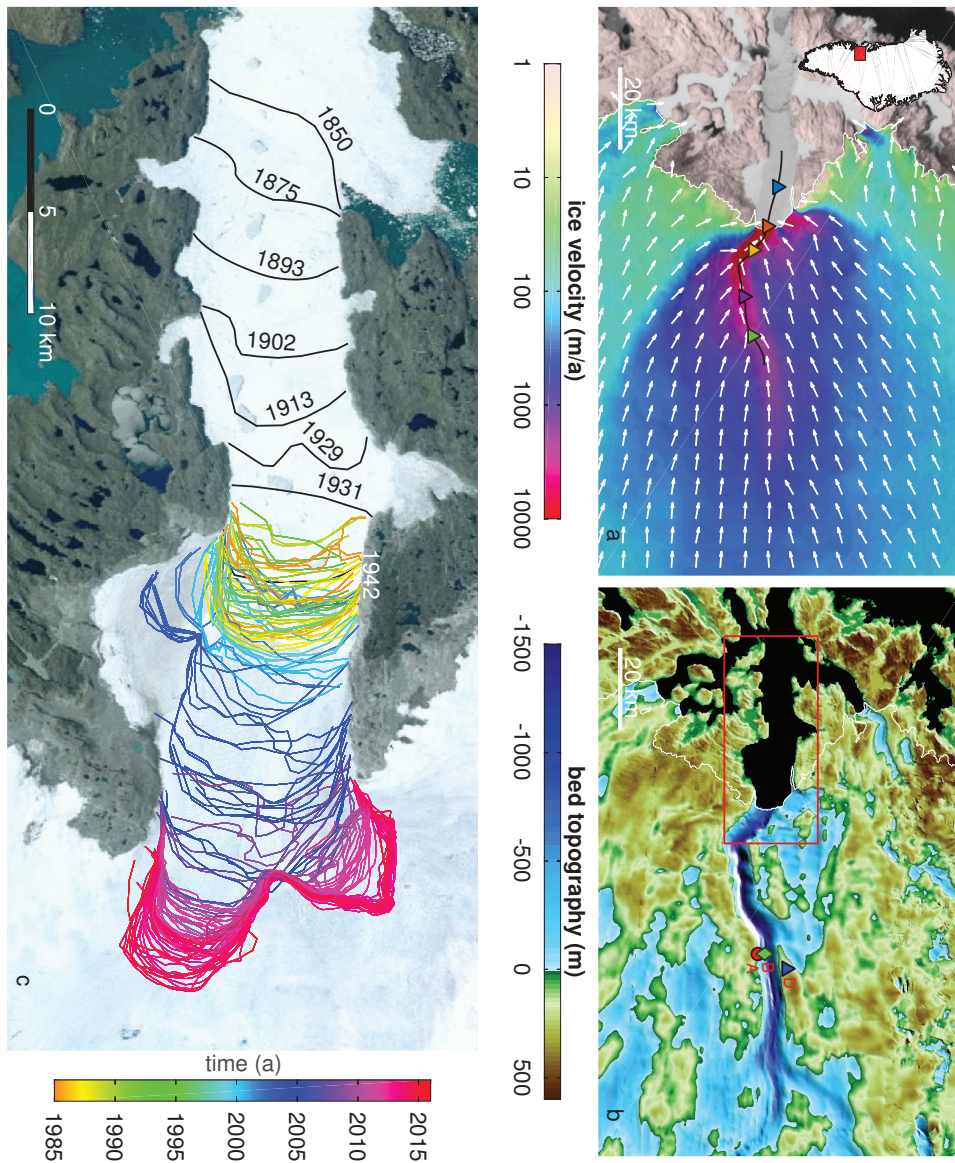


FIGURE 2.5: a) Observed ice surface velocity in region of fast flow in 2008/2009 (Rignot & Mouginot, 2012). The black flowline and coloured triangles are used in Fig. 2.6. b) Jakobshavn Isbræ's bedrock topography in the same region, shaded relief (Bamber *et al.*, 2013; Gogineni *et al.*, 2014; Morlighem *et al.*, 2014a). Coloured markers denote the borehole locations of the studies Iken *et al.* (1993) and Lüthi *et al.* (2002), cf. Fig. 2.7. c) Evolution of Jakobshavn Isbræ's calving front position in the red box inset in (b). Black lines are calving front positions retraced after the compilation presented in Georgi (1959). Recent calving front positions (1985 until end 2015) are colour-coded, and have been derived from Landsat 5-7 and TerraSAR-X satellite scenes (Rosenau *et al.*, 2013; Moon *et al.*, 2014). Satellite background image: Landsat 7 (July 1st, 2001) © Google Earth.

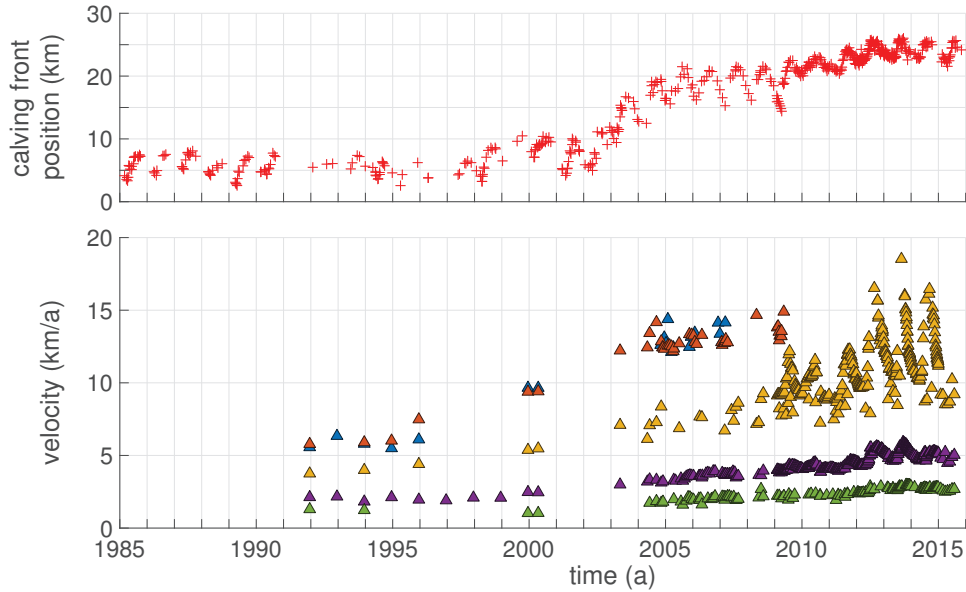


FIGURE 2.6: Red crosses: time series of observed calving front positions along the flowline in the ice stream (cf. Fig. 2.5a). Triangles: observed surface velocities at the locations corresponding in colour shown in Fig. 2.5a, compiled from Joughin *et al.* (2008), Joughin *et al.* (2012), Joughin *et al.* (2014), and Howat (2016) and J. Mouginot, pers.comm.

1. Phase I (until 1998) denotes the time prior to the disintegration of the ice tongue, during which the glacier has exhibited quasi-stable behaviour.
2. Phase II (1998 until fall 2003) corresponds to the period during which the ice tongue disintegrated, which triggered strong flow acceleration and mass loss.
3. Phase III (late 2003 trough today) corresponds to the time after the ice tongue had disintegrated, which triggered ongoing calving front retreat and strong glacier mass loss nearly year-round.

Phase I (until 1998)

Jakobshavn Isbræ has aroused early interest by glaciologists. We are therefore fortunate to have access to a wealth of observations on the glacier prior to the dawn of the modern satellite era. Seminal works by intrepid researchers like R. Bindshadler, K. Echelmeyer, A. Iken, and many others allow us to reconstruct the state of Jakobshavn Isbræ in considerable detail. This section summarizes their main findings.

During Phase I, the northern and southern branches merged and flowed into a floating ice tongue, which extended about 15 km into the Kangia up to the west end of Tissarissoq Ice Bay. A heavily crevassed zone on the ice tongue, called “Zipper”, marked the area of confluence of both branches, and forms downstream of an ice fall (cf. Fig. 2.1). The grounding line was located approximately where both branches merged. An “Ice Rumpel” located at the southern part of the ice tongue indicated a pinning point, which presumably stabilized the ice tongue (Echelmeyer & Harrison, 1990; Echelmeyer *et al.*, 1991; Joughin *et al.*, 2008, and Fig. 2.1). The calving front

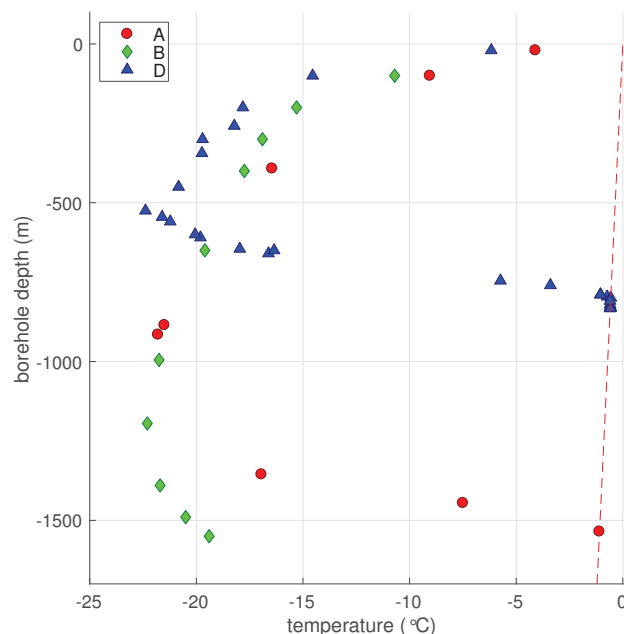


FIGURE 2.7: Measured temperatures in boreholes A,B, and D from Iken *et al.* (1993) and Lüthi *et al.* (2002), respectively. Boreholes A and D reached the ice base, borehole B did not. For borehole positions, cf. Fig. 2.5b. The dashed red line represents the pressure melting point temperature.

position varied stably along-flow around an annual mean position at the head of Tissarissuq Ice Bay (TIB) by ± 2.5 km (Sohn *et al.*, 1998), (Fig. 2.5). Calving during the presence of the ice tongue produced tabular icebergs, measuring up to 2 km.

Surface flow velocities in the ice stream during the years 1984 to 1986 ranged from 6 to 7 km a⁻¹ and showed little seasonal variation, which indicates that the floating ice tongue was able to provide substantial buttressing to the ice upstream (Echelmeyer & Harrison, 1990). The glacier continued to flow at these speeds in the 1990s. A small seasonal variation in summer 1995 detected by Luckman & Murray (2005) may have been a harbinger of the changes that were yet to come.

Mass balance assessments of Jakobshavn Isbræ until 1998 show that the glacier has been close to equilibrium, or perhaps in slight negative imbalance (Bindshadler, 1984; Peltó *et al.*, 1989; Echelmeyer *et al.*, 1992; Rignot & Kanagaratnam, 2006; Motyka *et al.*, 2010). Mass flux estimates across the grounding line range from 21.8 to 25.5 Gt a⁻¹ (Echelmeyer *et al.*, 1992; Rignot & Kanagaratnam, 2006). The ratio of ice discharge through calving to surface and basal melt was two (Echelmeyer *et al.*, 1992). Basal melting provided an estimated 20% of the total melt (Echelmeyer *et al.*, 1992). Nearly all of the meltwater generated from both surface and basal melting entered the Kangia near the calving front as either surface run-off or subglacial discharge (Echelmeyer & Harrison, 1990). Submarine melting rates underneath Jakobshavn Isbræ's floating ice tongue in the mid-1980s are about 228 ± 49 m a⁻¹ (Motyka *et al.*, 2011), which is one to two orders of magnitude higher than values measured at Antarctic ice streams (Cuffey & Paterson, 2010, p.119).

Knowledge about the thermal regime of Jakobshavn Isbræ stems almost exclusively from sparse vertical borehole measurements. Echelmeyer

et al. (1992) measured the ice temperature in shallow boreholes along the ice stream, and finds a linear relationship between ice temperature and ice surface elevation. The authors attribute a strong variation in temperature across the ice stream to high deformational warming in the shear margins. Iken *et al.* (1993) and Lüthi *et al.* (2002) measured temperatures and tilt in ice-thickness-penetrating boreholes about 50 km upstream of the terminus position at that time (cf. Fig. 2.5b). The results showed a strong temperature inversion along the vertical for all borehole profiles (Fig. 2.7). While the surface layers were at summer season to annual average 2 m surface air temperature (-4 to -7 °C), the temperature quickly dropped to -22.1 °C in the middle part of the ice column, only to sharply rise again to pressure melting point towards the base. The temperature profile reflects the flow characteristics of the glacier: cold glacier ice is advected from upstream, and warms through englacial dissipation of kinetic energy (strain heating), as well as heating through basal friction and geothermal heat flux. Since ice is a good thermal insulator and heat sources are concentrated at the base, the ice at the base may become temperate and form a layer of temperate ice (temperate layer). A borehole in the centre of the ice stream by Iken *et al.* (1993) did not reach the base, so that a basal temperate layer has not been observed there. However, the authors postulate the existence of a temperate layer of several hundred meters thickness there, which would considerably contribute to the ice motion, as temperate ice is soft (cf. Sect. 3.3.2). The small difference in temperature profiles between boreholes drilled in the centre versus those drilled at the margins of the ice stream suggests that strain heating in the shear margins at these locations is small. Drainage behaviour of the borehole liquid indicated the likely presence of a linked-cavity-type subglacial hydrologic drainage system. Lüthi *et al.* (2002) found a temperate layer of 30 m thickness adjacent to the ice stream. The tilt measurements reveal that basal sliding contributed about 60% to the surface ice velocities here. The authors interpreted their data with the help of a numerical model Funk *et al.* (1994). They inferred a microscopic water content of 1% near the cold-temperate transition surface (CTS), the interface between cold and temperate ice in the glacier, and a basal melting rate of about 0.1 m a^{-1} .

Phase II (1998 until fall 2003)

The pattern of stable calving front migration changed in 1998, when an unusually early break-up of the ice mélange in front of the glacier prolonged the calving season by almost two months (Joughin *et al.*, 2008). As a consequence, the calving front retreated 2 km further upstream than the multi-decadal minimum (Sohn *et al.*, 1998). In the summer of 1999, the calving front retreated an additional 2.5 km, and did not readvance back to its maximum extent at the head of Tissarissq Ice Bay in the following winter. While the calving front did so in the winters of 2000/2001 and 2001/2002, it retreated further inland each summer by about 2 km. In the winter of 2002/2003, the ice front did not re-advance as usual, but instead stagnated at the position of maximum summer retreat in 2002 (Podlech & Weidick, 2004). During the subsequent melt season in 2003, a large part of Jakobshavn Isbræ's ice tongue disintegrated, resulting in 7.5 km of calving front retreat (Fig. 2.5c).

Ice velocities in the fast flowing parts of the ice stream strongly increased in amplitude and seasonal variability during the break-up of the floating ice tongue, cf. Fig. 2.6 and Joughin *et al.* (2008). The flow acceleration rapidly travelled upstream, and spread from there to the surrounding ice sheet in a strongly dampened fashion. Annual average velocities increased by about 5% per year in the ice stream, and a slower $\sim 1.5\%$ per year in the northern branch during this phase. The speedup was not uniform, but followed a step change in 1998, ensued by a nearly year-long period of little change, prior to a large speedup in 2000. By spring 2003, the glacier's speed had increased to 12.6 km a^{-1} near the grounding line, a 70% increase compared to prior to the break-up of the ice tongue. The sparsely sampled data from 2000 to 2003 also suggest a non-uniform speedup, with a minor slowdown in 2001 (Joughin *et al.*, 2008).

After 1997, the lower elevation regions of the branches have been thinning strongly, which spread out to the surrounding ice sheet in a dampened pattern. Analysis of repeat airborne surveys revealed thinning rates of more than 10 m a^{-1} on grounded ice. Most of this thinning has been attributed to ice stretching caused by flow acceleration ("dynamic thinning") (Thomas *et al.*, 2003; Joughin *et al.*, 2008). The thinning signal increased with time to more than 15 m a^{-1} and extended tens of kilometres inland along the glacier's main trunk. Jakobshavn Isbræ's floating ice tongue thinned by about 320 m from 1997 to 2001, which lead to ungrounding of several square kilometres of ice (Thomas *et al.*, 2003). Large rifts, that had not been observed earlier, appeared in the northern part of the ice tongue near the grounding line from 2000 onwards. These rifts and the thinning weakened the ice tongue, which therefore produced much less resistance to upstream flow ("buttressing") (Joughin *et al.*, 2008). The thinning has been attributed to both flow acceleration and especially increased submarine melting (Krabbill *et al.*, 2004; Thomas *et al.*, 2003): decreasing heat loss of the Irminger Current into the Labrador sea caused an increase in subsurface water temperatures in Disko Bugt by about 1.1°C from 1997 onward (Yashayaev, 2007), which has been proposed as a cause for the destabilization of the ice tongue through increased submarine melt (Holland *et al.*, 2008).

The mass balance of Jakobshavn Isbræ rapidly turned negative with the disintegration of the ice tongue due to the increase in submarine melting and dynamic discharge. Jakobshavn Isbræ was losing 8 to 11.3 Gt a^{-1} of mass per year in 2000 (Howat *et al.*, 2011; Rignot & Kanagaratnam, 2006). The rate of mass loss increased over the following years to nearly 25 Gt a^{-1} by the end of 2002 (Howat *et al.*, 2011).

No published measurements of englacial temperature in the ice stream and its shear margins during the break-up of the ice tongue exist. We are therefore unable to say whether and how the thermal regime influenced the glacier's evolution at that time.

Phase III (late 2003 trough today)

The northern branch and ice stream of Jakobshavn Isbræ became disconnected in the summer of 2004, when yet another retreat of the calving front by 3 km completed the disintegration of the ice tongue. From then on, an ephemeral ice tongue built up every winter but quickly disintegrated at the onset of the melt season every year, so that the calving front in summer is

essentially grounded (Dietrich *et al.*, 2007). The terminus kept retreating at an average rate of 1 to 2 km a⁻¹, with annual fluctuation of its position of 1 to 3 km (Fig. 2.6).

Ice velocities linearly increased by 5% per year over much of the glacier's fast moving area. A strong, increasing seasonal fluctuation of up to 40% of the average velocity is superimposed on this trend, which is largest in the vicinity of the calving front (Fig. 2.6). During and after a calving event, terminus ice velocities may reach maxima of up to 25.5 km a⁻¹ (Rosenau *et al.*, 2013). The glacier readjusts to the new geometry over a period of 4 to 5 days, during which flow velocities decrease to pre-calving values (Amundson *et al.*, 2010). Ice sheet wide observations of ice surface velocity reveal a widespread inland flow acceleration of about 100 m a⁻¹ for about one month at the onset of the melt season. This velocity "spike" does not correlate with the calving front position, and is most apparent in areas where there is no other seasonal variation. This speedup appears to be a response to increased basal lubrication (Zwally *et al.*, 2002; Joughin *et al.*, 2008).

The thinning rates of Phase II continued and peaked to more than 20 m a⁻¹ in the ice stream during the following years (Joughin *et al.*, 2008; Hurkmans *et al.*, 2012; Helm *et al.*, 2014). From 2004 to 2010, the grounding line of Jakobshavn Isbræ retreated 3.5 ± 0.2 km, resulting in a total grounding line retreat of 6 km since 1985 (Rosenau *et al.*, 2013). The ice discharge across the grounding line increased to 46 km a⁻³ in 2005 (Rignot & Kanagaratnam, 2006). By the end of 2010, the glacier had lost 321 ± 12 Gt of ice, with two thirds of the loss occurring since summer 2005. 85 km² of ice area reduction due to calving front retreat accounts for nearly 20% of this loss. The glacier was now losing mass nearly throughout the year (Howat *et al.*, 2011). We are unaware of more recent publications on Jakobshavn Isbræ's mass balance since 2011, but given that the glacier continued to retreat and to flow at high speeds it is likely that its annual net mass balance stayed negative.

Only few temperature measurements exist from the time after the break-up of Jakobshavn Isbræ's ice tongue, and none of them are taken in the areas of fast flow. Lüthi *et al.* (2015) presented four full-depth temperature profiles from two drill sites in the ablation zone about 30 km north of Jakobshavn Isbræ's terminus. A temperature difference of up to 4 °C in two boreholes only 86 m apart illustrated the high horizontal variability of the ice sheet's thermal structure in the ablation zone, which they attributed to additional englacial heat sources in the ablation zone, such as cryo-hydrologic warming (Phillips *et al.*, 2010). The authors thus cautioned against interpretation of single boreholes in areas where englacial heat sources strongly affect the thermal structure of the ice.

2.3 Modelling Studies

The observations listed above describe rapid changes of Jakobshavn Isbræ over the last two decades, but they yield only little insight into the glacier's internal dynamics that cause and sustain the changes. Therefore, models have been employed to fill in these gaps. Here, we present a brief overview over the most relevant modelling studies on Jakobshavn Isbræ.

Funk *et al.* (1994) studied the thermal regime of Jakobshavn Isbræ using a two-dimensional (2D) thermodynamically coupled flow-band model, which simulates ice flow along a vertical slice of the ice sheet. The authors compared their model results with borehole temperature profiles published in Iken *et al.* (1993). They postulated the existence of a basal temperate layer of up to several hundred meter thickness extending from the ice sheet margin to about 200 km inland, formed by intense strain heating at the base. The authors attribute discrepancies between their model results and observations to three-dimensional flow effects, which are not accounted for in flow-band models.

Truffer & Echelmeyer (2003) used a Finite-Element model (cf. Sect. 3.4) to calculate three-dimensional (3D) flow through a cross-section of Jakobshavn Isbræ about 50 km upstream of the calving front. They found that the deep trough underneath Jakobshavn Isbræ determines the glacier's flow pattern. Vertical shear in an enhanced (i.e. artificially softened) basal layer, as well as lateral shear in the shear margins both contribute to ice motion. Modelled shear stress exceeded 300 kPa at the steep side walls of the trough. The authors inferred a basal melting rate beneath Jakobshavn Isbræ of about 0.5 m a^{-1} , and thus hypothesize that Jakobshavn Isbræ must possess an efficient drainage system. The authors conclude that the glacier possesses stable dynamics, since it is dominated by the bedrock topography.

Johnson *et al.* (2004) studied the flow dynamics of Jakobshavn Isbræ's floating ice tongue prior to its disintegration using a plane-stress model and a shelfy-stream approximation (SSA, cf. Sect. 3.3.2). None of the models is able to reproduce the observed velocities without resorting to unphysical model parameters, highlighting that the dynamics of the floating ice tongue are poorly understood.

Thomas (2004) studied impact of the force perturbation induced by the break-up of the ice tongue on the glacier using a set of equations specifically derived for this purpose. The author found that the net sum of driving and resisting forces of the ice stream is quite small, so that small changes in either one of the components is able to cause large changes in the net driving stress. He posed that calving of 4 km from the glacier's floating ice tongue in 1997/1998 likely caused a large drop in buttressing, and that basal drag in the ice stream is small compared to the lateral and driving stress (about 50 kPa vs. more than 300 kPa). The analysis identifies several negative feedback mechanisms between the mass transport and the stress regime, which would quickly balance any force perturbation at the calving front (like calving front retreat) once the force perturbation stops.

van der Veen *et al.* (2011) performed a force balance analysis of Jakobshavn Isbræ and found that the reduction in back stress alone caused by the break-up of the ice tongue (Thomas, 2004) was not sufficient to cause the observed acceleration along the ice stream. Instead, the authors surmised that the lateral margins of Jakobshavn Isbræ must have weakened substantially to allow the ice stream to accelerate. They proposed cryo-hydrologic warming (Phillips *et al.*, 2010) and/or weakening through an increase in microscopic water content (Lliboutry & Duval, 1985) as possible explanations for this effect. The lack of both thermodynamical coupling and the capability for prognostic simulations in their model did not allow the authors to investigate this question further.

Vieli & Nick (2011) studied the sensitivity of Jakobshavn Isbræ to calving front migration using a flow-band model (Nick *et al.*, 2010). The authors found that calving front retreat triggered flow acceleration at the terminus, which spread inland through several feedbacks: flow acceleration caused dynamic thinning and surface steepening, which increased the driving stress inland. At the same time, thinning caused a reduction in basal drag through grounding line retreat and decreasing the basal effective pressure. The authors concluded that the changes occurring at Jakobshavn Isbræ have been triggered at the terminus. The flow-band model parameterized the lateral drag of the ice stream, and did not include thermodynamic coupling. It was therefore not able to capture the interaction between the ice stream and the ice sheet, like lateral stress transfer and lateral ice influx.

Price *et al.* (2011) studied the response of Jakobshavn Isbræ to a one-step, one-time stress perturbation at the terminus using a three-dimensional (3D) thermodynamically coupled model (Price *et al.*, 2007). The study focusses on the contribution of Greenland to global sea level rise until 2100 and does not investigate details of Jakobshavn Isbræ's response to the stress perturbations. Moreover, the authors acknowledge that the resolution, physics and the simplified stress perturbation applied in the model do not allow to recreate Jakobshavn Isbræ's complex observed behaviour.

Joughin *et al.* (2012) extended the observational record of surface velocities and thinning rates presented in (Joughin *et al.*, 2008), and used a 1D stress-balance model and a 2D SSA model to relate changes in the glacier speed to the geometry through variations in basal friction and horizontal stress. The authors found that dynamic thinning of the glacier dampened the glacier's response to calving front retreat and that the bed in the trough provides little resistance to flow within about 20 km of the calving front, which agrees with Thomas (2004). Lateral stress transfer the ice stream's high driving stress to the bedrock adjacent to the ice stream. The authors propose the same mechanism for upstream glacier acceleration as described by Vieli & Nick (2011). Despite their finding of low basal resistance in the deep trough, the authors attributed about half of the observed speed-up to a thinning-induced drop in basal effective pressure at that location. However, the authors acknowledged that there is enough uncertainty to allow for other feedbacks such as speedup-induced softening of the margins through enhanced lateral shearing and thermal rheological feedbacks to contribute to the acceleration, which they were not able to test with their model.

Habermann *et al.* (2013) studied the evolution of the basal shear stress from inversions with a 2D SSA model (PISM, Bueler & Brown, 2009) during the years 1985, 2000, 2005, 2006 and 2008. Similar to Joughin *et al.* (2012), they found significant lowering of this value in the first 7 km upstream of the 2008 grounding line during the speedup in the 2000s, and relate it to lowering of the basal effective pressure.

Nick *et al.* (2013) applied the flow-band model used in Vieli & Nick (2011) to determine the future behaviour of Jakobshavn Isbræ and three other main Greenland outlet glaciers until 2200. The authors found that the dynamics of Jakobshavn Isbræ are highly sensitive to a reduction in ice mélange, enhanced hydro-fracturing through surface melt and forcing by submarine melting when an ice tongue is present. They projected further calving front and grounding line retreat, and that the mass loss of Jakobshavn Isbræ, which is dominated by dynamic discharge, would stay

roughly constant at an average of 18.7 to 22.8 Gt per year. However, their model shared the same shortcomings as stated under Vieli & Nick (2011), and thus did not address the impact of the thermal regime on flow dynamics of Jakobshavn Isbræ, nor the dynamic interaction between the ice stream and the surrounding ice sheet.

Seroussi *et al.* (2013) used a 3D higher-order ice flow model (HOM, cf. Sect. 3.3.2) to reproduce the present-day ice flow of the GrIS, and found that steady-state temperature profiles derived from present-day conditions represent the ice sheet's thermal regime to a reasonable degree. The results show that about 80% of Jakobshavn Isbræ's base (with exception of the areas at the central ice divide) is at pressure melting point. However, the study did not address the impact of rapid calving front retreat on the dynamics of the ice sheet. A maximum mesh resolution of 1 km may not have been sufficient to resolve the narrow and deep troughs of the outlet glaciers. The authors concluded that it is reasonable to use steady-state temperature profiles for short-term (decades to a century) projections, as the ice sheet at these time scales is far more sensitive to forcings like basal sliding and atmospheric conditions.

Muresan *et al.* (2016) studied the evolution of Jakobshavn Isbræ during 1990 to 2014 using a superposition of the shallow-ice approximation (SIA, Hutter, 1983) and the shallow-shelf or shelfy-stream approximation (cf. Sect. 3.3.2) in the Parallel Ice Sheet Model (PISM, Bueler & Brown, 2009; Winkelmann *et al.*, 2011), which includes the enthalpy method (cf. Sect. 3.3.3). The authors attempt to reproduce the observed calving front positions of Jakobshavn Isbræ by tuning atmospheric forcing and an submarine melting parameterization. They find that most of the glacier's current retreat is driven by the ocean parameterization and the glacier's subsequent response, which is largely governed by the bed geometry. The authors acknowledge several shortcomings of their study, of which the most relevant one is perhaps the mesh resolution dependency of their results. While the authors agree with Vieli & Nick (2011) and Joughin *et al.* (2012) on the thinning-induced mechanisms that transfer the speedup inland and note that shear margin weakening causes speedup in the early 1990s (van der Veen *et al.*, 2011), they do not investigate the contributions to the lateral shear margin weakening, nor do they present the evolving thermal regime of their modelled glacier.

Shapiro *et al.* (2016) used a Full-Stokes ice flow model (Elmer/Ice, Gagliardini *et al.*, 2013, cf. Sect. 3.3.2) to derive the basal shear stress under Jakobshavn Isbræ and two other Greenland outlet glaciers. In agreement with Thomas (2004) and Joughin *et al.* (2012), the authors find that the areas of fast ice flow coincide with areas of low (10 to 40 kPa) basal shear stress, and that most of the glacier's driving stress is balanced by lateral stress transfer ("lateral drag") to the bed underneath the shear margins. The authors discussed their results with opposing conclusions presented in Iken *et al.* (1993), Funk *et al.* (1994), and Lüthi *et al.* (2002), which state that most of Jakobshavn Isbræ's horizontal motion is due to vertical deformation, and showed that the boreholes presented in those studies were drilled in areas of localized high basal shear stress. This result cautions against the interpretation of single borehole measurements of englacial deformation. Moreover, they emphasize the need to model the lateral stress component in the

ice stream explicitly due to its large contribution to the glacier's momentum balance, and possibly its thermal regime. The presented stress-balance computations do not allow to conclude on the glacier's thermal regime, nor do they allow to evaluate the effect of calving front retreat on the interaction between the ice stream and the ice sheet.

2.4 Synopsis

The array of presented observations and modelling studies provides some insight into the flow dynamics of Jakobshavn Isbræ. The bedrock topography defines much of the glacier's flow in both the grounded and floating areas. This holds especially for the last 70 km of the deep trough, in which the ice stream is located. Here, driving stresses are high, but only little of the driving stress is supported by the bedrock underneath, and a large fraction of its horizontal motion is due to basal sliding. Instead, most of the driving stress is transferred to the steep trough side walls and adjacent ice sheet, which results in pronounced lateral shear margins to either side of the ice stream.

Ice velocities range from meters to hundreds of meters per year on the ice sheet, and rapidly accelerate in the shear margins to several kilometres per year in the fast-flowing branches. The position and thickness of the terminus exerts a strong control on the flow velocities of the branches, and large areas of the inland ice. The exact type and interplay of the underlying processes that influence the flow speeds are unclear. Moreover, the processes which sustain the widespread flow acceleration after the ice tongue disintegrated are poorly understood.

High submarine melting thins the ice tongue from underneath. Highest melting rates occur at the grounding line. The calving front migrates under the influence of ice flow and calving of icebergs. Calving rates at Jakobshavn Isbræ are sensitive to the presence of an ice mélange in front of the glacier, surface air temperatures and, possibly, submarine melting rates. The link between calving and atmospheric as well as oceanic forcing is poorly understood.

Jakobshavn Isbræ was roughly in equilibrium or in slight negative mass balance during presence of the floating ice tongue. Two-thirds of the ice was lost by calving, one third by melt. After the break-up of the ice tongue, the glacier's mass balance turned increasingly negative, and calving became the dominant form of ice loss.

Jakobshavn Isbræ has a highly variable, but poorly constrained polythermal regime, which is dominated by the advection of ice. Vertical temperature profiles in the vicinity of the ice stream show a strong temperature inversion, with a comparatively warm upper ice column, a cold core at medium depth and a temperate base. Some boreholes show a basal temperate layer of 30 m thickness, but the lateral extent of the temperate layer is unknown. The presence of a thick basal temperate layer in the centre of the ice stream has been postulated, but has not been directly observed.

The type of the basal hydrology system underneath Jakobshavn Isbræ is poorly constrained, but observations point towards an inefficient drainage system. Flow acceleration attributed to basal lubrication variability at the

onset of the melt season is short (about 1 month) and only significant in the ice sheet interior.

Explanatory hypotheses concerned with Jakobshavn Isbræ's acceleration after the break-up of its floating ice tongue can be categorized in three groups. On the one hand, Thomas (2004) proposes that the calving front retreat reduces the back force on the glacier so that it accelerates. On the other hand, van der Veen *et al.* (2011) show that this back force reduction is not sufficient to explain the inland acceleration of the glacier, and surmise that the shear margins of the ice stream must have weakened through e.g. thermal effects. Others, like Vieli & Nick (2011) and Joughin *et al.* (2012) argue that thermal effects are unsuitable to explain for example the seasonality in the velocity signal, and posit that inland acceleration is instead sustained through a thinning-induced feedback chain: acceleration triggered by calving front retreat leads to dynamic thinning, which simultaneously leads to driving stress increase and basal drag reduction, and thus further acceleration inland. Despite the fact that these hypotheses seemingly contradict each other, they have never been tested with an ice flow model. Most ice flow models lacked at least one of the crucial features to represent Jakobshavn Isbræ's flow dynamics, like lateral stress transfer, the thermal regime, and most importantly, the dynamically evolving calving front of Jakobshavn Isbræ (cf. Sect. 2.6 below).

2.5 Open Questions

Despite the extensive array of observations and modelling studies presented above, several questions about Jakobshavn Isbræ's dynamics remain unanswered:

1. What are the 3D thermal and stress regime of Jakobshavn Isbræ, in particular in areas of fast flow?
2. How did the changes in the glacier's stress regime since the disintegration of the ice tongue affect the glacier's thermal regime, and vice versa?
3. Which processes enable and sustain the glacier's acceleration?
4. Which mechanisms would help the glacier stabilize, and how much ice will the glacier have lost until then?

2.6 Model Requirements

Answering the open questions on Jakobshavn Isbræ requires thorough understanding of the glacier's thermodynamics. Therefore, they can be addressed using a numerical ice sheet model. What are the requirements that a numerical ice sheet model needs to fulfil in order to represent the glacier's most relevant features?

2.6.1 Feature Requirements

Firstly, the model needs to be able to simulate the transient evolution of the glacier and it should rely as much as possible on described physical

processes. So-called “tuning-parameters” or “enhancement-factors” (e.g.: Huybrechts *et al.*, 1991; Funk *et al.*, 1994; Truffer & Echelmeyer, 2003; Vieli & Nick, 2011) may obfuscate the physical processes underlying the glacier’s behaviour. Secondly, the dominating influence of the terminus position on Jakobshavn Isbræ demands the ability to dynamically evolve the calving front position in the model. Thirdly, dynamic lateral effects like stress transfer and mass influx are important to Jakobshavn Isbræ’s dynamics and need to be modelled explicitly, which excludes flow-band models from the list of suitable candidates. Lastly, the glacier’s polythermal regime requires a thermodynamically coupled model, which represents both cold and temperate ice. In order to fulfil this requirement, the model needs to be three-dimensional.

2.6.2 Technical Requirements

Besides the model features listed above, the technical requirements to the model are: the model needs to be tested and verified. Only then we can have confidence that results of a real-world glacier case are robust. The model’s ability to finely resolve areas crucial to ice flow such as highly localised ice streams is an advantage, as it help to minimize computational effort while maximising spatial resolution in regions where it matters. Three-dimensional, high-resolution modelling of a large outlet outlet in time is computationally expensive. A parallelized model architecture to share the computational load among multiple processors will help to cut computational time.

2.6.3 Model Choice

Creating a functioning ice flow model is a complex task. Instead, we choose to use one of the ice flow models that have emerged during the last two decades. The list of demands on the ice flow model made us opt for the Ice Sheet System Model (ISSM, Larour *et al.*, 2012a), a thermodynamically coupled, parallel, finite-element ice flow model. The ISSM was not able to capture Jakobshavn Isbræ’s polythermal regime fully nor its dynamically evolving calving front at the beginning of this PhD project, so that features that enable this need to be developed. ISSM is described in Sect. 3.5.

2.7 Objectives of this Thesis

The overarching objective of this thesis is to study the dynamic changes of Jakobshavn Isbræ before, during and after the disintegration of its ice tongue using ISSM, in order to determine the thermodynamic processes that cause and sustain the glacier’s observed widespread flow acceleration and thinning. In order to accomplish this task, we aim to:

1. implement crucial, but missing model features into ISSM (cf. Sect. 2.6). This step requires:
 - (a) completion and testing of the implementation of the enthalpy method (cf. Sect. 3.3.3),
 - (b) design, implementation, and testing of a method that allows for dynamic calving front evolution,

2. create a 3D thermodynamically coupled model of Jakobshavn Isbræ,
3. apply the calving-front-evolution method to assess the changes in thermal and stress regime of Jakobshavn Isbræ during the calving front retreat,
4. assess the mechanisms that sustain the acceleration of Jakobshavn Isbræ, and discuss current explanatory hypotheses for the changes (cf. Sect. 2.4) in that context,
5. identify fields where further study is required.

3 Modelling Glaciers and Ice Sheets

3.1 On the Use of Models

A model is any set of computable mathematical equations, algorithms and/or inequalities, which are designed to describe a real process. Models are applied in many fields of science where results can be quantified. There exist no general rules for the creation of a model. However, the modelling process can be subdivided into different stages with no strict chronological order (Burger, 2007):

- Understanding of the described process
- Choice of scales, and corresponding mathematical description
- Development of the mathematical model
- Sensitivity analysis and (optional) simplification of the model
- Numerical simulation
- Comparison of the solution to real data
- If necessary, improvement of the model or optimization of parameters
- Presentation of the results

Several points become clear from the list. First, the model user, the model and the model results mutually affect each other. Second, while using models and interpreting model results, it is important to keep in mind that models are always simplifications, which base on certain assumptions. Moreover, model input data sets carry errors and are often inconsistent. Therefore, the proof of robustness of the model results requires an extensive sensitivity analysis to the model input parameters.

These points reveal that any presented model result has no absolute validity, and can never replace measurements of the process itself. Plausible model results do not prove the validity of the assumptions underlying a model. If unaware, the model user risks to confirm his biases and support incorrect intuitions. Instead, the function of model use is to enhance the understanding of the modelled process, and thus to guide further study. Therefore, in the view of e.g. Oreskes *et al.* (1994), a model is most useful when used to challenge existing formulations, rather than attempting to validate or verify them.

3.2 Elements of Level-Set Methods

A *Level-Set Method* (LSM) is a conceptual framework which uses level-sets of functions for analysis of interfaces and slopes in Eulerian configuration. They have been developed in the 1980s by S. Osher and J. Sethian (Osher & Sethian, 1988), and are a popular tool in many numerical disciplines like image processing, computer graphics, computational geometry, optimization and computational fluid dynamics (Sethian, 2001; Osher & Fedkiw, 2006).

Let $\Omega \subset \mathbb{R}^m$ be an open subset of finite-dimensional space and $[0, T] \subset \mathbb{R}$ a time interval. The basic idea of a LSM is to both represent and evolve a boundary through an auxiliary function, $\varphi : \Omega \times [0, T] \rightarrow \mathbb{R}$, the *Level-Set Function* (LSF), which we set to be continuously differentiable. For $c \in \mathbb{R}$, we define the c -level-set of φ by:

$$\Gamma_c(t) = \{x \in \Omega : \varphi(x, t) = c\}. \quad (3.1)$$

Γ_c is thus defined implicitly by $\varphi = c$. Taking the material derivative of $\varphi = c$ on Ω , we obtain a transport equation for the c -level-set, the *Level-Set Equation* (LSE):

$$\frac{\partial \varphi}{\partial t} + \mathbf{w} \cdot \nabla \varphi = 0. \quad (3.2)$$

Here, \mathbf{w} is the velocity of the c -level-set. For numerical applications it is useful to define \mathbf{w} at least on an open environment around Γ_c , or the entire domain, Ω . Since the c -level-set of φ , and the 0-level-set of $\tilde{\varphi} = \varphi - c$ describe the same set of points, it is sufficient to consider only the 0-level-set of φ for analysis of shapes and the outline of a continuum like a glacier. We denote the 0-level-set of φ by $\Gamma(t) = \Gamma_0(t)$.

The LSE is a Hamilton-Jacobi-type partial differential equation (PDE). It requires an initial condition, $\varphi_0(x, t_0)$ for all x in Ω , and boundary conditions at inflow boundaries. The LSE is solved numerically, which requires sophisticated stabilization techniques: the solution to the LSE may develop noise and sharp gradients over time, which may impede the retrieval of its 0-level-set. Since we only care for the position of the 0-level-set in applications, we can apply routines for “reinitialization” of the LSF, i.e. replacing the old, degenerated LSF with a new one, which respects both the position of the old 0-level-set and $\|\nabla \varphi\| \simeq 1$. The nature of the modelled problem determines the frequency of how often we have to reinitialize the LSF.

The LSM introduces a powerful geometrical and analytical toolbox. Let $\varphi < 0$ define an area $\Omega_0 \subset \Omega$ with boundary Γ . Evaluation of whether a point $x \in \Omega$ is on Γ , or inside or outside of Ω_0 is done by looking at the sign of $\varphi(x, t)$. The unit surface normal on Γ is defined as:

$$\mathbf{n} = \frac{\nabla \varphi}{|\nabla \varphi|}, \quad (3.3)$$

since the gradient of φ is always perpendicular to the level-sets of φ . Since φ is defined on the entire domain Ω , this definition allows to continue the unit surface normal from Γ onto Ω . Similarly, computing volume and surface integrals of a function f defined on Ω_0 and Γ , respectively, becomes a question of evaluating the volume integral of $f \cdot \chi$ over Ω . Here χ is the characteristic function of the respective subset, which is easily constructed from φ .

The velocity of the ice boundary, w , is the sum of the ice velocity, v , and an accumulation-ablation flux, a :

$$w = v + a. \quad (3.4)$$

Ablation occurs for a pointing into the ice, and accumulation otherwise. Inserting Eq. (3.4) into the LSE (3.2) yields a *kinematic boundary condition*:

$$\frac{\partial \varphi}{\partial t} + v \cdot \nabla \varphi = -a \cdot \nabla \varphi. \quad (3.5)$$

It is known that the numerical scheme of the LSM does not conserve the volume nor the shape of Ω_0 accurately. To address this drawback, further sophisticated methods have been developed, like the combination of the original (Eulerian) LSM with a (Lagrangian) particle tracer method (Particle LSM, Enright *et al.*, 2002). The advantage of the LSM is that one can perform numerical computations involving curves and surfaces on a fixed discretization of the model domain, e.g. static Finite-Element meshes. The method facilitates following the boundary of continua that change their topology, which makes it a suitable tool to model the dynamic evolution of glaciers.

3.3 Large-scale Ice Sheet Thermodynamics

In this section, we state the equations that describe the large-scale thermodynamics of glaciers and ice sheets. They are derived from general principles of continuum mechanics, which are found in corresponding textbooks, e.g. Liu (2002). We refer to e.g. (Greve & Blatter, 2009) for a more detailed introduction of the equations stated here.

3.3.1 Mass Balance of Ice Sheets

Ice and Incompressibility

The ice found in glaciers and ice sheets is a polycrystalline material, which exhibits creep flow when a shear stress is applied (Hooke, 2005; Cuffey & Paterson, 2010). The deformation response to the applied stress is anisotropic due to its crystal structure and it changes over time in different creep phases (Cuffey & Paterson, 2010). It is common to assume for glaciers and ice sheets that the orientation of the crystals and ice grains is random, so that the overall response of ice to stress is isotropic (Greve & Blatter, 2009).

The density of an incompressible material is constant in both space and time. Strictly speaking, this does not hold for ice sheets: their density increases with depth, as fresh snow transforms to firn and compacts to ice. However, the largest density variations occur in the upper 50 to 100 m of the ice sheet (Cuffey & Paterson, 2010, p.16). Depending on the total thickness of the ice column, this typically decreases the average density of the ice column by 1 to 2%. Further below, both thermal expansion and compression alter the ice density with depth by at most 1% (Cuffey & Paterson, 2010). For these reasons, we assume that ice is an incompressible material here.

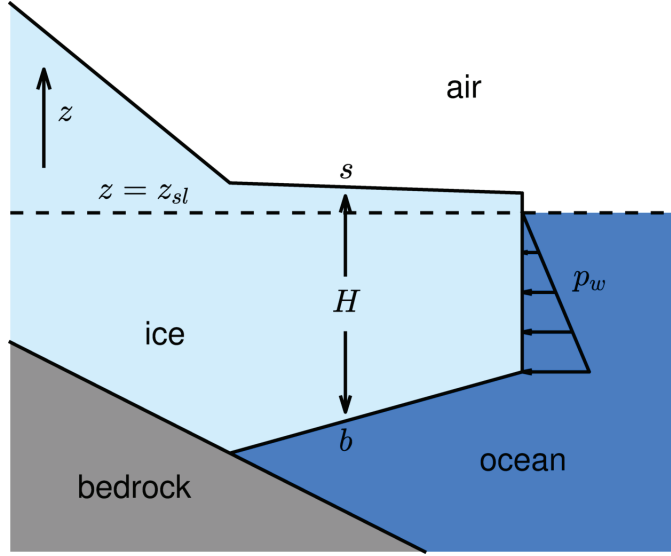


FIGURE 3.1: Schematic overview of the geometry of a marine-terminating outlet glacier and its ice tongue along the vertical, and the stress boundary condition at the calving front. Ice flow is to the right, and s is the ice surface elevation, b is the ice base, H is the ice thickness, z_{sl} is the sea level elevation, and p_w is the water pressure. The location where the ice detaches from the bedrock and starts floating is the grounding line.

Continuity Equation

The law of mass conservation states that the mass of a closed system remains constant over time. It is a fundamental concept of physics, and implies that mass that enters a system must either accumulate within the system or leave the system. The local form of the law reads:

Theorem 3.1. (Mass conservation) *Let $\Omega \subset \mathbb{R}^3$ be a material body of*

- *density $\rho : \Omega \times [0, T] \rightarrow \mathbb{R}_+^*$ and*
- *velocity $\mathbf{v} : \Omega \times [0, T] \rightarrow \mathbb{R}^3$*

for a time frame $[0, T]$. The mass conservation imposes:

$$\forall \mathbf{x} \in \Omega \quad \forall t \in [0, T], \quad \frac{d\rho}{dt} + \rho \nabla \cdot \mathbf{v} = 0 \quad (3.6)$$

The mass-balance equation (Eq. 3.6) reduces for incompressible materials to:

$$\nabla \cdot \mathbf{v} = 0, \quad (3.7)$$

which is also known as the *continuity equation* for incompressible materials.

Kinematic Boundary Conditions

We choose the coordinate system so that for a point $\mathbf{x} = (x, y, z)$, the x and y coordinate describe the horizontal components in 3D space and that the z coordinate describes its vertical direction. Let the velocity in 3D be $\mathbf{v} = (v_x, v_y, v_z)$. The ice surface, s , and ice base, b , are represented implicitly by the 0-level-sets of the functions:

$$F_s(\mathbf{x}, t) = s(x, y, t) - z \text{ and } F_b(\mathbf{x}, t) = z - b(x, y, t), \quad (3.8)$$

respectively. In this case, the kinematic boundary condition (3.5) becomes:

$$\frac{\partial s}{\partial t} = -v_x \frac{\partial s}{\partial x} - v_y \frac{\partial s}{\partial y} + v_z + a_s \quad (3.9)$$

at the ice surface, and

$$\frac{\partial b}{\partial t} = -v_x \frac{\partial b}{\partial x} - v_y \frac{\partial b}{\partial y} + v_z + a_b \quad (3.10)$$

at the ice base. Here, a_s and a_b denote the surface and base accumulation-ablation function, respectively. Accumulation occurs for positive values and ablation for negative values, respectively.

Ice Thickness Equation

Let $H(\mathbf{x}, t) = H(x, y, t) = s(x, y, t) - b(x, y, t)$ be the ice thickness (cf. Fig. 3.1), and

$$\mathbf{Q} = \begin{pmatrix} Q_x \\ Q_y \end{pmatrix} = \begin{pmatrix} \int_b^s v_x dz \\ \int_b^s v_y dz \end{pmatrix} \quad (3.11)$$

the volume flux. Vertical integration of the continuity equation (3.7) and application of the kinematic boundary conditions (3.9) and (3.10) at ice surface and base yields the *ice thickness equation*:

$$\forall \mathbf{x} \in \Omega, t \in [0, T], \quad \frac{\partial H}{\partial t} = -\operatorname{div} \mathbf{Q} + a_s - a_b \quad (3.12)$$

For a detailed derivation of this equation, see e.g. (Greve & Blatter, 2009).

3.3.2 Momentum Balance of Ice Sheets

We introduce a few fundamental variables of continuum mechanics. Let \mathcal{M}^2 the second-order tensor space. The symmetric *Cauchy stress tensor*, $\boldsymbol{\sigma} \in \mathcal{M}^2$, defines the state of stress at a point inside a continuum and at its boundaries. The pressure is defined as:

$$p = -\frac{1}{3} \operatorname{tr}(\boldsymbol{\sigma}), \quad (3.13)$$

where $\operatorname{tr}(\cdot)$ is the trace operator. Since one can apply any pressure to an incompressible material body without changing its shape, the applied stress cannot be determined from the deformation alone (Truesdell & Noll, 2004). It is therefore convenient to introduce the *deviatoric stress tensor*, $\boldsymbol{\sigma}' \in \mathcal{M}^2$:

$$\boldsymbol{\sigma} = \boldsymbol{\sigma}' - p\mathbf{I}, \quad (3.14)$$

where $\mathbf{I} \in \mathcal{M}^2$ is the identity tensor. The symmetric *strain-rate tensor*, $\dot{\boldsymbol{\epsilon}} \in \mathcal{M}^2$, describes the rate-of-change of the deformation of a material in the neighbourhood of a point:

$$\dot{\boldsymbol{\epsilon}} = \left(\frac{1}{2} \left(\frac{\partial v_i}{\partial x_j} + \frac{\partial v_j}{\partial x_i} \right) \right)_{ij}. \quad (3.15)$$

Its main diagonal components $\dot{\epsilon}_{ii}$ describe the body's dilatation rates in the respective spatial directions and the off-diagonal components $\dot{\epsilon}_{ij, i \neq j}$ represent the shear rates of the body, respectively. The *effective deviatoric stress*, σ'_e , and *effective strain rate*, $\dot{\epsilon}_e$, are the second invariant of the deviatoric stress tensor and the strain rate tensor, respectively:

$$\begin{aligned}\sigma'_e &= \frac{1}{2} \text{tr} (\boldsymbol{\sigma}')^2 \\ &= \frac{1}{2} [(\sigma'_{xx})^2 + (\sigma'_{yy})^2 + (\sigma'_{zz})^2] + \sigma'_{xy} + \sigma'_{xz} + \sigma'_{yz}\end{aligned}\quad (3.16)$$

$$\begin{aligned}\dot{\epsilon}_e &= \frac{1}{2} \text{tr} (\dot{\boldsymbol{\epsilon}})^2 \\ &= \frac{1}{2} [(\dot{\epsilon}_{xx})^2 + (\dot{\epsilon}_{yy})^2 + (\dot{\epsilon}_{zz})^2] + \dot{\epsilon}_{xy} + \dot{\epsilon}_{xz} + \dot{\epsilon}_{yz}\end{aligned}\quad (3.17)$$

Quasi-Static Flow

The balance of linear momentum is the extension of Newton's Second Law to bodies with continuous mass distribution:

Theorem 3.2. (Balance of linear momentum) *We consider the same system as in Theorem 3.1, subject to a body force $\rho \mathbf{b} : \Omega \times [0, T] \rightarrow \mathbb{R}^3$. The balance of linear momentum is:*

$$\forall \mathbf{x} \in \Omega \quad \forall t \in [0, T], \quad \rho \frac{d\mathbf{v}}{dt} = \rho \mathbf{b} + \nabla \cdot \boldsymbol{\sigma} \quad (3.18)$$

Two body forces act on glaciers: 1) the gravitational force $\rho \mathbf{g}$ and 2) the Coriolis force due to the rotation of the Earth, $2\rho \boldsymbol{\Omega} \times \mathbf{v}$. Here, $\boldsymbol{\Omega}$ is the angular velocity vector of the rotating reference frame. Then the balance of linear momentum (Eq. 3.18) becomes:

$$\rho \left(\frac{\partial \mathbf{v}}{\partial t} + (\mathbf{v} \cdot \nabla) \mathbf{v} \right) = \nabla \cdot \boldsymbol{\sigma} + \rho \mathbf{g} - 2\rho \boldsymbol{\Omega} \times \mathbf{v} \quad (3.19)$$

This non-linear PDE is difficult to solve. A scaling analysis reveals that acceleration and inertia term of glaciers and ice sheets are negligible (e.g. Greve & Blatter, 2009, p.111), even for the most extreme cases of glacier flow, like glacier surge. The Coriolis force is larger than the acceleration terms, but still 7 orders of magnitude smaller than the force exerted by the gravitational acceleration (Greve & Blatter, 2009). Dropping the corresponding terms, Eq. (3.19) simplifies to:

$$\nabla \cdot \boldsymbol{\sigma} + \rho \mathbf{g} = 0 \quad (3.20)$$

We require a constitutive equation ("material law") to describe how ice deforms in response to an applied stress field. Even though ice is an anisotropic, polycrystalline material, it is commonly treated as a perfectly isotropic, incompressible viscous fluid (Hooke, 2005, p.271), so that

$$\boldsymbol{\sigma}' = 2\mu \dot{\boldsymbol{\epsilon}}, \quad (3.21)$$

where the viscosity μ is a scalar value. Without further approximation, insertion of Eqs. (3.21) and (3.14) into (3.20) yields the *Full-Stokes model* for ice

flow:

$$\begin{aligned} 2\nabla \cdot (\mu \dot{\epsilon}) - \nabla p + \rho \mathbf{g} &= \mathbf{0}. \\ \nabla \cdot \mathbf{v} &= 0 \end{aligned} \quad (3.22)$$

This model has 4 equations for 5 unknowns: the three components of the velocity, $\mathbf{v} = (v_x, v_y, v_z)$, the pressure, p , and the viscosity, μ . Therefore, the Full-Stokes model needs to be closed by a constitutive equation as given by Glen's Flow Law (below). From here onwards, ρ denotes the ice density unless stated otherwise.

Boundary Conditions

Mechanical boundary conditions are required to solve the equations of momentum balance (3.22). Let \mathbf{n} be the outward-pointing unit normal on the respective ice boundary.

Ice-air boundary The atmospheric pressure, p_a , is negligible compared to the hydrostatic pressure of ice. Therefore, the ice-air boundary is treated as a free surface:

$$\boldsymbol{\sigma} \cdot \mathbf{n} = -p_a \mathbf{n} \equiv \mathbf{0}. \quad (3.23)$$

Ice-ocean boundary At the ice-ocean boundary, the hydrostatic pressure of water, p_w , applies, which linearly increases with depth (Fig. 3.1):

$$\boldsymbol{\sigma} \cdot \mathbf{n} = -p_w \mathbf{n} = \max(0, \rho_w g(z_{sl} - z)) \mathbf{n} \quad (3.24)$$

Here, ρ_w is the density of the sea water and z_{sl} the sea level elevation. The back stress exerted by an ice mélange is small compared to the water pressure and therefore usually neglected.

Ice-bedrock boundary At the ice-bedrock interface, we have to apply two boundary conditions. A Dirichlet boundary condition ensures the impenetrability of ice and bedrock:

$$\mathbf{v} \cdot \mathbf{n} = -a_b \quad (3.25)$$

Any motion perpendicular to the basal tangential plane is thus due to the basal accumulation-ablation function, a_b .

A Neumann boundary condition governs the motion along the basal tangential plane. The process of basal sliding of glaciers is fundamental to ice stream dynamics, yet poorly understood. It is generally described using a viscous friction law (Cuffey & Paterson, 2010, p.240):

$$\|\mathbf{v}_b\| = k N_{eff}^{-q'} \|\boldsymbol{\tau}_b\|^{p'} \quad (3.26)$$

Here,

- $\mathbf{v}_b = \mathbf{v} - (\mathbf{v} \cdot \mathbf{n})\mathbf{n}$ is the velocity component in the basal tangential plane,
- $N_{eff} = \rho g H - \rho_w g b$ is the basal effective pressure: the difference between ice overburden pressure and water pressure at the ice base,

- $\boldsymbol{\tau}_b = \boldsymbol{\sigma} \cdot \mathbf{n} - (\mathbf{n} \cdot \boldsymbol{\sigma} \cdot \mathbf{n})\mathbf{n}$ is the friction stress component along the basal tangential plane,
- $k, p', q' > 0$.

The values for p' and q' are a matter of debate. Commonly, $(p', q') = (3, 1)$ or $(p', q') = (3, 2)$ are used for sliding over hard rock, and $(p', q') = (1, 0)$ for sliding over soft, deformable sediment. Weertman's law for basal sliding (Cuffey & Paterson, 2010, p.232) is special case of this equation for $p' = 3$ and $q' = 1$. It reads in vector form:

$$\boldsymbol{\tau}_b = -k^2 N_{eff}^{r'} \|\mathbf{v}_b\|^{s'-1} \mathbf{v}_b := -\alpha^2 \mathbf{v}_b \quad (3.27)$$

It is $r' = q'/p'$ and $s' = 1/p'$. The coefficients k and α depend on the thermal and mechanical properties of ice and the bedrock.

Glen's Flow Law

Glen (1955) conducted uniaxial compression experiments on ice in secondary creep phase (e.g. Cuffey & Paterson, 2010, p.52), from which he determined a relation between the effective strain rate and effective stress of glacier ice:

$$\dot{\epsilon}_e = \left(\frac{\sigma'_e}{B} \right)^n \quad (3.28)$$

Empirically derived values of the *stress exponent*, n , range from 1.5 to 4.2, but a value of $n = 3$ is most consistent with field data, and therefore widely used in analyses of glacier dynamics (Cuffey & Paterson, 2010, p.55). Since $n > 1$, any increase in effective deviatoric stress will lead to an even larger increase in effective strain rate.

Nye (1957) extended Glen's flow law to tensorial form to cover multi-axial states of stress. For isotropic materials, the principal axes of the deviatoric stress $\boldsymbol{\sigma}'$ and the strain rate tensor $\dot{\epsilon}$ coincide. In this case, we obtain *Glen-Nye flow law*:

$$\dot{\epsilon} = \frac{\sigma_e'^{n-1}}{B^n} \boldsymbol{\sigma}' = A \sigma_e'^{n-1} \boldsymbol{\sigma}' \quad (3.29)$$

where $A = \frac{1}{B^n}$ is the *rate factor*. Exploiting Glen's original flow law, we can write the law as

$$\dot{\epsilon} = \frac{\dot{\epsilon}_e^{\frac{n-1}{n}}}{B} \boldsymbol{\sigma}', \quad (3.30)$$

so that through comparison with Eq. (3.21), we see that the viscosity of ice is:

$$\mu = \frac{B}{2\dot{\epsilon}_e^{\frac{n-1}{n}}} = \frac{1}{2A\sigma_e'^{n-1}} \quad (3.31)$$

This flow law is widely used in ice sheet modelling (Cuffey & Paterson, 2010, p.61). Some anisotropic laws are being developed (Thorsteinsson, 2001; Gillet-Chaulet *et al.*, 2005; Ma *et al.*, 2010), but they are beyond the scope of this thesis. The dependency of the viscosity on the effective deviatoric stress (Fig. 3.3) renders the equations of momentum balance (3.22) non-linear.

Controls on the Rate Factor

The rate factor of ice, A , is a function of various physical and chemical properties, like ice temperature, pressure, microscopic water content, ice density, grain size, impurities and fabric orientation, but their exact contribution is currently unclear (Cuffey & Paterson, 2010, p.64).

The temperature of ice, T , has the highest influence on A . The higher the temperature, the higher the rate factor. Over the whole range of temperatures in terrestrial ice, A nominally varies by three orders of magnitude (Cuffey & Paterson, 2010, p.64, and Fig. 3.2). Such a large sensitivity implies that temperatures need to be known well in order to model the ice flow correctly. Some empirical relationships between temperature and rate factor have been proposed, e.g. (Cuffey & Paterson, 2010, p.73). An Arrhenius relationship describes the temperature dependence:

$$A = A_0 \exp \left(-\frac{Q}{RT^*} \right). \quad (3.32)$$

Here, $R = 8.314 \text{ J mol K}^{-1}$ is the universal gas constant, and T^* is the Kelvin temperature relative to the pressure melting point temperature, T_{pmp} , which is 273.15 K at atmospheric pressure. Values of the pre-exponential constant, A_0 , and the activation energy, Q , make a sharp jump at $T^* = T_{pmp} - 10 \text{ K}$, to account for the much higher deformation rates of ice close to pressure melting point. T^* follows a linear relationship for pressures typical in glaciers and ice sheets ($p < 50 \text{ MPa}$):

$$T^* = T + \beta p. \quad (3.33)$$

Values of the Clausius-Clapeyron constant β range between $\beta = 7.42 \times 10^{-8} \text{ K Pa}^{-1}$ to $9.8 \times 10^{-8} \text{ K Pa}^{-1}$ (Hooke, 2005). We define the homologous temperature, T_{hom} , as the difference of the ice temperature to the pressure melting point temperature in degrees Celsius:

$$T_{hom} = T - T_{pmp} + \beta p. \quad (3.34)$$

Ice is called temperate, if its temperature is at pressure melting point ($T^* = T_{pmp}$) and cold otherwise.

The microscopic water content, W , softens temperate ice by facilitating geometric adjustments between neighbouring ice grains with different orientations. Measurements have found water content as high as 2.9 to 4.6% in a basal temperate layer of the GrIS (Brown *et al.*, 2017). Laboratory experiments on samples from a temperate glacier by Duval (1977) and Lliboutry & Duval (1985) suggest a softening effect of

$$A(W) = A(T^* = 273.15 \text{ K})(1 + 1.8125W[\%]) \quad (3.35)$$

for water contents up to 1%. The microscopic water content thus significantly influences the rate factor and viscosity of temperate ice in a glacier. No relationship is known for values larger than 1%, for which usually the rate factor value corresponding to 1% microscopic water content is prescribed. The ice under a 3000 m thick ice sheet is usually close to or at pressure melting point, which at this pressure is about 2 K lower than at

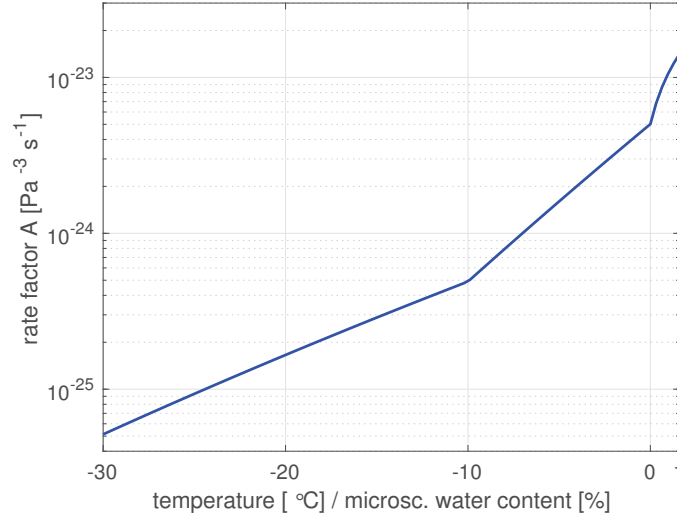


FIGURE 3.2: Rate factor $A(T_{hom}, W)$ for cold ice with $T_{hom} = -30^\circ\text{C}$ to temperate ice with 1% microscopic water content according to the law presented in Lliboutry & Duval (1985). The kink at -10°C is due to the piecewise definition of the pre-exponential constant, A_0 , and the activation energy, Q . The kink at 0°C is due to the linear softening of temperate ice, cf. Eq. 3.35.

the surface (cf. Eq. 3.33). The pressure dependency thus introduces a small but non-negligible contribution to the ice rate factor.

The porosity of ice has little effect on the viscosity from the density of pore close-off ($\rho \simeq 830 \text{ kg m}^{-3}$). Fabric orientation of ice stiffens and softens the ice considerably depending on the direction of the applied stress. Since the c -axis of ice crystals tends to re-orientate in favour of the direction of applied stress, this effect is usually neglected in analyses of glacier flow (Greve & Blatter, 2009), which also holds for the effect of grain size and impurities in the ice.

The Higher-Order Model (HOM)

Solving the Full-Stokes equations (3.22) is computationally expensive, and the aspect ratio of ice sheets allows to make certain assumptions which are used to simplify them. Therefore, several flow approximations have been derived. Here, we state the two flow approximations we use in this thesis, the *higher-order model* (HOM, Blatter, 1995; Pattyn, 2003) and the *shelfy-stream* or *shallow-shelf approximation* (SSA, Morland & Zainuddin, 1987; MacAyeal, 1989). Other flow approximations include the shallow-ice approximation (SIA, Hutter, 1983) and the L1L2 model (Schoof & Hindmarsh, 2010).

In all parts of an ice sheet, the vertical shear stresses σ_{xz} and σ_{yz} ($\leq 100 \text{ kPa}$) are small compared to the vertical normal stress, which is approximately equal to the pressure, p ($\mathcal{O}(p) = 10 \text{ MPa}$). Moreover, the ratios $\frac{\partial v_z}{\partial x} / \frac{\partial v_x}{\partial z}$ and $\frac{\partial v_z}{\partial y} / \frac{\partial v_y}{\partial z}$ are typically on the order of 1×10^{-6} (Greve & Blatter, 2009, pp.73-75). A simplified, approximated system of equations for the large-scale dynamics of ice sheets is derived from these observations:

Theorem 3.3. (Higher-Order Model) *Under the assumption, that*

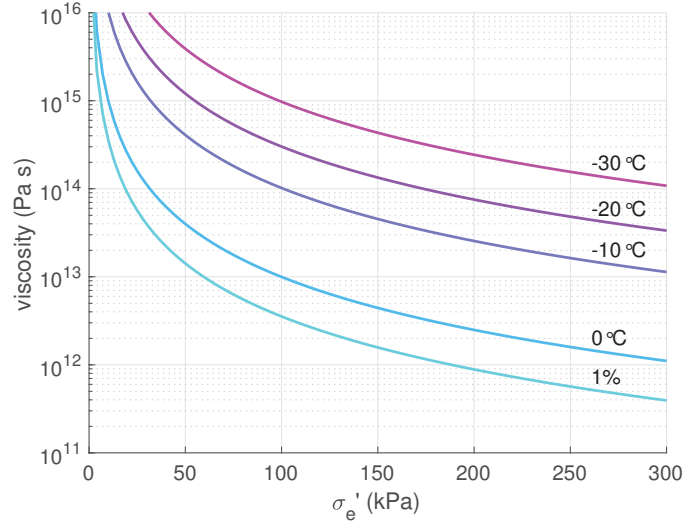


FIGURE 3.3: The ice viscosity as a function of effective deviatoric stress (Eq. 3.16) for a stress exponent $n = 3$ and cold ice at different ice temperatures and temperate ice with a microscopic water content of 1%, respectively.

- $\frac{\partial \sigma_{xz}}{\partial x} \ll \frac{\partial \sigma_{xz}}{\partial z}$ and $\frac{\partial \sigma_{xz}}{\partial y} \ll \frac{\partial \sigma_{xz}}{\partial z}$: variation in horizontal shear stress along the direction of shear is small compared to vertical changes of vertical stress, and
- $\frac{\partial v_z}{\partial x} \ll \frac{\partial v_x}{\partial z}$ and $\frac{\partial v_z}{\partial y} \ll \frac{\partial v_y}{\partial z}$: horizontal variations in vertical ice motion are negligible compared to vertical gradients of horizontal ice motion,

and using the constitutive equation (3.21), the equations of momentum balance (3.20) are simplified to:

$$\begin{aligned}
 4 \frac{\partial}{\partial x} \left(\mu \frac{\partial v_x}{\partial x} \right) + 2 \frac{\partial}{\partial x} \left(\mu \frac{\partial v_y}{\partial y} \right) + \frac{\partial}{\partial y} \left(\mu \left(\frac{\partial v_x}{\partial y} + \frac{\partial v_y}{\partial x} \right) \right) \\
 + \frac{\partial}{\partial z} \left(\mu \left(\frac{\partial v_x}{\partial z} \right) \right) = \rho g \frac{\partial s}{\partial x} \\
 4 \frac{\partial}{\partial y} \left(\mu \frac{\partial v_y}{\partial y} \right) + 2 \frac{\partial}{\partial y} \left(\mu \frac{\partial v_x}{\partial x} \right) + \frac{\partial}{\partial x} \left(\mu \left(\frac{\partial v_x}{\partial y} + \frac{\partial v_y}{\partial x} \right) \right) \\
 + \frac{\partial}{\partial z} \left(\mu \left(\frac{\partial v_y}{\partial z} \right) \right) = \rho g \frac{\partial s}{\partial y} \\
 v_z(x, y, z) = v_z(x, y, b) - \int_{b(x,y)}^z \frac{\partial v_x}{\partial x} + \frac{\partial v_y}{\partial y} dz'.
 \end{aligned} \tag{3.36}$$

The main simplification in the HOM is the elimination of the pressure variable through the hydrostatic approximation of the vertical normal stress component. This step drastically reduces the required computational effort for the solution of the equation system, and permits to derive a *floating condition*:

$$G(H, b) := \rho H - \rho_w(z_{sl} - b) = 0. \tag{3.37}$$

Ice is grounded where $G(H, b) > 0$, floating where $G(H, b) < 0$, and the grounding line is given by the 0-level-set of G .

The Shelfy-Stream Approximation (SSA)

In regions of small basal drag like ice shelves and regions of high basal sliding, vertical shear in the ice column becomes negligible. Moreover, the assumptions for the HOM hold. Morland & Zainuddin (1987) used these observations to simplify the equations of linear momentum balance (3.20) to a two-dimensional model for the flow of an unconfined ice shelf, and MacAyeal (1989) extended this model to sliding over easily deformable till:

Theorem 3.4. (Shelfy-Stream Approximation) Let $\bar{\mu} = \frac{1}{H} \int_b^s \mu dz$ be the vertically averaged ice viscosity. Under the assumptions that

- $\frac{\partial \sigma_{xz}}{\partial x} \ll \frac{\partial \sigma_{zz}}{\partial z}$ and $\frac{\partial \sigma_{yz}}{\partial y} \ll \frac{\partial \sigma_{zz}}{\partial z}$: variation in horizontal shear stress along the direction of shear is small compared to vertical changes of vertical stress,
- $\frac{\partial v_z}{\partial x} \ll \frac{\partial v_x}{\partial z}$ and $\frac{\partial v_z}{\partial y} \ll \frac{\partial v_y}{\partial z}$: horizontal variations in vertical ice motion are negligible compared to vertical gradients of horizontal ice motion,
- $\frac{\partial v_x}{\partial z} = 0$ and $\frac{\partial v_y}{\partial z} = 0$, and
- bedrock slopes are small,

Eq. (3.22) becomes:

$$\begin{aligned} \frac{\partial}{\partial x} \left(4H\bar{\mu} \frac{\partial v_x}{\partial x} + 2H\bar{\mu} \frac{\partial v_y}{\partial y} \right) + \frac{\partial}{\partial y} \left(H\bar{\mu} \left(\frac{\partial v_x}{\partial y} + \frac{\partial v_y}{\partial x} \right) \right) &= \rho g H \frac{\partial s}{\partial x} + \alpha^2 v_x \\ \frac{\partial}{\partial y} \left(4H\bar{\mu} \frac{\partial v_y}{\partial y} + 2H\bar{\mu} \frac{\partial v_x}{\partial x} \right) + \frac{\partial}{\partial x} \left(H\bar{\mu} \left(\frac{\partial v_x}{\partial y} + \frac{\partial v_y}{\partial x} \right) \right) &= \rho g H \frac{\partial s}{\partial y} + \alpha^2 v_y \end{aligned} \quad (3.38)$$

The terms in red colour are added for grounded ice only.

The SSA thus eliminates both pressure and vertical components of velocity, which yields a 2D, computationally cheap flow approximation, that includes lateral stress transfer (“membrane stress”). Field observations at Jakobshavn Isbræ show that a large fraction of the motion in fast-flowing areas is due to basal sliding (Lüthi *et al.*, 2002), and that much of the ice stream’s driving stress is balanced by lateral drag (van der Veen *et al.*, 2011), so that careful application of the SSA to Jakobshavn Isbræ is justified.

3.3.3 Energy Balance of Ice Sheets

Temperature and microscopic water content of ice have a strong influence on the rheology of ice (Sect. 3.3.2). Polythermal glaciers like Jakobshavn Isbræ consist of both cold and temperate ice (Iken *et al.*, 1993; Lüthi *et al.*, 2002). It is thus important to represent polythermal regimes in an ice sheet model.

The Enthalpy Method

Aschwanden *et al.* (2012) model the thermal state of a glacier through the specific inner energy density, E , which they call “enthalpy” for historical reasons. The “enthalpy method” bases on the concept that a small change in internal specific energy changes in cold ice only the temperature, T ,

whereas it drives melt in temperate ice, and thus changes only the microscopic water content, W . Here, we state the study's main results, and we refer the interested reader to Aschwanden *et al.* (2012).

In the enthalpy method, glacier ice is considered to be an ice-water mixture with corresponding partial densities $\hat{\rho}_i$ and $\hat{\rho}_w$, so that the bulk density of the mixture is $\rho_m = \hat{\rho}_i + \hat{\rho}_w$. The water content, W , of the mixture is $W = \hat{\rho}_w / \rho_m$. The enthalpy of cold ice is:

$$E_i(T) = \int_{T_0}^T C_i(\tilde{T}) d\tilde{T}, \quad (3.39)$$

where T_0 is a fix reference temperature, and $C_i(T)$ is the heat capacity of ice, which is a linear function that varies by about 10% in the temperature range typical for glaciers. Assuming that the heat capacity is constant, we obtain:

$$E_i(T) = C_i (T - T_0). \quad (3.40)$$

The enthalpy of ice at pressure melting point with $W = 0$ is denoted by:

$$E_{pmp}(p) = E_i(T_{pmp}(p)), \quad (3.41)$$

The CTS is the $E_{pmp}(p)$ -level-set of the glacier's enthalpy field, E . Melting of ice requires latent heat of fusion, L . Neglecting the possibility of super-cooled water (water in liquid phase, whose temperature is below pressure melting point), the enthalpy of the temperate ice mixture is:

$$E(W, p) = E_{pmp}(p) + WL. \quad (3.42)$$

In summary, the enthalpy of an ice mixture is:

$$E(T, W, p) = \begin{cases} C_i (T - T_0) & , \text{ if } T < T_{pmp}(p) \\ E_{pmp}(p) + WL & , \text{ if } T = T_{pmp}(p) \text{ and } 0 \leq W \leq 1 \end{cases} \quad (3.43)$$

This relationship is invertible under the reasonable assumption that $\frac{\partial E}{\partial T} = C_i > 0$ for $T < T_{pmp}(p)$, and $\frac{\partial E}{\partial W} = L > 0$ for $T = T_{pmp}(p)$:

$$T(E, p) = \begin{cases} T_0 + \frac{E_i}{C_i} & , \text{ if } E < E_{pmp}(p) \\ T_{pmp}(p) & , \text{ if } E \geq E_{pmp}(p) \end{cases} , \text{ and} \quad (3.44)$$

$$W(E, p) = \begin{cases} 0 & , \text{ if } E < E_{pmp}(p) \\ L^{-1} (E - E_{pmp}(p)) & , \text{ if } E \geq E_{pmp}(p). \end{cases} \quad (3.45)$$

The thermal state of ice is thus described completely with the tuple (E, p) , instead of the triple (T, W, p) , which makes the tuple the preferred state variables in a thermodynamically coupled ice sheet model.

The law of conservation of energy states that the total energy of a closed system remains constant. It is expressed by the First Law of Thermodynamics, which can be simplified to a local form for the enthalpy:

$$\rho_m \frac{dE}{dt} = -\text{div } \mathbf{q} + \Psi. \quad (3.46)$$

Here, \mathbf{q} is the heat flux and Ψ is the local heat production. The local heat production in ice, Ψ , is the rate at which kinetic energy is transformed into

heat (Greve & Blatter, 2009, p.35):

$$\Psi = \text{tr}(\boldsymbol{\sigma} \cdot \dot{\boldsymbol{\varepsilon}}). \quad (3.47)$$

Therefore, the total heat of a glacier is generally not a conserved quantity, in contrast to the total energy of the closed system.

The field equation for the enthalpy is derived from the equation of energy balance (Eq. 3.46) by formulating the heat flux, \mathbf{q} , in both cold and temperate ice. In cold ice, the heat flux is modelled to follow Fourier's law:

$$\mathbf{q} = -K_i(E)\nabla E. \quad (3.48)$$

Here, $K_i(E)$ is the thermal conductivity of cold ice. In temperate ice, the physical processes underlying heat flux are poorly understood. They are modelled as the sum of sensible and latent heat fluxes (Greve, 1997b):

$$\mathbf{q} = \mathbf{q}_s + \mathbf{q}_l. \quad (3.49)$$

The sensible heat flux in temperate ice arises from variations in the pressure-melting point temperature:

$$\mathbf{q}_s = -\kappa(E, p)\nabla T_{pmp}(p), \quad (3.50)$$

where $\kappa(E, p) = (1 - W(E, p))\kappa_i(E) + W(E, p)\kappa_w$ is the thermal conductivity of the ice-water mixture.

The latent heat flux is due to the mass flux of liquid water in ice. This process is poorly constrained by experimental knowledge in glacier ice. In the interest of finite spatial derivatives of the enthalpy, the authors (Aschwanden *et al.*, 2012) make a regularizing choice:

$$\mathbf{q}_l = -\kappa_0\nabla W = -K_0\nabla E, \quad (3.51)$$

where conductivities κ_0 and $K_0 = \kappa_0/L$ are small positive constants.

Inserting Eqs. (3.47), (3.48), (3.50), (3.51) into the energy balance equation (3.46) yields the *enthalpy field equation*:

$$\rho_m \frac{dE}{dt} = \nabla \cdot \left(\left\{ \begin{array}{c} K_i(E)\nabla E \\ \kappa(E, p)\nabla T_{pmp}(p) + K_0\nabla E \end{array} \right\} \right) + \text{tr}(\boldsymbol{\sigma} \cdot \dot{\boldsymbol{\varepsilon}}). \quad (3.52)$$

The upper line applies in cold ice, the lower line in temperate ice. Since the microscopic water content in ice is small, and the density of ice and water differ by less than 10%, one commonly sets ρ_m to be the density of ice.

Boundary Conditions

At the boundaries of ice, the ice mixture density, ρ_m , and the volumetric enthalpy, $\rho_m E$, jump from their value outside the ice to their value inside the ice, respectively. Boundary conditions for the enthalpy at these interfaces therefore have to be derived from jump conditions for mass and enthalpy, cf. Aschwanden *et al.* (2012). For a thorough introduction into jump conditions we refer to the common literature on continuum mechanics, e.g. Liu (2002).

Ice surface The temperature of the precipitation at the ice surface is rarely known, and the conductive heat flux into the ice is small and usually neglected. Therefore, one usually prescribes the air temperature at 2 m above the ice surface, T_{2m} , as a Dirichlet boundary condition at the ice surface:

$$E = E(T_{2m}, 0, p_{atm}). \quad (3.53)$$

Ice base (grounded) At the grounded ice base, a subglacial water layer with thickness η_b may be present, with whom the glacier exchanges mass and heat. Let $M_b = \rho_i a_b$ be the mass exchange rate. Under the assumptions that the subglacial water is at pressure melting point, and that its pressure is constant in space and time, one can show that:

$$-M_b = \frac{F_b - (\mathbf{q} - \mathbf{q}_{geo}) \cdot \mathbf{n}}{(1 - W)L}, \quad (3.54)$$

where \mathbf{q} is the heat flux at the ice base, \mathbf{q}_{geo} is the geothermal heat flux, \mathbf{n} is the unit surface normal pointing into the ice, and

$$F_b = -\boldsymbol{\tau}_b \cdot \mathbf{v}_b = \alpha^2 \|\mathbf{v}_b\|^2 \quad (3.55)$$

is the heat production through basal friction between ice and bedrock (with $\boldsymbol{\tau}_b$ as in Eq. (3.26)). For the right hand term, Eq. (3.27) has been applied.

A point at the ice base is defined as cold if the temperature in its neighbourhood is below pressure melting point, and if there is no subglacial water layer:

$$E < E_{pmp}(p) \text{ and } \eta_b = 0, \quad (3.56)$$

and as temperate otherwise. At a cold point at the base, $M_b = 0$ holds, so that Eq. (3.54) becomes a Neumann boundary condition:

$$\mathbf{q} \cdot \mathbf{n} = \mathbf{q}_{geo} \cdot \mathbf{n} + F_b. \quad (3.57)$$

At a temperate point of the ice base, all available heat is used for subglacial melt. In this case, Eq. (3.54) is used to compute the basal melting rate, and an insulating Neumann boundary condition is applied in case of positive thickness of the basal temperate layer:

$$K_0 \nabla E \cdot \mathbf{n} = 0, \quad (3.58)$$

and a Dirichlet boundary condition if only the base itself is temperate:

$$E = E_{pmp}(p). \quad (3.59)$$

An overview of the basal boundary condition and melting rate decision chart is sketched in Fig. 3.4. This chart is not applicable to a direct steady-state solver, which is used in ISSM (cf. Sect. 3.5). It creates a non-converging loop if sufficient basal heating erroneously creates a temperate layer with positive thickness, so that the basal heating would be switched off in the next solver iteration step. This "cools" the base back down below pressure melting point temperature, from where the cycle restarts. A workaround to this problem is described in Sect. 6.7.1.

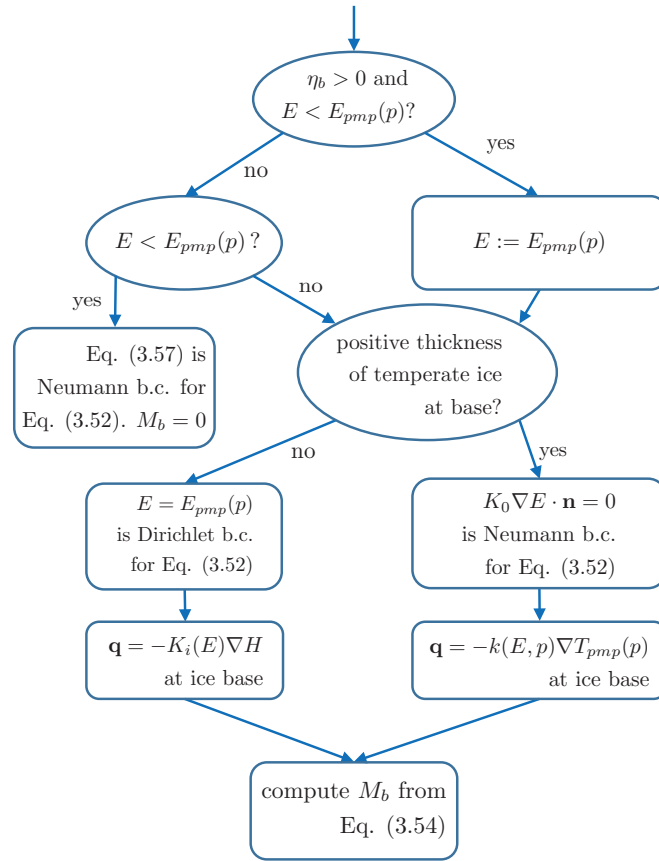


FIGURE 3.4: Decision chart for basal boundary conditions and basal melting rate computation of prognostic simulations. Adapted from Aschwanden *et al.* (2012), Fig. 5.

Ice base (floating) Glacier ice and ocean water exchange heat through a thin ocean mixed layer (Holland & Jenkins, 1999). Ocean heat exceeding $E_{pmp}(p)$ is used for melt, so that we assume the ocean to be at $E_{pmp}(p)$ for the heat flux. The heat flux through this boundary layer into the ice is parametrised as:

$$\mathbf{q} \cdot \mathbf{n} = -\frac{\rho_{ml}}{\rho_i} \gamma_{ml} (E|_{z=b} - E_{pmp}(p)), \quad (3.60)$$

where ρ_{ml} is the density of the mixed layer, and $\gamma_{ml} = \text{const}$ is a thermal exchange velocity between the ocean and the mixed layer. Similar to the grounded ice, this Neumann boundary condition becomes insulating once the temperature of the base reaches pressure melting point. The effect of ocean salinity on the pressure melting point temperature is not modelled explicitly.

Drainage of microscopic water content The enthalpy method does not introduce an upper limit for the microscopic water content, and modelled values may ramp up quickly to unphysical values due to positive feedbacks between the rate factor parametrisation and the strain heating. However, observations of values over 5% are rare (e.g. Pettersson *et al.*, 2004; Bradford & Harper, 2005; Brown *et al.*, 2017, and references therein). Moreover,

rate factor parametrisations such as Eq. (3.35) are only valid for $W < 1\%$. Therefore, Greve (1997b) introduced a drainage function, which removes a fraction $\frac{\partial W}{\partial t} = D(W)$ of the microscopic water content at every time step in the model. Drained water adds to the basal melting rate, to give an updated value that enters the subglacial water layer:

$$-\tilde{M}_b = -M_b + \int_b^s \rho_w D(W) dz. \quad (3.61)$$

This updated basal melting rate also enters the computation of the vertical velocities in Eq. (3.36).

3.4 The Finite-Element Method (FEM)

The Finite Element Method (FEM) provides a formalism to generate a discrete algorithm for approximating the solution of PDE. We will not describe the full theory behind the FEM here, but illustrate its general idea. The interested reader is referred to the standard literature, e.g. Zienkiewicz & Taylor (1989) and Brenner & Scott (2007).

The main idea behind the FEM is to write the PDE into an equivalent weak formulation, for which the existence and uniqueness of the solution can be shown (Lax-Milgram Theorem), and then project the problem into a finite-dimensional subspace through a Galerkin-method. There, Céa's Lemma ensures the best-approximation quality of the obtained Galerkin approximation, i.e. the solution of the discretized problem minimizes the distance to the solution of the original problem.

As an illustration, we apply here the FEM to the SSA field equations (3.38) for floating ice:

$$\begin{aligned} \frac{\partial}{\partial x} \left(4H\bar{\mu} \frac{\partial v_x}{\partial x} + 2H\bar{\mu} \frac{\partial v_y}{\partial y} \right) + \frac{\partial}{\partial y} \left(H\bar{\mu} \left(\frac{\partial v_x}{\partial y} + \frac{\partial v_y}{\partial x} \right) \right) &= \rho g H \frac{\partial s}{\partial x} \\ \frac{\partial}{\partial y} \left(4H\bar{\mu} \frac{\partial v_y}{\partial y} + 2H\bar{\mu} \frac{\partial v_x}{\partial x} \right) + \frac{\partial}{\partial x} \left(H\bar{\mu} \left(\frac{\partial v_x}{\partial y} + \frac{\partial v_y}{\partial x} \right) \right) &= \rho g H \frac{\partial s}{\partial y} \end{aligned} \quad (3.62)$$

Let's assume that the water pressure applies at the calving front, Γ_N , and a homogeneous Dirichlet boundary condition at the other boundaries, Γ_D :

$$\begin{aligned} \boldsymbol{\sigma}' \cdot \mathbf{n} &= \mathbf{f} = \left(\frac{\rho g H^2}{2} - \frac{\rho_w g b^2}{2} \right) & \text{on } \Gamma_N \\ \mathbf{v} &= \mathbf{0} & \text{on } \Gamma_D. \end{aligned} \quad (3.63)$$

Let the space of admissible velocities be:

$$\mathcal{V} = \left\{ \mathbf{v} \in (\mathcal{H}^1(\Omega))^2, \forall \mathbf{x} \in \Gamma_D : \mathbf{v} = \mathbf{0} \right\}. \quad (3.64)$$

The Sobolev space, $\mathcal{H}^1(\Omega)$, is the space of square-integrable functions, which have a square-integrable first derivative. The problem in local form, Eqs.

(3.62), (3.63), is equivalent to its weak formulation:

$$\begin{aligned}
& \forall \boldsymbol{\varphi} = (\varphi_x, \varphi_y) \in \mathcal{V}, \\
& \int_{\Omega} 2\bar{\mu}H \left(2\frac{\partial v_x}{\partial x} + \frac{\partial v_y}{\partial y} \right) \frac{\partial \varphi_x}{\partial x} + \bar{\mu}H \left(\frac{\partial v_x}{\partial y} + \frac{\partial v_y}{\partial x} \right) \frac{\partial \varphi_x}{\partial y} d\Omega \\
& + \int_{\Omega} 2\bar{\mu}H \left(2\frac{\partial v_y}{\partial y} + \frac{\partial v_x}{\partial x} \right) \frac{\partial \varphi_y}{\partial x} + \bar{\mu}H \left(\frac{\partial v_x}{\partial y} + \frac{\partial v_y}{\partial x} \right) \frac{\partial \varphi_y}{\partial y} d\Omega \\
& = \int_{\Gamma_N} \mathbf{f} \cdot \boldsymbol{\varphi} d\Gamma - \int_{\Omega} \rho g H \nabla s \cdot \boldsymbol{\varphi} d\Omega
\end{aligned} \tag{3.65}$$

The idea of the Galerkin method is to project this problem from the infinite-dimensional space \mathcal{V} into a finite-dimensional subspace, $\mathcal{V}_h \subset \mathcal{V}$. Let $\{\varphi_i, i = 1, \dots, n\}$ be the basis of \mathcal{V}_h , with $n \in \mathbb{N}$. Since \mathcal{V}_h is finite-dimensional, it is sufficient to test the weak formulation with the basis vectors $\{\varphi_i, i = 1, \dots, n\}$ only. We obtain a set of n equations, $i \in \{1, \dots, n\}$:

$$\begin{aligned}
& \int_{\Omega} 2\bar{\mu}H \left(2\frac{\partial v_x}{\partial x} + \frac{\partial v_y}{\partial y} \right) \frac{\partial \varphi_{ix}}{\partial x} + \bar{\mu}H \left(\frac{\partial v_x}{\partial y} + \frac{\partial v_y}{\partial x} \right) \frac{\partial \varphi_{ix}}{\partial y} d\Omega \\
& + \int_{\Omega} 2\bar{\mu}H \left(2\frac{\partial v_y}{\partial y} + \frac{\partial v_x}{\partial x} \right) \frac{\partial \varphi_{iy}}{\partial x} + \bar{\mu}H \left(\frac{\partial v_x}{\partial y} + \frac{\partial v_y}{\partial x} \right) \frac{\partial \varphi_{iy}}{\partial y} d\Omega \\
& = \int_{\Gamma_N} \mathbf{f} \cdot \varphi_i d\Gamma - \int_{\Omega} \rho g H \nabla s \cdot \varphi_i d\Omega
\end{aligned} \tag{3.66}$$

If we write the Galerkin approximation, $\mathbf{v}_h \in \mathcal{V}_h$, to the solution of the original problem, $\mathbf{v} \in \mathcal{V}$, as:

$$\mathbf{v}_h = \sum_{j=1}^n \lambda_j \boldsymbol{\varphi}_j, \tag{3.67}$$

with real coefficients $\lambda_j, j = 1, \dots, n$, and if we replace \mathbf{v} in Eq. (3.66), we obtain:

$$\begin{aligned}
& \sum_{j=1}^n \lambda_j \int_{\Omega} 2\bar{\mu}H \left(2\frac{\partial \varphi_{jx}}{\partial x} + \frac{\partial \varphi_{jy}}{\partial y} \right) \frac{\partial \varphi_{ix}}{\partial x} + \bar{\mu}H \left(\frac{\partial \varphi_{jx}}{\partial y} + \frac{\partial \varphi_{jy}}{\partial x} \right) \frac{\partial \varphi_{ix}}{\partial y} d\Omega \\
& + \sum_{j=1}^n \lambda_j \int_{\Omega} 2\bar{\mu}H \left(2\frac{\partial \varphi_{jy}}{\partial y} + \frac{\partial \varphi_{jx}}{\partial x} \right) \frac{\partial \varphi_{iy}}{\partial x} + \bar{\mu}H \left(\frac{\partial \varphi_{jx}}{\partial y} + \frac{\partial \varphi_{jy}}{\partial x} \right) \frac{\partial \varphi_{iy}}{\partial y} d\Omega \\
& = \int_{\Gamma} \mathbf{f} \cdot \varphi_i d\Gamma - \int_{\Omega} \rho g H \nabla s \cdot \varphi_i d\Omega
\end{aligned} \tag{3.68}$$

This is a system with n equations for n unknowns, v_1, \dots, v_n . Let $\mathbf{K} = (k_{ij})_{ij}$ be the matrix that represents the left-hand side, with:

$$\begin{aligned}
k_{ij} &= \int_{\Omega} 2\bar{\mu}H \left(2\frac{\partial \varphi_{jx}}{\partial x} + \frac{\partial \varphi_{jy}}{\partial y} \right) \frac{\partial \varphi_{ix}}{\partial x} + \bar{\mu}H \left(\frac{\partial \varphi_{jx}}{\partial y} + \frac{\partial \varphi_{jy}}{\partial x} \right) \frac{\partial \varphi_{ix}}{\partial y} d\Omega \\
& + \int_{\Omega} 2\bar{\mu}H \left(2\frac{\partial \varphi_{jy}}{\partial y} + \frac{\partial \varphi_{jx}}{\partial x} \right) \frac{\partial \varphi_{iy}}{\partial x} + \bar{\mu}H \left(\frac{\partial \varphi_{jx}}{\partial y} + \frac{\partial \varphi_{jy}}{\partial x} \right) \frac{\partial \varphi_{iy}}{\partial y} d\Omega,
\end{aligned} \tag{3.69}$$

The components of the right-hand side, $\mathbf{F} = (f_i)_i$, are:

$$f_i = \int_{\Gamma} \mathbf{f} \cdot \boldsymbol{\varphi}_i d\Gamma - \int_{\Omega} \rho g H \nabla s \cdot \boldsymbol{\varphi}_i d\Omega, \quad (3.70)$$

and let $\mathbf{V} = (\lambda_j)_j$, then Eq. (3.68) becomes:

$$\mathbf{KV} = \mathbf{F}. \quad (3.71)$$

We are free to choose a basis of the solution space. Commonly, one opts for basis functions which are 1 on one mesh vertex, and 0 on all others. In this case, the mesh construction is a crucial point, as it defines the solution space, and matrix \mathbf{K} is a sparse matrix system, which is solved by specialized solvers efficiently.

The FEM is widely employed in solid mechanics, and has more recently found its application to computational fluid mechanics. Its solid mathematical foundation and its ability to use unstructured meshes for arbitrary geometries provide certain advantages over other discretization methods, like the Finite Difference or Finite Volume Methods.

3.5 The Ice Sheet System Model (ISSM)

In this thesis, we use the parallelized, multi-purpose framework for ice flow modelling provided by the Ice Sheet System Model (ISSM, Larour *et al.*, 2012a). ISSM is developed by an international core team at the Jet Propulsion Laboratory, Pasadena, CA and the University of California, Irvine, CA, both USA. ISSM is able to perform both diagnostic and prognostic model simulations for 2D and 3D ice sheets. Various ice flow approximations, like the Full-Stokes model, HOM, SSA, SIA and L1L2 have been implemented into the ISSM. The ice thickness is evolved by solving the ice thickness equation (3.12), and the temperature evolution is governed either by a “cold-ice” approach (Larour *et al.*, 2012a), or the enthalpy gradient method described in Sect. 3.3.3. The corresponding basal boundary conditions have been implemented by the author as a part of this PhD-thesis at the end of 2013. ISSM provides inverse methods to infer poorly constrained model parameters, like the basal roughness, the ice viscosity parameter or the bedrock elevation through data assimilation of observations at the ice surface through classic adjoint methods (Nocedal & Wright, 2006; Morlighem *et al.*, 2010; Morlighem *et al.*, 2011). The grounding line for simplified models, like the SSA and HOM, evolves through a subelement-migration-scheme (Seroussi *et al.*, 2014a). In collaboration with the ISSM team, the author implemented the capability for dynamic ice front evolution through a Level-Set Method in 2014, as described in Sect. 3.2.

ISSM relies on the Finite Element Method (Sect. 3.4) for discretization of the model equations. It employs static, adaptive mesh generation of unstructured, anisotropic meshes, which reduces discretization errors in areas crucial to ice flow while minimizing the number of required degrees of freedom. Three-dimensional meshes are generated through vertical extrusion of previously generated two-dimensional meshes. Triangular (2D) and prismatic (3D) linear Lagrange finite elements are employed to discretize the model equations. The non-linearity introduced by the dependency of

the viscosity on the strain rate in Glen's flow law with $n = 3$ is treated with an iterative fixed-point method (Picard's scheme). Model equations for momentum-, mass-, and energy balance are solved in an iterative, decoupled fashion. Prognostic runs use an implicit time-stepping scheme.

The discretized equation systems can be solved on one CPU on a desktop computer, but ISSM's real strength is its massively parallelized architecture, which enables it to run on supercomputers, and allows for high-resolution, continental-scale simulations. The mesh is partitioned by METIS, which distributes the computational effort optimally among the processors. The Message Passing Interface (MPI, Gropp *et al.*, 1996; Gropp & Lusk, 1996) ensures the framework's parallelism. Finally, the Portable Extensible Toolkit for Scientific Computation package (PETSc, Balay *et al.*, 1997; Balay *et al.*, 2008; Balay *et al.*, 2009) is employed for the solution of the discretized equation systems by using both iterative and direct solvers, like the MUltifrontal Massively Parallel Sparse direct Solver (MUMPS, Amestoy *et al.*, 2001; Amestoy *et al.*, 2006). ISSM's parallel architecture has important implications for code development, as it is for example of interest to keep communication between separate mesh partitions to a minimum. Simple topological operations like determining the neighbouring mesh element are therefore undesirable.

ISSM is written in C/C++ (Kernighan, 1988; Stroustrup, 1997), and has a user interface in MATLAB. The C/C++ core and the MATLAB environment are interfaced through the MATLAB External API (mex-modules). This approach combines the extensive library of predefined functions and powerful plotting capabilities of MATLAB with the fast C/C++ language, making it well suited for the processing, display and analysis of large and complex data sets. Code development uses the Apache Subversion software versioning system (SVN, Pilato *et al.*, 2008). Automated suites of simple test cases ("Nightly Runs") ensure the functionality of the framework during development. A user interface in Python (<https://www.python.org>) is under development, but does currently not provide the same range of capabilities as the MATLAB interface does. The ISSM software package is freely available for download via SVN under a BSD 3-Clause License from its website (<https://issm.jpl.nasa.gov/>). A help forum is found at <https://issm.ess.uci.edu/forum/index.php>.

4 Enthalpy benchmark experiments for numerical ice sheet models

Introductory Remarks

This chapter and the following two are three publications, which make up the main body of this doctoral thesis. An introductory text (“Context”) precedes every publication and explains its motivation, its associated work effort, its aim, its significance for the thesis, and an interpretation of the results. The author’s contribution is declared in the respective sub-section “Contributions”.

Context

A glacier’s thermal regime has a strong influence on its mass balance and the rheology of the ice (cf. Sects. 3.3.2, 3.3.3). An ice flow model thus requires an accurate thermal model. In this thesis, we rely on the enthalpy method outlined in Sect. 3.3.3, as it allows to capture the polythermal regime of Jakobshavn Isbræ. It is necessary to test and verify the implementation of the method before applying it to complex real-world glacier cases. For the enthalpy method, special attention should be paid to two aspects: first, the position of the CTS should be accurate, since temperate ice at the base is much more easily deformable than cold ice (cf. Sect. 3.3.2). Second, the complex enthalpy boundary condition scheme at the grounded ice base should be thoroughly tested, as it is able to change the type of boundary condition depending on the basal thermal state, and its correct functioning is crucial for the mass balance and the thermodynamics of a modelled ice sheet. However, simple test cases for the enthalpy method with analytical solutions did not exist to date, and needed to be formulated.

The enthalpy field equation (3.52) had been implemented in ISSM and applied to Greenland in Seroussi *et al.* (2013). This implementation, however, lacked the dynamic basal boundary condition scheme (Sect. 3.3.3), a rheology which takes the positive microscopic water content of temperate ice into account (e.g. Lliboutry & Duval, 1985), as well as a suitable treatment of the thermal conductivity discontinuity in finite elements which are intersected by the CTS. The author implemented, debugged and maintained the missing modules into ISSM with counselling by H. Seroussi and M. Morlighem.

The authors of the following paper had two aims: 1) to present two simple test cases, so-called “benchmarks”, as well as their corresponding analytical solution, which are usable to test the functionality of the implemented basal boundary condition scheme and the correct positioning of the

CTS in an ice sheet model, and 2) to use those benchmarks to test the implementation of the enthalpy method in three numerical ice sheet models, TIM-FD³ (Kleiner & Humbert, 2014), COMIce (Rückamp *et al.*, 2010), and ISSM.

In this thesis, we apply the enthalpy method in ISSM to Jakobshavn Isbræ. ISSM's discretization of the equations of momentum and mass balance as well as the grounding line migration have been tested thoroughly (Larour *et al.*, 2012a; Pattyn *et al.*, 2013; Seroussi *et al.*, 2014a), which was not yet the case for the enthalpy method. The benchmarks provide sensitivity estimates of ISSM's enthalpy solution to model input parameters and aspects of the discretization, which would be difficult to estimate in complex, real-world glacier model geometries.

The performance of ISSM in the benchmark experiments shows that the implementation of the basal boundary conditions behaves as expected (Exp. A). We also find that the position of the CTS depends on the vertical resolution of the model, the ratio of temperate and cold ice thermal conductivities, and likely the type of discretization of the model equations (Exp. B): a significant negative temperature offset of up to 0.9 °C above the CTS, and a positive water content offset of about +0.5% below the CTS in the enthalpy solution are attributed to the implementation of the mixed-element conductivity. Computational resources limit the degree of vertical resolution in real-world glacier models, which is typically comparable to the lowest resolution tested in this paper. The error estimate of the CTS position is thus about the thickness of one vertical layer in the model, which can be several tens of metres in thick parts of the ice sheet. Moreover, the offset occurs in a region which is crucial to ice flow due to the concentration of deformation at the base.

Contributions

Exp. A has been designed by authors Kleiner and Rückamp. Exp. B has been adapted from Greve & Blatter (2009, p.246). Authors Kleiner (TIM-FD³), Rückamp (COMIce) and Bondzio (ISSM) performed all enthalpy benchmarks themselves with their respective model. The model results were discussed among all authors. First author Kleiner coordinated the writing and typesetting of the document, and created the figures from the model results, which the authors Rückamp and Bondzio provided to him. Kleiner wrote the main body of the introduction, experiment description and result section, and inserted comments and contributions from all co-authors. Kleiner, Rückamp and Bondzio wrote the respective model description parts. The discussion and conclusion part were written in a joint effort by all authors. The analytical solution for Exp. A has been derived and written by Kleiner. The analytical solution for Exp. B has been written and adapted for the enthalpy by Bondzio.

Authors and Affiliations

Thomas Kleiner¹, Martin Rückamp¹, Johannes H. Bondzio¹ & Angelika Humbert^{1,2}

1. Alfred Wegener Institute, Helmholtz Centre for Polar and Marine Research, Bremerhaven, Germany
2. University of Bremen, Bremen, Germany

Abstract

We present benchmark experiments to test the implementation of enthalpy and the corresponding boundary conditions in numerical ice sheet models. Since we impose several assumptions on the experiment design, analytical solutions can be formulated for the proposed numerical experiments. The first experiment tests the functionality of the boundary condition scheme and the basal melt rate calculation during transient simulations. The second experiment addresses the steady-state enthalpy profile and the resulting position of the cold–temperate transition surface (CTS). For both experiments, we assume ice flow in a parallel-sided slab decoupled from the thermal regime.

We compare simulation results achieved by three different ice flow-models with these analytical solutions. The models agree well to the analytical solutions, if the change in conductivity between cold and temperate ice is properly considered in the model. In particular, the enthalpy gradient on the cold side of the CTS goes to zero in the limit of vanishing temperate-ice conductivity, as required from the physical jump conditions at the CTS.

4.1 Introduction

Ice sheets and glaciers can be distinguished by their thermal structure into cold, temperate and polythermal ice masses. While in cold ice the temperature is below the pressure melting point, in temperate ice the pressure melting point is reached. In temperate ice, the heat generated by viscous deformation can not give rise to temperature changes, but will be used for melting (Fowler, 1984; Blatter & Hutter, 1991). Thus temperate ice may contain a liquid water content (moisture). Polythermal ice masses contain both cold ice and temperate ice, separated by the cold–temperate transition surface (CTS, Greve, 1997a; Greve, 1997b). The large ice sheets in Greenland and Antarctica show the polythermal structure of a Canadian-type glacier, which are mostly cold except for a temperate layer at the base (Aschwanden *et al.*, 2012, and references therein). The liquid water inclusion in temperate ice makes this ice considerably softer than cold ice, resulting in a strong relationship between viscosity and moisture content (Duval, 1977; Lliboutry & Duval, 1985). The importance of this feature for the ice dynamics is obvious especially for temperate ice at the base where stresses are highest.

The enthalpy scheme presented in Aschwanden & Blatter (2009) and Aschwanden *et al.* (2012) describes temperature and water content in a consistent and energy conserving formulation. Changes in the enthalpy are

caused by changes of temperature in the cold ice part and by changes of the water content in the temperate ice part. The CTS position is implicitly given as the level-set of the pressure melting point and can be derived from the enthalpy field. Therefore, no restriction to the topology and shape of the CTS exists and there is no need to track it as in front-tracking models (e.g. Hutter *et al.*, 1988; Blatter & Hutter, 1991; Greve, 1997b; Greve, 1997a). Compared to the front-tracking models, neither jump conditions nor kinematic conditions are required at the CTS.

The enthalpy scheme has already been used in model studies for the Greenland Ice Sheet. In the “reference-implementation” of Aschwanden *et al.* (2012), the enthalpy scheme was compared to a cold-ice scheme. A simplified version of the enthalpy scheme (regarding basal boundary conditions and ice rheology) was used to assess the effect of the initial thermal regime on century-scale simulations (Seroussi *et al.*, 2013). Thus far, we are lacking analytical solutions for thermo-mechanically coupled polythermal ice flow to test the enthalpy implementations in ice sheet models.

Here, two numerical experiments for the enthalpy field are presented for which analytical solutions exist. Similar to other studies on ice sheet modelling (Huybrechts *et al.*, 1996; Bueler *et al.*, 2005; Pattyn *et al.*, 2012), we aim to verify the enthalpy method by comparing numerical solutions to analytical solutions under simplified boundary conditions. While artificially constructed exact solutions require additional compensatory terms to be incorporated in the numerical model (e.g. Bueler *et al.*, 2005; Bueler *et al.*, 2007), the proposed experiments are chosen in a way that numerical models should be able to perform them with no or only minor modifications of their source codes. Therefore it is ensured that the models run through the same model components and execute the same code for the proposed numerical experiments and for real-world simulations.

4.2 Theory

4.2.1 Governing Equations

Compared to thermodynamics usage, the enthalpy described in Aschwanden *et al.* (2012) is the specific internal energy. The work associated with changing the volume is not considered, since ice is assumed to be incompressible. The use of the name “enthalpy” is made to match other cryospheric applications (e.g. Notz & Worster, 2006). In the enthalpy approach, temperature T and moisture W are diagnostically computed from the modelled enthalpy field E (units: J kg^{-1}). The following transfer rules are used

$$E(T, W, p) = \begin{cases} C_i(T - T_0), & \text{if } E < E_{pmp} \\ E_{pmp} + WL, & \text{if } E \geq E_{pmp}, \end{cases} \quad (4.1)$$

where p is the pressure, T_0 is a reference temperature (to have positive values for the enthalpy for typical temperatures in glaciers), and L the latent heat of fusion. The enthalpy of the solid ice at the pressure melting point is defined as $E_{pmp} = E_s(p) = C_i(T_{pmp}(p) - T_0)$, where $T_{pmp}(p) = T_0 - \beta p$ is the pressure melting point temperature, β is the Clausius–Clapeyron constant and T_0 is the melting point at standard pressure (see Table 4.1 for parameter values).

The enthalpy field equation of the ice-water mixture depends on whether the mixture is cold ($E < E_{pm p}$) or temperate ($E \geq E_{pm p}$):

$$\rho_i \left(\frac{\partial E}{\partial t} + \mathbf{v} \cdot \nabla E \right) = -\nabla \cdot \mathbf{q}_i + \Psi, \quad (4.2)$$

with the ice density ρ_i , the ice velocity vector $\mathbf{v} = (v_x, v_y, v_z)$, the conductive flux \mathbf{q}_i , and the heat source by internal deformation Ψ . The conductive flux in cold ice is represented by Fourier's law in enthalpy form with the conductivity $K_c = \kappa_i/C_i$. In temperate ice the conductive flux is composed of the sensible heat flux (caused by variations in the pressure melting point) and latent heat flux, thus

$$\mathbf{q}_i = - \begin{cases} K_c \nabla E, & \text{if } E < E_{pm p} \\ \kappa_i \nabla T_{pm p}(p) + K_0 \nabla E, & \text{if } E \geq E_{pm p}. \end{cases} \quad (4.3)$$

At the present state, K_0 is poorly constrained. To test the sensitivity of the models on this parameter, different values have been used according to Table 4.1.

Quantity	Value	Units
Seconds per year, spy	31 556 926	s a^{-1}
Gravitational acceleration, g	9.81	m s^{-2}
Density of ice, ρ_i	910	kg m^{-3}
Density of water, ρ_w	1000	kg m^{-3}
Reference temperature, T_0	223.15	K
Melting point at standard pressure, T_0	273.15	K
Specific heat capacity, C_i	2009.0	$\text{J kg}^{-1} \text{K}^{-1}$
Thermal conductivity, κ_i	2.1	$\text{W m}^{-1} \text{K}^{-1}$
Experiment A (Aschwanden <i>et al.</i> , 2012):		
Ice thickness, H	1000	m
Geothermal flux, q_{geo}	0.042	W m^{-2}
Latent heat of fusion, L	3.34×10^5	J kg^{-1}
Clausius–Clapyron constant, β	7.9×10^{-8}	K Pa^{-1}
Moisture mass diffusivity, K_0	$\kappa_i/C_i \times 10^{-1}$	$\text{kg m}^{-1} \text{s}^{-1}$
Experiment B (Greve & Blatter, 2009):		
Ice thickness, H	200	m
Geothermal flux, q_{geo}	0.0	W m^{-2}
Latent heat of fusion, L	3.35×10^5	J kg^{-1}
Clausius–Clapyron constant, β	0.0	K Pa^{-1}
Rate-factor, A	5.3×10^{-24}	$\text{Pa}^{-3} \text{s}^{-1}$
Moisture diffusion coefficient, K_0	$\kappa_i/C_i \times 10^{-1}$	
	\vdots	
	$\kappa_i/C_i \times 10^{-5}$	$\text{kg m}^{-1} \text{s}^{-1}$

TABLE 4.1: Used constants and model parameters.

4.2.2 Boundary Conditions

At the upper ice surface, the enthalpy is prescribed from the surface temperature with zero moisture content corresponding to a Canadian-type polythermal glacier (cf. Blatter & Hutter, 1991). In the following description of the basal conditions $T'(p) = T - T_{pmp}(p) + T_0 = T + \beta p$ is the temperature relative to the melting point, H_w is the basal water layer thickness, and \mathbf{n}_b is the outward pointing normal vector. The type of basal boundary condition (Neumann or Dirichlet) is time dependent. The decision chart for local conditions given in Aschwanden *et al.* (2012, Fig. 5) need to be evaluated at every time step. The chart encompasses four different situations:

Cold base (dry): if the glacier is cold at the base and without a basal water layer (i.e. $E < E_{pmp}$ and $H_w = 0$), then

$$K_c \nabla E \cdot \mathbf{n}_b = q_{\text{geo}}. \quad (4.4)$$

The geothermal flux is the only source of heat as basal sliding and therefore frictional heating is forbidden for ice with temperatures below the pressure melting point. The geothermal flux is assumed to be constant, thus changes of the heat storage in the underlying bedrock cannot affect the basal heat budget of the ice.

Temperate base: if the glacier is temperate at the base without an overlying temperate ice layer, but with melting conditions at the base (i.e. $E \geq E_{pmp}$, $H_w > 0$ and $\nabla T' \cdot \mathbf{n}_b < \beta/K_c$), then

$$E = E_{pmp}. \quad (4.5)$$

This condition applies to basal ice maintained at the enthalpy of the pressure melting point, when the geothermal flux and frictional heating (caused by sliding) exceed the heat flux away from the base into the ice. In this case the remaining heat is used for melting.

Temperate ice at base: if the glacier is temperate at the base with an overlying temperate ice layer (i.e. $E \geq E_{pmp}$, $H_w > 0$ and $\nabla T' \cdot \mathbf{n}_b = \beta/K_c$), we let

$$K_0 \nabla E \cdot \mathbf{n}_b = 0. \quad (4.6)$$

The proposed insulating Neumann boundary condition suppresses the diffusive enthalpy flux into the temperate ice layer even in the case of $K_0 \neq 0$. In this case the energy at the base is balanced by the basal melting rate calculation.

Cold base (wet): if the glacier is cold, but has a liquid water layer at the base that is refreezing (i.e. $E < E_{pmp}$ and $H_w > 0$), then

$$E = E_{pmp}. \quad (4.7)$$

It is assumed here that the subglacial water is at the pressure melting point and the heat stored in the water layer does not allow the basal enthalpy to be below the pressure melting point (continuity of temperature). As a consequence, the refrozen ice has a zero water content.

Note that, in addition to the temperate base condition, $E \geq E_{pmf}$, it is necessary to check if there is a temperate layer of ice above, $\nabla T' \cdot \mathbf{n}_b = \beta/K_c$.

Since we are dealing with polythermal glaciers, melting of ice or refreezing of liquid water at the base plays a role. The calculated melting/refreezing rate, a_b (units: m s^{-1} ice equivalent), obeys

$$a_b = \frac{F_b - (\mathbf{q}_i - \mathbf{q}_{\text{geo}}) \cdot \mathbf{n}_b}{L\rho_i}, \quad (4.8)$$

with the frictional heating F_b due to basal sliding, the heat flux in the ice \mathbf{q}_i , and the geothermal flux \mathbf{q}_{geo} entering the ice at the base.

Although explicit boundary conditions for CTS are not required in the enthalpy scheme, they are used to evaluate the numerical results and to derive analytical solutions later in the text. According to Greve, 1997a, melting, freezing and parallel flow conditions must be distinguished depending on the CTS velocity. The enthalpy method allows for all three conditions in general. However, the basal boundary conditions used in Aschwanden *et al.* (2012) only permit melting conditions, as Eq. (4.6) inhibits the increase of enthalpy towards the CTS. Further, the numerical models applied here do not allow a discontinuous enthalpy solution in case of freezing or parallel flow conditions ($W > 0$ at the CTS).

In case of melting conditions at the CTS, the total enthalpy flux (advective and diffusive) at both sides of the CTS must be equal

$$\rho v E^+ + K_c \nabla E^+ \cdot \mathbf{n}_{\text{CTS}}^+ = \rho v E^- - K_0 \nabla E^- \cdot \mathbf{n}_{\text{CTS}}^-, \quad (4.9)$$

where the superscripts “+” and “−” denote the cold and the temperate side of the interface, respectively, and $\mathbf{n}_{\text{CTS}}^+$ and $\mathbf{n}_{\text{CTS}}^-$ are the normal vectors pointing toward the CTS. This is based on the general assumption that the total heat flux leaving a representative volume through a particular face must be identical to the flux entering the next representative volume through the same face.

At the CTS, ice at its pressure melting point and without any moisture flows into the temperate layer. Hence, the enthalpy is continuous at the CTS

$$E^+ = E^-. \quad (4.10)$$

Assuming a horizontal CTS and according to Eqs. (4.9) and (4.10), the enthalpy derivative at the CTS is discontinuous in the given case of $K_c \neq K_0$:

$$K_c \left. \frac{\partial E}{\partial z} \right|^+ = K_0 \left. \frac{\partial E}{\partial z} \right|^-. \quad (4.11)$$

The condition further implies that for $K_0 \rightarrow 0$ the enthalpy gradient on the cold side of the CTS (+) vanishes.

4.3 Numerical Models

The numerical models used here are all three-dimensional flow models including a thermal component for ice. They all allow the evolution of the ice thickness, although this is not applied here.

4.3.1 TIM-FD³ (finite differences)

In the Thermocoupled Ice-flow Model (TIM-FD3, Kleiner & Humbert (2014)), the relevant equations are discretised using finite-differences in terrain-following (sigma) coordinates. For the advective terms in Eq. (4.2) the hybrid difference scheme of Spalding (1972) is used. This scheme switches between the second-order central-difference scheme and the first-order upwind-difference scheme according to the local cell Peclet number. It allows stable numerical solutions for the advection dominated transport in the temperate ice layer.

The conductive terms in Eq. (4.2) are discretised using second-order central-difference scheme for the second derivative, where the conductivities are evaluated midway between the grid nodes (e.g. Greve & Blatter, 2009, Chap. 5.7.3). The transport due to sensible heat flux in the temperate layer

$\Gamma = \nabla \cdot (\kappa_i \nabla T_{pmp}(p)) = -\beta \nabla \cdot (\kappa_i \nabla p)$ is assumed to be small and considered as a source term in the model. The time stepping is performed using a semi-implicit Crank–Nicolson scheme with a constant time step.

Special attention is required for the diffusion term, since the conductivity is discontinuous at the CTS. The most straightforward procedure for obtaining the interface conductivity would be to assume a linear variation of the conductivity between nodes (arithmetic mean). However, this approach cannot handle the abrupt changes of conductivity at the CTS. We use the harmonic mean of the conductivities, as suggested by Patankar (1980, Chap. 4.2.3) not only at the CTS but for all conductivities evaluated between grid nodes.

4.3.2 ISSM (finite element)

The open source Ice Sheet System Model (ISSM; <https://issm.jpl.nasa.gov/>) is applied here. A detailed model description can be found e.g. in Larour *et al.* (2012a). It now implements the entire set of field equations and boundary conditions of the enthalpy formulation presented by Aschwanden *et al.* (2012). Since Seroussi *et al.* (2013), the implementation has been completed by adding the basal boundary condition and basal melting rate scheme as described in Aschwanden *et al.* (2012, Fig. 5).

The enthalpy field equation is discretised using a finite-element method with linear elements. The steady-state equation and implicit time stepping scheme, respectively, give rise to a nonlinear system. It is solved using a parallelized solver. The numerical scheme can be stabilised using artificial diffusion or streamline upwind diffusion. For best comparison to the respective analytical solutions no numerical stabilization has been used here. Jumps in heat conductivity at the CTS are being accounted for by taking a volume-weighted harmonic mean of the heat conductivities over the element, cf. Patankar (1980).

4.3.3 COMice (finite element)

Numerical solutions are obtained using the COMice model (Rückamp *et al.*, 2010) that is based on the commercial finite-element software COMSOL Multiphysics[®] (www.comsol.com). The domain is approximated by a structured triangular mesh with vertical equidistant layers. Enthalpy (Eq. 4.2) is solved with first-order Lagrange elements stabilized with streamline

diffusion. The time derivatives are discretized using the implicit backward Euler scheme. An adaptive time stepping method according to Hindmarsh *et al.* (2005) controls the chosen time step with respect to a given tolerance. We apply Newton's method to solve the resulting system of nonlinear algebraic equations at each time step.

The step of the conductivity from $K_c(E)$ to K_0 at the CTS is implemented using Comsol's built-in operator `circumcenter(expr)`:

$$K(E) = \begin{cases} K_c, & \text{if } \text{circumcenter}(E) < E_{pmp} \\ K_0, & \text{else.} \end{cases} \quad (4.12)$$

The operator interpolates the enthalpy solution to the circumcentre of the mesh element to which the point belongs. In doing so, `circumcenter(E)` is constant on each triangle and discontinuous along the edges. Therefore the conductivity jump is located on a mesh edge. This implementation shows better and faster convergence compared to other tested methods like a Heaviside function or a smoothed Heaviside function as used in the COMSOL implementation of Aschwanden & Blatter (2009) to compute the conductivity jump at the CTS. For post-processing, the CTS position is linearly interpolated between nodes.

4.4 Experiment Description

4.4.1 Experiment A: parallel sided slab (transient)

The simulation setup is designed to test the implementation of the basal decision chart for boundary conditions and melting rates (Aschwanden *et al.*, 2012, Fig. 5). Depending on the different thermal situations that occur at the base, the numerical code may have to switch between Neumann and Dirichlet boundary conditions for the enthalpy and the corresponding basal melting rate calculation. The main idea of this setup is to test the reversibility during transient simulations. The conservation of water volume is also addressed here. An initially cold ice body that runs through a warmer period with an associated build up of a liquid water layer at the base must be able to return to its initial steady state. This requires refreezing of the liquid water at the base. To test this behaviour we assume a simple heat conducting block of ice.

A parallel sided slab of ice of constant thickness H is considered. The surface is parallel to the bed and has a constant inclination $\gamma = 0^\circ$ to guarantee $|v| = 0$ and $\Psi = 0$. To make the setup basically vertical 1-D, in order to be able to consider only vertical heat transport, we impose periodic boundary conditions at the sides of the block. Hence the horizontal extension does not play a role. The geothermal flux q_{geo} at the base is constant. All parameters and their values are listed in Table 4.1.

The model run is as follows:

Initial phase (I): starting under cold conditions with an imposed surface temperature of $T_s = T_{s,c} = -30^\circ\text{C}$ and an isothermal initial temperature field $T(0, z) = T_{s,c}$ the simulation is run for 100 ka.

Warming phase (II): the surface temperature is switched to $T_s = T_{s,w} = -10^\circ\text{C}$ and the simulation is continued for another 50 ka.

Cooling phase (III): the surface temperature is switched back to the initial value of $T_s = T_{s,c}$ and the simulation is continued for further 150 ka.

Since Ψ is zero, a temperate layer of ice at the base will not form and cold ice conditions hold everywhere inside the ice. The ice thickness and vertical alignment of the block is held constant over time although a significant water layer can be build up during the warming phase. Further, the water is stored at the base and no restriction of the maximum water layer thickness is applied.

4.4.2 Experiment B: polythermal parallel sided slab (steady state)

To test the numerical solution for enthalpy in a vertical ice column with ice advection, we apply the “Slab with Melting Conditions at the CTS” setup with a known analytical solution for $K_0 = 0 \text{ kg m}^{-1} \text{ s}^{-1}$ (Greve & Blatter, 2009, Chap. 9.3.6). However, the knowledge about latent heat flux in temperate ice is poorly constrained as laboratory experiments and field observations are scarce. We vary the values of K_0 to highlight the effect on the resulting polythermal structure.

Similar to Experiment A, a parallel sided slab of constant ice thickness H and a constant surface and bed inclination γ in the x -direction is considered (Table 4.1). Ice flow is decoupled from the thermal quantities by using a constant flow rate factor A . The velocity throughout the ice column is prescribed as:

$$v_x(z) = \frac{A(\rho g \sin \gamma)^3}{2}(H^4 - (H - z)^4), \quad (4.13)$$

$$v_y(z) = 0, \quad (4.14)$$

$$v_z(z) = -a_s^\perp = \text{const.} \quad (4.15)$$

Note that this setup is not mass conservative, as there is no process considered that balances the accumulation rate required for a constant ice thickness. For simplicity we do not account for ice thickness evolution. The geothermal flux q_{geo} is set to zero and basal sliding is neglected ($F_b = 0$). Strain heating $\Psi = 4\mu\dot{\epsilon}_{\text{eff}}^2$ is the only source of heat, where μ and $\dot{\epsilon}_{\text{eff}}$ are the viscosity and the effective strain rate. The Glen-Steinmann power-law rheology (Glen, 1955; Steinmann, 1954) for the deformation of ice is used, thus

$$\mu = \frac{1}{2}A^{-1/3}\dot{\epsilon}_{\text{eff}}^{-2/3}, \quad (4.16)$$

$$\dot{\epsilon}_{\text{eff}} = \frac{1}{2} \frac{\partial v_x}{\partial z} = A(\rho g \sin \gamma)^3 (H - z)^3. \quad (4.17)$$

The strain heating is largest at the base and reaches $\sim 2.6 \times 10^{-3} \text{ W m}^{-3}$.

According to the assumptions in Greve & Blatter (2009, p. 246), the enthalpy conductivity K_0 in the temperate ice is zero, and the enthalpy flux at the cold site of the CTS (Eq. 4.11) must vanish. The CTS in this experiment is uniquely determined because the vertical velocity is downward. At the ice surface ($z = H$), the enthalpy is prescribed corresponding to the surface temperature $T_s = -3^\circ \text{C}$ and zero water content. At the ice base ($z = 0$), one of the boundary conditions given in Eqs. (4.4)–(4.7) holds depending

on the basal thermal conditions. All simulations start from a constant enthalpy corresponding to a temperature of $-1.5\text{ }^{\circ}\text{C}$ and zero water content. An analytical solution for the steady state enthalpy profile based on the solution of Greve & Blatter (2009) is given in Appendix 4.8.2. The solution leads to a CTS position of approx. 19 m above the bed. The conductivity ratio $\text{CR} = K_0/K_c$ varies from $\text{CR} = 10^{-1}$ to 10^{-5} for TIM-FD³ and COMice and to 0 for ISSM, respectively for this setup. The simulations are performed on vertically equidistant layers using different vertical resolutions $\Delta z = (10.0, 5.0, 2.0, 0.5)\text{ m}$.

Note that in both experiments outlined above, no frictional heating at the base occurs. Drainage of moisture that exceeds a certain limit to the base needs to be considered, when a coupling of moisture to the ice viscosity is used, but is also ignored in this study. The implementation of a basal hydrology model is beyond the scope of this study, hence basal water is accumulated at the place of origin with no restriction to the water layer thickness.

4.5 Results

4.5.1 Experiment A

The setup does not allow for a temperate ice layer and therefore enthalpy variations are given only by temperature variations. The simulated basal temperatures, basal melting rates and the basal water layer thicknesses over time are shown in Fig. 4.1.

As heat conduction is the only process of heat transfer, the vertical enthalpy profiles are linear in the steady states, which are reached at the end of each phase. At the steady states of the initial (I) and the cooling (III) phase, the total vertical temperature gradient is given by the geothermal flux at the base and Eq. (4.4). This leads to the basal temperature of $T_b^{(I,III)} = T_{s,c} + Hq_{\text{geo}}/\kappa_i = -10\text{ }^{\circ}\text{C}$ and zero melting at the base, revealed by all three models ($|\Delta T| < 5 \times 10^{-2}\text{ }^{\circ}\text{C}$).

In the warming phase (II), the basal temperature reaches the pressure melting point after a few thousand years and a basal water layer develops based on the basal melting rates. At the end of this phase, temperatures reach the steady state ($|\Delta T| < 5 \times 10^{-2}\text{ }^{\circ}\text{C}$) and the basal melting rates can be calculated based on the steady state temperature gradient between the surface and the base according to Eq. (4.8) as

$$a_b^{(II)} = \frac{1}{\rho_w L} \left(q_{\text{geo}} + \kappa_i \frac{T_{s,w} - T_{\text{pmp}}}{H} \right). \quad (4.18)$$

For this setting, the basal melting rate is $a_b^{(II)} = 3.12 \times 10^{-3}\text{ m a}^{-1}$ water equivalent (w.e.). The models agree well with Eq. (4.18) as shown in Fig. 4.1 ($|\Delta a_b^{(II)}| < 10^{-5}\text{ m a}^{-1}\text{ w.e.}$).

Phase III can be separated into two different parts: phase IIIa where the base is temperate because of the remaining basal water layer from phase II, and phase IIIb, where all subglacial water is refrozen and the base returns to cold conditions. As long as a basal water layer exists, the basal temperature is kept at pressure melting point independent of the applied surface temperature and temperature profile according to Eq. (4.7). At the end of phase

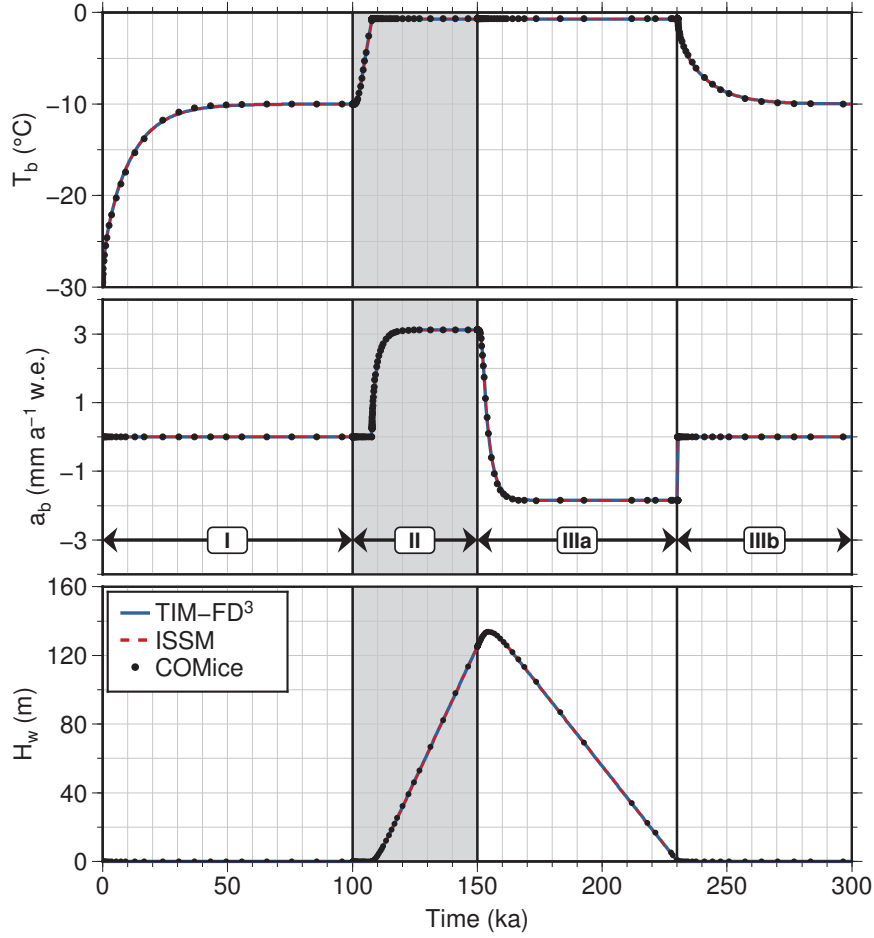


FIGURE 4.1: Results for Experiment A simulated with TIM-FD³ (blue), ISSM (red) and COMice (black) overlay each other. Phases I to III are described in the main text. The warming phase II is shaded in grey.

IIIa, the basal melting rates can therefore be found by replacing $T_{s,w}$ with $T_{s,c}$ in Eq. (4.18). Due to the low surface temperature refreezing conditions arise and reach steady state values of $a_b^{(\text{IIIa})} = -1.84 \times 10^{-3} \text{ m a}^{-1} \text{ w.e.}$ at the end of this phase as shown by the model solutions ($|\Delta a_b^{(\text{IIIa})}| < 10^{-5} \text{ m a}^{-1} \text{ w.e.}$).

Since we do not have included neither a hydrology model nor a reasonable upper limit for the subglacial water layer thickness, it is free to reach arbitrary thicknesses. That, in turn, is an advantage of the setup, as we want to observe the system behaviour over longer time periods. The simulations lead to a maximum water layer thickness of $\sim 130 \text{ m}$ that occurs a few thousand years after the end of the warming phase (II). A realistic liquid water layer thickness of about 2 m would vanish in a few time steps and would not allow for steady state considerations at the end of IIIa.

We have chosen phase IIIa to compare not only the quasi steady state solutions of the models at the end of each phase, but also the transient behaviour of the models compared to the analytical solution. For the comparison, we use the basal melting rate instead of the temperature profile, since the correct melting rate requires a correct temperature profile and is easier to compare. In Fig. 4.2, the simulated basal melting rates for the first 20 ka of phase IIIa are compared to the analytical solution given in Appendix

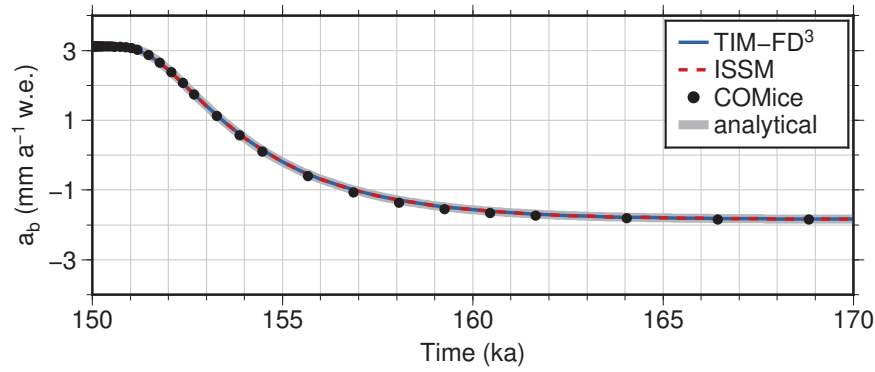


FIGURE 4.2: Simulation results compared to the analytical solution (thick solid grey line) for phase IIIa in Experiment A. TIM-FD³ as blue solid line, ISSM as red dashed line, and COMice as black filled circles.

4.8.1.

After ~ 1000 years, the cold signal from the surface reaches the base and melting starts to decrease until the temperature gradient in the overlying ice does not allow for further melting and refreezing sets in. All models agree well with the analytical solution. The COMice solution is sometimes slightly below the analytical solution because of the very large time steps. The transition between melting and freezing occurs after ~ 4684.7 years in the analytical solution. Model simulations show this transition at a comparable modelled time.

All model results clearly reveal reversibility: after the whole simulation period of 300 ka, the models return to the initial steady state at the end of phase I.

4.5.2 Experiment B

Here, model results of the steady state simulations of experiment B are compared to the analytical solution given in Appendix 4.8.2. For TIM-FD³ and COMice, the steady state is assumed after 1000 model years, while in ISSM a thermal steady state solver is applied. The final steady state CTS positions for all simulations are shown in Fig. 4.3.

For the maximum value of temperate ice conductivity ($CR = 10^{-1}$) and the highest vertical resolution ($\Delta z = 0.5$ m) the models result in a CTS position slightly below 36 m. In these simulations, the thickness of the temperate ice layer is almost doubled compared to the results achieved by using the smallest value of temperate ice conductivity ($CR = 10^{-5}$) with the same vertical resolution. The CTS positions decrease with decreasing CR and converge to the analytical solution. The models have approximately the same spread for the different vertical resolutions. The spread of the CTS position is smallest for $CR = 10^{-3}$, independent of the applied model. Compared to ISSM, TIM-FD³ and COMice implementations do not allow for solving the case $K_0 = 0$ as in the analytical solution.

The steady state enthalpy profiles and the corresponding temperature and moisture profiles are shown in Fig. 4.4 together with the analytical solution given in Appendix 4.8.2. The profiles are shown for the lowest (10 m) and highest (0.5 m) vertical resolution and the lowest conductivity ratio $CR = 10^{-5}$ used by all models. The results of all models agree well with the

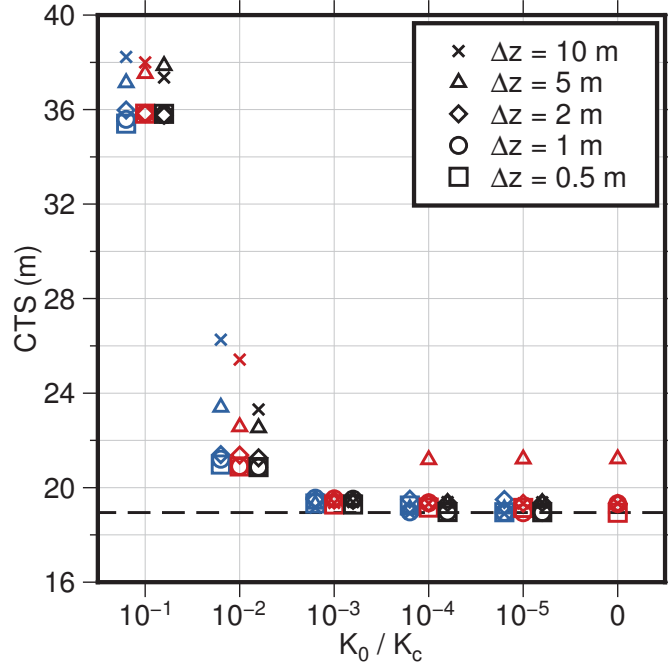


FIGURE 4.3: Comparison of simulated steady state CTS positions for different values of the temperate ice conductivity in Experiment B. The different models are shown as: TIM-FD³ (blue), ISSM (red) and COMice (black). Results of different models are slightly shifted on the x axis to not overlay each other. The dashed black line indicates the CTS position of the analytical solution derived for $K_0 = 0$.

analytical solution for high resolutions. At coarser resolutions, the simulated enthalpy profiles differ noticeably from the analytical solution. In the following, we compare enthalpy differences as $\Delta E = E_{\text{analytic}} - E_{\text{simulated}}$.

In the ISSM simulation with the coarsest resolution ($\Delta z = 10$ m), the enthalpy differs from the analytical solution by $\sim 1720 \text{ J kg}^{-1}$ close to the CTS. This results in a temperature difference of $\sim 0.9^\circ\text{C}$ in the cold-ice part. TIM-FD³ and COMice reveal also a lower enthalpy at the cold side of the CTS compared to the analytical solution, but only to a minor extent (TIM-FD³: $\sim 0.2^\circ\text{C}$, COMice: $\sim 0.1^\circ\text{C}$). Note, the analytical solution only holds for $K_0 = 0$, thus small differences are expected here.

As the method chosen for interpolating heat conductivities in ISSM strongly favours the lower value, a quasi isolating layer thicker than in the analytical solution is artificially created. Thus, heat flux into the upper cold ice column decreases, and that column cools. Vice versa, excess heat is accumulated in the lower temperate ice column, such that this part of the ice column heats up. The result is a negative temperature and positive water fraction offset. It scales with vertical mesh resolution, but stays detectable even on the highest mesh resolution tested here.

In the TIM-FD³ simulation with the coarsest resolution ($\Delta z = 10$ m), the enthalpy difference ΔE is largest at the base ($\sim 2530 \text{ J kg}^{-1}$). As the base is temperate, this difference in the enthalpy corresponds to a difference in the basal water content of $\sim 0.8\%$. With this resolution the temperate ice layer needs to be resolved within the lowermost three grid points. The slope in the profile is caused by second order one-sided discretisation (e.g. Payne & Dongelmans, 1997) of the basal boundary condition (Eq. 4.6)

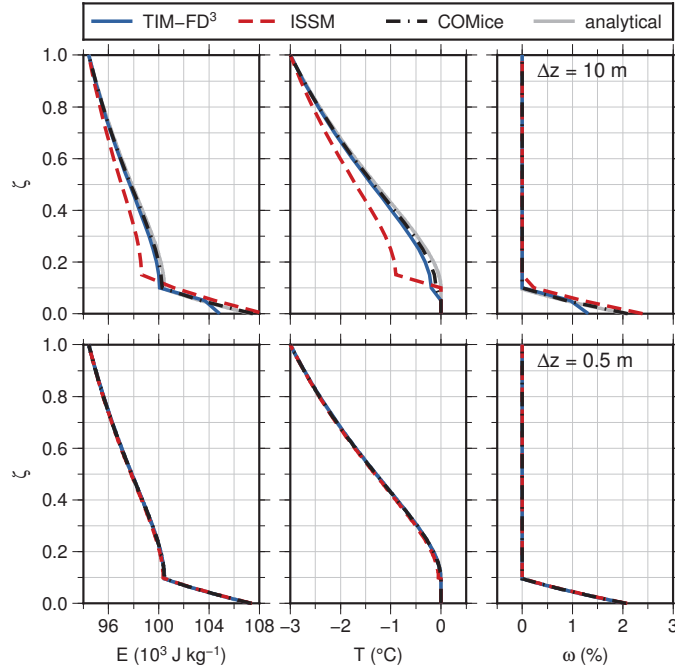


FIGURE 4.4: Simulated steady state profiles of the enthalpy, E , the temperature, T , and the water content, W for TIM-FD³ (blue), ISSM (red) and COMice (black) compared to the analytical solution (grey). $\zeta = z/H$ is the normalised vertical coordinate. The vertical resolution is $\Delta z = 10$ m (upper row) and $\Delta z = 0.5$ m (lower row), $CR = K_0/K_c = 10^{-5}$. In the lower row the model results overlay the analytical solution.

in TIM-FD³. Compared to the FE models neither strain heating nor transport of heat is considered for basal grid nodes.

With increasing vertical resolution, the maximum deviation from the analytical solution decreases for all models. For the highest resolution ($\Delta z = 0.5$ m) and $CR = 10^{-5}$ the maximum differences are $\sim 150 \text{ J kg}^{-1}$, $\sim 100 \text{ J kg}^{-1}$, and $\sim 10 \text{ J kg}^{-1}$ for TIM-FD³, ISSM and COMice, respectively. The differences remain positive, thus the enthalpy is slightly underestimated. Only ISSM is able to perform the experiment with $K_0 = 0$ as in the analytical solution, but the maximum enthalpy difference does not further decrease. As expected from Eq. (4.11), all models show small enthalpy gradients at the cold side of the CTS.

The observed order of accuracy measured as the root-mean-square deviation (RMSD) to the analytical solution has been obtained in the series of vertical mesh refinements from $\Delta z = 10$ m to 0.5 m and is shown in Figure 4.5. The models TIM-FD³ and ISSM show approximately first-order convergence as $\Delta z \rightarrow 0$, while in COMice the RMSD drops only for Δz below 2 m. The finite difference discretisation scheme in TIM-FD³ is formally second-order accurate in space (and time) and the finite element models ISSM and COMice use linear basis functions, thus one would expect second-order convergence as $\Delta z \rightarrow 0$ for smooth problems. However, this is not the case here, since the observed order of accuracy depends on the strength of discontinuities (conductivity ratio between cold and temperate ice) and on the CTS implementation details.

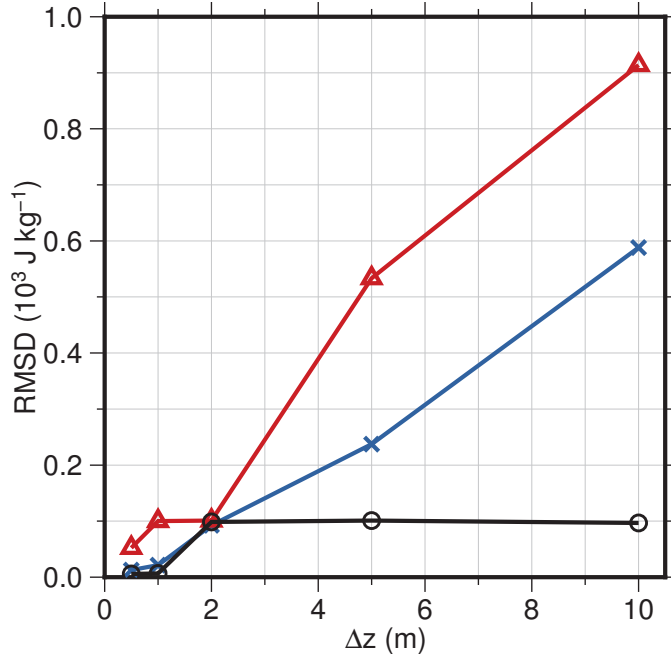


FIGURE 4.5: The root-mean-square deviation (RMSD) of the model results to the analytical solution (Experiment B) for different vertical grid resolutions Δz . Model results for TIM-FD³ (blue crosses), ISSM (red triangles) and COMice (black circles) are obtained for the lowest conductivity ratio $CR = K_0/K_c = 10^{-5}$ applied to all models.

4.6 Discussion

All three models are able to run the time dependent experiment A and agree with the analytical solutions in terms of absolute values, timing and reversibility. However, not all types of basal boundary conditions have been tested here. Since the absence of strain heating suppresses the formation of a temperate ice layer at the base, the insulating boundary condition (Eq. 4.6) could not be tested.

Beside the test of the implementation of the boundary conditions, this experiment addresses the importance of a basal water layer. Although the surface temperature changes, the basal temperature is kept at pressure melting point as long as a basal water layer exists. The amount of water at the base is crucial for the temperatures in the ice, because it acts as an energy buffer. It slows down the response of basal temperatures to surface cooling. The water layer thicknesses simulated here are unrealistic high compared to conditions under real ice masses. More realistic simulations would require a subglacial hydrology model, but this is beyond the scope of this paper.

Experiment B addresses whether the models are able to reproduce the steady state analytical solution for certain polythermal conditions including advection, diffusion and strain heating. The models agree well with the analytical solution for $K_0 \rightarrow 0$, if the vertical resolution is high. All models meet the transition conditions for the melting CTS, although no explicit boundary conditions are implemented. An adequate treatment of the abrupt change of conductivity at the CTS in the numerical discretisation scheme is required to achieve this behaviour. The usage of an arithmetic

mean (TIM-FD³) or a Heaviside as well as a smoothed Heaviside function (COMice) for the conductivity jump leads to oscillations in the enthalpy solution that are visible e.g. in a time varying CTS position. Consequently, no steady state solution is reached under these conditions. The harmonic mean approach of Patankar (1980, Chap. 4.2.3) for the conductivity (TIM-FD³ and ISSM) leads to a continuous heat flux at the CTS and violates the condition of Eq. (4.11) (non-continuous). Nevertheless, the harmonic mean strongly favours the lower conductivity K_0 for small ratios $CR = K_0/K_c$ and this leads to the apparent jump in $\partial E/\partial z$.

TIM-FD³ tends to underestimate the water content at the base of a temperate ice layer. This would result in stiffer ice at the base. In typical applications of the model the vertical layers are not equidistant as in this study, but refined towards the base. We therefore expect only a minor influence on the velocity field. ISSM simulations underestimate the temperature in the cold part accompanied by an overestimation of the water content in the basal temperate layer at coarse resolution. Implications for the overall stiffness are hard to obtain. Ice would deform more in the temperate part at the base, but less in the cold part above.

The understanding of moisture transport in the temperate ice is poor. If the latent heat flux can be represented as in Aschwanden *et al.* (2012), then it is crucial to consider the assumption made on the chosen value of K_0 . Simulations with a relatively high value of K_0 would lead to a much thicker temperate ice layer in contrast to simulations where $K_0 \approx 0$. Stable numerical solutions could be obtained for temperate ice diffusivities in the chosen range of $K_0 \approx 10^{-4}$ to $10^{-8} \text{ kg m}^{-1} \text{ s}^{-1}$ and 0 for ISSM. The lower bound is therefore several magnitudes lower than $K_0 = 10^{-4} \text{ kg m}^{-1} \text{ s}^{-1}$ as the lowest value possible for a stable solution in Aschwanden & Blatter (2009). If one assumes a vanishing latent heat flux in the temperate part of a glacier, we would recommend to use a value of $K_0 \approx 10^{-6} \text{ kg m}^{-1} \text{ s}^{-1}$ ($CR = 10^{-3}$). For this value, the CTS positions of all models are close to the analytical solution and show the smallest spread with varying vertical resolutions (Fig. 4.3).

The evolution equation for the enthalpy field is similar to the temperature evolution equation already implemented in thermomechanically-coupled ice sheet models. Therefore an enthalpy scheme allows one to convert so-called 'cold-ice' models into polythermal ice models with only minor modifications, but with the restriction of melting conditions at the CTS. The question whether exclusive melting conditions at the CTS are valid in an ice sheet is not conclusive. At least simulations of the Greenland Ice Sheet based on a two-layer front-tracking scheme performed with the polythermal ice model SICOPOLIS indicate that freezing conditions are relatively rare (Greve, 1997a; Greve, 1997b). In the most recent version of SICOPOLIS the enthalpy scheme by Aschwanden *et al.* (2012) and a modified version of this scheme have been implemented as conventional one-layer enthalpy scheme and one-layer melting CTS scheme, respectively (Blatter & Greve, 2015). Thus comparisons to the two-layer front-tracking scheme can be performed for continental scale ice sheets in the future.

The dynamics of glaciers, ice caps and ice sheets are strongly linked to the description of the rheology of temperate ice and its uncertainties. Besides the limited knowledge on the rheology of temperate ice, the current experimentally-based relationship for the flow rate factor is only valid for

water contents up to 1 % (Duval, 1977; Lliboutry & Duval, 1985). However, actual water contents found in temperate and polythermal glaciers are sometimes substantially larger (up to 5 %, Bradford & Harper, 2005). The advantage of deriving the water content by solving numerically for the enthalpy is limited by the use of a flow rate factor with a restricted validity range. Consequently, deformation experiments with temperate ice are urgently needed.

4.7 Conclusions

The proposed numerical experiments provide tests for the enthalpy implementation in numerical ice sheet models. All models applied here (TIM-FD³, ISSM, COMice) are able to perform these experiments successfully and agree to the analytical solutions. The enthalpy scheme determines the cold-temperate transition surface (CTS) and the vertical enthalpy profile in a polythermal glacier correctly without the need of tracking the CTS explicitly and applying additional conditions at this internal boundary. This is in particular the case for high vertical resolution for all three models. TIM-FD³ and COMice also perform well for low vertical resolution, while the ISSM solution shows a significant enthalpy difference to the analytical solution although the analytical CTS position is met. There is a clear need for an empirical determination of the temperate ice conductivity K_0 and an improved description of the temperate ice rheology.

4.8 Appendix: Analytical Solutions

4.8.1 Basal Melt Rate in Experiment A

To derive the basal melting rate for phase (IIIa) of Experiment A, it is assumed that the temperature is in steady-state at the end of the warming phase (II). For this setup, Eq. (4.2) simplifies to the one-dimensional form

$$\rho_i \frac{\partial E}{\partial t} = \frac{\partial}{\partial z} \left(K_c \frac{\partial E}{\partial z} \right). \quad (4.19)$$

We have only cold ice conditions in the interior of the ice body and K_c as well as ρ_i are constants. Based on the transfer rules in Eq. (4.1), Eq. (4.19) can be written as an evolution equation for the temperature:

$$\frac{\partial T}{\partial t} = \kappa \frac{\partial^2 T}{\partial z^2} \quad \text{and} \quad \kappa = \frac{\kappa_i}{\rho_i c_i}. \quad (4.20)$$

We determine the evolution of $T(z, t)$ starting from the initial condition (steady state temperature profile of phase II)

$$T(z, 0) = T_0(z) = T_{pmp} + (T_{s,w} - T_{pmp})z/H \quad (4.21)$$

and Dirichlet conditions at the upper and lower surface

$$T(H, t) = T_{s,w} \quad \text{and} \quad T(0, t) = T_{pmp}. \quad (4.22)$$

The basal temperature is kept at pressure melting point by the basal water layer (Eq. 4.7). Solutions of the heat equations can be found by separation of variables and Fourier analysis and require homogeneous boundary conditions. Therefore, the temperature deviation Θ is used instead of T , thus:

$$T(z, t) = T_{\text{eq}}(z) + \Theta(z, t), \quad (4.23)$$

where the steady state profile for this setup is again a linear

$$T_{\text{eq}}(z) = T_{\text{pmp}} + (T_{\text{s,c}} - T_{\text{pmp}})z/H. \quad (4.24)$$

Substitution of Eq. (4.23) into Eq. (4.20) and application of the steady state solution $T_{\text{eq}}(z)$ implies that $\Theta(z, t)$ satisfies the homogeneous heat equation

$$\frac{\partial \Theta}{\partial t} = \kappa \frac{\partial^2 \Theta}{\partial z^2} \quad (4.25)$$

with homogeneous Dirichlet boundary conditions,

$$\Theta(0, t) = \Theta(H, t) = 0 \quad \text{for } t > 0 \quad (4.26)$$

and the initial condition

$$\Theta(z, 0) = T_0(z) - T_{\text{eq}}(z) \quad \text{for } 0 \leq z \leq H. \quad (4.27)$$

The solution of Eqs. (4.25)–(4.27) for Θ can be obtained using the method of separation of variables and leads to (e.g. Dubin, 2003):

$$\Theta(z, t) = \sum_{n=1}^{\infty} A_n e^{\lambda_n t} \sin \frac{n\pi z}{H}, \quad \text{where } \lambda_n = -\kappa \left(\frac{n\pi}{H} \right)^2. \quad (4.28)$$

Setting $t = 0$ the Fourier coefficients A_n can be found by matching the initial condition Eq. (4.27)

$$\Theta(z, 0) = \sum_{n=1}^{\infty} A_n \sin \frac{n\pi z}{H} = T_0(z) - T_{\text{eq}}(z), \quad (4.29)$$

thus for the Fourier sine series, the coefficients A_n are determined as

$$A_n = \frac{1}{H} \int_0^H (T_0(z) - T_{\text{eq}}(z)) \sin \frac{n\pi z}{H} dz. \quad (4.30)$$

Inserting the initial condition (Eq. 4.21) and the steady state profile (Eq. 4.24) into Eq. (4.30) leads to

$$A_n = (-1)^{n+1} \frac{2(T_{\text{s,w}} - T_{\text{s,c}})}{n\pi}. \quad (4.31)$$

Based on the analytical solution of the temperature profile (Eq. 4.28), the basal melting rate (Eq. 4.8) is

$$a_b = \frac{q_{\text{geo}} - q_i}{\rho L} = \frac{1}{\rho L} \left(q_{\text{geo}} + k \left. \frac{\partial T}{\partial z} \right|_{z=0} \right), \quad (4.32)$$

where

$$\begin{aligned} \left. \frac{\partial T}{\partial z} \right|_{z=0} &= \left. \frac{\partial T_{\text{eq}}(z)}{\partial z} \right|_{z=0} + \left. \frac{\partial \Theta(z, t)}{\partial z} \right|_{z=0} \\ &= \frac{T_{\text{s,c}} - T_{\text{pmp}}}{H} + \sum_{n=1}^{\infty} \frac{n\pi}{H} A_n e^{\lambda_n t}. \end{aligned} \quad (4.33)$$

The sum is evaluated up to $n = 25$ to produce the analytical solution shown in Fig. 4.2.

4.8.2 Analytical Solution Experiment B

The following derivation of the analytical solution to experiment is a modification of the derivation of the “parallel-sided polythermal slab” provided by Greve & Blatter (2009). Under the assumptions given there and the variable transform $z = \zeta H$, the enthalpy field Eq. (4.2) reduces to

$$\mathcal{D} \frac{\partial^2 E}{\partial \zeta^2} + \mathcal{M} \frac{\partial E}{\partial \zeta} = -\mathcal{K} (1 - \zeta)^4, \quad \text{if } E < E_{\text{pmp}} \quad (4.34)$$

$$\mathcal{M} \frac{\partial E}{\partial \zeta} = -\mathcal{K} (1 - \zeta)^4, \quad \text{else.} \quad (4.35)$$

Here,

$$\mathcal{D} = \frac{K_{\text{i}}}{\rho}, \quad \mathcal{M} = H a_{\text{s}}^{\perp}, \quad \mathcal{K} = \frac{2A}{\rho} (\rho g \sin \gamma)^4 H^6. \quad (4.36)$$

Let E^+ be a solution of Eq. (4.34) and E^- a solution to Eq. (4.35). Then the enthalpy solution for the entire ice column is given by $E = E^- \mathbb{I}_{[0, \zeta_{\text{m}})} + E^+ \mathbb{I}_{[\zeta_{\text{m}}, 1]}$, where ζ_{m} is the position of the CTS.

At the CTS, the continuity condition for the enthalpy Eq. (4.10) holds and due to the neglect of water conductivity in temperate ice the right hand side of Eq. (4.11) is zero. A solution E^+ to Eq. (4.34) is given by a solution to the homogeneous differential equation E_{h} associated to Eq. (4.34) and a particular solution E_{p} :

$$E^+ = E_{\text{h}} + E_{\text{p}}, \quad \text{with} \quad (4.37)$$

$$E_{\text{h}}(\zeta) = c_1 e^{-\mathcal{M}\zeta/\mathcal{D}} + c_2, \quad \text{and} \quad (4.38)$$

$$E_{\text{p}}(\zeta) = \sum_{k=1}^5 a_k \zeta^k. \quad (4.39)$$

The coefficients a_1, \dots, a_5 of E_{p} can be found by balancing powers in Eq. (4.34), cf. Greve & Blatter (2009). The three remaining unknowns, c_1 , c_2 and ζ_{m} , can now be derived from the conditions at the CTS (Eqs. 4.10 and 4.11)

and the given surface enthalpy. Inserting E^+ yields:

$$E_s = c_1 e^{-\mathcal{M}/\mathcal{D}} + c_2 + \sum_{k=1}^5 a_k \quad (4.40)$$

$$E_{pmp} = c_1 e^{-\mathcal{M}\zeta_m/\mathcal{D}} + c_2 + \sum_{k=1}^5 a_k \zeta_m^k \quad (4.41)$$

$$0 = -c_1 \frac{\mathcal{M}}{\mathcal{D}} e^{-\mathcal{M}\zeta_m/\mathcal{D}} + \sum_{k=1}^5 k a_k \zeta_m^{k-1}. \quad (4.42)$$

With c_1 from Eq. (4.42), c_2 from Eq. (4.40), Eq. (4.41) becomes an implicit definition for ζ_m , whose root can be determined using a numerical solver. Then c_1 and c_2 follow accordingly.

A solution E^- for the temperate ice part can be found by integrating the temperate version of Eq. (4.35) directly. E^- is then fully determined by Eq. (4.11):

$$E^-(\zeta) = E_{pmp} + \frac{\mathcal{K}}{5\mathcal{M}} \left((1 - \zeta)^5 - (1 - \zeta_m)^5 \right). \quad (4.43)$$

Acknowledgements

The authors would like to thank H. Blatter, R. Greve, F. J. Navarro, J. Otero and F. Ziemen for fruitful discussions on enthalpy and ice sheet models. We acknowledge the support of the ISSM developer team (E. Larour, H. Seroussi and M. Morlighem) for the implementation of the enthalpy formulation in ISSM.

5 Modelling calving front dynamics using a Level-Set Method: Application to Jakobshavn Isbræ, West Greenland

Context

Observations suggest that the terminus position is a major control on the dynamics of Jakobshavn Isbræ (Sect. 2.2). The glacier's terminus is a steep ice cliff, which towers up to 90 m over the water level (Echelmeyer *et al.*, 1991). Ice cliffs like this exert a significant driving stress on the ice in its vicinity (Weertman, 1957). Jakobshavn Isbræ discharges a large fraction of its ice by calving (Echelmeyer *et al.*, 1991; Howat *et al.*, 2011). Its terminus position advances with the motion of the ice, and retreats with calving and ocean melting at the vertical face. Despite the wide array of observations, it is unclear which mechanisms sustain its widespread acceleration and thinning (cf. Sect. 2.4).

Various explanatory hypotheses concerned with the sustained speedup exist (see Sect. 2.3), but could not be tested with ISSM, because it did not feature a calving-front-tracking scheme. Ice margin retreat was approximated through thinning the margins through high melting rates. This approach is not suitable to model a seasonally migrating calving front. Reproducing the calving front retreat through heavily increased melting would be unphysical, distort the modelled glacier's ratio of melting to calving, and would not result in the same backstress evolution, as it would be difficult to reproduce the terminus' steep ice cliff this way. It was thus necessary to design and implement a numerical scheme to allow dynamic calving front evolution for ISSM's 2D and 3D model simulations.

The aim of the following publication is to introduce a Level-Set Method (LSM, Osher & Sethian, 1988, and Sect. 3.2) for dynamic calving front position evolution in an ice sheet model. The LSM is an Eulerian boundary tracking approach, and is thus well suited for use in models which employ static meshes, like ISSM. The publication describes the theoretical framework of the method, which is generally applicable in current ice sheet models, and provides implementation details for ISSM. The perturbation study of Jakobshavn Isbræ proves the method's applicability to complex, real-world glacier geometries. In this thesis, this publication serves to introduce and test the calving front-tracking scheme, which is a necessary step before we apply it to the three-dimensional, thermodynamically coupled model of Jakobshavn Isbræ in Chap. 6.

The test setups in the appendix show the correct functioning of the LSM, and provide assessments of the mesh resolution required for accurate tracking of the calving front. The perturbation experiments on Jakobshavn Isbræ give qualitative insights to its two-dimensional flow dynamics: they highlight the importance of lateral effects like momentum transfer and mass influx as well as the dominating role of the calving front position on the glacier's dynamics. However, it is not possible to draw quantitative conclusions from this study: calving rates are prescribed instead of being dynamically computed, and the influence of three-dimensional effects on the stress regime and the thermal regime is not captured. Therefore, a three-dimensional, thermodynamically coupled model study of Jakobshavn Isbræ's evolution using a suitable calving rate parametrisation is necessary to address these points.

Contributions

Conceptual design, implementation, testing and maintenance of the LSM in ISSM was done by Bondzio, with counselling by H. Seroussi and M. Morlighem. The publication text was written by Bondzio and proof-read by all co-authors. All numerical experiments presented in the publication were performed by Bondzio. All figures except Fig. 5.2 were created by Bondzio.

Authors and Affiliations

Johannes H. Bondzio¹, Hélène Seroussi², Mathieu Morlighem³, Thomas Kleiner¹, Martin Rückamp¹, Angelika Humbert^{1,4} & Eric Y. Larour²

1. Alfred Wegener Institute, Helmholtz Centre for Polar and Marine Research, Bremerhaven, Germany
2. Jet Propulsion Laboratory - California Institute of Technology, Pasadena, CA, USA
3. Department of Earth System Science, University of California Irvine, Irvine, CA, USA
4. University of Bremen, Bremen, Germany

Abstract

Calving is a major mechanism of ice discharge of the Antarctic and Greenland Ice Sheets, and a change in calving front position affects the entire stress regime of marine terminating glaciers. The representation of calving front dynamics in a two or three dimensional ice sheet model remains non-trivial. Here, we present the theoretical and technical framework for a Level-Set Method, an implicit boundary tracking scheme, which we implement into the Ice Sheet System Model (ISSM). This scheme allows us to study the dynamic response of a drainage basin to user-defined calving rates. We apply the method to Jakobshavn Isbræ, a major marine terminating outlet glacier of the West Greenland Ice Sheet. The model robustly reproduces the high sensitivity of the glacier to calving, and we find that enhanced calving triggers significant acceleration of the ice stream. Upstream acceleration is sustained through a combination of mechanisms. However, both lateral stress and ice influx stabilise the ice stream. This study provides new insights into the ongoing changes occurring at Jakobshavn Isbræ, and emphasises that the incorporation of moving boundaries and dynamic lateral effects, not captured in flow-line models, is key for realistic model projections of sea level rise on centennial time scales.

5.1 Introduction

Calving of icebergs is a major mean of ice discharge for marine terminating glaciers around the world. It accounts for about half of the ice discharge of the Greenland and Antarctic Ice Sheets (Cuffey & Paterson, 2010; Rignot *et al.*, 2013). This process causes calving front retreat, which leads to reduced basal and lateral stress and results in upstream flow acceleration.

In order to assess the impact of calving on the dynamics of outlet glaciers using an ice sheet model, we need to include a dynamically evolving calving front. This requires tracking the calving front position and adjusting the boundary conditions accordingly. Addressing these issues is rather straightforward for 1D-flow-line or 2D-flow-band models (Nick *et al.*, 2009; Vieli & Nick, 2011), where the calving front is tracked along the flow-line. However, this type of model lacks the consistent representation of lateral

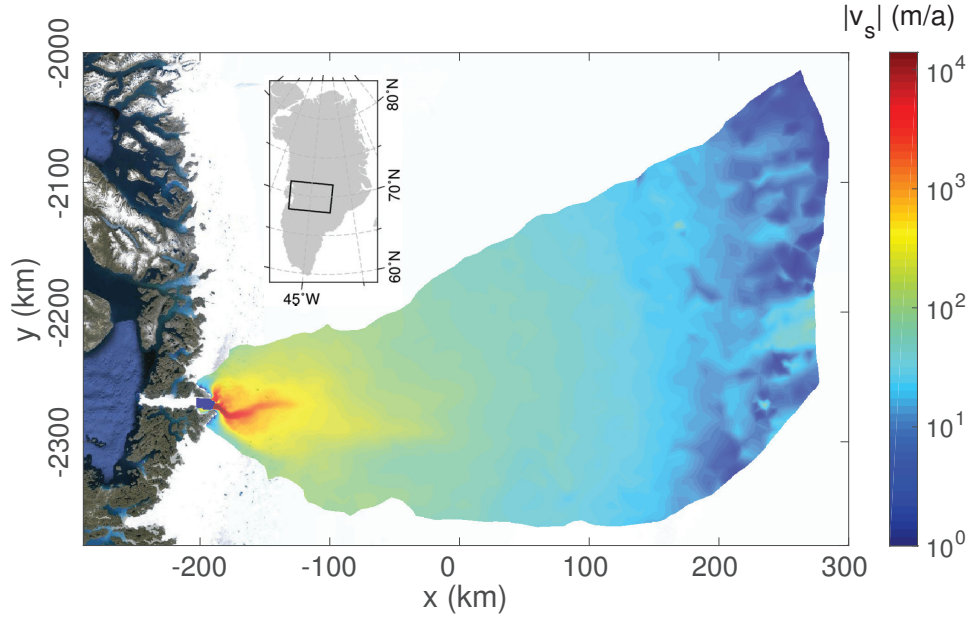


FIGURE 5.1: Observed ice surface velocities 2008/2009 (Rignot & Mouginot, 2012) of the Jakobshavn Isbræ drainage basin (logarithmic scale). Background image from Google Earth ©.

momentum transfer and lateral ice influx from tributaries for example, which have to be parametrised instead. This parametrisation may neglect feedback effects important for simulations on decadal to centennial time scales, e.g. catchment area entrainment (Larour *et al.*, 2012b).

It is therefore critical to include a front tracking scheme in 2D-horizontal and 3D models, which has been addressed by only a few ice sheet models (e.g. Jouvét *et al.*, 2008; Winkelmann *et al.*, 2011). Various approaches to model the evolution of the shape of ice exist. Explicit methods track the position of a set of points, which represent the calving front. They require a complex technical framework to allow for geometric operations like folding and intersection of the continuum boundary, tracking singularities in curvature, and determining the position of a point in space relative to the modelled continuum. Alternatively, the Level-Set Method (LSM, Osher & Sethian, 1988) represents the continuum boundary implicitly by a contour, or “level-set”, of a so-called “Level-Set Function” (LSF). It easily handles topological changes of the modelled continuum, like splitting and merging. The LSM is based on a partial differential equation similar to the mass transport equation solved by ice sheet models. This makes the method straightforward to implement, and allows for the application to continental scale ice sheet simulations. Although the method does not necessarily conserve volume accurately, it is well established in Continuum Fluid Mechanics (Chang *et al.*, 1996; Groß *et al.*, 2006). A LSM has been applied to represent the ice surface in 2D-flow-band models (Pralong & Funk, 2004), but not to model real ice sheets yet.

Understanding calving dynamics remains challenging because of the diversity of factors involved in calving events. Bathymetry, tides and storm swell, as well as sea ice cover, ice mélange and temperatures of both sea water and air are possible factors influencing calving rates. However, their effect, their respective share and their interplay seem to vary from glacier to

glacier, and are not well understood (Cuffey & Paterson, 2010; Krug *et al.*, 2015). Therefore, no universal calving rate parametrisation exists to date (Benn *et al.*, 2007), and we rely here on user-defined calving rates. However, incorporating calving rate parametrisations in the LSM should be straightforward.

Jakobshavn Isbræ is a major marine terminating glacier in West Greenland, which drains about 6.5% of the Greenland Ice Sheet (Zwally *et al.*, 2011). It is characterised by two branches, which today terminate into a 50 km long ice-choked fjord (Figs. 5.1 and 5.2). The southern branch exhibits high flow velocities, which are confined to a narrow, deep trough of about 5 km width. The trough retrogradely slopes inland to a maximum depth of about 1700 m below sea level (Gogineni *et al.*, 2014), and discharges most of the ice of the drainage basin (Rignot & Mouginot, 2012). We refer to the fast-flowing area as “ice stream”, and to the surrounding slow-moving ice as “ice sheet”. Those areas are separated by pronounced shear margins on either side of the ice stream. Observations have shown that the fast flowing areas of Jakobshavn Isbræ exhibit a weak bed with a basal layer of temperate, soft ice (Lüthi *et al.*, 2002). Basal sliding and shear in this layer cause most of these areas’ horizontal motion. A large fraction of the ice stream’s momentum is transferred to the adjacent ice sheet by lateral stress. It is thus well justified to use the two-dimensional shelfy-stream approximation (SSA, MacAyeal, 1989) to simulate this glacier.

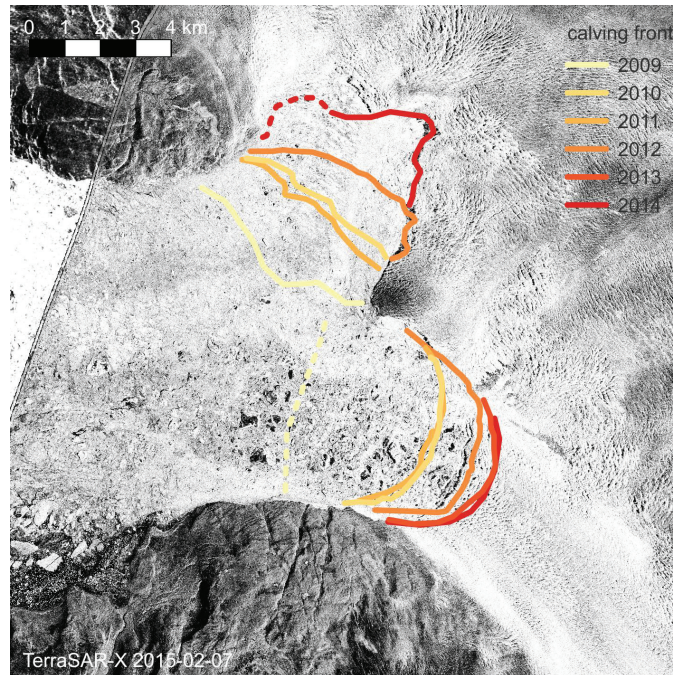


FIGURE 5.2: Winter (Feb-Mar) calving front positions from 2009 to 2014 overlaid on a TerraSAR-X scene from 2015-02-07 (© DLR). Dashed lines are used in case of ambiguous calving front positions.

Until the late 1990s, Jakobshavn Isbræ had a substantial floating ice tongue, which extended well into the fjord, and was fed by both branches. The calving front position remained fairly constant from 1962 to the 1990s (Sohn *et al.*, 1998), and the glacier exhibited negligible seasonal variations in flow speed (Echelmeyer & Harrison, 1990). In the 1990s, the glacier started

a phase of acceleration, thinning and retreat, that followed the breakup of its ice tongue. Seasonal variations in calving front position and flow velocity increased sharply (Joughin *et al.*, 2004; Joughin *et al.*, 2008). Today, the glacier is one of the fastest ice streams in the world. It is still far from equilibrium and is a major contributor to global sea level rise (Howat *et al.*, 2011; Joughin *et al.*, 2014). Observations suggest that the calving front position is a major control on the ice stream dynamics (Podrasky *et al.*, 2012; Rosenau *et al.*, 2013; Moon *et al.*, 2014).

Various hypotheses have been proposed to explain the mechanisms behind this change. All identify the breakup of the floating ice tongue as the initial trigger of this dramatic chain of events, but different mechanisms have been proposed to explain the sustained acceleration, thinning and retreat of the glacier. Studies by Joughin *et al.* (2012) and Habermann *et al.* (2013) propose loss of buttressing and changes in basal conditions as the main cause behind the ongoing acceleration. On the other hand, van der Veen *et al.*, 2011 argue that weakening of the lateral shear margins has significantly amplified the upstream acceleration. Several modelling studies of the glacier, which use 1D-flow-line and 2D-flow-band models, project unstable retreat of the glacier along its southern trough for up to 60 km inland within the next century (Viel & Nick, 2011; Joughin *et al.*, 2012; Nick *et al.*, 2013). Other modelling studies argue that this type of ice stream is stable as long as it is fed by the surrounding ice sheet (Truffer & Echelmeyer, 2003). However, numerical 2D-planview modelling efforts of Jakobshavn Isbr  so far lacked the representation of a dynamically evolving calving front. Hence, the hypotheses could not be tested in a satisfactory manner.

We present here a LSM-based framework to model the dynamic evolution of a calving front. This method is a step towards better physical representation of calving front dynamics in 2D and 3D ice sheet models. We describe the implementation of the method into the Ice Sheet System Model (ISSM, Larour *et al.*, 2012a), a parallel, state-of-the-art ice sheet model, and apply it here to Jakobshavn Isbr  in order to model its dynamic response to perturbations in calving rate.

5.2 Theory

5.2.1 Ice Flow Model

We employ the SSA on both floating and grounded ice. It neglects all vertical shearing but includes membrane stresses. The ice viscosity, μ , follows Glen's flow law (Glen, 1955):

$$2\mu = B\dot{\epsilon}_e^{\frac{1-n}{n}} \quad (5.1)$$

Here, $n = 3$ is Glen's flow law coefficient, B the ice viscosity parameter, and $\dot{\epsilon}_e$ the effective strain rate. We apply a Neumann stress boundary condition at the ice-air and ice-water interface, corresponding to zero air pressure and hydrostatic water pressure, respectively. A linear friction law links basal shear stress, σ_b , to basal sliding velocity, v_b , on grounded ice:

$$\sigma_b = -\alpha^2 N_{eff} v_b, \quad (5.2)$$

where α denotes the basal friction parameter. We calculate the effective basal pressure, N_{eff} , assuming that sea water pressure applies everywhere at the glacier base, which is a crude approximation far from the grounding line. The ice thickness, H , evolves over time according to the mass transport equation:

$$\frac{\partial H}{\partial t} = -\nabla \cdot (H\mathbf{v}) + a_s + a_b. \quad (5.3)$$

Here, \mathbf{v} is the depth-averaged horizontal ice velocity, and a_s and a_b are the surface and basal mass balance, respectively. We determine the grounding line position using hydrostatic equilibrium, and treat it with a sub-element parametrisation (Seroussi *et al.*, 2014b). We refer the reader to Larour *et al.*, 2012a for details on the solution of these equations in ISSM.

TABLE 5.1: Symbols and model parameters

Symbol	Quantity
μ	Ice viscosity
B	Ice viscosity parameter
$\dot{\epsilon}_e$	Effective strain rate
n	Glen’s flow law parameter
α	Basal friction parameter
N_{eff}	Effective basal pressure
\mathbf{v}	Depth-averaged horizontal ice velocity
H	Ice thickness
a_s	Surface mass balance
a_b	Basal mass balance
Ω	Computational domain
Ω_i	Ice domain
Ω_c	Ice free domain
Γ	Ice boundary
Γ^h	Numerical ice boundary
φ	Level-Set Function
\mathbf{n}	Unit surface normal
\mathbf{w}	Level-set velocity
a^\perp	Ablation rate
c^\perp	Calving rate
m^\perp	Melting rate
s	Scaling function
p	Perturbation function
Δt	Perturbation duration
p_0	Perturbation strength
L	Seasonal calving period length
ϕ_0	Phase shift
Q_{cf}	Calving flux

5.2.2 Level-Set Method

Let Ω be a computational domain in 2D or 3D space, and φ a real, differentiable function on $\Omega \times \mathbb{R}_+$, called “Level-Set Function” (LSF). For any $c \in \mathbb{R}$,

we define the contour, or “ c -level-set”, of φ by $\varphi(\mathbf{x}, t) = c$. Taking its material derivative yields the “Level-Set Equation” (LSE):

$$\frac{\partial \varphi}{\partial t} + \mathbf{w} \cdot \nabla \varphi = 0. \quad (5.4)$$

This Hamilton-Jacobi type partial differential equation describes how level-sets move with the local value of the velocity \mathbf{w} , which is called level-set velocity. We need to provide an initial condition $\varphi_0(\mathbf{x}) = \varphi(\mathbf{x}, t = 0)$ to solve the LSE.

We use φ to partition Ω into three disjoint subdomains: the ice domain, $\Omega_i(t)$, its complement, $\Omega_c(t)$, and their common boundary, $\Gamma(t)$:

$$\begin{cases} \varphi(\mathbf{x}, t) < 0 \Leftrightarrow \mathbf{x} \in \Omega_i(t) \\ \varphi(\mathbf{x}, t) = 0 \Leftrightarrow \mathbf{x} \in \Gamma(t) \\ \varphi(\mathbf{x}, t) > 0 \Leftrightarrow \mathbf{x} \in \Omega_c(t) \end{cases}$$

We omit the time dependence of these sets in the remainder of this article. By construction, Γ , the 0-level-set of φ , separates Ω_i and Ω_c .

We extend \mathbf{n} , the outward-pointing unit normal of Γ , onto Ω using the LSF by:

$$\mathbf{n} = \frac{\nabla \varphi}{|\nabla \varphi|}. \quad (5.5)$$

For details on the Level-Set Method and its applications, we refer to Osher & Sethian (1988) and Sethian (2001).

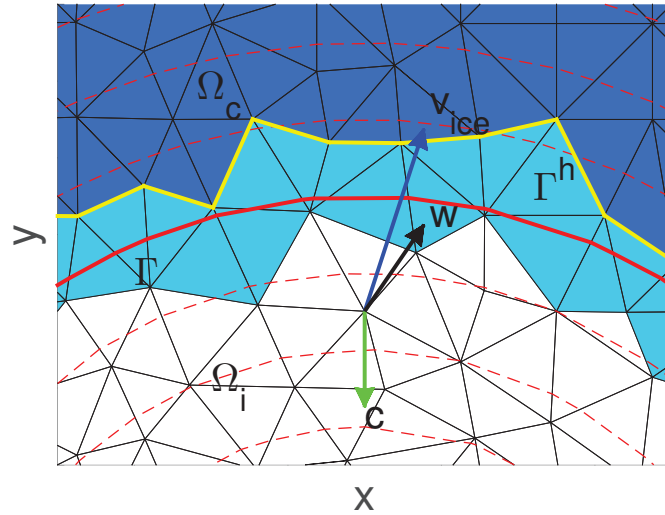


FIGURE 5.3: Schematic of the numerical ice margin. The red dashed lines denote different contour lines (level-sets) of the LSF φ . The thick red line marks the 0-level-set, Γ , the yellow line the numerical calving front Γ^h . Dark blue triangles are ice-free elements, white ones are ice-filled and the light blue ones are the front elements. The three vectors show an example of the level-set velocity $\mathbf{w} = \mathbf{v} + \vec{c}$, $\vec{c} = -c^\perp \mathbf{n}$ at a finite element node.

The boundary position of an ice sheet evolves with the sum of the ice velocity \mathbf{v} along \mathbf{n} and an ablation rate, a^\perp :

$$\mathbf{w} \cdot \mathbf{n} = \mathbf{v} \cdot \mathbf{n} - a^\perp. \quad (5.6)$$

It follows that the ice boundary is stationary if and only if $a^\perp = \mathbf{v} \cdot \mathbf{n}$, i.e. the ablation rate matches the ice velocity perpendicular to the ice boundary. The ablation rate needs to be prescribed, either based on observations or through a parametrisation.

Note that no limitations have been made so far with respect to the dimension of the problem in this section. Accordingly, the method could be applied to model the evolution of the glacier thickness and lateral extent simultaneously (Pralong & Funk, 2004). However, in this 2D-planview model study, we use the LSM to model only the horizontal extent of the ice sheet. Its vertical extent is described by the mass transport equation (5.3).

We model lateral ablation as the sum of a melting rate, m^\perp , and a calving rate, c^\perp : $a^\perp = c^\perp + m^\perp$. For simplicity, we assume in the remainder of the article that lateral ablation occurs in the form of calving exclusively, i.e. $m^\perp = 0$. Calving itself is assumed to be a quasi-continuous process, consisting of frequent, but small calving events. With (5.5) and (5.6), the LSE becomes:

$$\frac{\partial \varphi}{\partial t} + \mathbf{v} \cdot \nabla \varphi = c^\perp |\nabla \varphi|, \quad (5.7)$$

which is also known as “Kinematic Calving Front Condition” (KCFC, Greve & Blatter, 2009). Both the calving rate and ice velocity need to be provided on the entire 2D computational domain Ω in order to solve the KCFC. An example of a calving rate field will be given in section 5.3.2, and is shown in Fig. 5.4. The KCFC implies that all level-sets of φ , including the calving front Γ , move at a given time with the local sum of the horizontal ice velocity and calving rate along the normal \mathbf{n} (Fig. 5.3). We define the calving flux Q_{cf} as the ice flux crossing the calving front:

$$Q_{cf} = \int_{\Gamma} c^\perp(r) H(r) dr. \quad (5.8)$$

The ice velocity components and the ice thickness are only defined on Ω_i , and need to be extended onto Ω_c (see also section 5.2.3). Any scalar field, S , is extrapolated onto Ω_c by solving:

$$\mathbf{n} \cdot \nabla S = 0, \quad (5.9)$$

while keeping S fixed on Ω_i . This type of extrapolation has the tendency to preserve $|\nabla \varphi| = \mathcal{O}(1)$, when we use the extrapolated ice velocity field to solve the KCFC (Zhao *et al.*, 1996).

5.2.3 Implementation

ISSM relies on the Finite Element Method (FEM) to solve partial differential equations. It applies a Continuous Galerkin FEM using triangular (2D) and prismatic (3D) Lagrange finite elements, and uses anisotropic mesh refinement to limit the number of degrees of freedom while maximizing spatial resolution in regions of interest.

We discretise the KCFC (5.7) and extrapolation equation (5.9) using linear finite elements on the same mesh as the one used to model the ice dynamics. We stabilise both equations with artificial diffusion (Donea & Huerta, 2003), which after thorough testing proved to be the most robust

stabilisation scheme. We integrate over time using a semi-implicit time-stepping scheme. We solve the KCFC, and the field equations for ice flow modelling in a decoupled fashion. The KCFC is solved first with input data from the previous time step. We then update the numerical ice domain using the new LSF as described below, and update boundary conditions accordingly. Finally, we solve the momentum balance and the mass transport equation on the updated ice domain.

The 0-level-set of φ , Γ , does in general not coincide with the finite element mesh edges due to its implicit representation. It intersects a number of elements (“front elements”) with a hyperplane, which divides them into an ice-filled and an ice-free part (Fig. 5.3). This has various implications on the numerical level. When assembling the system stiffness matrices for ice flow modelling, exclusive integration over the ice-filled part of the element would be required. The stress boundary condition at the calving front would have to be applied at the intersecting hyperplane. Currently, ISSM is not capable of resolving those submesh scale processes.

Therefore, we either fully activate or deactivate a mesh element at every time step. Only active elements are considered for the numerical discretisation of the respective field equations. We activate an element if at least one of its vertices is in Ω_i or Γ , and the element is then considered to be entirely filled with ice. We flag the element as ice free if it lies entirely inside Ω_c , and it is deactivated. As a consequence, the numerical calving front, Γ^h , runs along mesh edges, and is updated in a discontinuous manner (Fig. 5.3). We apply the stress boundary condition along Γ^h for numerical consistency. Calving front normals on Γ and Γ^h may differ significantly in direction. However, stress components tangential to \mathbf{n} cancel out along Γ^h , so that the integrated stress exerted at the calving front is close to the one applied along Γ . For all further calculations where a normal is involved, like extrapolation, the normal to the LSF (5.5) is used.

The numerical calving front is by definition further downstream than Γ . This may lead to slightly higher resistive lateral stress at the calving front, whose magnitude depends on the excess ice area of the intersected front element and the front geometry. We use a fine mesh resolution in the vicinity of the calving front to limit this effect.

We extrapolate the calving front thickness onto the ice-free domain using equation (5.9). This yields realistic ice thickness and ice thickness gradients across the front elements, that would otherwise lead to overestimated driving stress and underestimated water pressure at the ice-ocean interface. If not corrected, those two effects unrealistically increase ice velocities at the calving front, which then feed back into the mass transport and LSM schemes.

We present two experiments for validation of the LSM implemented here in the Appendix. The first experiment shows that the ice margin is advected with the prescribed level-set velocity w . The linear representation of the LSF on an unstructured mesh causes a small error in the exact level-set position, which depends on element size and cancels out over time. The second test shows that errors in volume conservation introduced by the LSM decrease with finer mesh resolution, and are below 0.2% after 100 years for a mesh resolution of 1 km. In the application to Jakobshavn Isbræ, we use a front element size of 0.5 km. The potential volume loss inherent

to this implementation of the LSM is thus far below current uncertainties of model input data.

Inclusion of the LSM requires additional computational effort for the extrapolation of field variables, to solve the KCFC, and for extra iterations of the momentum balance solver, since the stress boundary conditions at the calving front change frequently. Its amount depends on the flow approximation and especially on whether the model setup is close to a stable configuration or not. Using SSA, the additional computational cost reaches up to 25%, of which 11% is caused by the solution of the KCFC.

5.3 Data and Model Setup

5.3.1 Jakobshavn Isbræ Model Setup

We use Jakobshavn Isbræ's drainage basin from Zwally *et al.*, 2011 to generate a 2D-horizontal finite element mesh with element size varying from 500 m in the fjord and areas of fast flow to 10 km inland (Fig. 5.4). We choose this high mesh resolution to minimise calving front discretisation errors, and to resolve the fjord and the deep trough accurately in the model. The resulting mesh has about 10,000 vertices and 19,000 elements. Due to high flow velocities, the Courant-Friedrich-Lewy condition (CFL, Courant *et al.*, 1928) dictates a time step on the order of days for the solution of the momentum balance equation, the mass transport equation, and the KCFC.

We use bed topography from Morlighem *et al.*, 2014b, derived using a mass conservation approach (Morlighem *et al.*, 2011). The ice surface elevation is taken from GIMP (Howat *et al.*, 2014), and ice thickness is the difference between ice surface and ice base elevation. Bathymetry of the ice-choked fjord of Jakobshavn Isbræ is difficult to measure and currently poorly known. As a first order estimate, we apply a parabolic profile of 800 m depth along the ice fjord, fitted via spline interpolation to known topography data. We rely on Ettema *et al.* (2009) for the surface mass balance, and, as a first approximation, use their surface temperatures to initialize our ice viscosity parameter, B , based on the table from Cuffey & Paterson, 2010. Surface temperatures range from $\sim -8^\circ\text{C}$ near the coast to $\sim -28^\circ\text{C}$ near the divide. Basal mass balance is set to zero and no thermal model is run. All these forcings are kept constant over time.

We infer a basal friction coefficient, α , in (5.2) using an adjoint-based inversion (MacAyeal, 1993; Morlighem *et al.*, 2010) of surface velocities from 2009 (Rignot & Mouginot, 2012). In regions like the fjord, where there is no ice today, we apply an area-averaged value of $\alpha = 30 \text{ kg}^{1/2} \text{ m}^{-1/2} \text{ s}^{-1}$. At the margins of the computational domain we prescribe zero horizontal ice velocities in order to prevent mass flux across this boundary. The friction parameter is kept fixed over time for all model simulations.

Inconsistencies in model input data cause sharp readjustments of the glacier state at the beginning of each simulation, which would make it difficult to distinguish between such effects and those of the applied forcing (Seroussi *et al.*, 2011). Therefore, we relax the model prior to the experiments using a fixed, piecewise linear LSF φ_0 , whose 0-level-set corresponds to the mean annual calving front position of 2009 (Fig. 5.4). Since the glacier

in this configuration is far from steady state, model relaxation causes considerable thinning across the glacier's catchment area. In order not to deviate too much from present day's geometric setting we choose a 100 year relaxation time period. Note that the grounding line retreats during the relaxation due to dynamic thinning, so that the glacier forms a new floating ice tongue. This ice tongue extends about 15 km to a local topographic maximum in the southern trough and 3 km into the northern one (Fig. 5.4). The relaxed geometry constitutes the initial state for our experiments. Due to this deviation in geometry, providing quantitative insights into Jakobshavn Isbræ is beyond the scope of this study. However, the main characteristics of the ice stream (e.g. its large drainage basin and the narrow outlet channel) are preserved, so that the results presented in this paper qualitatively represent the behaviour of Jakobshavn Isbræ.

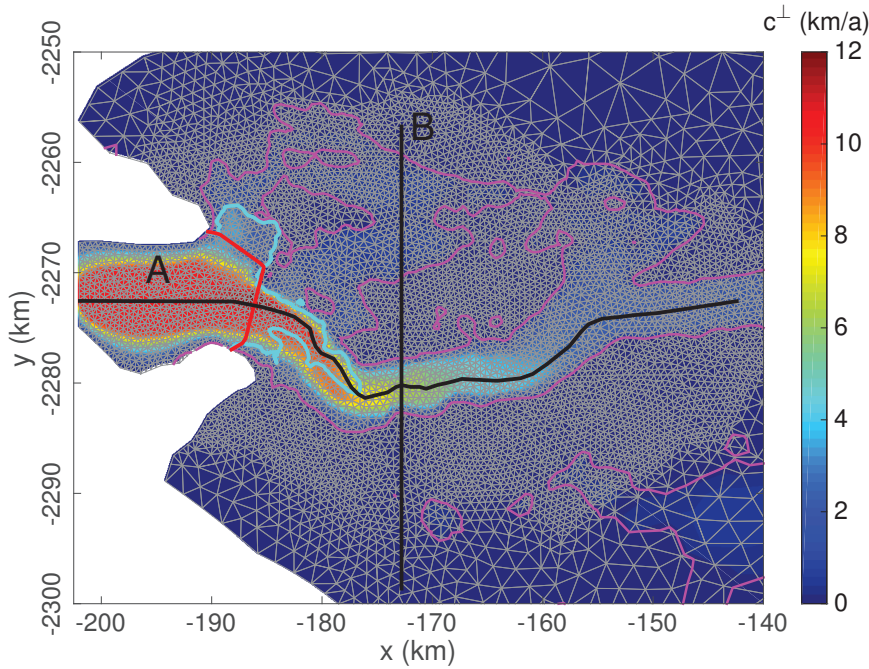


FIGURE 5.4: Calving rate field c_0^\perp in the region of fast flow, which has been derived from modelled ice velocities at the end of the relaxation run. The red line indicates the 0-level-set of the initial LSF used for geometry relaxation and as start position for the calving front during the experiments. The turquoise line marks the grounding line. Purple contours indicate zero bedrock elevation. Black lines are the “along-trough” (A) and “across-trough” (B) profiles used in Fig. 5.6. The finite element mesh is displayed in grey.

5.3.2 Description of Experiments

We set

$$c_0^\perp = q|v_0| \quad (5.10)$$

as a basic calving rate estimate, where v_0 is the velocity field at the end of the geometry relaxation run, extended onto Ω_c (Fig. 5.4). The continuous function q is equal to 1 in areas where the bed lies below -300 m, and linearly drops to 0 in areas of positive bed elevation. It prevents calving to

occur in areas with a glacier bed above sea level, as suggested by observations of tidewater glaciers (Brown *et al.*, 1982). The choice of the calving rate estimate is motivated by the small observed angle between \mathbf{v}_0 and \mathbf{n} at the calving front ($\mathbf{v}_0 \approx |\mathbf{v}_0| \mathbf{n}$). Then $\mathbf{w}_0 \cdot \mathbf{n} = \mathbf{v}_0 \cdot \mathbf{n} - c_0^\perp \approx 0$, so that we can expect this calving rate estimate to yield a stationary calving front, if applied to a geometry that is in steady state. We scale c_0^\perp over time with a scaling function, s , which allows for the representation of seasonal cycles, and a perturbation function, p , to modify the calving rate for some period of time. The applied calving rate is then: $c^\perp(\mathbf{x}, t) = c_0^\perp(\mathbf{x}) s(t) p(t)$.

We perform three suites of experiments in order to analyse the impact of the calving rate on the glacier's dynamics. The calving front is now allowed to freely evolve in response to c^\perp . All experiments run for 120 years.

In experiment A, we keep the calving rate constant over time, i.e. we set both $s(t) = p(t) = 1$. Hence, $c^\perp(\mathbf{x}, t) = c_0^\perp(\mathbf{x})$. This experiment, although not physically motivated, is used to evaluate whether a stable calving front position can be reached using the LSM, and for comparison to the experiments described below.

In experiment suites B and C, we represent the seasonal cycle by scaling c_0^\perp by $s(t) = \max(0, \pi \sin(2\pi(t/L - \phi_0)))$, with a phase shift $\phi_0 = 4/12$ and a period $L = 1$ a. We perturb the calving rate during a limited duration, Δt , with a perturbation strength $p_0 \geq 0$: $p(t) = \begin{cases} p_0, & \text{if } t_0 < t < t_0 + \Delta t, \text{ and} \\ 1, & \text{else.} \end{cases}$

We start the perturbation at $t_0 = 20$ a for all experiments. In experiment suite B, we perform 5 experiments with $\Delta t = 1$ a, while varying p_0 from 0 to 4 by increments of 1. In experiment suite C, we keep $p_0 = 2$ fixed, and set Δt as 2, 4 and 8 years. We use the notation B< p_0 > and C< Δt > to identify single experiments, e.g. B1 for experiment B with perturbation strength $p_0 = 1$, which represents the case of unperturbed periodic calving. B1 is used as a control run the other experiments can be compared to. Table 5.2 lists all the experiments performed here.

TABLE 5.2: Table of experiments

Name	p_0	Δt	Name	p_0	Δt	Name	p_0	Δt
A	1	0	B2	2	1	C2	2	2
B0	0	1	B3	3	1	C4	2	4
B1	1	1	B4	4	1	C8	2	8

5.4 Results

Figure 5.5 shows calving front positions for experiments A, B1, B2 and C4. Under constant calving rate forcing, the calving front remains at a stable position after minor readjustments in the first decade of the simulation. In experiment A, the calving front undergoes gradual retreat over time due to the slowdown of the glacier caused by its ongoing thinning. When we perturb the calving rate, the calving front migrates, and higher calving rates lead to larger retreats. The retreat is highest in areas of fast flow, and

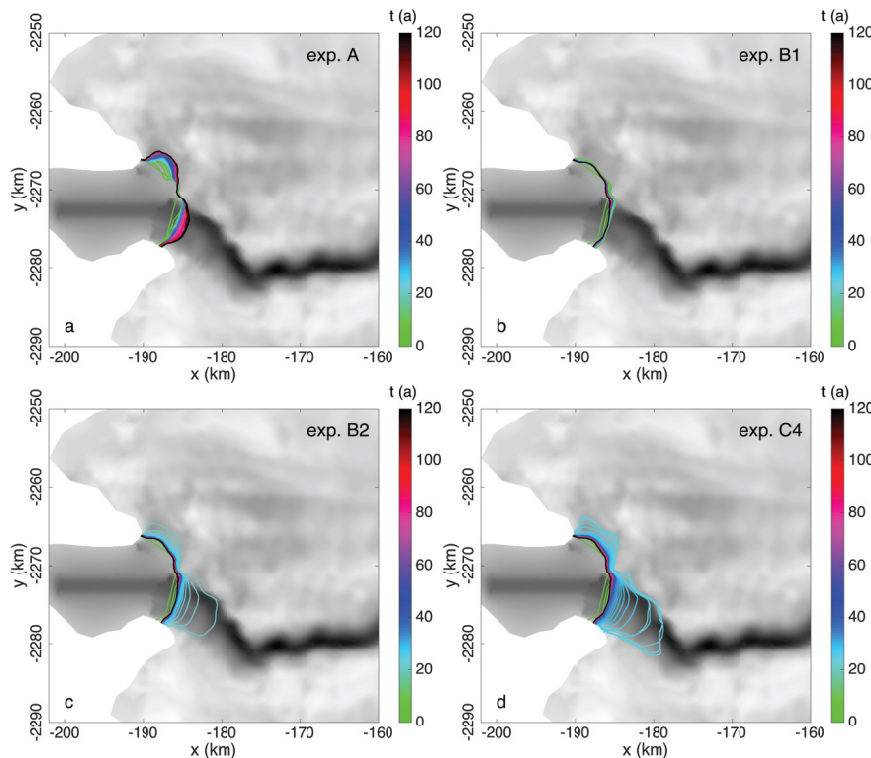


FIGURE 5.5: Calving front positions for experiments A, B1, B2 and C4 at the start of each year, plotted over basal topography (grey).

strongly decreases towards the ice stream margins. This yields the characteristic concave shape of a retreating calving front. The modelled calving front positions and their shape are in good agreement with observations (Fig. 5.2). The retreat rate during continued phases of calving decreases to zero, so that the calving front reaches a new stable position 9 km upstream of its initial position (Fig. 5.5d). In experiments B and C, the calving front returns to a similar position as in the unperturbed experiment B1 within ten to twenty years after the perturbation stops.

Figure 5.6 shows ice velocity, geometry and strain rates for experiment C4 along two lines, which go along and across the southern trough, respectively (Fig. 5.4). During the first 20 years prior to the perturbation, the ice thickness in the floating part decreases by about 100 metres (Fig. 5.6a). As the calving front retreats during the perturbation, the ice velocity increases (Fig. 5.6b), and the ice thickness adjusts accordingly (Fig. 5.6a). The ice thinning leads to a fast retreat of the grounding line in the regions of locally retrograde bed, and temporarily stabilises over local along-trough topographic maxima, referred to as “local highs”. The southern trough has many local highs, which act as pinning points and are critical for flow dynamics, in agreement with earlier results from Vieli & Nick (2011). The acceleration of the ice stream extends tens of kilometres upstream, to areas of grounded ice (Fig. 5.6b). Thinning and acceleration are strongest over the ice stream, and spread out to the surrounding ice sheet in a dampened fashion. These thinning and acceleration patterns increase surface and velocity gradients, especially in the shear margins (Fig. 5.6c), where the effective strain rates gradually increase up to a factor of 4 in experiment C4 (Fig. 5.6d), which corresponds to a drop in viscosity of about 60% (equation 5.1).

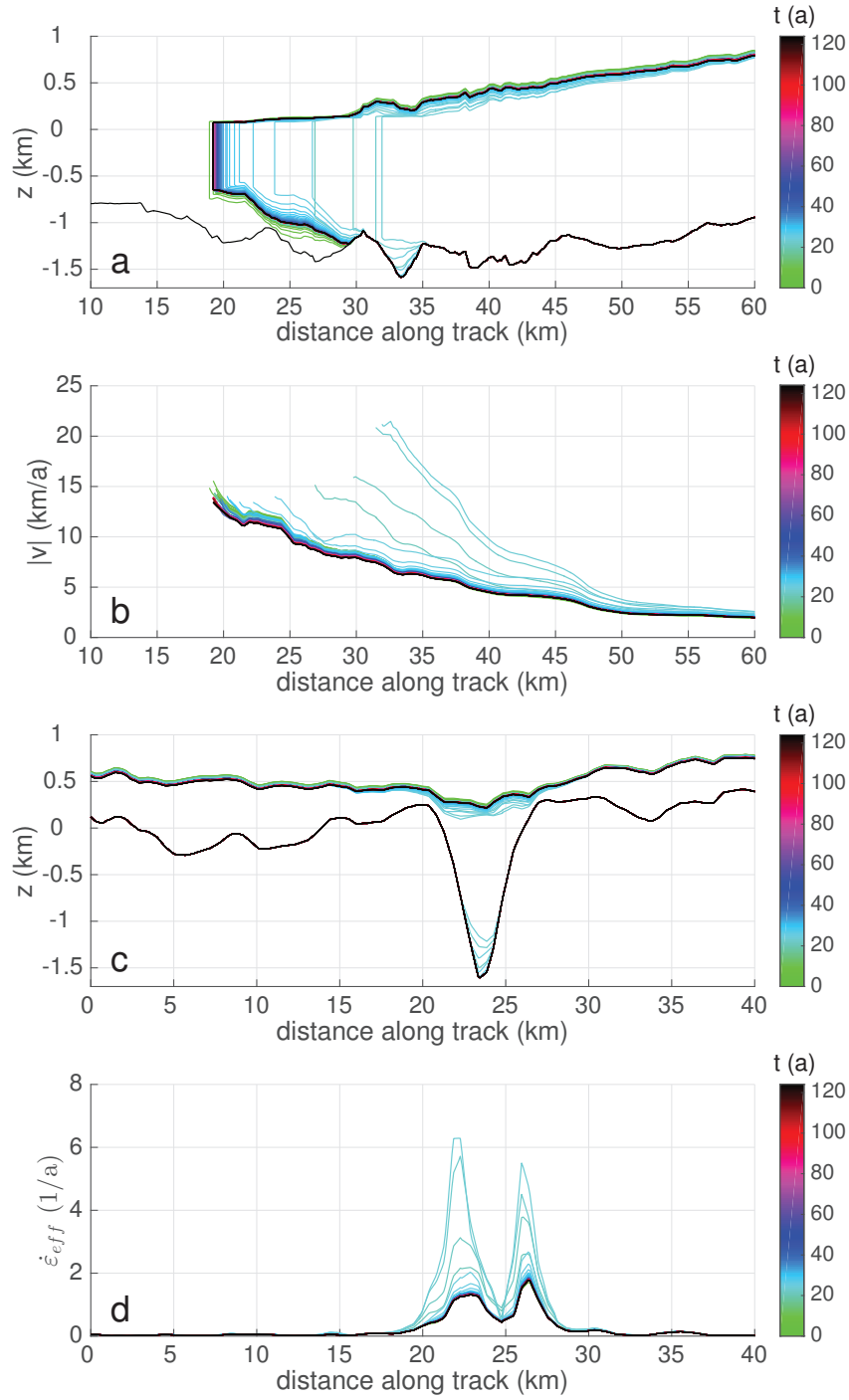


FIGURE 5.6: Section profiles of ice geometry (a) and ice velocity (b) along-trough, as well as ice geometry (c) and effective strain rates (d) across-trough for experiment C4 at the end of the calving season in October each year. Positions of the lines are given in Fig. 5.4.

This substantially weakens the mechanical coupling between the ice stream and the surrounding ice sheet.

Figure 5.7 shows the intra-annual variability of ice properties at the calving front and grounding line for experiments A, B1, B2 and C4. All shown variables reflect the characteristics of the applied calving rate forcing. The

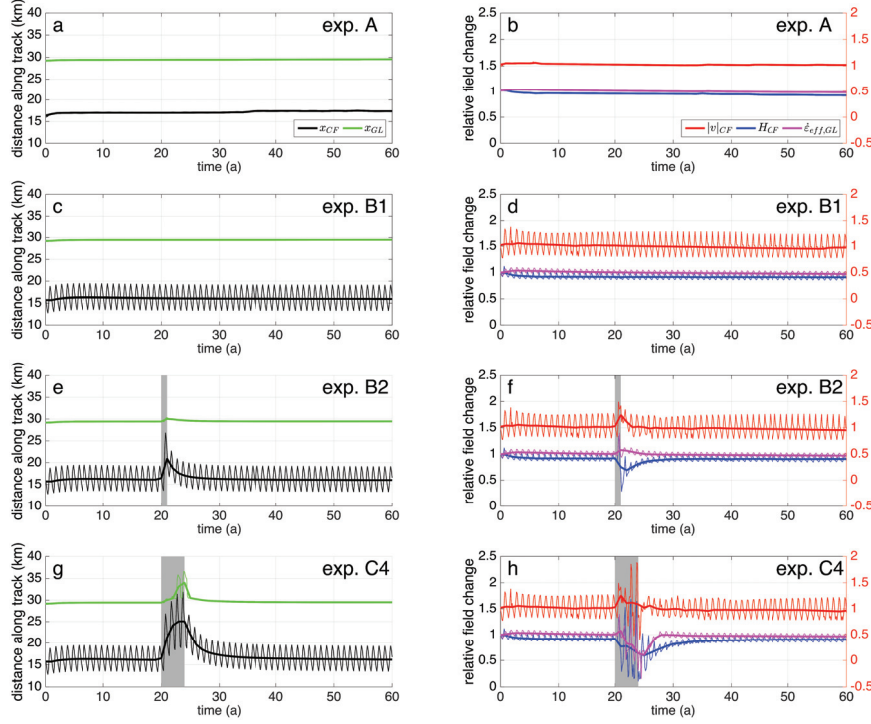


FIGURE 5.7: Calving front and grounding line positions along-trough (left column), calving front thickness, ice velocity and effective strain rate relative to their initial value along-trough (right column) over time for experiments A, B1, B2 and C4. Perturbation intervals are marked in grey. Relative values for ice velocity have been shifted up by 0.5 for better visibility (red y-axis).

constant calving rate applied in experiment A leads to a steady configuration (Fig. 5.7a and 5.7b). For an unperturbed periodic calving rate forcing (Fig. 5.7c and 5.7d), the calving front position oscillates around a constant annual mean value by ± 3 km, while the grounding line position remains unchanged at kilometre 29. Ice velocities and thickness at the calving front act in phase with the calving front position, while the response of strain rates at the grounding line is delayed by about a month. The ice velocity varies over a year by $\pm 20\%$, which corresponds to about $\pm 2 \text{ km a}^{-1}$, the ice thickness by $\pm 13\%$, or $\pm 100 \text{ m}$, and effective strain rates at the grounding line by $\pm 7\%$, or $\pm 0.1 \text{ a}^{-1}$.

The response to a calving rate perturbation scales with p_0 and Δt . When the calving rate doubles (B2, C4), the calving front retreats initially at an average rate of 4.5 km a^{-1} . The calving front stabilizes 9 km upstream for longer perturbations (Fig. 5.7g). The intra-annual variability of the calving front position doubles to ± 6.5 km. The grounding line position is hardly affected by small calving rate perturbations, but large perturbations trigger fast retreats of several kilometres, which in turn cause drastic, but short-lived flow accelerations (Figs. 5.7g and 5.7h). The annual average ice velocity increases by 10%, and its intra-annual variability doubles to $\pm 38\%$ (Fig. 5.7h). The mean calving front thickness decreases by 30% towards the end of the perturbation of experiment C4, and experiences large variations up to $\pm 75\%$. This high thickness variability is due to the front retreating

into areas of thick ice in summer followed by stretching and thinning during calving front advance in winter. For small perturbations, variations of effective strain rates at the grounding line quadruple to $\pm 25\%$ (Fig. 5.7f). Once the calving rate perturbation stops, all variables display remarkable reversibility.

When calving is temporarily turned off (experiment B0, not shown here), the response of the glacier is reversed: the calving front advances, creating a convex ice tongue. Meanwhile, the ice stream decelerates, thickens, and the grounding line advances. After the perturbation, the glacier retreats into a state slightly thicker and faster than the one of experiment B1.

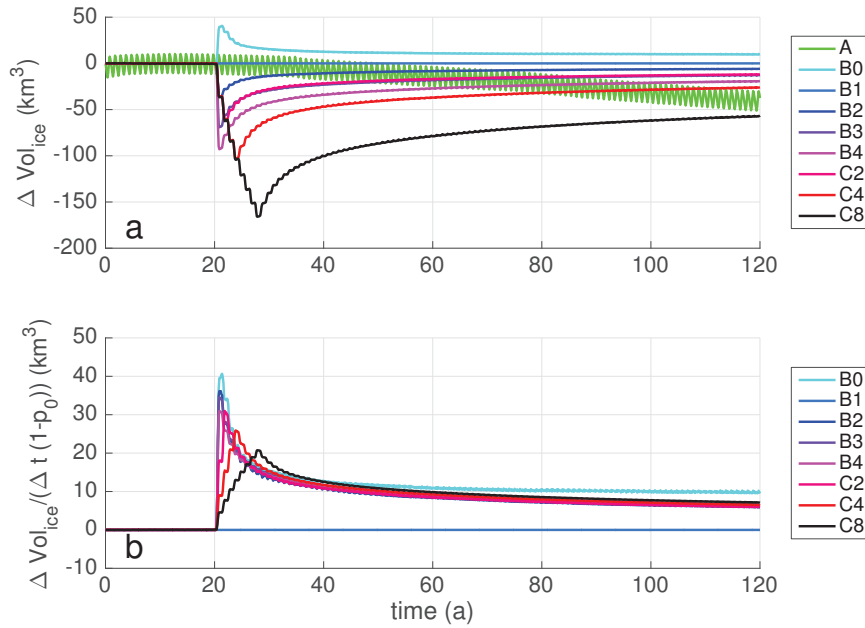


FIGURE 5.8: a: Absolute difference in ice volume for the different simulations with respect to experiment B1. The non-oscillating ice volume profile of experiment A causes its difference to experiment B1 to oscillate. b: The volume differences from experiments B and C divided by $\Delta t(1 - p_0)$, the measure of the time-integrated calving rate perturbation.

Figure 5.8a shows the evolution of the ice volume with respect to experiment B1, the control run. The glacier in experiment B1 continues to lose volume at an average rate of $-22.8 \text{ km}^3 \text{ a}^{-1}$ due to the ongoing geometry relaxation. In experiment A, Jakobshavn Isbræ loses an additional $0.4 \text{ km}^3 \text{ a}^{-1}$, which corresponds to the gradual retreat of the calving front. Enhanced calving causes additional volume loss proportional to $\Delta t(1 - p_0)$, the measure of the time-integrated calving rate perturbation (Fig. 5.8b). If the calving rate is doubled, the additional volume loss reaches $35.7 \text{ km}^3 \text{ a}^{-1}$ in the first year, but decreases with time, as the calving front thins and retreats into areas of lower calving rates. Those numbers agree well with recent ice discharge observations (Howat *et al.*, 2011). Over the first decade after the perturbation, all modelled glaciers recover 40 to 60% of the volume deviation to the control run.

5.5 Discussion

The applied calving rate determines the behaviour of the calving front and the ice stream. In our simulations, larger perturbation strengths p_0 lead to faster calving front retreats. In the case of long perturbations (experiments C4 and C8), the calving front reaches a new stable position. A stable calving front position requires the calving rate to be larger than the ice velocity if the calving front advances, and similarly, if the calving front retreats, the calving rate needs to be lower than the ice velocity.

Several mechanisms determine how the model responds to the calving rate forcing. First, a calving rate increase leads to a retreat of the calving front position, ice stream acceleration and dynamic thinning in the vicinity of the terminus. Second, this dynamic thinning increases surface slopes and therefore the driving stress. As the glacier locally speeds up, the ice thinning propagates upstream. The ice stream thins much faster than the surrounding ice sheet, which steepens the surface across the shear margins. Lateral inflow of ice into the ice stream hence increases until it balances the calving flux. This limits the thinning of the ice stream. Thinning of the ice stream in turn leads to grounding line retreat and reduction in basal effective pressure, which both reduce basal drag significantly in the vicinity of the grounding line. We showed that grounding line retreat leads to short-lived, but drastic increases in ice flux. This mechanism is qualitatively the same as the one described in Vieli & Nick (2011) and Joughin *et al.* (2012). Several pinning points along the retrograde trough of the southern branch, as well as the lateral stress transfer and mass influx prevent the modelled ice stream from being prone to the Marine Ice Sheet Instability (Weertman, 1974; Schoof, 2007), a hypothesis which states that grounding line positions are unstable on retrograde slopes. This corroborates earlier results by Gudmundsson *et al.* (2012), who presented examples of stable grounding line positions on retrograde beds. However, due to large uncertainties in the input data, and since some physical processes are not represented in our experiments, evaluation of this question for Jakobshavn Isbræ is beyond the scope of this study.

A third mechanism is related to the calving front lengthening during its retreat (e.g. figure 5.5). The lengthening causes tributaries of the main ice stream to calve directly into the fjord, thereby increasing the calving flux Q_{cf} (equation 5.8) and thinning of the terminus vicinity.

Finally, the ice stream accelerates faster than the surrounding ice sheet, which increases strain rates at the shear margins. This reduces the ice viscosity in these areas, which mechanically decouples the ice stream from the ice sheet, allowing the ice stream to accelerate further. This positive feedback confines the initial thinning to the ice stream, and is controlled by the rate at which ice enters the ice stream. This mechanism is essential for enabling ice stream acceleration tens of kilometres upstream of the grounding line, since large fractions of the ice stream's driving stress are balanced by lateral stress. This corroborates force balance arguments produced earlier by van der Veen *et al.*, 2011.

In experiments A and B1, we apply the same annual mean calving rate. However, due to the lack of seasonal cycle in calving rate the mechanical coupling between the ice stream and ice sheet is higher in experiment A. The ice stream velocity is therefore lower, causing gradual calving front

retreat and additional ice volume loss. This illustrates that volume change estimates from models with and without seasonal cycles of calving may differ. Our results suggest that including both a dynamically evolving calving front as well as seasonal cycles are critical for accurate projections of future contributions of ice sheets to global sea level rise on decadal to centennial time scales.

Response mechanisms not covered here will likely include feedbacks with damage mechanics and thermodynamics due to the increased strain rates. During longer perturbations, ice surface lowering will probably affect the surface mass balance and the drainage basin outline.

The reversibility of the calving front configuration after the calving rate perturbation is a robust feature across all experiments. The short duration of the perturbation, the prescribed calving rates, and the geometry of the glacier are responsible for this behaviour. The volume change in all experiments never exceeds 0.1% of the initial glacier volume in the experiments shown here. Once the perturbation stops, the surrounding ice sheet continues to replenish the ice stream, which allows for its quick recovery.

The modelled glacier response to enhanced calving is in good qualitative agreement with observations, which corroborates that calving is a major control on this glacier. The similar shape of the modelled and observed calving front suggests that calving rates are indeed proportional to its flow speed during the glacier's current retreat. However, the reversibility of the modelled calving front position is in contrast to Jakobshavn Isbræ's actual behaviour. Sustained high calving rates are therefore necessary to explain the continued retreat of the glacier, as our results suggest that the glacier would have re-advanced otherwise. Accurate model input data, representation of all relevant physical processes and incorporation of a suitable calving rate parametrisation will be necessary for quantitative analysis of this dynamic ice stream.

5.6 Conclusions

In this study, we present the theoretical framework for coupling a Level-Set Method (LSM) to ice dynamics and implement it into ISSM. The LSM proves to be a robust method for modelling the dynamic evolution of a calving front. We apply this technique to Jakobshavn Isbræ using prescribed calving rates, and we find that the glacier is highly sensitive to this forcing, which agrees well with observations.

Calving rate perturbations strongly affect the ice stream through several linked mechanisms. First, changes in calving rate cause calving front migration and alter the ice discharge. Second, the resulting thickness change at the calving front spreads out to the surrounding ice sheet. Third, thinning-induced grounding line retreat causes further ice stream acceleration and creates a positive feedback. Finally, shear margin weakening caused by the ice stream acceleration decreases lateral drag resisting ice flow. This positive feedback mechanism sustains significant acceleration of the ice stream tens of kilometres upstream of the grounding line.

The surrounding ice sheet is barely affected by short periods of enhanced calving. It stabilises the ice stream and allows for quick reversibility of the calving front position through lateral ice influx and stress transfer once the calving rates are set back to their initial values.

Since the calving front position and dynamic lateral effects are critical to simulate and understand the behaviour of marine terminating glaciers, the inclusion of moving boundaries in 2D-planview and 3D models is key for realistic sea level rise projections on centennial time scales. This method is a step towards better physical representation of calving front dynamics in ice sheet models.

5.7 Appendix: Validation of the Level-Set Method

We present two simple test setups to validate the LSM. The first is designed to show the accurate advection and shape preservation properties of the method. The second setup aims to give an estimate for the volume change introduced by the LSM for different mesh resolutions.

5.7.1 Advection

Let Ω be a 50 km square with the initial LSF as:

$$\varphi_0(\mathbf{x}) = \|\mathbf{x} - \mathbf{x}_0\|_2 - R,$$

where $\mathbf{x}_0 = (25, 25)$ km and $R = 12.5$ km, so that the initial 0-level-set describes a circle in the middle of the domain. We prescribe a constant velocity $\mathbf{v} = (\cos(\pi/4), \sin(\pi/4))$ km a⁻¹ everywhere. We advect φ_0 over 10 years with time steps of 0.1 a, and keep track of the 0-level-set.

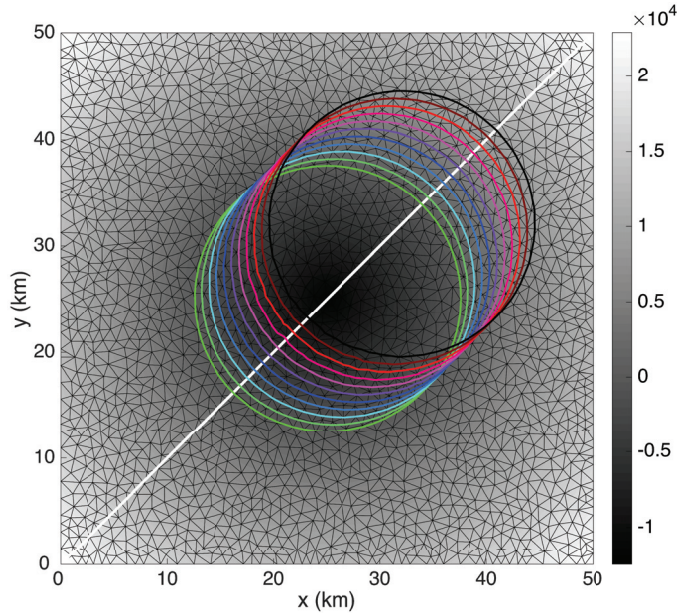


FIGURE 5.9: Zero-level-set positions at the start of every year, plotted over φ_0 , which is in grey scale. An example of the mesh with element size 1 km is marked in black. The white diagonal marks the line along which the velocity of the 0-level-set is tracked.

Figure 5.9 shows the 0-level-set position at the beginning of every year. The LSM preserves the initial circular shape, and can be used to model both advance and retreat of a calving front. We measure the advection speed of

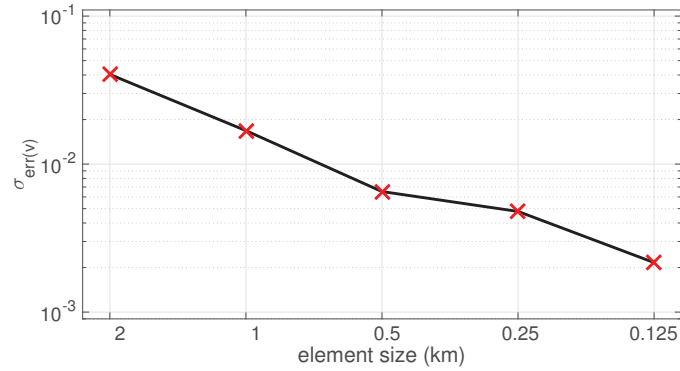


FIGURE 5.10: Standard deviation of the relative numerical error in advection velocity of the 0-level-set depending on mesh element size.

the 0-level-set along the diagonal marked in white in Fig. 5.9. Figure 5.10 shows the standard deviation of the numerical error relative to the prescribed advection speed taken over time for different element sizes. The numerical error is due to the linear interpolation of the curved shape, which causes variations of the level-set velocity around the prescribed value. The standard deviation of the error linearly decreases with mesh resolution, and drops below 1% for elements sizes below 0.5 km. We therefore choose a mesh resolution of 0.5 km in the vicinity of the calving front in our simulations.

5.7.2 Volume Conservation

Let Ω be a $200 \times 20 \text{ km}^2$ rectangle with an initial LSF given by:

$$\varphi_0(\mathbf{x}) = (1, 0) \cdot \mathbf{x} - 100 \text{ km}.$$

The initial lateral extent is thus a $100 \times 20 \text{ km}^2$ rectangle. The geometry corresponds to the Ice Shelf Ramp presented in Greve & Blatter (2009). The ice thickness linearly decreases from 400 m at the grounding line ($x = 0$ km) to 200 m at the calving front ($x = 100$ km). We apply zero surface accumulation and basal melt, as well as zero grounding line velocity and free slip boundary conditions at $y = 0$ km and $y = 20$ km. The ice sheet spreads under its own weight for 100 years.

Fig. 5.11 shows the evolution of the ice volume for different element sizes. All simulations show volume loss due to the free flux boundary condition at the numerical ice front, which is not entirely balanced by the volume added through the ice thickness extrapolation. The volume loss decreases with element size, and is below 0.2% of the initial ice volume after 100 years for an element size of 1 km. This volume loss is far below current uncertainties of other model input data.

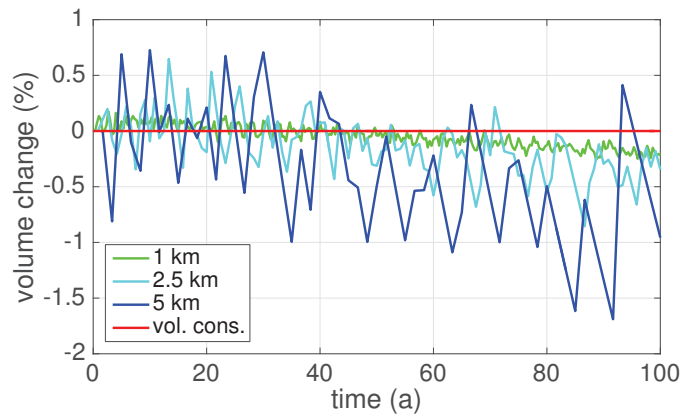


FIGURE 5.11: Evolution of the relative ice volume change for different element sizes. The red line shows volume conservation.

5.8 Acknowledgements

A. Humbert acknowledges support of the DLR proposal HYD2059 which provides TerraSAR-X data for the project HGF-Alliance Remote Sensing and Earth System Dynamics. The authors thank the referees G. Jouvét and J. Bassis as well as the editor O. Gagliardini for their helpful and insightful comments.

6 The Mechanisms behind Jakobshavn Isbræ's Acceleration and Mass Loss: a Thermodynamically Coupled Model Study

Context

Several hypotheses that explain Jakobshavn Isbræ's widespread acceleration after the disintegration of the floating ice tongue exist (cf. Sect. 2.4). However, they are in part contradictory to each other, and have been derived using simplified models (Thomas, 2004; van der Veen *et al.*, 2011; Vieli & Nick, 2011; Joughin *et al.*, 2012) or suffered from mesh resolution problems (Muresan *et al.*, 2016). Therefore, the thermodynamic mechanisms responsible for Jakobshavn Isbræ's widespread acceleration are still unclear.

The following publication has several aims. Firstly, we aim to publish the extension of the LSM presented in Bondzio *et al.* (2016) (Chap. 5) to 3D thermodynamically coupled case. Secondly, we aim to show that the model tools which have been developed during this thesis are applicable to a highly dynamic real-world outlet glacier like Jakobshavn Isbræ. Thirdly, we aim to reproduce Jakobshavn Isbræ's thermodynamic state and behaviour from beginning of 1985 until end of 2015, during which the calving front position retreated more than 20 km (cf. Fig. 6.1c), in order to answer the array of open questions formulated in Sect. 2.5.

The necessary model requirements to reproduce Jakobshavn Isbræ's dynamic response to calving front retreat have been identified in Sect. 2.6. The missing numerical tools, i.e. the enthalpy method and the LSM for dynamic calving front evolution, have been introduced and verified in the two first publications (Chaps. 4 and 5). The ISSM is therefore now prepared to be applied to the real-world glacier case of Jakobshavn Isbræ. The results of this study are presented in the following publication and Chap. 7.

In this study, we successfully reproduce Jakobshavn Isbræ's thermodynamic response to the observed calving front retreat. The resolution and the degree of matching of the observations are unprecedented in published literature (cf. Truffer & Echelmeyer, 2003; Vieli & Nick, 2011; Joughin *et al.*, 2012; Muresan *et al.*, 2016). The results show that the deep trough underneath the ice stream creates a stress regime where the driving stress is balanced by lateral drag, and that is therefore highly sensitive to perturbations in ice viscosity of the shear margins, which corroborates findings presented in Bondzio *et al.* (2016). Since the trough reaches far inland, and ice viscosity is strain-rate-dependent (cf. Sect. 3.3.2) stress perturbations

through calving front retreat are able to cause widespread inland acceleration. Therefore, the calving front position is currently the dominant control on the glacier's dynamics. Shear margin warming through enhanced strain heating contributes 5 to 10% to the total acceleration. Deep troughs with low basal drag are a common feature underneath many outlet glaciers of the GrIS (Shapiro *et al.*, 2016). We argue that the proposed mechanism for glacier acceleration holds in a similar fashion for these glaciers as well. Our results have implications for the type of models that are feasible to produce projections of future eustatic sea level rise, since it is important to capture the migrating calving front position, the thermal regime and especially the interaction of the ice stream with the shear margins for simulations of rapidly changing glaciers. Since the behaviour of Jakobshavn Isbræ is mainly controlled by basal topography, the calving front position, the ice rheology law and the thermal regime, we find that accurate projections of eustatic sea level rise will depend crucially on the emergence of a reliable calving rate parametrisation applicable in continental-scale ice sheet models and an improved rheology law for temperate glacier ice with microscopic water content higher than 1%.

Contributions

Conceptual design, implementation, testing and maintenance of the LSM for the 3D thermodynamically coupled case in ISSM was done by Bondzio, with counselling of H. Seroussi and M. Morlighem. The steady-state enthalpy method boundary conditions were designed, implemented, tested and maintained by Bondzio. Jakobshavn Isbræ model setup and development was done by Bondzio. The publication text was written by Bondzio and proof-read by all co-authors. The supplementary online material text was written by Bondzio, except for the paragraph that describes the derivation of the observed surface flow velocities in 1991/1992, which was contributed by J. Mouginot. All numerical experiments presented in the publication were designed and performed by Bondzio. All figures of the publication and the supplementary online material were created by Bondzio.

Johannes H. Bondzio^{1,2}, Mathieu Morlighem¹, Hélène Seroussi³, Thomas Kleiner², Martin Rückamp², Jeremie Mouginot¹, Twila Moon⁴, Eric Y. Larour³ & Angelika Humbert^{2,5}

1. Department of Earth System Science, University of California Irvine, Irvine, CA, USA
2. Alfred Wegener Institute, Helmholtz Centre for Polar and Marine Research, Bremerhaven, Germany
3. Jet Propulsion Laboratory - California Institute of Technology, Pasadena, CA, USA
4. Geographical Sciences and Bristol Glaciology Centre, University of Bristol, Bristol, UK
5. University of Bremen, Bremen, Germany

- Calving front migration is responsible for 90% of Jakobshavn Isbræ's acceleration.
- Inland acceleration is due to a non-linear viscosity feedback in the shear margins.
- The glacier is likely to lose mass at a rate comparable to today for at least the next century.

The mechanisms causing widespread flow acceleration of Jakobshavn Isbræ (JI), West Greenland, remain unclear despite an abundance of observations and modelling studies. We model the glacier's evolution from 1985 to 2016 using a thermodynamically coupled ice flow model. The model captures the timing and 90% of the observed changes by forcing its calving front position with observations. The calving front position is the dominant control on JI since its driving stress is balanced by lateral shear. The ice viscosity in the shear margins instantaneously drops in response to calving front retreat, which allows for faster flow. Gradual shear margin warming contributes 5 to 10% to the total acceleration. These mechanisms and JI's overdeepened trough allow for widespread flow acceleration. JI currently sustains the conditions for continued retreat, and we expect that the glacier will contribute to eustatic sea level rise at a rate comparable or higher than today.

Jakobshavn Isbræ is the fastest marine-terminating outlet glacier of the Greenland Ice Sheet (GrIS) (Rignot & Mouginot, 2012). The disintegration of its

floating ice tongue between 1998 and 2004 triggered rapid calving front retreat, as well as widespread flow acceleration and mass loss (Joughin *et al.*, 2008; Howat *et al.*, 2011). Since the disintegration, it has been contributing to eustatic sea level rise at an increasing rate, reaching about 0.1 mm a^{-1} in 2011 (Howat *et al.*, 2011). The mechanisms that sustain the acceleration remain unclear despite an abundance of observations (e.g. Csatho *et al.*, 2008; Joughin *et al.*, 2008; Joughin *et al.*, 2014) and modelling studies (e.g. Truffer & Echelmeyer, 2003; Thomas, 2004; van der Veen *et al.*, 2011; Joughin *et al.*, 2012). Many marine-terminating outlet glaciers of the GrIS are undergoing similar dynamic changes (Moon *et al.*, 2014), and it is therefore crucial to better understand these changes to provide reliable projections of the GrIS's future contribution to eustatic sea level rise.

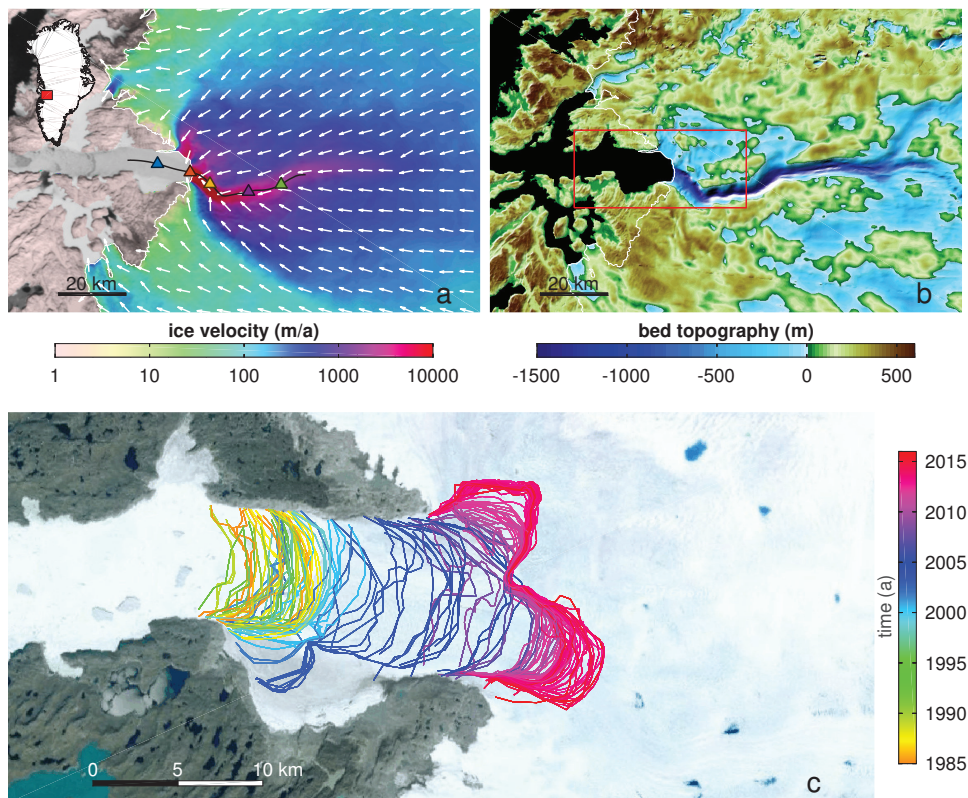


FIGURE 6.1: State and evolution of JI. a) Observed surface flow velocities, logarithmic scale (Rignot & Mouginot, 2012). White arrows show the flow direction. The calving front evolution in Fig. 6.2a is tracked along the black flow line. Coloured triangles denote the locations for velocity comparison in Fig. 6.2b. b) Bedrock topography in the same region, shaded relief (Morlighem *et al.*, 2014a). c) Observed calving front positions of JI from 1985 until end 2015, derived from Landsat 5-8, ERS-1&2 and TerraSAR-X satellite imagery. Map location is shown by red inset in b). Satellite background image: Landsat 7 (July 1st, 2001) © Google Earth.

Jakobshavn Isbræ discharges its ice into the ocean through two branches (Fig. 6.1a) that disconnected in 2004, following the disintegration of the ice tongue (Joughin *et al.*, 2008). The main branch, commonly referred to as “ice stream” (Cuffey & Paterson, 2010) and as JI in this text, flows significantly faster than the northern branch, and is located in a deep (-1700 m below sea level) and narrow (about $5\text{--}6 \text{ km}$ wide) trough (Fig. 6.1b, Gogineni *et al.*,

2014; Morlighem *et al.*, 2014a). Pronounced shear margins exert a strong control on the flow regime and characterize JI (e.g. Truffer & Echelmeyer, 2003).

Three hypotheses have been proposed to explain the speed-up of JI. The first hypothesis (H1, Thomas, 2004) suggests that thinning of the floating ice tongue and retreat of the calving front reduce the buttressing on the upstream ice, which leads to ice flow acceleration. The second hypothesis (H2, van der Veen *et al.*, 2011) states that the ice viscosity in the shear margins must have dropped by over 60%, therefore reducing lateral drag, as the loss of buttressing alone is not sufficient to explain the observed acceleration of upstream areas. According to the third hypothesis (H3, Vieli & Nick, 2011; Joughin *et al.*, 2012), dynamic-thinning-induced feedbacks and basal hydrological processes following the disintegration both increased the driving stress and decreased the basal drag of the ice stream causing sustained acceleration inland.

These three hypotheses were derived using models that did not include certain important processes, relied on coarse resolution observations and lead to different conclusions (Truffer & Echelmeyer, 2003; Thomas, 2004; van der Veen *et al.*, 2011; Joughin *et al.*, 2012), underlining that the mechanisms at play are not fully understood. Recent developments in ice flow modelling, including moving boundary capabilities in ice sheet models (Bondzio *et al.*, 2016) and the new availability of high-resolution model input data (Joughin *et al.*, 2014; Morlighem *et al.*, 2014a; Howat *et al.*, 2014; Noël *et al.*, 2015), make it possible to overcome these shortcomings and to provide a more complete analysis. Here, we investigate the mechanisms that sustain the glacier's ongoing acceleration and mass loss using high-resolution input data and a migrating calving front in the Ice Sheet System Model (ISSM, Larour *et al.*, 2012a), a state-of-the-art, finite-element ice flow model.

6.2 Ice Flow Model

We compute the ice velocities using the Higher-Order Model (Blatter, 1995; Pattyn, 2003). We use a linear viscous basal friction law (Budd *et al.*, 1984), and assume that ice deformation follows a non-linear, isotropic flow law (Glen, 1955; Nye, 1957) with a stress exponent $n = 3$. We compute the ice viscosity, μ , as:

$$\mu = (1 - D) \frac{B(T, W)}{2\dot{\epsilon}_e^{\frac{n-1}{n}}}. \quad (6.1)$$

Here, $\dot{\epsilon}_e$ is the effective strain rate, and the ice viscosity parameter, B , depends on the ice temperature, T , and the microscopic water content, W (Cuffey & Paterson, 2010; Lliboutry & Duval, 1985). A constant damage parameter D varying between 0 (no damage) and 1 (fully damaged) softens the ice (Borstad *et al.*, 2012). The grounding line evolves based on hydrostatic equilibrium following a sub-element migration scheme (Seroussi *et al.*, 2014a). We model the thermal regime using an energy-conserving enthalpy formulation (Aschwandten *et al.*, 2012), which has been verified and validated in ISSM in previous studies (Seroussi *et al.*, 2013; Kleiner *et al.*, 2015). We track the calving front position using a Level-Set Method (Bondzio *et al.*, 2016), that has been extended from two horizontal dimensions to three dimensions (3D) for this study, by assuming that the calving

front remains vertical throughout the simulation. The model does not account for basal hydrology nor cryo-hydrological warming (Phillips *et al.*, 2010).

6.3 Model and Experiment Setup

We set up a 3D thermodynamically coupled model of Jakobshavn Isbræ in 1985, calibrated using available data sets (cf. Supplementary Online Material (SOM, Sect. 6.7, Text S1). We mesh the glacier's drainage basin (Rignot & Mouginot, 2012) with a horizontal resolution of 400 m in regions of high strain rates and steep bedrock slopes and up to 4 km elsewhere. The horizontal mesh is vertically extruded into 17 layers that are more closely spaced towards the base. The resulting mesh consists of about 675,000 prismatic $P1 \times P1$ elements. We use a time step of about one day.

We simulate JI's evolution from January 1st, 1985 until December 31st, 2015. Along the lateral boundary, except the calving front, we prescribe observed surface velocities (Rignot & Mouginot, 2012), as well as ice temperatures from a thermodynamically coupled simulation of the GrIS (Seroussi *et al.*, 2013). At the ice surface, we impose annual average surface temperatures and annual cumulative surface mass balance from RACMO2.3 (Noël *et al.*, 2015). At the ice base, we prescribe the geothermal heat flux by Shapiro & Ritzwoller (2004), and the basal boundary conditions of the enthalpy method adjust dynamically to the thermal state of the base (Fig. 5, Aschwanden *et al.*, 2012). The basal friction coefficient, inferred from 1990s conditions, is kept constant throughout the run. The submarine melting rate is modelled as a piecewise linear function of depth (cf. Favier *et al.* (2014)). We impose an ice-tongue-averaged melting rate of 350 m a^{-1} until 1990, and 270 m a^{-1} from 1990 through 1995, accounting for an observed drop in ocean water temperatures (Motyka *et al.*, 2011). From 1996 onwards, we increase the average melting rate to 540 m a^{-1} in order to represent the observed warming of ambient ocean temperatures (Holland *et al.*, 2008; Enderlin & Howat, 2013).

We force the calving front position explicitly from over 500 observations (Fig. 6.1c), which have been compiled from Landsat 5-8, ERS-1&2 and TerraSAR-X satellite scenes (cf. Moon *et al.*, 2014). We interpolate this forcing linearly in the time between two observations. All other forcings and boundary conditions are kept constant.

6.4 Results

Fig. 6.2 compares model results and observations. Prior to the disintegration of the ice tongue, the modelled ice velocities match the observations (Fig. 6.2b) and the glacier loses about 5.5 Gt of ice per year (Fig. 6.2c). The calving front retreat from 1998 onwards triggers strong flow acceleration and mass loss. Ice velocities develop an increasing seasonal variability in regions of fast flow, which is most pronounced close to the calving front. Annual average ice velocities double until 2011 along the entire ice stream (cf. SOM, Fig. 6.9). Seasonal variations in ice velocity are 20 to 40% of the annual average velocity. The highest ice velocities occur at the calving front during rapid retreat when the terminus is grounded (cf. SOM, Movie S1).

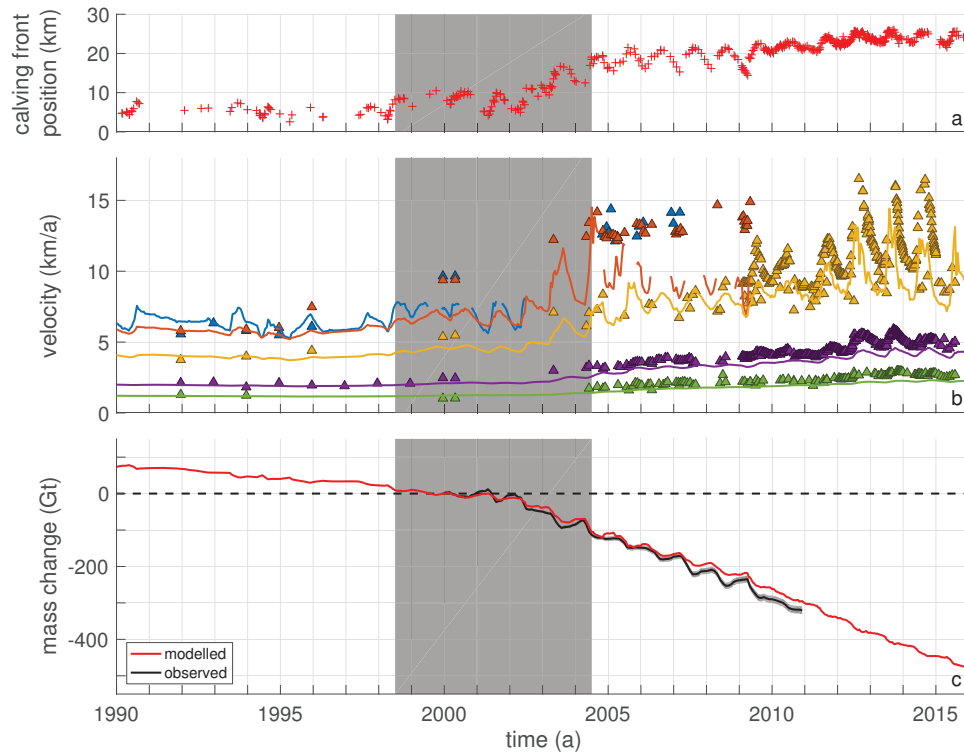


FIGURE 6.2: Comparison of observations and model results. a) Calving front positions from satellite observations along the flow-line in Fig. 6.1a. b) Comparison of observed velocities (triangles) and modelled velocities (lines). Colours correspond to the triangle locations shown in Fig. 6.1a. Lines are discontinuous when the calving front retreats upstream of the corresponding location. c) JI's modelled mass change (red line) relative to Jan 1st, 2000. The black line with error envelope shows observed mass changes (Howat *et al.*, 2011), and the black dashed line represents no volume change. The grey boxes mark the period of ice tongue disintegration.

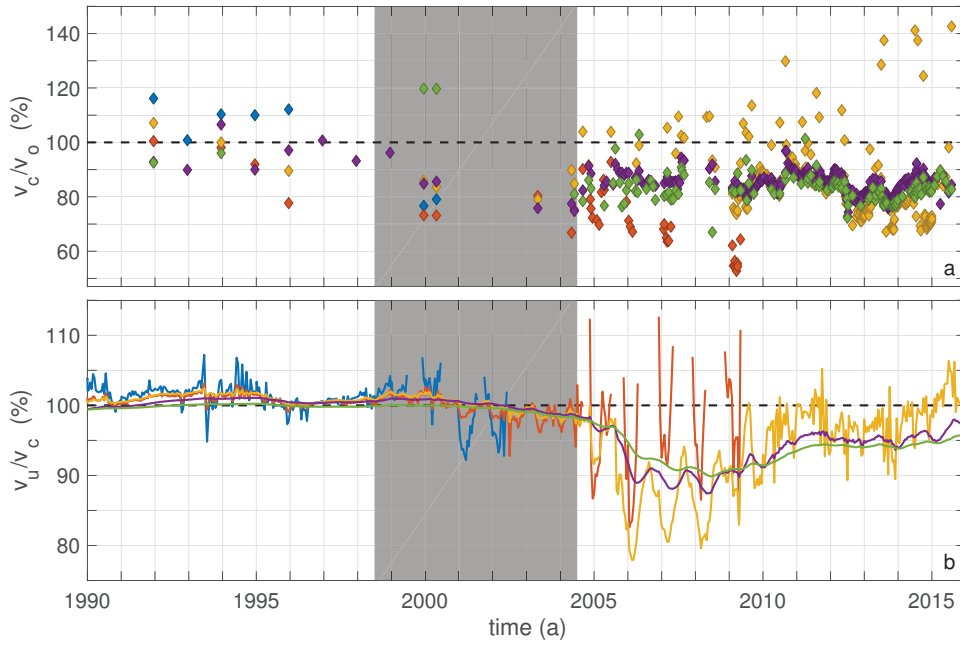


FIGURE 6.3: Contribution of the calving front position and thermodynamic coupling to the modelled ice velocity. a) Ratio of thermodynamically coupled (v_c) and observed ice surface velocities (v_o). b) Ratio of modelled ice surface velocities without (v_u) and with (v_c) thermodynamic coupling. The black dashed lines represent exact matching of the considered velocity values. Marker and line colours, respectively, correspond to the colours of the triangles in Fig. 6.1a. Lines are discontinuous when the calving front retreats upstream of the corresponding location. The grey patches mark the time of the ice tongue disintegration.

Both the timing and amplitude of summer and winter velocities are in good agreement with observations. Basal sliding contributes between 60 to 100% to the ice motion of JI. The modelled glacier's rate of mass loss rapidly increases in time, reaching an average value of about -34.1 Gt a^{-1} from 2004 onwards (Fig. 6.2c), in close agreement with observations (Howat *et al.*, 2011). A sensitivity analysis (cf. SOM, Fig. 6.7) shows that our results depend weakly on the prescribed submarine melting rate, and only if a floating ice tongue is present. Model simulations with a fix calving front position show no seasonal variation (cf. SOM, Fig. 6.8).

Fig. 6.3a shows the ratio of modelled and observed ice surface velocities. Prior to the ice tongue's disintegration, modelled and observed velocities agree within 10%. During and after the disintegration, the model reproduces 80 to 90% of the observed acceleration. The highest differences of more than 20% occur at locations closest to the calving front, where ice velocities are sensitive to the exact calving front position and basal topography. Ratios show only little seasonal variation inland.

Fig. 6.3b shows the ice velocity ratio of a thermodynamically coupled simulation and an "uncoupled" one with identical model settings, in which the enthalpy is kept constant in time. Prior and during the disintegration, ice velocities agree within 1 to 2%. However, the thermodynamically coupled velocities rapidly increase relative to the uncoupled ones by an average of 10% from the end of the disintegration onwards. The ratio develops a strong seasonal signal that is strongest near the terminus, and decreases

to about 5% after 2009.

Fig. 6.4 shows the evolution of JI's longitudinal stress transfer and lateral drag. The depth-averaged longitudinal stress scales with ice thickness, and reaches maximum values of up to 12 MPa in the centre of the trough. A large stress gradient in the last 20 km of the trough before the calving front produces high driving stresses. Lateral drag is 200 – 300 kPa along the ice stream's shear margins, and reaches up to 575 kPa at the steep trough walls on the lowest 28 km upstream of the 1990s' calving front position. Calving front retreat causes a complex response in the stress regime in the area that corresponds to the flow acceleration (Fig. 6.4, 1b-d, 2b-d). Longitudinal stress transfer along JI decreases gradually by up to 2 MPa due to thinning and calving front retreat. The buttressing reduction is largest close to the calving front and spreads upstream along JI and its tributaries in a dampened fashion. Lateral drag increases gradually by 85 to 230 kPa inside the shear margins, and drops by up to 180 kPa in narrow bands flanking the trough and the northern branch.

Fig. 6.5a shows that JI's depth-averaged ice viscosity varies over more than 4 orders of magnitude, from as low as 1.51×10^{12} Pa s in the shear margins, up to more than 2.42×10^{16} Pa s inland. The soft ice in the shear margins allows for high flow velocities in the ice stream. The annual average ice viscosity decreases by 20 to more than 60% during the calving front retreat (Fig. 6.5, b-d). The viscosity drop originates from the calving front, instantaneously spreads along JI in a linearly dampened fashion, and spreads from there to the surrounding ice sheet in a diffusive pattern (cf. SOM, Movie S2). The largest drop occurs in the shear margins and near the calving front. The thermal regime of the glacier is advection-dominated (cf. SOM, Figs. 6.15a, 6.16 & Movie S3), and enhanced strain heating following the disintegration warms the shear margins by up to 2 °C (cf. SOM, Fig. 6.15b-d), which contributes 20 to 30% to the total viscosity drop.

6.5 Discussion

The combination of the deep trough under JI and the non-linear rheology of ice creates a stress regime that is highly susceptible to stress perturbations, caused e.g. by calving front retreat. In agreement with earlier studies (Thomas, 2004; Joughin *et al.*, 2012; Shapero *et al.*, 2016), basal drag in the centre of the ice stream is an order of magnitude lower than the driving stress (cf. SOM, Figs. 6.11, 6.12), which is transferred laterally to the adjacent steep trough walls, causing high horizontal strain rates (cf. SOM, Fig. 6.10). Consequently, the ice viscosity in the shear margins is more than two orders of magnitude lower than the surroundings, and highly sensitive to changes in effective strain rate, temperature and microscopic water content (Eq. 6.1). A small increase in either one variable triggers an instantaneous positive feedback by softening the ice, which in turn allows for higher strain rates and higher strain heating. Therefore, stress perturbations through calving front retreat are swiftly transferred upstream along deep parts of the bedrock topography with low basal drag, which characterizes most of the deep trough under JI. Hence, calving front retreat is able to trigger widespread acceleration, and calving rates are currently the main control on the behaviour of JI. Ensuing dynamic thinning steepens the shear

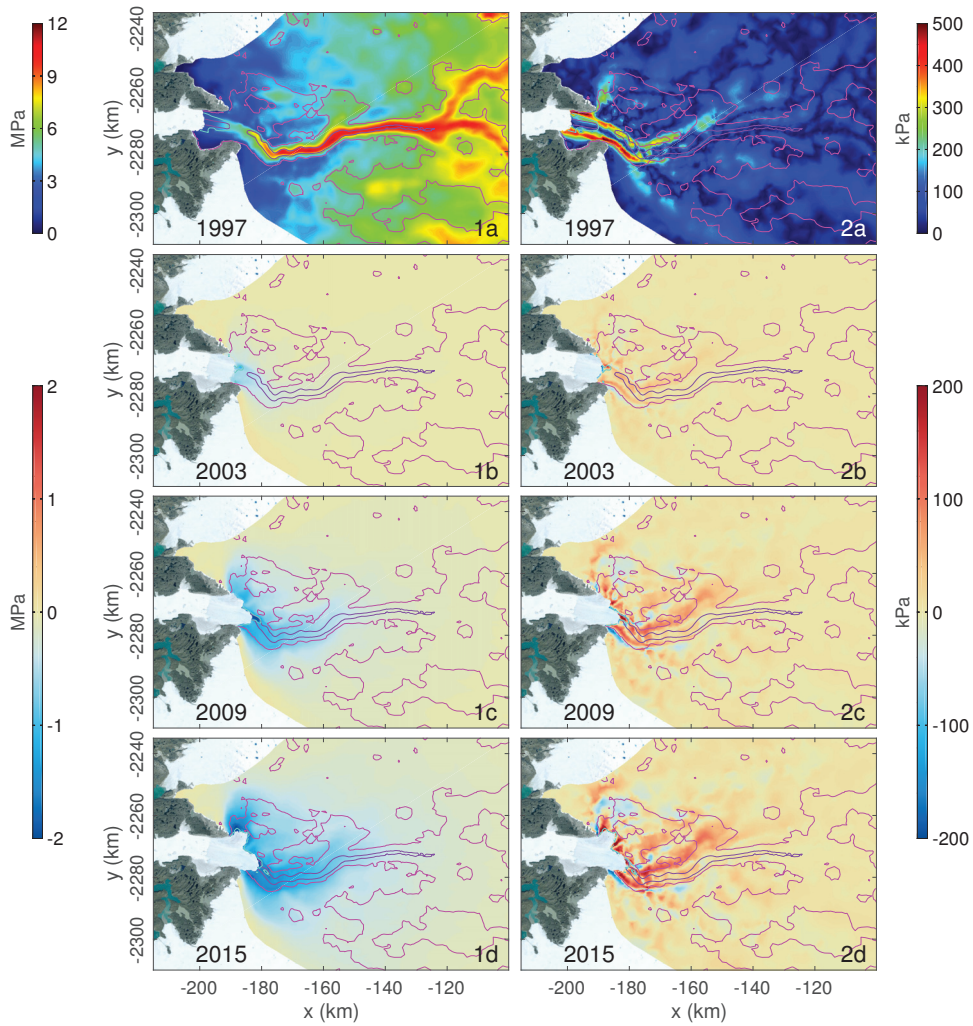


FIGURE 6.4: Evolution of Jakobshavn Isbræ's stress regime. Left column (1): depth-averaged absolute of longitudinal stress. 1a) Annual average in 1997. 1b-d) Change compared to 1997 in indicated years. Right column (2): depth-averaged lateral drag. 2a) Annual average in 1997. 2b-d) Change compared to 1997 in indicated years. Pink and purple lines denote bedrock contours at 0 and -1000 m elevation, respectively. The light green line denotes the average modelled grounding line position for each year. Satellite background image: Landsat 7 (July 1st, 2001) © Google Earth.

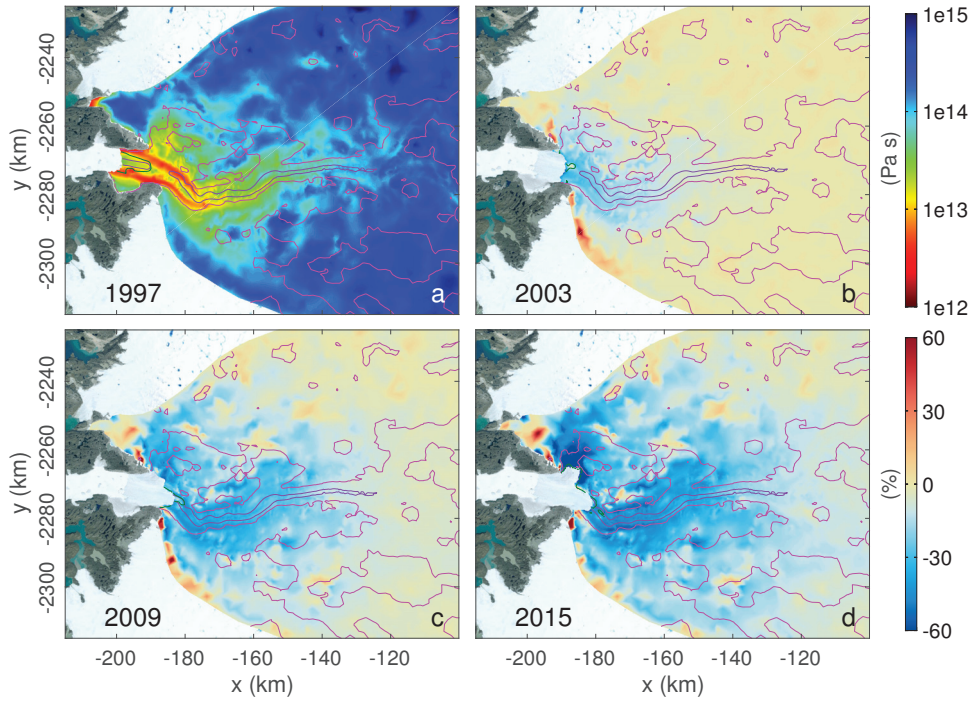


FIGURE 6.5: Evolution of Jakobshavn Isbræ's depth-averaged ice viscosity. a) Annual average in 1997 (top colour bar). b-d) Change compared to 1997 in indicated years (bottom colour bar). Pink and purple lines denote bedrock contours at 0 and -1000 m elevation, respectively. The light green line denotes the average modelled grounding line position for each year.

Satellite background image: Landsat 7 (July 1st, 2001) © Google Earth.

margins and increases driving stresses inland, which softens these regions too (cf. SOM, Figs. 6.11, 6.13).

The explanatory hypotheses H1, H2 and H3 all highlight different aspects of the mechanism interplay during calving front retreat. In agreement with H1, we find that calving front retreat reduces buttressing which is swiftly transferred inland by both the viscosity drop in the shear margins and dynamic thinning. Contrary to H2, the shear margin weakening is a response to the calving front retreat, instead of an initial cause for the flow acceleration. The importance of lateral drag transfer for the behaviour of this glacier underlines the need for explicit modelling of the dynamics of the shear margins through 2D plan-view or 3D ice flow models. In agreement with H3, the thinning-induced driving stress increase through surface steepening contributes to the flow acceleration, especially in the areas surrounding JI. However, the viscosity-related adjustment spreads inland along JI's trough at a speed much higher than the geometrical adjustment (cf. SOM, Movie S2), whose speed is about ice velocity (Nye, 1963; Bind-schadler, 1997). Therefore, the geometrical adjustment proposed in H3 is secondary to the initial viscosity drop and is mainly responsible for the acceleration of the ice surrounding the deep trough, where basal friction is high. Grounding line retreat and a drop in ice overburden pressure affect the glacier flow only in the lowest 8 to 10 km upstream of the grounding line, which corroborates results presented in Habermann *et al.* (2013).

Enhanced strain heating gradually softens the shear margins during

continued calving front retreat, so that ice flow velocities of a thermodynamically coupled simulation are higher than those of an uncoupled simulation after the disintegration of the ice tongue. This observation underlines that modelling the thermal regime is important in simulations of rapidly changing glaciers.

The model captures the exact timing as well as 80 to 90% of the observed acceleration simply by forcing it with the observed calving front position. Therefore, we are confident that the viscosity drop and the geometrical adjustment are the main drivers behind the observed inland acceleration of JI. Physical processes such as major variations in basal hydrology (Joughin *et al.*, 2012; Lampkin *et al.*, 2013), sudden englacial warming (van der Veen *et al.*, 2011), cryo-hydrological warming (Phillips *et al.*, 2010) and development of englacial damage are not necessary to explain the extent and amplitude of JI's observed velocities.

Several factors cause the underestimation of flow velocities in the model. First, as the calving front position must coincide with element edges, the calving front position is displaced up to one finite element width (400 m) downstream of the observed position, which systematically increases buttressing in the model (Bondzio *et al.*, 2016). Second, it is known that the stress exponent, n , for ice under high shear stress is likely to be greater than 3 (Cuffey & Paterson, 2010), which would give higher flow velocities. Third, accounting for highly deformable ice with a microscopic water content of locally well above 1% in the ice viscosity parameter (Lliboutry & Duval, 1985) would help to improve the fit between model and observations.

The proposed mechanisms for glacier acceleration imply that JI is currently sustaining the necessary conditions for continued retreat. Currently, simulations of the glacier's future evolution are challenged due to the lack of a suitable calving rate parametrisation (Benn *et al.*, 2007). Observations suggest that JI's calving rates are controlled by air and ocean temperatures, ice mélange rigidity, strain rates and bedrock topography (Sohn *et al.*, 1998; Benn *et al.*, 2007; Joughin *et al.*, 2008; Alley *et al.*, 2008; Amundson *et al.*, 2010; Cassotto *et al.*, 2015; Morlighem *et al.*, 2016). Since the Earth's climate system will continue to warm (IPCC-AR5, 2013), which should weaken the ice mélange, and strain rates are currently high while the glacier adjusts to the new calving front position, we expect that the glacier will not re-advance in the coming years to decades. The recent decline in calving front retreat rates in 2015/2016 may suggest glacier stabilization. However, the glacier is currently losing mass year-round, which will cause further intermittent grounding line retreat and ice tongue destabilization. Under the most conservative assumption of calving front stabilization at the current position, the glacier would continue to contribute 2.77 ± 0.78 mm to eustatic sea level rise until 2100 due to ongoing geometry adjustment to the new calving front position (cf. SOM, Fig. 6.17). Since the glacier will continue to lose mass, and the available bedrock topography of JI's trough shows no feature that would allow for glacier stabilization for the next 60 to 70 km along-flow, we find a scenario of continued intermittent calving front retreat significantly more likely. This scenario represents a commitment to eustatic sea level rise from JI for at least the next several decades at a rate comparable or higher than today.

Deep troughs with similar stress regimes are a common feature under many marine-terminating outlet glaciers of the GrIS (Morlighem *et al.*, 2014a; Shapero *et al.*, 2016), and we expect that the mechanisms described here apply to these glaciers as well. It is therefore critical to explicitly account for the interplay of the lateral drag transfer through shear margins, the thermal regime, and the migrating calving front in model simulations of this type of glaciers. This makes flow-line and flow-band models (Nick *et al.*, 2009; Vieli & Nick, 2011) unsuitable for producing realistic projections of future eustatic sea level rise of the GrIS (Nick *et al.*, 2013). Moreover, realistic projections will depend on whether the scientific community is able to produce a material law for temperate ice with microscopic water contents higher than 1% and a calving rate parametrisation that is suitable for continental-scale ice sheet models.

6.6 Conclusions

In this study, we model the dynamic evolution of JI using a thermodynamically coupled 3D ice flow model, whose only seasonal forcing is the calving front position imposed from observations. The model captures the exact timing and about 80 to 90% of the observed widespread acceleration, the glacier's thermal regime, as well as the observed mass loss.

The calving front position is currently the main control on the dynamics of JI due to the low basal drag in the deep trough, which creates a stress regime where most of the driving stress is transferred laterally to the steep trough walls. The non-linear ice viscosity in the shear margins instantaneously drops in response to a stress perturbation caused by calving front retreat, which allows for faster flow and dynamic thinning. Geometrical adjustment to ice stream thinning spreads the viscosity drop to the areas adjacent to the trough. Shear margin warming through enhanced strain rates after the disintegration of the floating ice tongue contributes 5 to 10% to the total acceleration. The combination of these mechanisms and JI's overdeepened trough, which reaches several hundred kilometres inland, allows for widespread flow acceleration. These mechanisms are likely to apply to many other marine-terminating outlet glaciers of the GrIS and the interplay of calving front migration, shear margins and the thermal regime is important to account for in projections of future eustatic sea level rise.

JI currently sustains the conditions for continued retreat, and we expect that the glacier will continue to contribute to eustatic sea level rise for at least the next several decades at a rate comparable or higher than 0.1 mm a^{-1} .

Acknowledgements

This work was performed at the University of California Irvine under a contract with the National Aeronautics and Space Administration, Cryospheric Sciences Program (#NNX15AD55G). We thank R. Rosenau for providing digitized calving front positions of JI. The authors declare that they have no competing financial interests.

6.7 Supplementary Online Material

Contents

1. Text S1
2. Figures S1 to S12
3. Movies S1 to S3

Additional Supporting Information (Files uploaded separately)

1. Movie S1: Horizontal ice surface velocity, 1990-2016
2. Movie S2: Ice viscosity change relative to 1990, 1990-2016
3. Movie S3: Thermal regime along the vertical of profiles I & II, cf. Fig. 6.6, 1990-2016

Introduction

6.7.1 Text S1: Jakobshavn Isbræ Model Setup

We set up the Jakobshavn Isbræ model of 1985 in four steps. In the first step, we choose Jakobshavn Isbræ's drainage basin (Rignot & Mouginot, 2012) as the horizontal outline of the computational domain, which we mesh anisotropically. The mesh width ranges from 400 m in regions of high strain rates and high basal gradients up to 4 km elsewhere. The resulting 2D mesh has about 42,000 triangular elements. We emulate Jakobshavn Isbræ's largely unknown fjord bathymetry through a parabolic profile with maximum depth of $z = -1100$ m, which we fit to available data using spline interpolation. Under the ice cover, we rely on a basal topography data set derived using a mass-conservation approach (Morlighem *et al.*, 2014a). At the location where the grounding line has been observed in the 1980s (Echelmeyer *et al.*, 1991), we insert a sill with maximum elevation $z = -700$ m for enhanced grounding line stability. Furthermore, we insert a shallow bump (summit at $z = -200$ m) near the calving front, where a small ice rise has been observed (Echelmeyer *et al.*, 1991, cf. Fig. 6.6). We combine two data sets to create the initial surface elevation. Firstly, we use a photogrammetry-derived surface elevation model of Jakobshavn Isbræ's lower elevation region in 1985 (Korsgaard *et al.*, 2016). We fill the data gaps inland using the surface elevation data set given by the Greenland Mapping Project (Howat *et al.*, 2014), which we fit to the former data set using an elevation offset proportional to present day ice flow velocities. We derive the floating ice base elevation and the grounding line position from hydrostatic equilibrium, and define the ice thickness as the difference between the ice surface elevation and the ice base elevation. We use an initial temperature of -10°C and zero microscopic water content to derive the initial ice viscosity parameter (Cuffey & Paterson, 2010). We insert a damage parameter confined to the ice stream's shear margins for better fit of observed velocities during the data assimilation simulation (cf. third step), which drops linearly from 0.3 near the calving front to 0 about 70 km inland. For all following simulations, we impose observed ice flow velocities at the computational domain's lateral perimeter and water pressure at the calving front.

We model submarine melting underneath the ice tongue using a continuous, piecewise linear melting function of depth (cf. Favier *et al.*, 2014). The submarine melting rate function is zero from $z = 0$ m to $z = -200$ m, then increases to its maximum value at $z = -800$ m, and stays at this value for greater depths. Maximum submarine melting rates vary between experiments and are specified below. No melting is applied at the vertical face of the calving front.

In a second step, we perform a transient model relaxation. Inconsistencies between the various model input data sets may corrupt the solution of a thermodynamically coupled steady-state simulation (Seroussi *et al.*, 2011). It is therefore common to let the model freely evolve (“relax”) for some time to balance out these inconsistencies. However, in order to not deviate too far from given model input data sets, we choose a short model relaxation duration of only 10 years. For the relaxation, we apply the 2D shelfy-stream approximation (Morland & Zainuddin, 1987; MacAyeal, 1989) for ice velocities on a fixed ice domain corresponding to the 1985 ice extent, and constant ice temperatures. We rely on constant present-day climate forcings (Ettema *et al.*, 2009), and we use a maximum submarine melting rate of 256.6 m a^{-1} in order to maintain a stable grounding line position.

In a third step, we use data assimilation to derive an initial velocity, basal friction and enthalpy field by matching a target surface velocity field in a 3D thermodynamically coupled steady-state simulation (Morlighem *et al.*, 2010). We use the relaxed geometry to create a 3D model of Jakobshavn Isbræ by vertically extruding the 2D mesh into 17 layers, which are spaced relative to the ice thickness. The layer spacing becomes denser towards the base, in order to ensure that the layer at the ice base is everywhere less than 10 m thick, even in the thickest parts of the glacier, like the ice stream. The high vertical resolution is necessary in order to be able to resolve basal temperate layers of observed thicknesses (about 30 m (Lüthi *et al.*, 2002)). The resulting mesh consists of about 675,000 prismatic $P1 \times P1$ elements. The 3D ice velocity field is from now on computed using the higher-order model (Blatter, 1995; Pattyn, 2003), and the thermal regime is computed using the enthalpy-formulation (Aschwanden *et al.*, 2012). At the ice surface, we prescribe present-day surface temperatures lowered by 5 K for best match of observed ice temperatures. At the drainage basin perimeter, we impose ice temperatures from a thermodynamically coupled simulation of the Greenland Ice Sheet (Seroussi *et al.*, 2013). At the ice base, we apply geothermal heat flux (Shapiro & Ritzwoller, 2004). The enthalpy formulation’s original basal boundary condition scheme (Fig. 5 in Aschwanden *et al.*, 2012) is not applicable for direct solvers as employed for steady-state simulations in ISSM. Therefore, we adapt the basal boundary condition scheme for the steady-state case: under the assumption that all microscopic water content at the base drains immediately, we prescribe pressure melting point enthalpy at any basal location that becomes temperate during the solution process. This procedure may introduce an inconsistency between the thermal solution of a steady-state simulation and the solution of a transient spin-up, which does allow for positive water content at the base. It is therefore necessary to allow for some transient relaxation of the steady-state enthalpy field solution afterwards. However, we find that deviations between steady-state and transient thermal profiles are below 2% water content at the base, and re-adjust quickly to the transient boundary condition scheme.

During the data assimilation, we match a surface ice velocity field from 1991 to 1992, which has been derived by analysing a series of satellite SAR images acquired by ERS-1/ESA from October 1st, 1991 to May 31st, 1992 (Mouginot *et al.*, 2012). ERS-1 data are from the 3-day repeat campaign. Offsets between image pairs are derived using a speckle tracking method and converted to ice surface displacement assuming surface parallel flow. We processed all available interferometric pairs from the 3 to 36-days repeat cycles. The resulting offsets were filtered, calibrated and combined in a single annual averaged mosaic (Mouginot *et al.*, 2012). The averaging is done by attributing different weights for each velocity estimate based on the spatial resolution and time interval between the two acquisitions. We estimate the errors to range between 10 and 200 m a^{-1} depending on the number and the time interval of the stacked pairs, but typically over Jakobshavn Isbræ, we found errors in absolute velocity around 50 m a^{-1} . Inland data gaps were filled using present-day velocities (Rignot & Mouginot, 2012), which have been scaled down to give a smooth transition between both data sets. In ice-free areas and underneath floating ice, we apply an area-averaged basal friction parameter of $30 \text{ kg}^{1/2} \text{ m}^{-1/2} \text{ s}^{-1}$. The basal friction parameter is kept constant in all simulations.

In the fourth step, we perform a thermal relaxation run in order to bridge potential inconsistencies between the thermal steady-state solution and a transient spin-up solution. For this simulation, we keep the geometry and ice velocities fix, and we change the prescribed ice surface temperature linearly over the first 5 years to the average present day forcing (Ettema *et al.*, 2009), which causes considerable warming of the ice column over time. In order to not deviate too much from observed ice temperatures, we choose a short thermal relaxation duration of 150 years. The resulting thermal field is therefore not in steady-state, but we achieve a good match with existing observations (Fig. 6.14). The resulting model fields serve as initial conditions for the following experiments.

Shown below are results for experiments in which we varied the submarine melting rate. The horizontal average taken over the floating ice tongue varies in time as the ice tongue evolves in shape. Horizontally-averaged submarine melting rates in 1998 are 200, 350, 540 and 630 m a^{-1} , which we label experiments A, B, C and D, respectively. The melting rate range corresponds to observations (Motyka *et al.*, 2011; Enderlin & Howat, 2013), and is obtained by choosing a maximum melting rate value at depth of 209, 418, 836 and 1254 m a^{-1} , respectively.

6.7.2 Figures S1

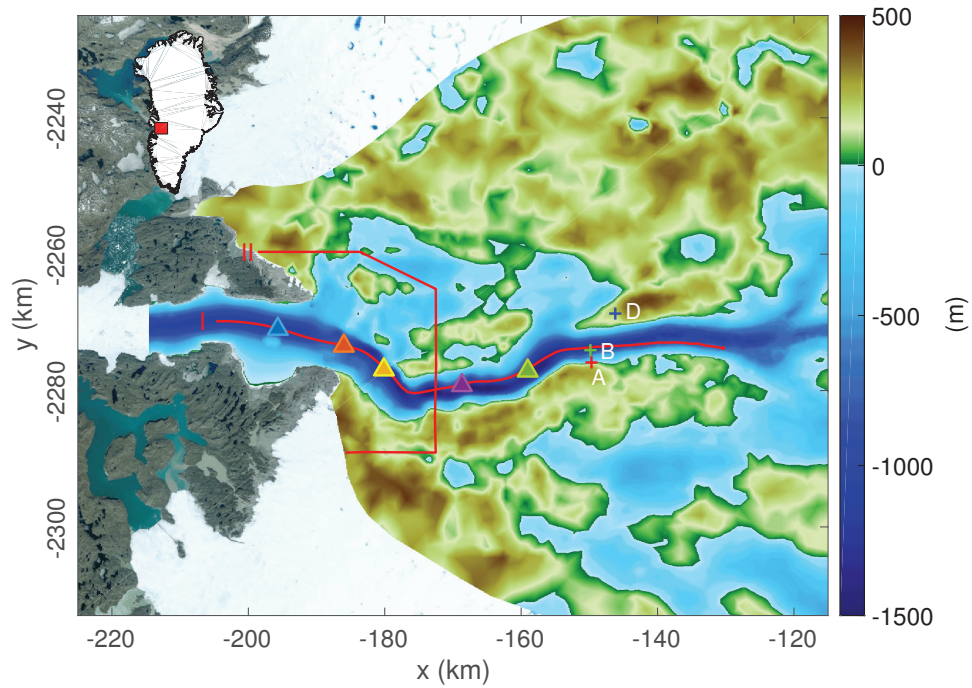


FIGURE 6.6: The model's bedrock geometry near the terminus, and locations used in the figures below. The coloured triangles mark the locations for velocity comparison in Figs. 6.7b, 6.8b. The red lines (profiles I & II) are used in Fig. 6.16. Red, green and blue crosses (A, B, D) are borehole locations used in Fig. 6.14.

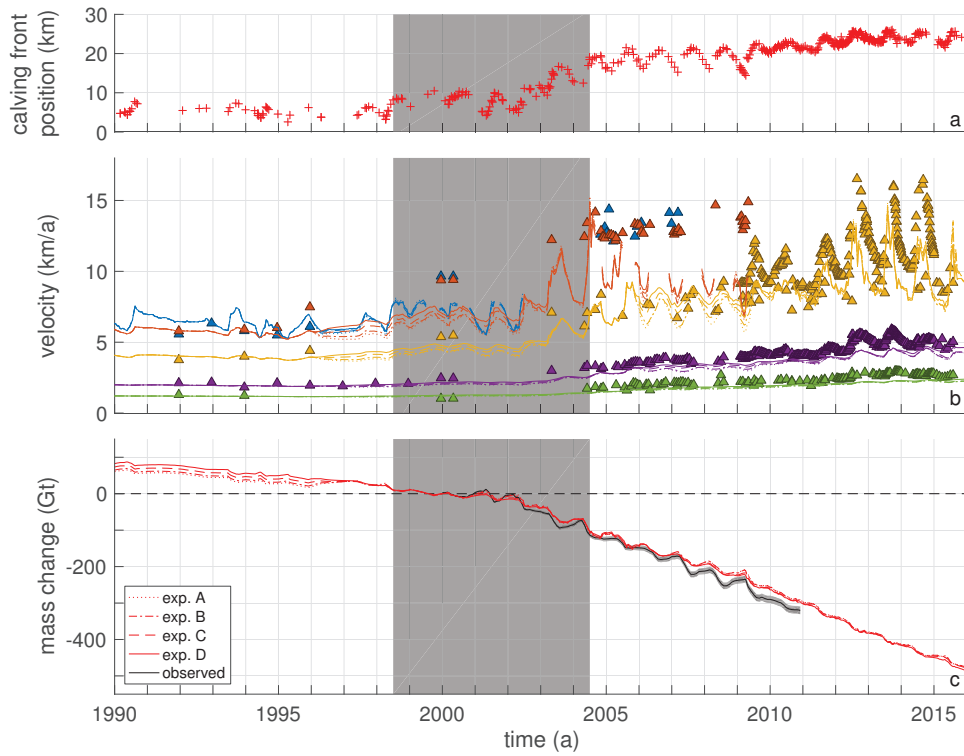


FIGURE 6.7: Comparison of observations and thermodynamically coupled model results for different submarine melting rate functions (cf. Text S1), which are identified with different line styles (cf. legend). a) Imposed calving front position along profile I shown in Fig. 6.6. b) Comparison of observed velocities (triangles) and modelled velocities (lines). Colours correspond to the triangle locations shown in Fig. 6.6. Lines are discontinuous when the calving front retreats upstream of the corresponding location. c) Modelled mass change relative to Jan 1st, 2000. The black line with error envelope shows observed mass changes (Howat *et al.*, 2011). The black dashed line represents no volume change. The grey boxes mark the period of ice tongue disintegration.

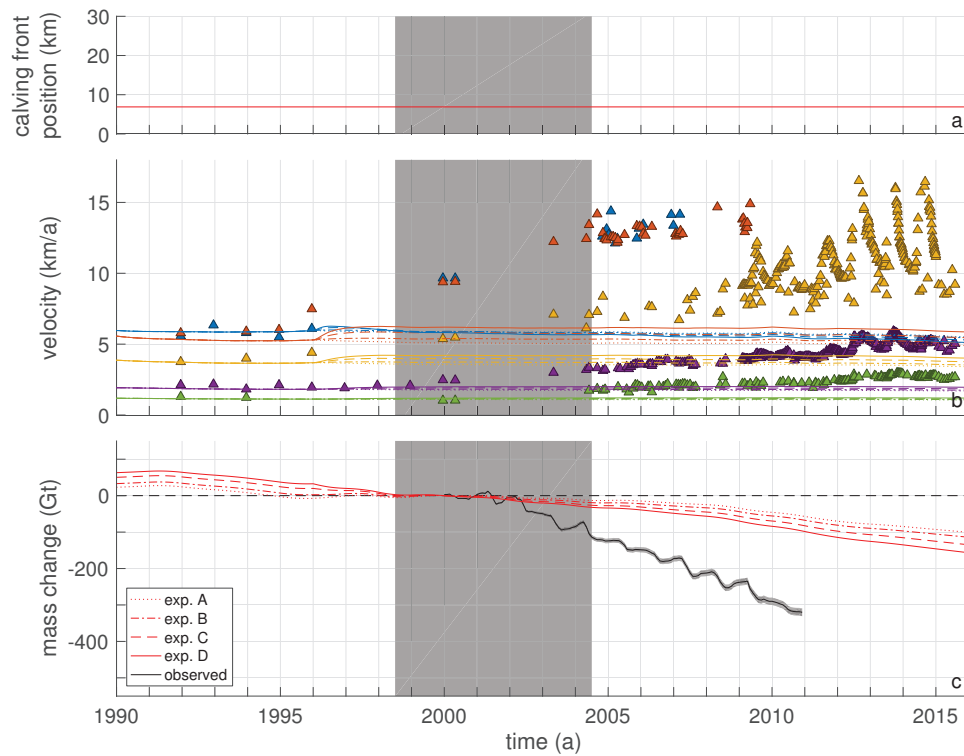


FIGURE 6.8: Comparison of observations and thermodynamically coupled model results with the calving front kept fix at the 1985 position for different submarine melting rate functions (cf. Text S1), which are identified with different line styles (cf. legend). a) Imposed calving front position along profile I shown in Fig. 6.6. b) Comparison of observed velocities (triangles) and modelled velocities (lines). Colours correspond to the triangle locations shown in Fig. 6.6. c) Modelled mass change relative to Jan 1st, 2000. The black line with error envelope shows observed mass changes (Howat *et al.*, 2011). The black dashed line represents no volume change. The grey boxes mark the period of ice tongue disintegration.

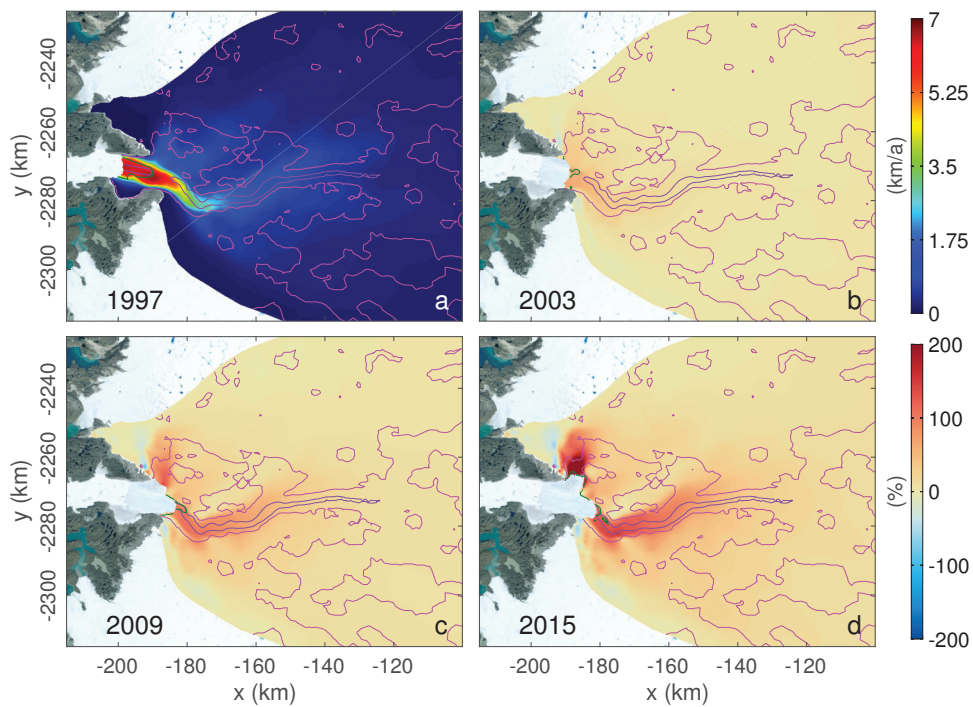


FIGURE 6.9: Modelled ice surface velocity. a) Annual average value in 1997 (top colour bar). b-d) Relative change in annual average value compared to 1997 in the indicated years (bottom colour bar). Pink and purple lines denote bedrock contours at 0 and -1000 m elevation, respectively. The green line shows the annual average modelled grounding line position. Satellite background image: Landsat 7 (July 1st, 2001) © Google Earth.

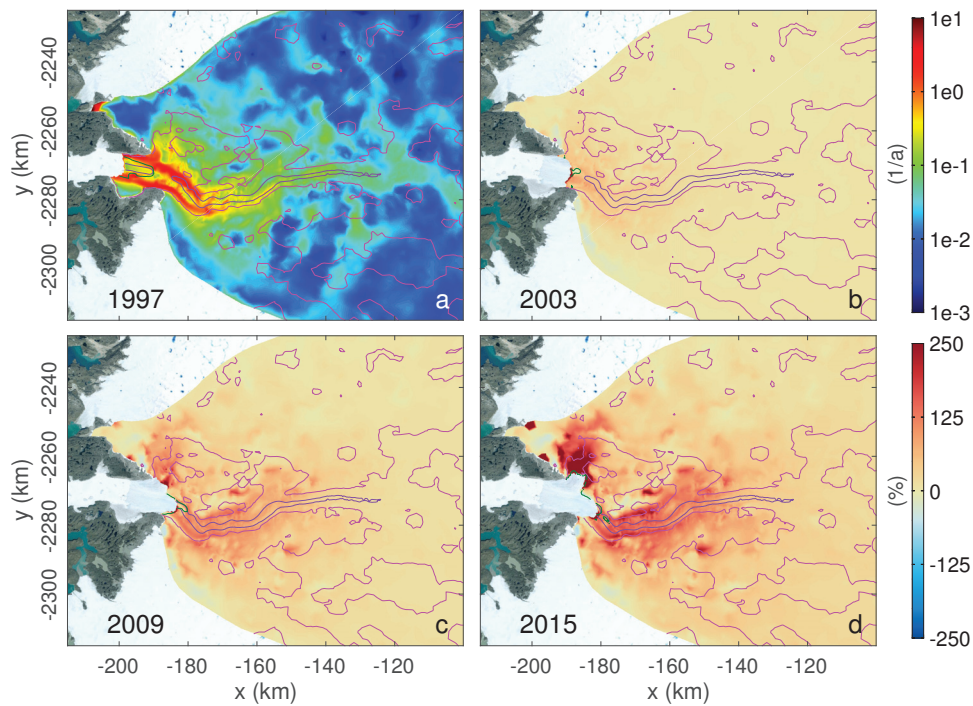


FIGURE 6.10: Modelled depth-averaged effective strain rate. a) Annual average value in 1997 (top colour bar). b-d) Relative change in annual average value compared to 1997 in the indicated years (bottom colour bar). The relative change is up to 550% at the terminus of the northern branch in 2015. Pink and purple lines denote bedrock contours at 0 and -1000 m elevation, respectively. The green line shows the annual average modelled grounding line position. Satellite background image: Landsat 7 (July 1st, 2001) © Google Earth.

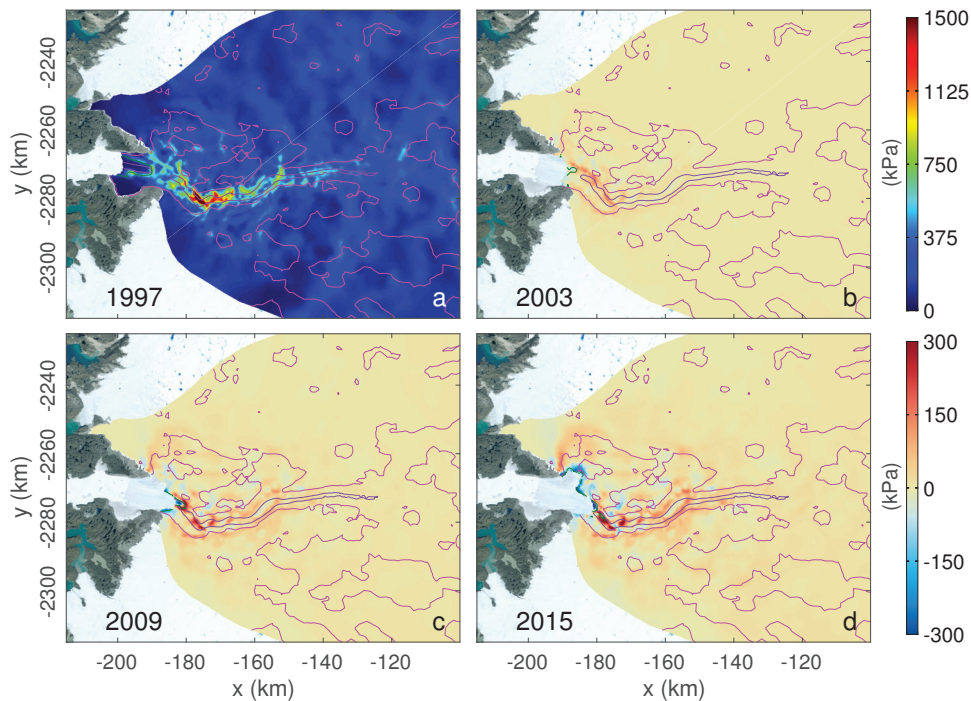


FIGURE 6.11: Modelled driving stress. a) Annual average value in 1997 (top colour bar). b-d) Change in annual average value relative to 1997 in the indicated years (bottom colour bar). Pink and purple lines denote bedrock contours at 0 and -1000 m elevation, respectively. The green line shows the annual average modelled grounding line position. Satellite background image: Landsat 7 (July 1st, 2001) © Google Earth.

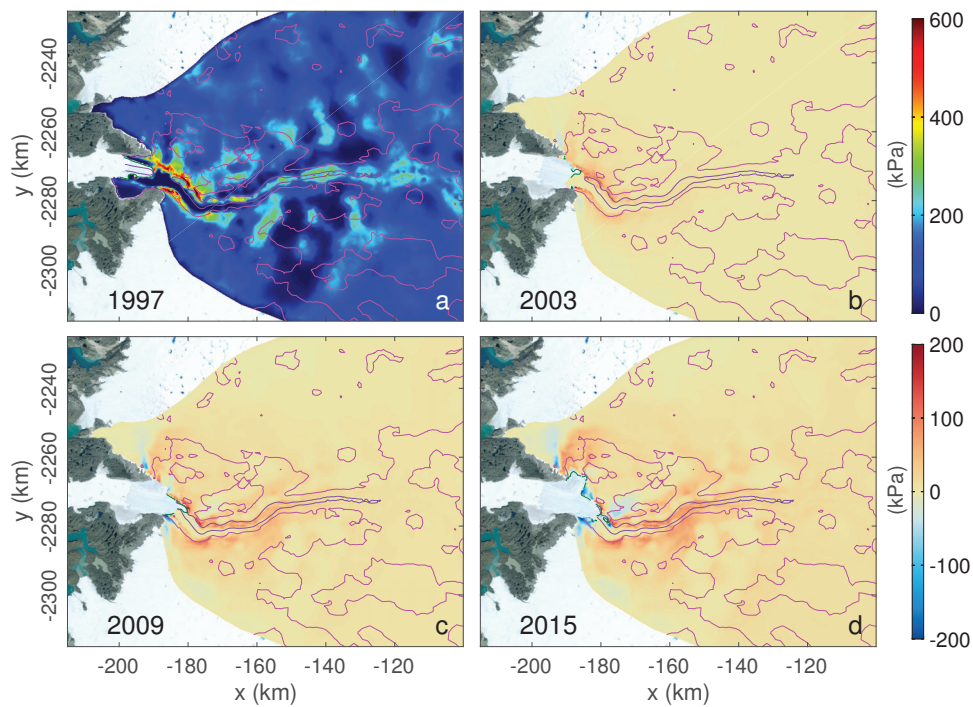


FIGURE 6.12: Modelled basal drag on grounded ice. a) Annual average value in 1997 (top colour bar). b-d) Change in annual average value relative to 1997 in the indicated years (bottom colour bar). Pink and purple lines denote bedrock contours at 0 and -1000 m elevation, respectively. The green line shows the annual average modelled grounding line position. Satellite background image: Landsat 7 (July 1st, 2001) © Google Earth.

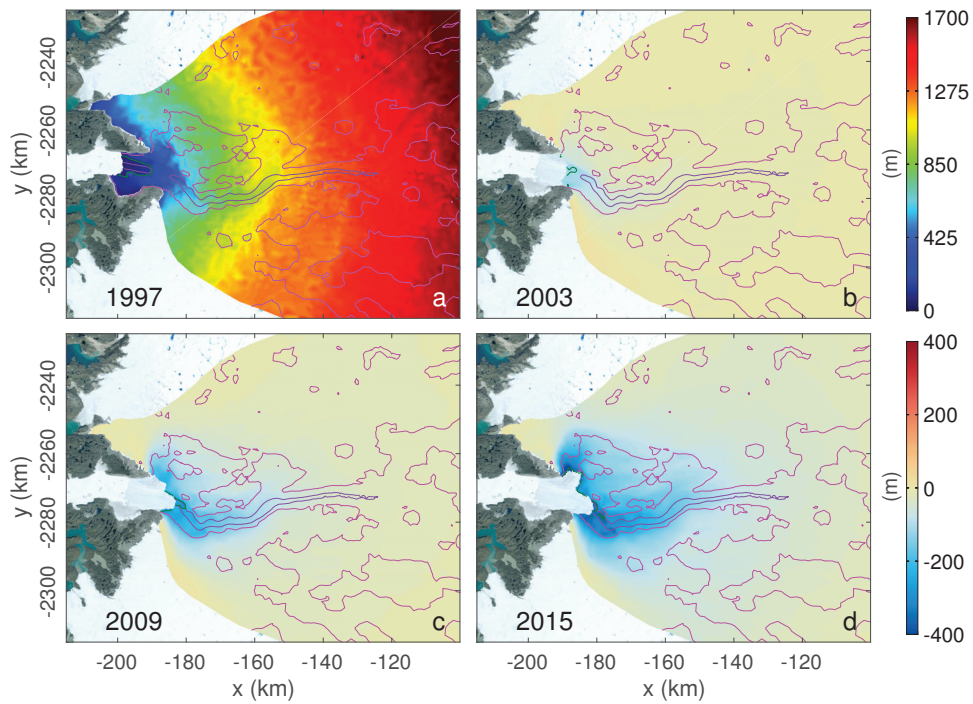


FIGURE 6.13: Modelled ice surface elevation. a) Annual average value in 1997 (top colour bar). b-d) Change in annual average value compared to 1997 in the indicated years (bottom colour bar). Pink and purple lines denote bedrock contours at 0 and -1000 m elevation, respectively. The green line shows the annual average modelled grounding line position. Satellite background image: Landsat 7 (July 1st, 2001) © Google Earth.

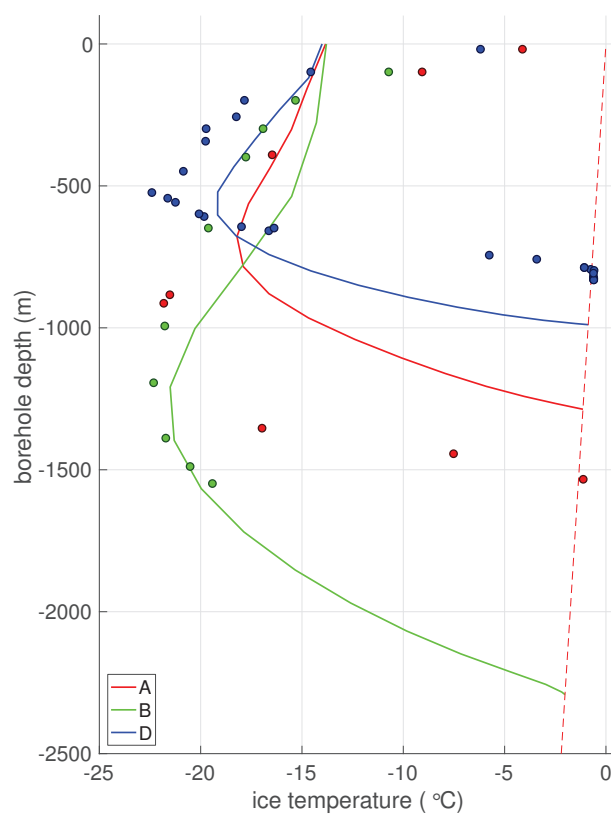


FIGURE 6.14: Comparison of modelled and observed ice temperatures. Shown are modelled ice temperatures (lines) at the end of the thermal relaxation run, and observed ice temperatures (circles) measured along three boreholes (locations A, B, D in Fig. 6.6, cf. Iken *et al.*, 1993; Lüthi *et al.*, 2002). The red dashed line denotes the pressure melting point temperature.

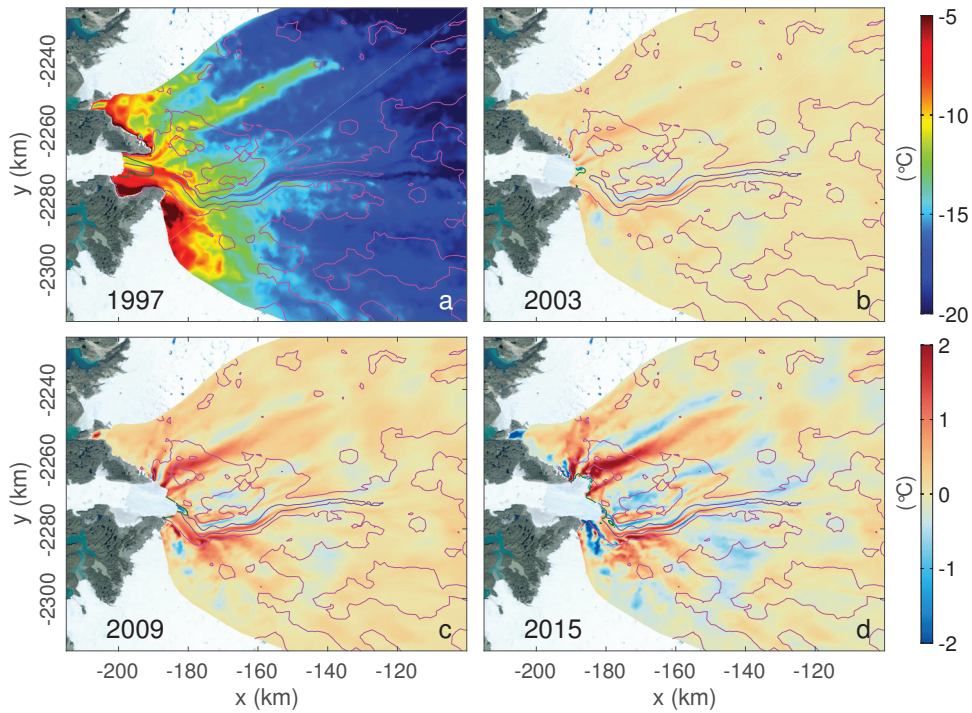


FIGURE 6.15: Modelled depth-averaged ice temperature. a) Annual average value in 1997 (top colour bar). b-d) Change in annual average value compared to 1997 in the indicated years (bottom colour bar). Pink and purple lines denote bedrock contours at 0 and -1000 m elevation, respectively. The green line shows the annual average modelled grounding line position. Satellite background image: Landsat 7 (July 1st, 2001) © Google Earth.

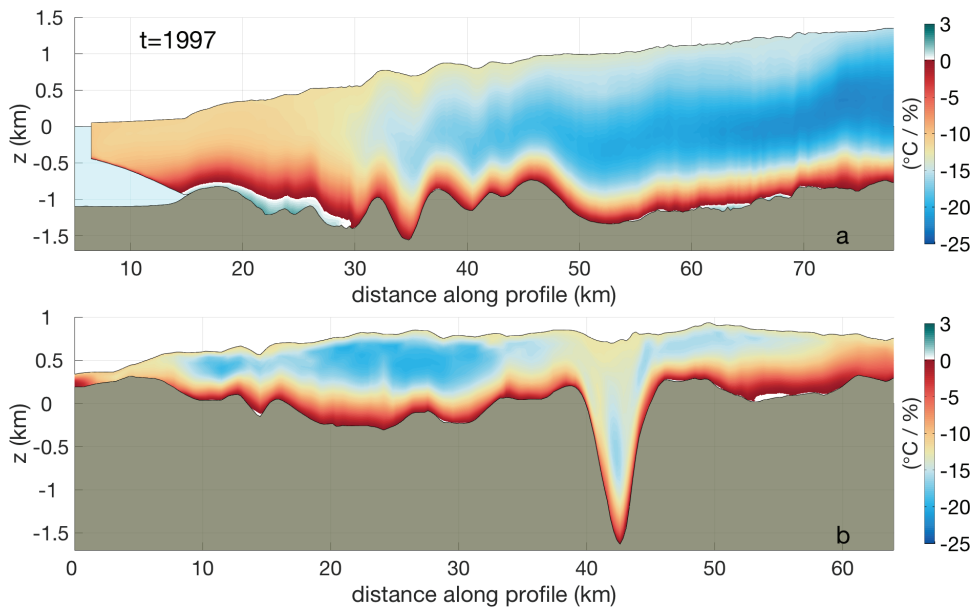


FIGURE 6.16: Thermal regime of Jakobshavn Isbræ in 1997 along the vertical of a) profile I and b) profile II, cf. Fig. 6.6. Grey area is bedrock, light blue area is ocean.

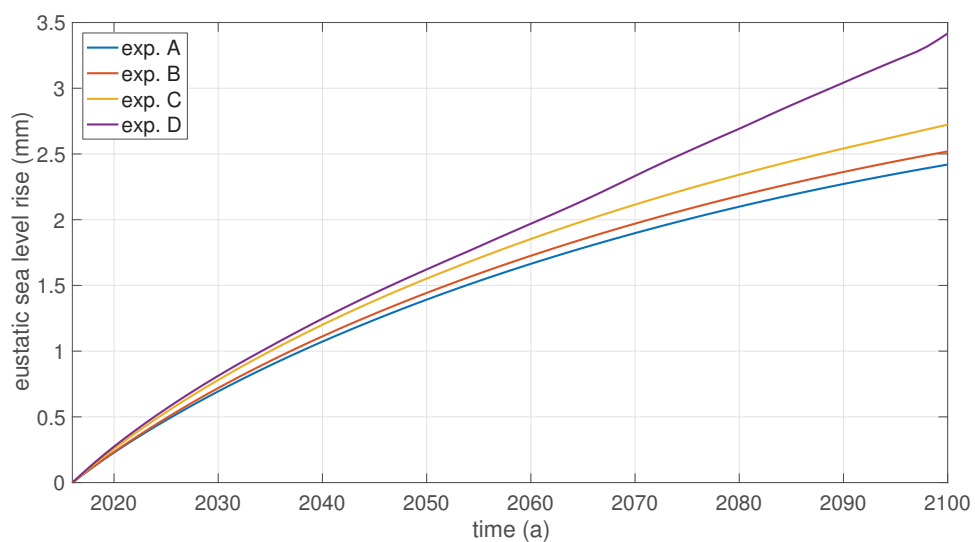


FIGURE 6.17: Future contribution of Jakobshavn Isbræ to eustatic sea level rise for the scenario of calving front stabilization in 2016. The legend labels refer to the different submarine melting rate functions, cf. Text S1, which are kept constant in time.

7 Jakobshavn Isbræ's Thermodynamic Regime

7.1 Additional Results

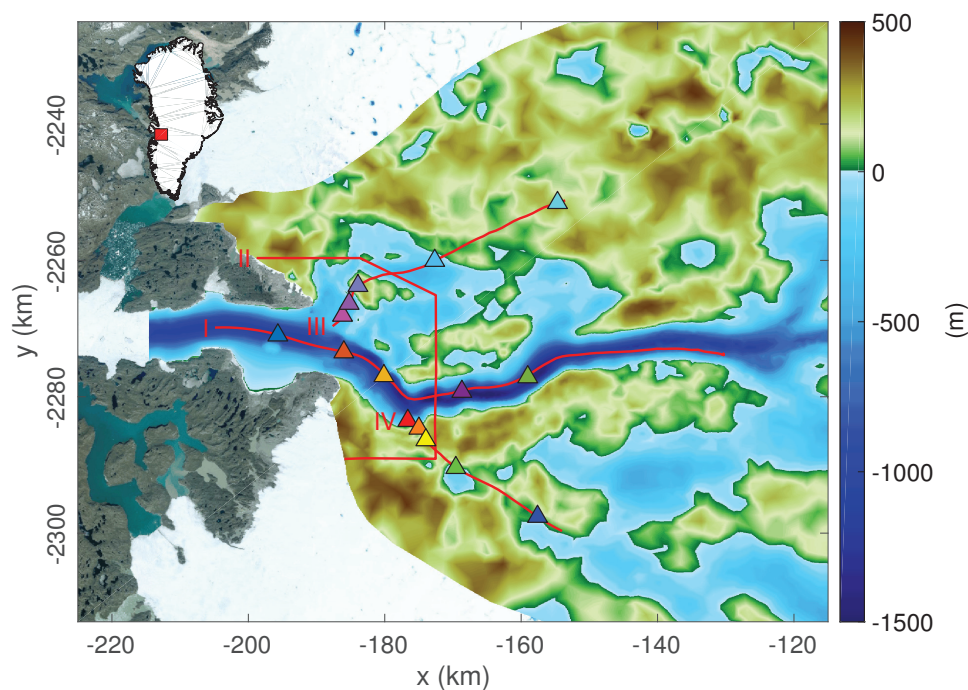


FIGURE 7.1: Overview of bedrock topography of Jakobshavn Isbræ near the terminus, and various locations used throughout this section. The profiles I & II (red lines) are used in Figs. 7.4, 7.5, and 7.7. The triangles show the locations for the velocity comparison along the flowline profiles III & IV used in Figs. 7.2 and 7.10.

Additional model results, that were not included into the previous publication due to space limitations, are presented and discussed in this section. The results give additional insight into the thermodynamics of Jakobshavn Isbræ. We will present several physical glacier quantities along the locations and profiles shown in Fig. 7.1. The locations are colour-coded and follow three flow-lines along the ice stream (profile I), the northern branch (profile III), and a southern tributary to the ice stream (profile IV), respectively, which have been derived from an observed ice surface velocity field from 1991/1992 (cf. Sect. 6.7.1). The profiles I & II are the same as used in the previous chapter. The northern branch is of interest since it reacted in a different way to the disintegration of the floating ice tongue than the ice stream, and the southern tributary exemplifies the dynamics of ice that flows laterally into the ice stream.

7.1.1 Stress Regime

Results

The northern branch flows slower than the ice stream (Fig. 7.2b). Prior to the disintegration, its flow speed in the model does not exceed 1.8 km a^{-1} , which is up to 0.3 km a^{-1} slower than observations.

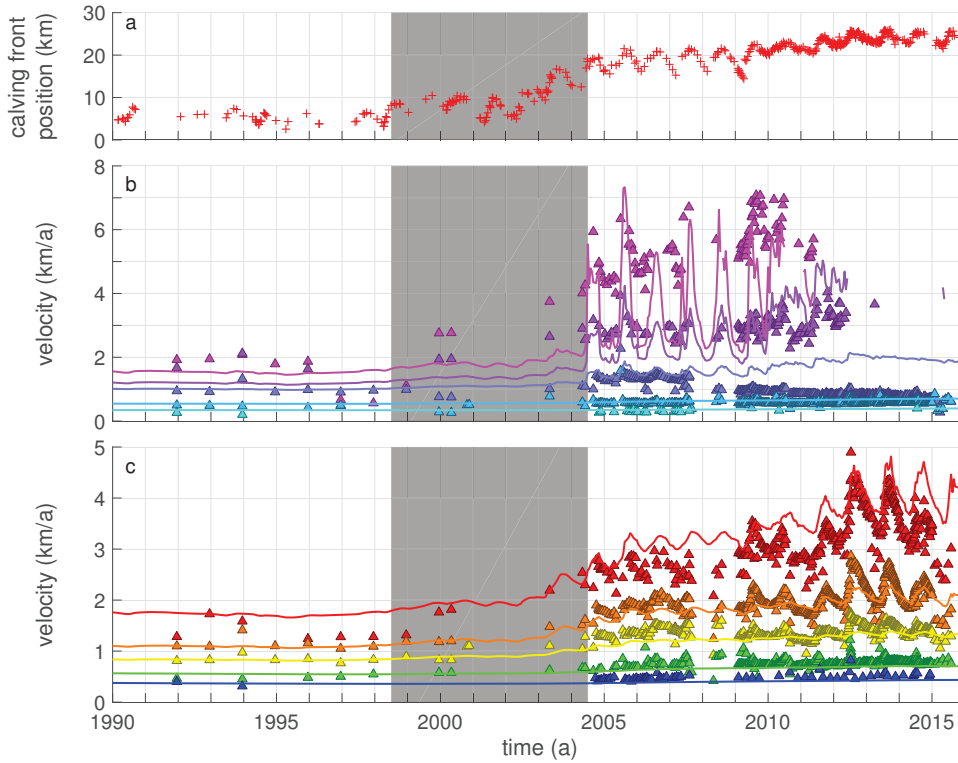


FIGURE 7.2: Comparison of model and observations over time. a) Observed calving front position along the profile I (Fig. 7.1). b, c) Comparison of observed (triangles) and modelled (lines) ice surface velocities along the northern branch (b) and the southern tributary (c). Note the different y-axis range in b) and c). Line and triangle colours correspond to triangle location colours shown in Fig. 7.1. The grey boxes mark the period of ice tongue disintegration.

During the disintegration of the ice tongue, observations show a gradual velocity increase to double of its 1990s value. Modelled ice flow velocities increase by at most 25% until 2004, and exhibit only little (5%) seasonal variation during this period. However, they drastically increase to 5.5 km a^{-1} in summer 2004 and 7.3 km a^{-1} in summer 2005 near the terminus once it retreats upstream of the ice fall (cf. Fig. 2.1). Winter velocities do increase only slightly up to 2.5 km a^{-1} , which causes large seasonal variations in ice velocity of up to 217%. The modelled seasonal variation exceeds the observed one, which we estimate from available observations to be about 58%, possibly slightly higher as observations are sparse. Observed ice velocities further upstream decrease from 2008 onwards to less than 1 km a^{-1} , while the modelled ice velocities slowly decelerate to about 2 km a^{-1} . The modelled seasonal variability diminishes from 2010 onwards and has practically vanished by 2013.

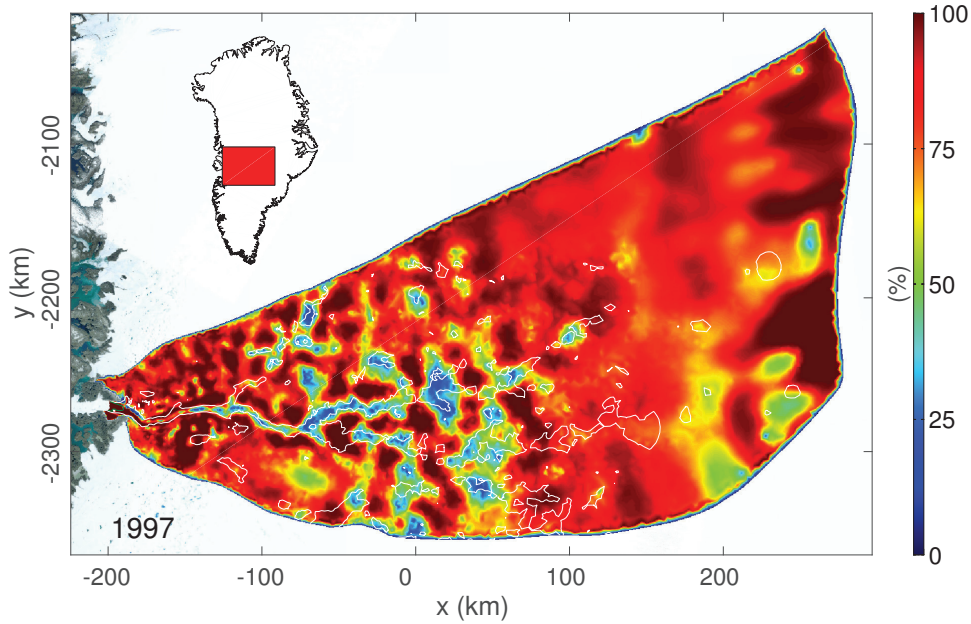


FIGURE 7.3: Annual average ratio of basal to surface ice velocities in 1997. White lines denote glacier bed elevation contours at -250 m. Satellite background image: Landsat 7 (July 1st, 2001) © Google Earth.

The southern tributary flows fastest at locations near the ice stream, which mirror the ice stream's flow characteristics: modelled ice velocities are at up to $1.8 \pm 0.1 \text{ km a}^{-1}$ until the disintegration of the ice tongue, after which they gradually increase in magnitude and seasonality to $4.1 \pm 0.5 \text{ km a}^{-1}$ from 2013 onwards (Fig. 7.2c). While the model matches the annual average velocity well, the seasonality in the model is lower than observed. The strong seasonality in ice velocity rapidly decreases inland and vanishes at the two most inland locations of both the northern branch and the southern tributary (turquoise lines, Fig. 7.2b; green and blue line, Fig. 7.2c), which is in agreement with observations. However, observed ice velocities show an increase of 40% to 80% at these locations at the onset of the melting season every year ("velocity spike"), whose duration is much shorter (about 1 month) than that of the annual velocity cycle in the ice stream. The velocity spike does not appear in the model results.

Fig. 7.3 shows that basal sliding in the model contributes up to 100% to the ice motion inland outside of the deep trough, in the ice stream's shear margins, and on the last 28 km in the centre of the ice stream before the terminus. The contribution drops sharply (less than 35%) inland in the deep trough and at the steep walls near the terminus, where high basal drag creates significant vertical shear (cf. Fig. 6.12). High contributions near the eastern ice divide are caused by errors in observed ice velocities (cf. Rignot & Mouginot, 2012), which cause an underestimation of the basal drag during the data assimilation. The ratio of basal to surface velocities of 1997 presented here is characteristic for our model of Jakobshavn Isbræ, and changes little over time.

Fig. 7.4a shows a characteristic velocity distribution of 1997 along the vertical of profiles I and II (cf. Fig. 7.1). Ice flow accelerates along-flow from about 1 km a^{-1} inland to 7 km a^{-1} at the floating tongue. The strongest acceleration occurs in the last 30 km before the calving front. Ice velocities

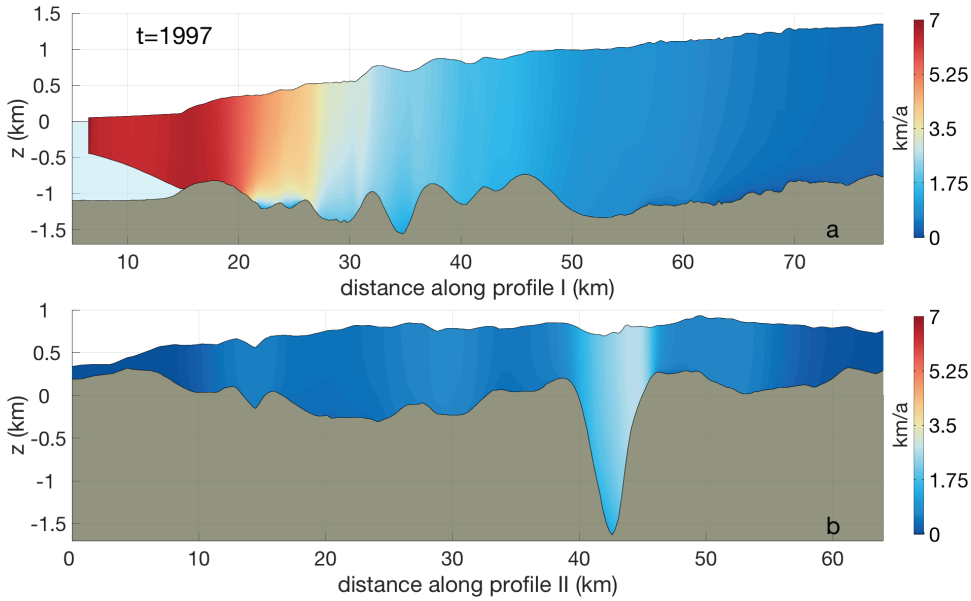


FIGURE 7.4: Vertical section plot of the annual average ice velocity in 1997 along profiles I (a) and II (b) (Fig. 7.1). Ice flow direction of b) is out of the paper plane. Grey area is bedrock, light blue area is ocean.

are lowest at the base and the contribution of basal sliding to the ice motion increases from about 50% inland to 100% from the last 5 km upstream of the grounding line onwards. Localized “pockets” of slow ice at the base (between kilometres 22 and 26) cause high vertical shear (cf. Fig. 7.6a). Fig. 7.4b shows that areas of fast flow are confined to deep parts of the bedrock. The maximum ice velocity along this profile is located south (right) of the trough due to the curved along-flow profile of the trough at this location (cf. Fig. 7.1) and high lateral stress (cf. Fig. 6.4a). Outside the trough, the ice flow velocity and ice thickness are weakly linked.

Fig. 7.5 shows the highly inhomogeneous pattern in vertical ice motion that characterizes much of the areas of fast flow. Vertical ice motion in the ice stream is an order of magnitude larger (up to 1.04 km a^{-1}) than inland (Fig. 7.5a). The increase in magnitude occurs between kilometre 50 and 40, where ice flow accelerates and the bedrock becomes bumpy along this profile. Vertical ice motion in the ice stream corresponds to the product of horizontal ice motion and the along-flow slope of the bedrock, and stays about constant along the entire vertical ice column in a slightly upstream-arching fashion, which causes undulations at the ice surface that resemble the bedrock. Local deviations from this pattern are caused by lateral effects, such as upward ice motion due to converging flow (e.g. between kilometres 29 and 30, Fig. 7.5a). Vertical ice velocities along profile II show that the ice that enters the deep trough at this location flows downward at 340 m a^{-1} to the centre of the tributary (Fig. 7.5b), which causes large vertical extension of the ice column. Outside of the trough, there is no clear trend in vertical ice motion.

Fig. 7.6a shows that effective strain rates along-flow range over several orders of magnitude, from as low as $1 \times 10^{-2} \text{ a}^{-1}$ in the upper ice column inland to up to 6 a^{-1} at the ice base between kilometres 22 and 26. Effective strain rates are usually highest near the ice base due to high basal shear.

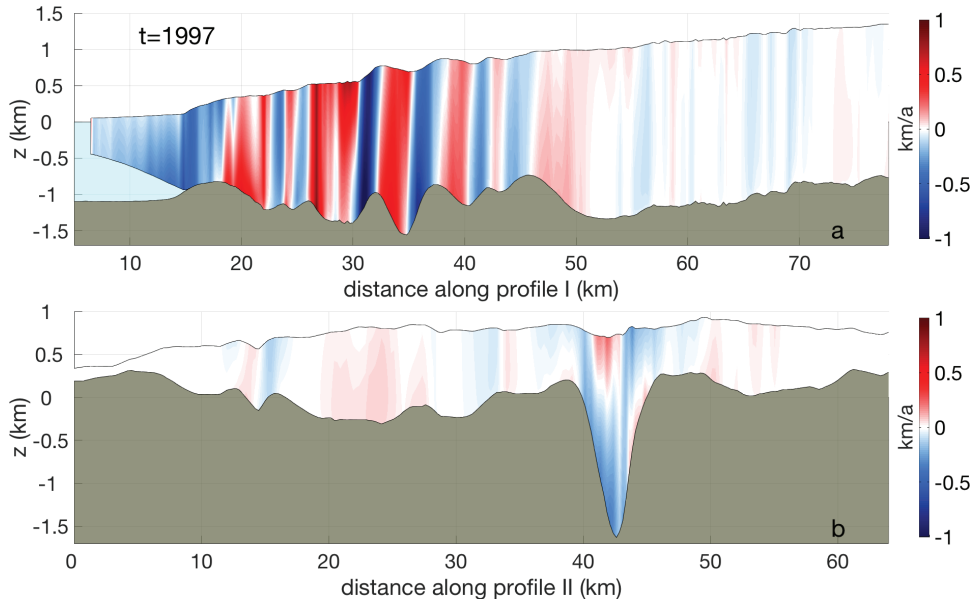


FIGURE 7.5: Vertical section plot of the annual average vertical ice velocity component in 1997 along profiles I (a) and II (b) (Fig. 7.1). Grey area is bedrock, light blue area is ocean.

Downstream of kilometre 45, high longitudinal strain rates cause high effective strain rates throughout the ice column.

Fig. 7.6b shows the abrupt transition in strain rates between the fast-flowing branches and the surrounding ice. Effective strain rates increase from less than $1 \times 10^{-2} \text{ a}^{-1}$ near the ice margin to an average of $2 \times 10^{-1} \text{ a}^{-1}$ in the deep trough. Highest values of up to 1.3 a^{-1} are found at base of the deep trough's centre and at its southern margin. Both branches of fast flow are surrounded by bands of 5 to 10 km width of enhanced basal shear. There, the laterally transferred driving stress of the branches is balanced by basal drag.

Fig. 7.7 shows that the ice viscosity drops along-flow as effective strain rates and the enthalpy increase (cf. Fig. 6.16). It is generally lowest in a thin band near the base (down to $1 \times 10^{12} \text{ Pa s}$), where effective strain rates and enthalpy values are highest (cf. Figs. 6.16, 7.6). Highest ice viscosities are found in the central ice column (up to $2 \times 10^{14} \text{ Pa s}$), where ice temperatures are minimal and strain rates are low. The across-flow profile (Fig. 7.7b) shows that the ice viscosity inside the shear margins of the ice stream is an order of magnitude lower (about $1 \times 10^{13} \text{ Pa s}$) than outside of them (about $1 \times 10^{14} \text{ Pa s}$). However, a core of cold ice advected from upstream (cf. Fig. 6.16) stands out as a stiff local feature in the centre of the ice stream.

Discussion

The floating ice tongue exerts some buttressing on the northern branch, but most of its driving stress near the terminus is taken up by the shallow and sticky bedrock under the ice fall (cf. Figs. 2.1, 6.12a). Detachment from this sticky spot causes high seasonal velocity variability of the northern branch from 2004 onwards. The observed gradual increase of flow velocities during the disintegration of the ice tongue is not captured by the model, which is likely due to differences in ice tongue thickness and strength during the

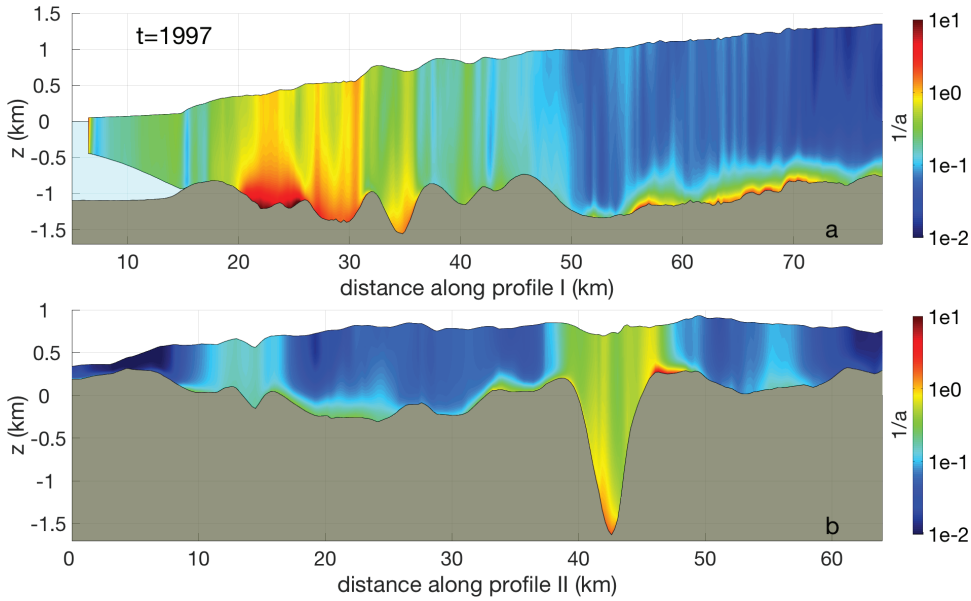


FIGURE 7.6: Vertical section plot of the annual average effective strain rates in 1997 along profiles I (a) and II (b) (Fig. 7.1). Colour scale is logarithmic. Ice flow direction of b) is out of the paper plane. Grey area is bedrock, light blue area is ocean.

disintegration: large rifts appeared on the northern side of the floating ice tongue from 2000 onwards that had not been observed earlier and that decreased the ice tongue's ability to buttress the northern branch (Joughin *et al.*, 2008). Rifting and damage evolution is not included in our model. Contrary to locations near the terminus, inland model flow velocities remain constant or decrease after 2008. Our model results do not allow to explain what causes the observed deceleration inland, which suggest that processes not modelled here, e.g. damage and rifting, likely caused this slowdown.

The influence of the ice stream on flow speeds of the southern tributary is rapidly dampened inland. Locations near the ice stream are affected by the seasonal variation due to lateral tensile stress transfer. Inland, the lateral stress is rapidly balanced by basal drag, which is an order of magnitude larger there than at the base of the trough (cf. Fig. 6.12a). This illustrates the importance of the basal properties for the inland spreading of the stress perturbation caused by calving front migration.

The high vertical velocities in the ice stream are consistent with the flow velocities, and are in good agreement with observations (e.g. Nagler *et al.*, 2017, , and references therein). However, the modelled vertical ice velocities are sensitive to inconsistencies between geometry input data sets. In our model, we choose a short geometry relaxation duration of only 10 years, which is ample to dampen inconsistencies in regions of fast flow, but not sufficient for inland regions where flow velocities are low. Inconsistencies in model geometry may cause erroneous vertical velocities, as those of the HOM are derived in a post-processing step from the horizontal velocity components using the continuity equation (Eqs. 3.36, 3.7 and Greve & Blatter (2009)). Erroneous vertical velocities may corrupt the thermal solution in these regions, cf. Seroussi *et al.* (2011) and Sect. 7.1.2. Using longer relaxation periods prior to the experiments may help to produce a more consistent vertical velocity field. Since the Full-Stokes approximation (cf. Sect.

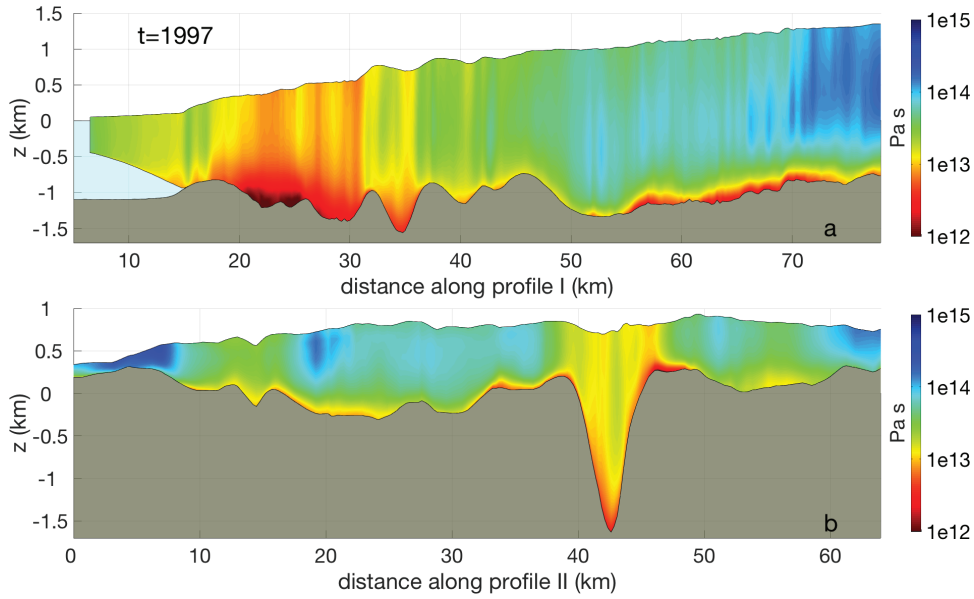


FIGURE 7.7: Vertical section plot of the annual average ice viscosity in 1997 along profiles I (a) and II (b) (Fig. 7.1). Colour scale is logarithmic. Grey area is bedrock, light blue area is ocean.

3.3.2) is even more sensitive to geometry inconsistencies than the HOM, it should only be applied to a model once its geometry yields a realistic vertical velocity field for the HOM.

The velocity spike at inland locations is attributed to adjustments of the basal hydrological drainage system to increased surface melt water supply variability at the onset of the melting season (Joughin *et al.*, 2008), which is known to increase basal slipperiness (e.g. Zwally *et al.*, 2002; Schoof, 2010). Our results support this hypothesis, as basal hydrology is not included in our model, and the model does not capture the velocity spike.

7.1.2 Thermal Regime

Results

In order to differentiate between temperature changes caused by ongoing model relaxation vs. those caused by the acceleration, we show the difference in average ice column temperature to a control run, in which the calving front position is kept fix (Fig. 7.8). Warming and cooling occur in bands along-flow, and this pattern amplifies with calving front retreat. The centres of both the northern branch and the ice stream (upstream of $x = -175$ km) cool, while the shear margins generally heat up. Little temperature change of less than $\pm 0.3^\circ\text{C}$ occurs until 1997. As the calving front retreats, the sign of the temperature difference remains mostly the same, yet its magnitude increases. Highest relative warming of up to 4.3°C until 2015 occurs in the shear margins of the northern tributary, while strongest relative cooling by up to -3.8°C occurs in the southern shear margins near the terminus of the ice stream. In this region of thin ice, changes in prescribed annual average ice surface temperature are able to strongly influence the depth-average ice temperature. The pattern of temperature change resembles that of Fig. 6.15b,c,d, but is about 1°C smaller in amplitude.

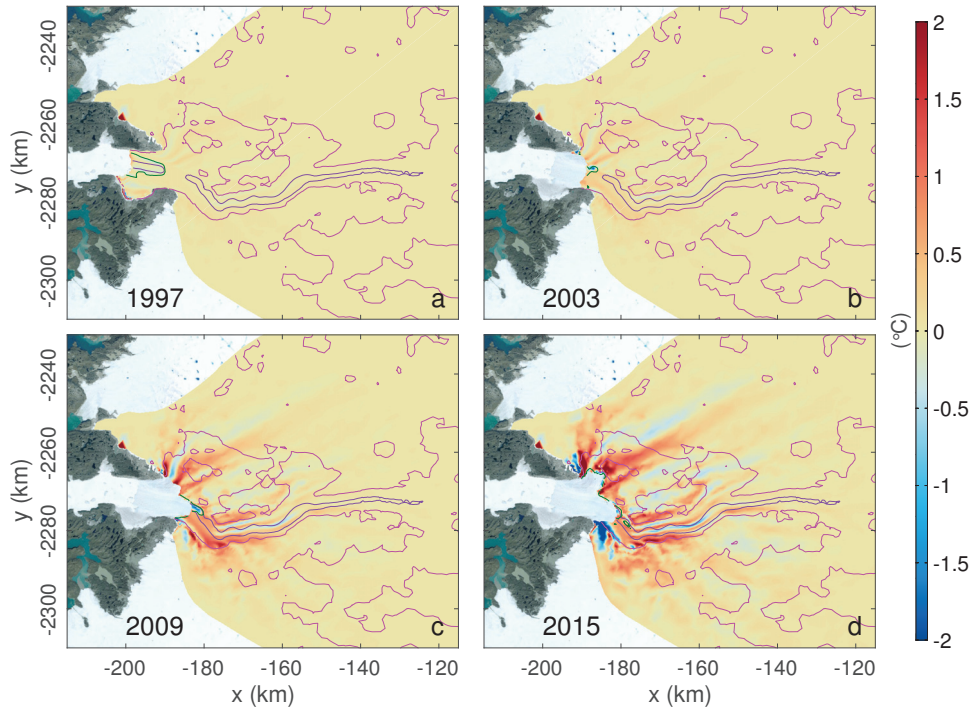


FIGURE 7.8: Modelled difference in depth-averaged ice temperature between simulations with evolving and fixed calving front position, respectively, for different years. Pink and purple lines denote bed elevation contours at 0 and -1000 m elevation, respectively. The green line shows the annual average modelled grounding line position. Satellite background image: Landsat 7 (July 1st, 2001) © Google Earth.

Fig. 7.9 provides an overview over the modelled thermal regime of Jakobshavn Isbræ, with focus on the ice base. Vertically averaged ice temperatures are lowest near the ice divide (-32°C), and gradually warm towards the terminus, reaching -5°C near the southern tributary (Fig. 7.9a). The warming occurs slightly faster in the southern part of the drainage basin. The average temperature of the ice stream is about 4°C lower relative to its surroundings.

Similar to the average ice temperature, the basal homologous ice temperature, T_{hom} , (Eq. 3.34) is lowest near the ice divide (-18°C), and gradually increases along-flow, forming a streaky pattern of alternating warmer and colder bands. Basal temperatures are higher towards the south of the drainage basin, and first patches of temperate basal ice occur at about 300 km distance from the terminus in the centre of the drainage basin. Over the last 200 km along-flow, about 80% of the ice base is temperate. Microscopic water content values of 1 to 2% are found in isolated patches on the ice sheet and in a more concentrated, along-flow pattern in the trough. Highest values of up to 3.2% occur in the trough, 15 km upstream of the grounding line.

The modelled temperate layer thickness is spotted, and isolated clusters of elements develop a temperate layer of finite thickness (Fig. 7.9c). Temperate layers form only in regions with a temperate base, and range in thickness from tens of metres inland up to 400 m in the last 10 km before the grounding line in the deep trough. A layer of up to 150 m thickness forms

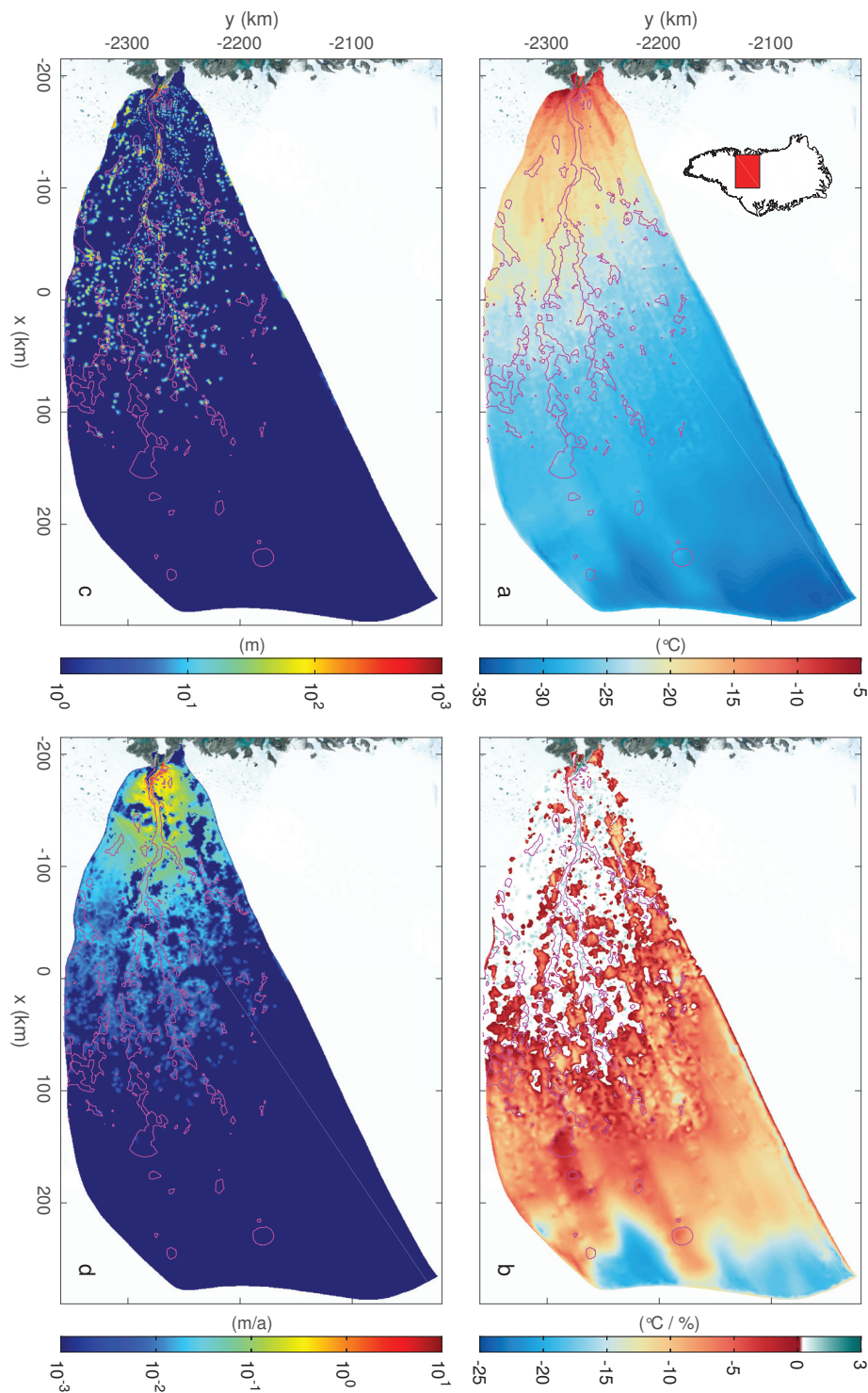


FIGURE 7.9: Modelled thermal basal state of Jakobshavn Isbræ in 1997. a) vertically averaged ice temperature, b) basal homologous temperature and microscopic water content, c) temperate layer thickness, d) subglacial melting rate (grounded ice only, logarithmic scale). Pink lines denote bed elevation contours at -250 m. Satellite background image: Landsat 7 (July 1st, 2001) © Google Earth.

in the overdeepened trough in the last 140 km before the terminus, but vanishes 50 km before the terminus due to strong downward flow of cold ice (cf. 7.5b).

Basal melting occurs at all locations where the base is temperate (Fig. 7.9d). The subglacial melting rate scales with the basal sliding velocity, ranging from several millimetres per year water equivalent (w.e.) inland up to 4 m a^{-1} w.e. near the grounding line of the northern tributary.

The observed strong temperature inversion in the vertical (cf. Fig. 6.14) is visible along the profiles I and II (Fig. 6.16). The ice surface is at prescribed surface air temperature, and the ice temperature gradually drops off to its minimum (about -15 to -22°C) in a cold core of ice slightly below the middle of the ice column. From the cold core, the ice temperature sharply rises to pressure melting point at the base. Downstream of kilometre 30, the ice abruptly warms through enhanced dissipation of kinetic energy (strain heating) in the shear margins, at the ice base and in the ice stream itself, which annihilates the temperature inversion. There, a basal temperate layer of up to 200 m thickness with microscopic water content up to 2% develops along this profile. Isolated patches of up to 50 m temperate layer thickness are also found further upstream between kilometres 54 and 72, which is a region of high basal shear (Fig. 7.6). In the profile across-flow (Fig. 6.16b), the cold core shows clearly in the centre of the ice stream and in the region between the northern tributary and the ice stream.

Discussion

Jakobshavn Isbræ's thermal regime is polythermal and advection-dominated since the ice conductivity is low compared to the high flow velocities. Englacial warming through strain heating, and basal heating through geothermal heat flux and basal frictional heating warms the ice on its way towards the terminus. The model captures the strong observed vertical temperature inversion well – bearing in mind the large uncertainties in the model input parameters and approximation errors (Fig. 6.14). The temperature inversion characterizes wide areas of the glacier. The central cold core of ice has been advected from cooler areas upstream.

We see the modelled temperate layer thickness as realistic, as the enthalpy benchmarks (Chap. 4) show that ISSM accurately reproduces the temperate layer thickness even at low vertical mesh resolution. However, we caution against seeing the spotted distribution of the basal temperate layer as representative, see discussion of model limitations (Sect. 7.2).

The microscopic water content in the temperate layer is in the range of observed values for the GrIS (e.g. Brown *et al.*, 2017), and frequently exceeds the critical value of 1% for which currently no ice rheology is known (Liboutry & Duval, 1985). The model prescribes an ice viscosity parameter corresponding to 1% microscopic water content at these locations, so that we expect that englacial deformation near the base is higher than modelled here. This would allow for higher strain heating and for higher basal drag in the deep trough. Higher strain heating at the base would create a thicker and more easily deformable basal temperate layer, which creates a positive feedback. However, given that observations show only finite basal temperate layer thicknesses, a balance between strain rate increase and corresponding viscosity drop must occur at some point.

The comparison of observed to modelled ice temperatures at boreholes A, B, and D (Fig. 6.14, and Iken *et al.*, 1993; Lüthi *et al.*, 2002) shows that – despite a good match – the upper modelled ice column is too cold, the central ice column is too warm, and the ice base again is too cold at the borehole locations. The offset at the ice surface is likely due to the combination of the firn column being warmed by percolation of surface meltwater (all boreholes were drilled during July and August), a low vertical mesh resolution at the ice surface in the model which is unable to capture strong curvature in the enthalpy solution, and the prescription of annual average air temperatures in the model, which are lower than summer air temperatures. The offset at the base is likely caused by errors in ice velocities and underestimation of englacial strain heating at the base, as discussed above. The enthalpy benchmark experiments (Chap. 4) show that the current implementation of the enthalpy method in ISSM underestimates the ice temperature in cold ice and overestimates the microscopic water content in temperate ice, which is the opposite pattern of what we find here from the comparison. Therefore, the temperature offset detected during the benchmark experiments has no large influence on the overall model results.

Calving front retreat and the ensuing flow acceleration has a significant impact on the thermal regime in the ice stream and in areas of fast flow. Significant shear margin warming occurs relative to a control run through enhanced strain rates. Shear margin warming is therefore responsible for the faster flow velocities of a thermodynamically coupled run compared to an uncoupled simulation. Moreover, calving front retreat is able to destroy the thick basal temperate layer in the trough near the terminus, since it leads to ungrounding of these areas, and the temperate ice is quickly melted by submarine melting or simply calved away. This supports the hypothesis that observed “blue ice” areas of Jakobshavn Isbræ’s calved icebergs are temperate ice (Lüthi *et al.*, 2009).

Our modelled enthalpy of Jakobshavn Isbræ is lower than that of the corresponding area presented in Seroussi *et al.* (2013). We explain this discrepancy with the temperature lowering by 5 K that we apply to the prescribed ice surface temperatures, whereas Seroussi *et al.* (2013) prescribe present-day temperatures.

7.1.3 Geometry

Results

Fig. 7.10 shows that while the ice surface elevation remains about constant until 1996, increased submarine melting rates and especially calving front retreat trigger strong surface lowering along the ice stream, the northern branch and the southern tributary. Surface lowering rates are highest on grounded parts of the ice stream near the grounding line from 2003 through 2006, reaching about 36 to 51 m a^{-1} on annual average (Fig. 7.10a). The surface lowering signal is dampened along the ice stream, and is about 10 to 16 m a^{-1} at a location 50 km upstream of the original calving front position (green line, Fig. 7.10a). The seasonal surface elevation variability near the grounding line is up to $\pm 28 \text{ m}$ in 2004, and is strongly dampened inland, so that it vanishes at the most inland locations shown here (green lines).

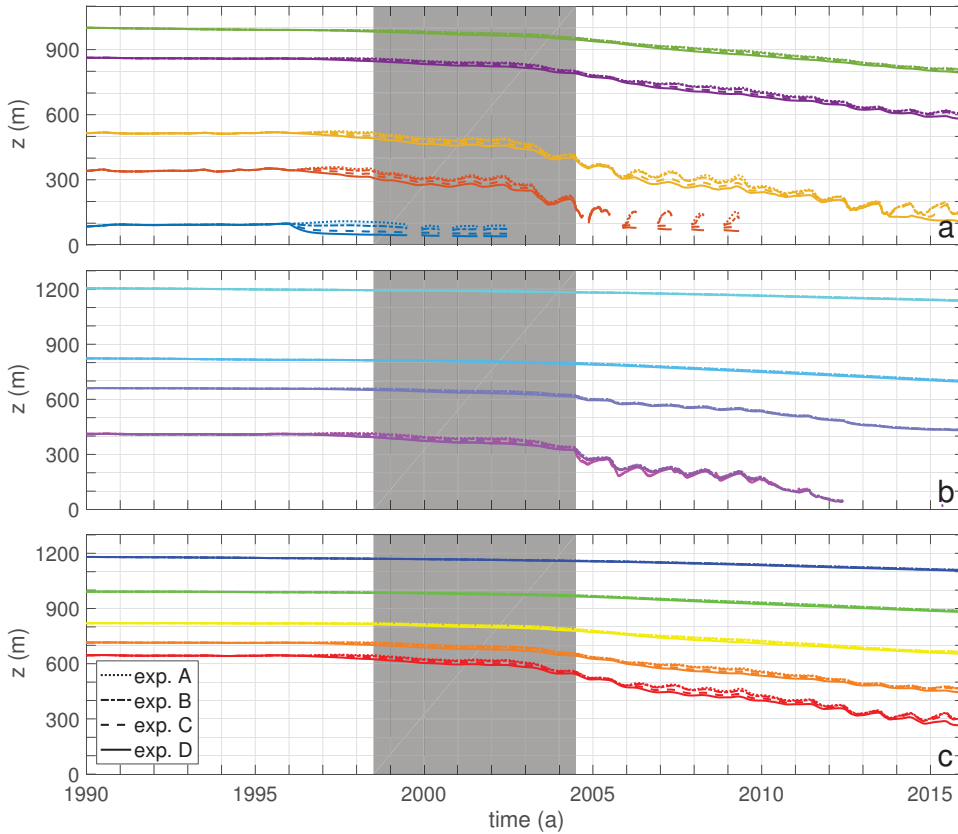


FIGURE 7.10: Timelines of surface elevation at different locations along a) the ice stream, b) the northern branch, c) a southern tributary to the ice stream for different submarine melting rate functions (cf. legend, experiment labels as in Sect. 6.7). Line colours correspond to the triangle locations shown in Fig. 7.1. Lines are discontinuous when the calving front retreats upstream of the corresponding location. The grey boxes mark the period of ice tongue disintegration.

The ice surface has lowered up to 402 m at the location represented by the yellow line in Fig. 7.10a between 1996 and 2016.

The surface of the northern branch lowers less (60 m) than ice stream until the completion of the disintegration of the ice tongue in 2004 (Fig. 7.10b). However, high summer flow velocities cause strong dynamic surface lowering of up to $83 \pm 36 \text{ m a}^{-1}$ near the terminus in summer 2004, which decreases to 4 to $10 \pm 0.5 \text{ m a}^{-1}$ at the most inland location (turquoise line).

In the southern tributary of the ice stream, the response in surface elevation is strongly dependent on the distance from the ice stream (Fig. 7.10c). Locations close to the ice stream show the highest surface lowering rates and highest variability comparable to values of the ice stream (up to $40 \pm 10 \text{ m a}^{-1}$ between 2003 and 2004, red and orange lines). The surface lowering rates decrease to 5 to 14 m a^{-1} further inland, with vanishing seasonal variability (yellow, green and blue lines).

The surface lowering on grounded ice is weakly sensitive to the applied submarine melting rate (less than 10% of the total surface lowering). On floating ice, the surface elevation adjusts in about one year to the change in applied submarine melting rate in 1996, and stays constant from then

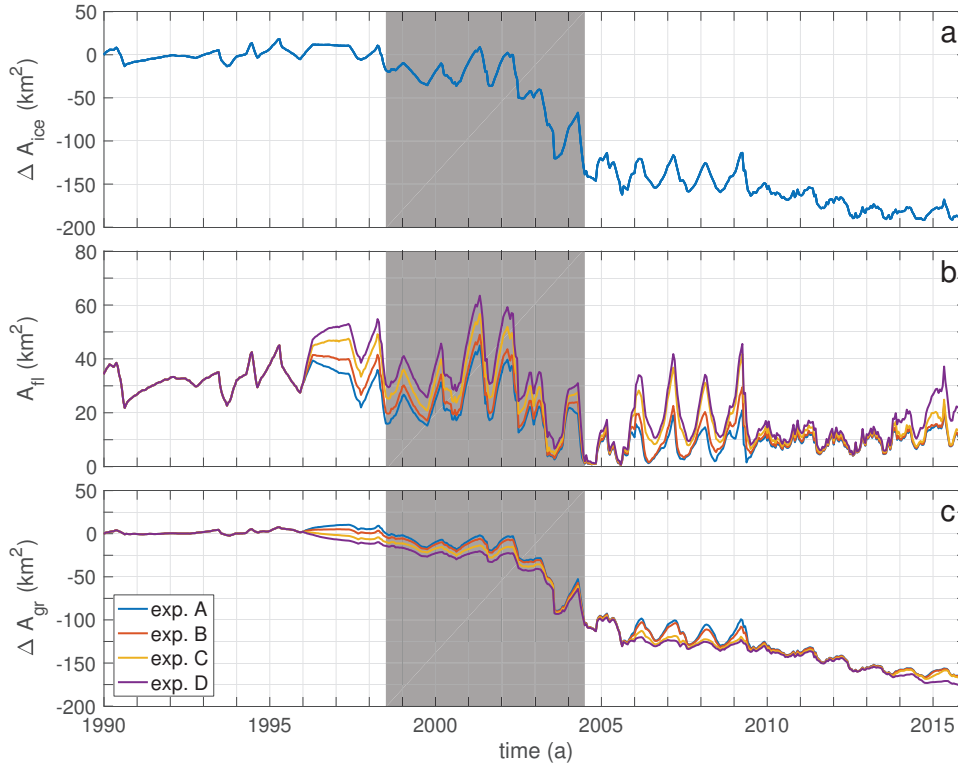


FIGURE 7.11: Timelines of a) change in ice extent area, b) floating ice area, and c) change in grounded ice area extent. The grey boxes mark the period of ice tongue disintegration. Experiment labels as in Sect. 6.7.

on onward (blue lines, Fig. 7.10a). Strongest surface lowering occurs for highest submarine melting rates, and the range of surface elevations for floating ice in 1998 for different melting rates is 60 m, which corresponds to an ice tongue thickness difference of about 543 m.

Fig. 7.11a shows that the annual average ice area extent remains constant until the disintegration of the ice tongue, and varies annually by about $\pm 10 \text{ km}^2$, which corresponds to about 1.7 to 2 km seasonal calving front migration along the fjord. The timelines overlap since the calving front position in the model is prescribed. During the disintegration of the ice tongue, the average ice extent decreases rapidly by about 130 km^2 until summer 2004, which gradually continues so that a total of 184 km^2 ice area was lost between 1998 and 2015.

Submarine melting rates have a strong impact on the floating ice tongue area, as the calving front position in our model is prescribed. Higher submarine melting rates lead to a larger floating ice area. The total spread is 20 km^2 for different melting rate functions (Sect. 6.7) and an average value of 43 km^2 in summer 1997 (Fig. 7.11b). During the disintegration, the floating ice area decreases so that almost no floating ice is left in summer 2004 for all experiments, and the terminus is essentially grounded for all following summers, with exception for the section over the deep trough. An ephemeral ice tongue builds up every winter, which rapidly disintegrates every spring.

The characteristics of total grounded ice extent (Fig. 7.11c) mirror those of the total ice area extent as the terminus is essentially grounded after the disintegration of the ice tongue. The area of grounded ice extent remains

constant with minor seasonal variation ($\pm 2 \text{ km}^2$) and a spread of 20 km^2 in 1997, depending on the applied melting rate functions. Even the highest melting rates applied here are not able to cause significant grounding line retreat prior to the disintegration.

Discussion

Modelled surface lowering rates of an average 22.2 m a^{-1} after the ice tongue disintegration are in excellent agreement with observations (e.g. Thomas *et al.*, 2003; Joughin *et al.*, 2008; Hurkmans *et al.*, 2012; Helm *et al.*, 2014). Dynamic thinning dominates the ice geometry evolution during calving front retreat: the surface lowering rate is up to an order of magnitude higher than local surface melting rates (cf. Fig. 2.3d), and develops a pronounced seasonal signal that scales with the ice velocities. Lateral inflow of ice replenishes the accelerating ice stream, and this dynamically thins the surrounding areas. Thin areas close to the land-terminating ice sheet margin decelerate, stiffen and gradually melt away during each successive melting season. Even though these areas may appear as ice covered on satellite imagery, they are essentially dead ice and do not contribute to the flow dynamics of the glacier.

The modelled terminus is essentially grounded during summer from 2004 onwards, which is in good agreement with observations (Dietrich *et al.*, 2007; Amundson *et al.*, 2010; Joughin *et al.*, 2012). The loss of 38 km^2 of grounded ice area from 2004 to 2010 corresponds well to 3.5 km of grounding line retreat observed by Rosenau *et al.* (2013). Lateral inflow of ice stabilizes the grounding line position of the ice stream. This delays the grounding line retreat along the partially retrograde trough to such a degree that none of the applied submarine melting rates is able to destabilize the grounding line in our experiments. Even rapid and sustained calving front retreat is challenged to produce sufficient thinning of the ice stream to produce grounding line retreat further than the terminus position. The grounding line stabilization through lateral inflow was to be expected from theoretical studies (Gudmundsson *et al.*, 2012), and comes as no surprise as the trough is narrow, so that only a small fraction of the glacier's lateral ice boundary is exposed to the high ablation rates there. However, the strong dynamic thinning of the ice adjacent to the ice stream sets a limit to its capacity to stabilize the grounding line during continued calving front retreat.

We find that the floating ice tongue is of critical importance for Jakobshavn Isbræ's stability. Jakobshavn Isbræ's flow acceleration and dynamic thinning rates scale inversely with the extent of the floating ice tongue. Strongest flow acceleration and thinning occurs while the ice tongue is absent, e.g. in summer 2004.

7.1.4 Mass Balance

Results

The total annual cumulative surface mass balance (SMB) of Jakobshavn Isbræ varies between 20 and 43 Gt a^{-1} , with lower average values from 2005 onwards (Fig. 7.12a). The glacier gains on average 36 Gt of ice per year through snowfall, and loses about 5.8 Gt per year through surface melting

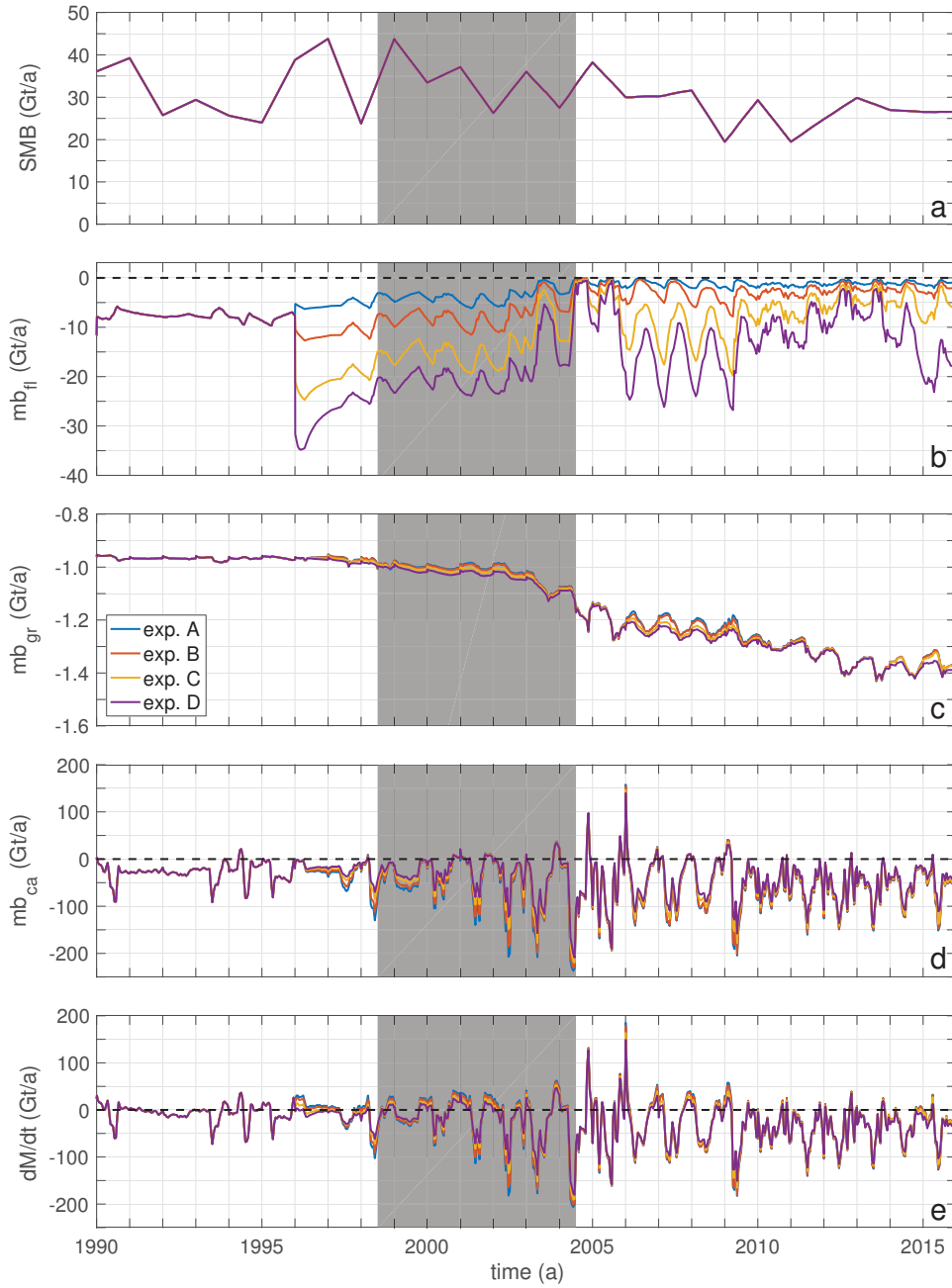


FIGURE 7.12: Evolution of the total integral of a) surface mass balance, b) basal melting under floating ice, c) basal melting under grounded ice, d) ice discharge due to calving, taken over the corresponding faces of the glacier. e) Evolution of the mass change rate of Jakobshavn Isbræ. Positive contributions denote glacier mass gain, negative ones denote mass loss. The grey boxes mark the period of ice tongue disintegration. Black dashed lines correspond to zero mass balance. Experiment labels as in Sect. 6.7.

(not shown here). No correlation between the SMB and the dynamics of the glacier is found on these time scales.

The total mass discharge through submarine melting scales with the area of floating ice (cf. Fig. 7.11b) and the submarine melting rate (Fig. 7.12b). The average mass loss is 8 Gt a^{-1} until 1996, and varies widely from 4 Gt a^{-1} for exp. A (lowest submarine melting rate) to 21 Gt a^{-1} for exp. D (highest submarine melting rate) in 1998. The mass loss caused by submarine melting vanishes once the terminus becomes grounded during summer from 2004 onwards.

Mass loss through subglacial melting under grounded ice scales with basal sliding velocities (Fig. 7.12c), and is $0.96 \pm 0.01 \text{ Gt a}^{-1}$ until the disintegration of the ice tongue. Afterwards, it increases gradually to $1.38 \pm 0.04 \text{ Gt a}^{-1}$ between 2013 and 2015. Subglacial melting rates are weakly sensitive to the mass loss through submarine melting, with higher submarine melting causing slightly higher subglacial melting (3% spread) as the glacier slides faster over the bed.

Amplitude and variability of the ice discharge through calving are considerably higher than the discharge through melting, since calving events discharge a large amount of ice in a relatively short period of time (Fig. 7.12d). The discharge rate of calving, mb_{ca} , presented here is calculated as the difference between the total mass change rate and all other components of the glacier's mass balance:

$$mb_{ca} = \frac{\partial M}{\partial t} - (\text{SMB} + mb_{fl} + mb_{gr}), \quad (7.1)$$

where mb_{fl} and mb_{gr} are the total mass loss through submarine and subglacial melting, respectively. Positive ice discharge values are a model artefact caused by the extrapolation of the ice thickness at the calving front (cf. Sect. 5.2.3). Prior to the disintegration of the ice tongue, Jakobshavn Isbræ discharges about $25 \pm 48 \text{ Gt a}^{-1}$ of ice through calving. This rate increases to an average of $60 \pm 115 \text{ Gt a}^{-1}$ in 2003, and remains elevated at about this value for the remainder of the simulation, while the variability decreases to $\pm 75 \text{ Gt a}^{-1}$.

The total mass balance of Jakobshavn Isbræ (Fig. 7.12e) exhibits a similar trend and variability as the ice discharge through calving. Prior to the disintegration, the annual average mass balance is slightly negative at about $-5.5 \pm 2.5 \text{ Gt a}^{-1}$. The annual average mass balance decreases rapidly towards $-41 \pm 110 \text{ Gt a}^{-1}$ in 2003 and 2004, and remains between -25 and -45 Gt a^{-1} for the remainder of the simulation.

Prior to the disintegration of the ice tongue, 59.1% of Jakobshavn Isbræ's total ablation is due to calving, 25.3% is due to submarine melting, 13.4% is due to surface melting and 2.2% is due to subglacial melting. These ablation ratios shift to 82.1% for calving, 7.9% for submarine melting, 8.2% for surface melting, and 1.8% for subglacial melting after 2010.

Discussion

The modelled glacier's mass balance is dominated by mass loss through calving, and from 2009 onwards, the glacier loses mass nearly throughout the year, which agrees well with observations (Echelmeyer *et al.*, 1992; Rignot & Kanagaratnam, 2006; Howat *et al.*, 2011). Due to the dominance of

calving for the glacier's mass balance, the annual average mass budget is rather insensitive to the applied submarine melting rate distribution: the time-lines of the glacier's mass change for different submarine melting rates overlap for each summer in which the terminus becomes grounded (Fig. 6.7). The dominance of mass loss through calving explains why no correlation can be established between fjord water temperatures and glacier behaviour after the disintegration of the ice tongue (Gladish *et al.*, 2015).

The mass loss through subglacial melting is the smallest contributor to the mass budget. Assuming that all subglacial meltwater exits at Jakobshavn Isbræ's grounding line as subglacial discharge, the amount of modelled mass loss through subglacial melting corresponds to a subglacial discharge flux of $33.5 \pm 0.3 \text{ m}^3 \text{ s}^{-1}$. This value is half to a third of estimates presented in Echelmeyer & Harrison (1990), which can be explained by the underestimation of the basal temperature and the basal temperate layer thickness discussed above. A warmer base with a smoother temperate base distribution would yield higher mass loss through subglacial melting. Enhanced basal sliding caused by calving front retreat increases the mass loss through subglacial melting by 45% until 2016. Subglacial discharge influences the submarine melting rates (Jenkins, 2011; Xu *et al.*, 2012), which is not modelled here. However, most of Jakobshavn Isbræ's subglacial discharge during summer is fed by runoff so that the increase in subglacial melting is likely to influence the submarine melting rates in winter only.

The modelled glacier continuously loses 2.5 to 5.5 Gt of mass per year in a present-day climatic setting with the calving front position kept fix, even for submarine melting rates significantly lower than observed (Fig. 6.8c, Exp. A). Moreover, our estimate of mass loss through subglacial melting is likely at least 1 Gt a^{-1} too low, as discussed above, so that the modelled mass loss is likely about 20 to 40% too conservative. This is within the error bars of early (Bindshadler, 1984; Pelto *et al.*, 1989; Echelmeyer *et al.*, 1992; Rignot & Kanagaratnam, 2006; Motyka *et al.*, 2010) and state-of-the art mass balance estimates (J.Mouginot, pers.comm.), which find that Jakobshavn Isbræ was in equilibrium or perhaps slight negative imbalance prior to the ice tongue disintegration.

7.2 Limitations

The model study presented here is subject to some limitations, which have to be considered when using and interpreting its results. We caution against seeing our basal thermal regime and subglacial melting rates (Fig. 7.9) as qualitatively representative for Jakobshavn Isbræ. While the deviation to the actual basal thermal regime is not large, observations suggest that the basal thermal regime is more smooth than modelled here (e.g. Brown *et al.*, 2017). We use a short, 10-year model geometry relaxation period, which is not sufficient to eliminate all geometry inconsistencies inland. Therefore, the momentum balance solver may produce locally erroneous vertical ice velocities, which either decrease the basal temperate layer thickness and the basal enthalpy by downward advection of cold ice, or warm the ice column by upward advection of warm ice from the base. This is able to locally corrupt the glacier's advection-dominated thermal regime. Longer geometry relaxation durations will help to provide a more realistic basal

thermal regime. The quality of the modelled basal thermal regime does not influence our conclusions on the causes for Jakobshavn Isbræ's widespread flow acceleration, as the basal drag is temperature-independent.

The model of Jakobshavn Isbræ does not include basal hydrology. However, adjustments of the subglacial hydrology system at the onset of each melting season are likely to cause short but pronounced velocity spikes inland (Joughin *et al.*, 2008). Since the glacier's ice tongue is sensitive to the ice supply from upstream, this effect may become significant for simulations on timescales of centuries to millennia. It has no significance for the velocity of the ice stream, which is modulated by the calving front position.

Our model provides only little insight into the subglacial processes that control the glacier's basal sliding, and does not allow to infer the nature of the substrate underneath Jakobshavn Isbræ. In particular, we can not infer the cause for the low basal drag in the centre of the ice stream near the terminus. Since the minimum ice viscosity parameter in the model is that of temperate ice with 1% microscopic water content (cf. Sect. 3.3.2), accounting for warmer and softer ice in the model may yield higher basal drag in the trough.

7.3 Jakobshavn Isbræ's Future Evolution

Jakobshavn Isbræ's deep and narrow trough that remains below sea level for about 400 km inland indicates that the outlet glacier will remain marine-terminating for the foreseeable future. The glacier will therefore remain sensitive to ocean forcing and maintain a stress regime similar to that of today. Major controls on the glacier's current behaviour are the floating ice extent, the bedrock topography, and its mass balance. Reliable projections of Jakobshavn Isbræ's future evolution are challenged by the lack of a calving rate parametrisation as well as large errors in bedrock topography near the grounding line, and would require mass balance estimates from coupled climate and ocean models. Therefore, we are not able here to draw more specific conclusions on Jakobshavn Isbræ's future behaviour than those presented in Chap. 6.5.

The floating ice tongue has a critical stabilizing function for Jakobshavn Isbræ, and glacier stabilization is only expected if a new floating ice tongue is able to form. Currently, warming ocean temperatures obstruct the formation of a stable ice tongue by thinning any floating ice from underneath. Warming air temperatures and dynamic lowering of the ice surface increase the ablation zone area, which will increase the subglacial discharge and hence maintain high submarine melting rates. Moreover, enhanced air temperatures will increase calving rates by facilitating hydro-fracturing of meltwater-filled crevasses (van der Veen, 1998) and weakening the ice mélange's ability to stabilize the calving front (Amundson *et al.*, 2010). Finally, no feature is apparent along the next 60 to 70 km of the trough that would allow for longer grounding line and calving front stabilization. We therefore see the formation of a stabilizing ice tongue as unlikely for the next decades, which would maintain the glacier's current high rate of mass loss. We caution against the use of the calving front position as the only evaluation tool to assess the stability of the glacier, as other characteristics such as glacier's mass balance should also be accounted for.

7.3.1 A Hypothesis for Jakobshavn Isbræ's Long-term Behaviour

Currently, it is assumed that Jakobshavn Isbræ was stable during the 35 years prior to the ice tongue disintegration (Bindshadler, 1984; Sohn *et al.*, 1998; Joughin *et al.*, 2008). We challenge the existing hypothesis since

1. observations show considerable thinning of inland areas of Jakobshavn Isbræ from 1985 to 1997 (Motyka *et al.*, 2010) despite a stable calving front position,
2. Jakobshavn Isbræ was possibly in slight negative mass balance prior to the disintegration of the ice tongue (cf. Sect. 7.1.4),
3. observations during this period are sparse, and
4. Jakobshavn Isbræ's calving front has been retreating since at least 1850 (Georgi, 1959, and Fig. 2.5c).

We propose an alternative hypothesis for Jakobshavn Isbræ's long-term behaviour based on our synopsis of observations and model results. We surmise a three-phase cyclic response behaviour of Jakobshavn Isbræ while it is in negative mass balance. In the first phase, Jakobshavn Isbræ is losing mass continuously, as it likely did prior to the disintegration of its ice tongue (cf. Sect. 7.1.4). The thinning glacier gradually loses its capability to balance the ice tongue's mass loss, which in turn thins and provides gradually less buttressing to the ice stream that feeds it. This creates a positive feedback mechanism between dynamic thinning and ice tongue buttressing. The thinning ice tongue is able to maintain much of its buttressing and extent if shallow pinning points like the "Ice Rump" in the Tissarisoq Ice Bay (Fig. 2.1) are present, and the ice stream and ice tongue may thus appear as stable on aerial and satellite imagery. However, as the ice tongue thins, it becomes increasingly vulnerable to destabilizing events like a sudden increase in air or ocean temperature.

The second phase of strong flow acceleration, dynamic thinning and calving front retreat is triggered by the disintegration of the thinned ice tongue (Podlech & Weidick, 2004; Joughin *et al.*, 2004), a complex fracturing process that is known to occur rapidly for other floating ice extension as well (e.g. Rack & Rott, 2004). In case of Jakobshavn Isbræ, ice tongue disintegration appears to have been triggered by an increase in ocean temperatures and the ensuing detachment of the ice tongue from the Ice Rump (Holland *et al.*, 2008; Joughin *et al.*, 2008).

During the third phase, the glacier terminus has retreated sufficiently into thick inland ice, so that lateral inflow of ice into the trough now again allows for the formation of a floating ice tongue. Inland areas require centuries to millennia to adjust to the new calving front position (Viel & Nick, 2011), and the exact retreat and stabilization pattern will be modulated by the trough geometry (Enderlin *et al.*, 2013; Morlighem *et al.*, 2016). If the mass balance of the retreated glacier remains negative, the glacier will re-enter the first phase, which closes the cycle.

Our hypothesis opposes the existing one, as it states that the glacier is continuously adjusting to its climatic setting. In contrast to the existing one, it would explain Jakobshavn Isbræ's past observed phases of strong intermittent thinning since the onset of the 20th century (Csatho *et al.*, 2008). Its

dependence on the glacier's mass balance implies that this cycle would accelerate with ongoing climate warming, which would cause more frequent phases of rapid retreat and strong mass loss in the future.

We are not able to test the hypothesis using our model, since it would require a calving rate parametrisation suitable for continental-scale ice sheet models, which is lacking as of today. Our model setup does not allow to investigate the mechanisms that cause the ice tongue's disintegration, nor what maintains the glacier's high calving rates, both of which are currently an active field of research (van der Veen, 1998; Humbert & Steinhage, 2011; Humbert, 2012) and (Benn *et al.*, 2007; Alley *et al.*, 2008; Bassis, 2011; Krug *et al.*, 2014; Astrom *et al.*, 2014), respectively. We formulate it as a plausible alternative to the existing hypothesis as a result of the in-depth study of available observations and the glacier's dynamics in the model.

7.4 Future Work

The results of this doctoral thesis represent a major step towards a better understanding of the recent dynamic changes of Jakobshavn Isbræ. However, as our understanding increases, two questions remain:

1. How to close the remaining gap between the model results and the observations?
2. How will Jakobshavn Isbræ evolve in the future?

Better understanding of Jakobshavn Isbræ's dynamics will result in a better match of observations and a smaller error in projections of Jakobshavn Isbræ's future behaviour. However, errors in observations and numerical approximation routines as well as model simplifications (Chap. 3) set a limit to the reproducibility of observed dynamics and therefore to our intellectual understanding of the glacier's dynamics. The efforts for future model improvement have therefore to be put into perspective with the current demands on science and the available resources.

7.4.1 Closing the Gap to Observations

The non-linear rheology of ice drives the response of the glacier inland, and available material laws for glacier ice with high microscopic water content or at high shear stress is a large source of uncertainty in glacier models. While it is common to use a stress exponent $n = 3$ in ice sheet modelling, it is known that the actual value for n may vary from 1.8 to 4.2 in different glacier settings (Cuffey & Paterson, 2010). Current material laws, like the one used in this study, are tuned towards $n = 3$, but higher values may be better suited for regions of high stress (Cuffey & Paterson, 2010) like the shear margins, which control much of Jakobshavn Isbræ's rapid change. Since calving introduces rapid stress perturbations, a visco-elastic material law could be applied for better modelling of the glacier's response on short time scales. Given the good agreement of model results and observations, we see no need to use an anisotropic material law to model Jakobshavn Isbræ.

The heat content of ice has a major influence on the ice viscosity (Sect. 3.3.2), and the Jakobshavn Isbræ's thermal regime changes significantly following the disintegration of the ice tongue (Chap. 6). Especially the microscopic water content of ice significantly softens the ice, but available studies present values only for values up to 1% (Lliboutry & Duval, 1985), despite that significantly higher values have been measured in glacier ice (Vallon *et al.*, 1976; Brown *et al.*, 2017). Potential material laws have to be tested on their ability to reproduce the observed flow acceleration of different glaciers. Moreover, it is important to gain a better understanding of the transport mechanism of microscopic water content in temperate ice (cf. recent efforts by Hewitt & Schoof, 2017), which influences the thickness of the basal temperate layer (Chap. 4).

Basal sliding is a major control on Jakobshavn Isbræ's ice motion, but the data assimilation technique applied in this study gives no understanding of the physical processes that determine the slipperiness of the bed. Projections of Jakobshavn Isbræ's future evolution will need to take changes in the physical processes at the ice base into account. Transient data assimilation techniques based on automatic differentiation (Larour *et al.*, 2014) are able to provide a differentiated insight into basal processes. Recent studies show that basal sliding laws other than the linear viscous one used in this study, like a plastic sliding law, may provide a better fit between observations and model results (Habermann *et al.*, 2013; Gillet-Chaulet *et al.*, 2016; Minchew *et al.*, 2016). Work on accounting for the thermal state of the ice sheet in the basal friction parameter as well as improving basal hydrology schemes is currently underway. Future simulations of Jakobshavn Isbræ should employ longer geometry relaxation periods, which will help to eliminate geometry inconsistencies that corrupt the glacier's thermal regime. The use of higher-order finite elements for the discretization of the enthalpy field equation will help to capture the strong curvature in the enthalpy solution that occurs at the CTS.

7.4.2 Creating Reliable Projections

Reliable projections of Jakobshavn Isbræ's future evolution and its contribution to eustatic sea level rise for the next decades to centuries requires an integrated approach involving all fields of glaciology such as field measurement campaigns, ice-core science, engineering, theoretical glaciology, remote sensing and numerical modelling.

Ice-sheet-wide observations of for example ice surface velocity, bedrock elevation, ice surface elevation, calving-front and grounding line position, glacier mass balance components, ice temperature, and geothermal heat flux are invaluable model input data sets required for the calibration of a thermodynamically coupled model of Jakobshavn Isbræ. Field campaigns and satellite missions that deliver these products should be continued.

As Jakobshavn Isbræ's trough reaches far inland, so that its stress regime will remain similar to that of today, projections of the glacier's future behaviour will crucially depend on the emergence of a calving rate parametrisation that is applicable to large-scale ice sheet models. The LSM implemented during this doctoral thesis allows to apply any user-defined calving rate parametrisation. Potential parametrisations are to be tested by their

ability to reproduce past observations, which is another argument for maintaining a continuous record of observations at Jakobshavn Isbræ.

Longer-term projections of Jakobshavn Isbræ's future behaviour require to improve the implemented LSM, so that the boundary conditions at the calving front face are applied at sub-element scale, and so that the volume-preservation property of the LSM is improved. The calving front position in the model intersects in general some front elements, but stress and thermal boundary conditions are currently applied along mesh element edges. Application of the boundary conditions along the calving front position as inferred from the LSF requires using a different type of finite elements, such as XFEM (Moes *et al.*, 1999). The volume-conservation property of the LSM could be improved by applying a Particle Level-Set Method (cf. Enright *et al.*, 2002).

Currently, a fine mesh resolution has to be chosen wherever the calving front and grounding line may wander during the simulation, which may be a large fraction of the model domain for long-duration simulations. This causes unnecessarily high computational cost, which could be reduced by automatic remeshing routines (e.g. Babuška & Guo, 1992), that refine a coarse sub-mesh selectively over time. This would allow for longer simulations and higher overall numerical precision in regions where it matters.

Finally, Jakobshavn Isbræ's long-term evolution is controlled by its climatic setting. Therefore, reliable projections require the coupling of the ice flow model to a climate and an ocean circulation model. Since the stabilizing ice tongue is highly sensitive to submarine melting rates, higher priority should be given to coupling with an ocean model, such as the MITgcm (Marshall *et al.*, 1997) and AWI's FESOM (Wang *et al.*, 2014).

8 Conclusions

8.1 Achievements

The aim of this thesis is to study the dynamic changes of Jakobshavn Isbræ before, during and after the disintegration of its ice tongue between 1998 and 2004 using the Ice Sheet System Model (ISSM, Larour *et al.*, 2012a), in order to determine the thermodynamic processes that cause and sustain the glacier’s observed widespread flow acceleration and thinning. We assess the current scientific understanding of the dynamics of Jakobshavn Isbræ in a literature review (Chap. 2). Remaining open questions about Jakobshavn Isbræ’s thermodynamics are formulated in Sect. 2.5. ISSM’s usability to answer these questions is evaluated in Sect. 2.6, which identifies two crucial missing model features in ISSM, that had to be added during this doctoral thesis. We state the objectives of the thesis in Sect. 2.7, and describe the required fundamentals of Level-Set Methods and continuum mechanics applied to ice sheet modelling in Chap. 3.

The first objective is to implement the two missing model features into ISSM. The first missing feature is the complete implementation of the energy-conserving enthalpy method (Aschwanden *et al.*, 2012), which had only been partially implemented so far (Seroussi *et al.*, 2013). Jakobshavn Isbræ has a polythermal regime (Iken *et al.*, 1993; Lüthi *et al.*, 2002), and the thermal regime has a strong influence on the ice viscosity parameter (Sect. 3.3.2). The task included the implementation and maintenance of the dynamic basal boundary condition scheme for both transient (Fig. 3.4) and steady-state simulations (Sect. 6.7.1), a rheology law that includes the microscopic water content of temperate ice (Lliboutry & Duval, 1985), as well as the sub-element scale treatment of the heat conductivity discontinuity (Patankar, 1980) in finite elements that are intersected by the cold-temperate transition surface (CTS). Testing and verification of the method resulted in the publication “*Enthalpy benchmark experiments for numerical ice sheet models*” (Kleiner *et al.*, 2015), Chap. 4. ISSM is able to perform the numerical tests proposed in the paper successfully, and analytical solutions are matched for high resolutions. For lower vertical resolution, the ISSM solution shows a non-negligible difference to the analytical solution although the analytical CTS position is met.

The second missing feature is the model’s ability for dynamic calving front evolution. Observations indicate that the calving front position is a major control on the dynamics of Jakobshavn Isbræ (Chap. 2). Therefore, we design and implement a Level-Set Method (LSM, Osher & Sethian, 1988) for dynamic calving front evolution in ISSM. Verification of the LSM and its applicability to large-scale outlet glaciers is shown in the publication “*Modelling calving front dynamics using a level-set method: application to Jakobshavn Isbræ, West Greenland*” (Bondzio *et al.*, 2016), Chap. 5. The LSM is an important step towards a more process-based modelling of the dynamics of glaciers. It provides a powerful and flexible framework to dynamically

evolve the calving front position in ice flow models, and to apply arbitrary user-defined calving rates to a real-world glacier model, as shown for example in Morlighem *et al.* (2016).

We achieve the second objective of this thesis by creating a functioning, 3D, high-resolution, fully thermodynamically coupled model of Jakobshavn Isbræ using ISSM. The model computes ice velocities using the higher-order model (HOM, Sect. 3.3.2), and derives the thermal regime using the completed enthalpy method. The model is calibrated using state-of-the-art glacier data products, and matches observations well (Sect. 6.7.1).

We address the third objective by applying the array of created methods to the model of Jakobshavn Isbræ, and by performing a transient numerical modelling study of the glacier's thermodynamic response to the calving front retreat that started in 1998. In the absence of a reliable calving rate parametrisation, we compile a record of over 500 calving front positions from satellite imagery over the simulation time span from January 1st, 1985 until December 31st, 2015. We prescribe the observed calving front positions in the model using the LSM. The model captures the exact timing and about 80 to 90% of the observed widespread acceleration, as well as the observed mass loss. The degree of reproduction of the observations by the model is unmatched in today's publication history. We achieve the fourth objective by assessing and discussing the mechanisms that sustain the acceleration of Jakobshavn Isbræ in the publication "*The mechanisms behind Jakobshavn Isbræ's acceleration and mass loss: a thermodynamically coupled model study*", Chap. 6, which we submitted to the journal *Geophysical Research Letters*.

8.2 Thermodynamics of Jakobshavn Isbræ

The next two sections address the open questions formulated in Sect. 2.5. The questions (Q1,Q2,...) are repeated for convenience.

8.2.1 Overview

Q1: What are the 3D thermal and stress regime of Jakobshavn Isbræ, in particular in areas of fast flow?

The deep trough under Jakobshavn Isbræ, which reaches several hundred kilometres inland, is crucial for both the thermal regime and the stress regime of the glacier. Jakobshavn Isbræ's driving stress is balanced by basal drag, and it needs to be distributed to adjacent areas through lateral stress transfer in case basal drag is low. This holds in particular for the last 50 km of the ice stream in the trough, so that the low ice viscosity in the shear margins allows for high flow velocities. Basal sliding contributes more than 50% to the overall ice motion over wide areas of the drainage basin, and up to 100% in the last 30 km of the ice stream. We are not able to study the physical processes causing the basal drag distribution using our model.

Jakobshavn Isbræ's polythermal regime is advection-dominated, and the measured strong temperature inversion is characteristic for most of Jakobshavn Isbræ, with exception for the last 25 km of the ice stream, where the

temperature inversion vanishes due to intense strain heating. The ice gradually warms along-flow through englacial strain heating and subglacial heating caused by basal friction and geothermal heat flux. Jakobshavn Isbræ's ice base is temperate on the last 200 to 300 km before the calving front. A basal temperate layer of several tens of metres up to 400 m thickness forms in regions of high englacial deformation. The microscopic water content in temperate ice exceeds the critical value of 1%, for which no material law is currently known at many locations.

Jakobshavn Isbræ's mass loss is dominated by calving and the glacier was likely in slight negative negative imbalance already prior to the disintegration of the ice tongue, losing about 2.5 to 5.5 Gt of ice per year. Lateral inflow of ice replenishes the ice stream and allows Jakobshavn Isbræ to maintain a stable grounding line position despite high submarine melting rates.

8.2.2 After the Ice Tongue's Disintegration

Q2: How did the changes in the glacier's stress regime since the disintegration of the ice tongue affect the glacier's thermal regime, and vice versa?

Calving front retreat in the model causes widespread inland acceleration and mass loss, which are in good agreement with observations. Dynamic thinning decreases buttressing to upstream regions, and increases the driving stress in the ice stream and its surroundings. The ice temperature changes in bands along-flow due to advection from ice from upstream. Enhanced strain rates after the disintegration of the floating ice tongue warm the shear margins by up to 4.3 °C. Enhanced basal sliding and englacial shear warms the ice base and increases subglacial melting rates by 45%.

Q3: Which processes enable and sustain the glacier's acceleration?

The calving front position is currently the main control on the dynamics of the ice stream since the ice viscosity drops instantaneously in response to a stress perturbation caused by calving front retreat, which allows for faster flow. The effect of this material response plays out most pronouncedly in the ice stream's shear margins, through which most of the ice stream's driving stress is transferred to the trough walls. This effect is able to trigger widespread inland flow acceleration and dynamic thinning since the trough reaches far inland and basal drag in the trough is low. Geometrical adjustment to the ice stream thinning spreads the viscosity drop to the areas adjacent to the trough. Ice warming through enhanced strain rates contributes 5 to 10% to the total acceleration by softening the ice. Deep troughs with similar stress regimes are a common feature for many marine-terminating outlet glaciers of the GrIS (Morlighem *et al.*, 2014b; Shapero *et al.*, 2016), to whom these mechanisms are likely to apply too. We conclude that the interplay of the migrating calving front, the shear margins and the thermal regime is important to account for in projections of future eustatic sea level rise.

8.3 Outlook

8.3.1 Jakobshavn Isbræ's Future Evolution

Q4: Which mechanisms would help the glacier stabilise, and how much ice will the glacier have lost until then?

Jakobshavn Isbræ's floating ice tongue has a critical stabilising function for the ice stream, and glacier stabilisation is only expected once a new ice tongue forms. However, incomplete understanding of the ice tongue's dynamics, the absence of a suitable calving rate parametrisation and the high sensitivity of the glacier to error-prone model input data like the bed topography near the grounding line challenge reliable projections of the glacier's future development. The deep trough will keep Jakobshavn Isbræ sensitive to oceanic forcing for the foreseeable future, and the lack of a basal feature in the trough that would allow for grounding line stabilisation suggests that the ice stream currently sustains the conditions for continued retreat. Therefore, we expect that the glacier will continue to contribute to eustatic sea level rise for at least the next several decades at a rate comparable or higher than 0.1 mm a^{-1} .

We propose a new hypothesis for Jakobshavn Isbræ's behaviour while it is in negative mass balance, which better explains observations of strong intermittent thinning in the past. The glacier cycles through three phases of 1) gradual mass loss and ice tongue thinning, 2) strong mass loss triggered by ice tongue disintegration, and 3) formation of a stabilizing ice tongue once the calving front has retreated sufficiently into thick inland ice. We are not able to test the hypothesis here due to model limitations, e.g. the lack of a calving rate parametrization.

8.3.2 Fields of Further Study

We achieve the fifth and last objective of this thesis by identifying fields where further study is required (Sect. 7.4). Future work on modelling Jakobshavn Isbræ should focus on closing the gap between model results and observations through enhanced understanding of the glacier's dynamics, in order to produce more reliable projections of the glacier's future behaviour in a warming climate. Fulfilling this aim demands for an integrated approach that combines observations, numerical modelling, and theoretical considerations.

An improved material law for ice under high shear stress or with microscopic water content higher than 1% is desirable to close the gap between model results and observations. Improved understanding of the transport of microscopic water content in temperate ice is important for model estimates on temperate layer thickness. The data assimilation technique applied here to derive the basal drag provides little information about the physical processes contributing to basal sliding. Accounting for the basal thermal state during the data assimilation technique and applying transient data assimilation techniques based on automatic differentiation will further our understanding of basal processes. Different basal sliding laws should be tested to assess their ability to improve the fit between observations and model results.

Ice-sheet wide monitoring of important model input data sets like ice flow velocities, glacier geometry and glacier mass balance is required for model calibration and should be continued. As the calving front position controls Jakobshavn Isbræ's behaviour, reliable projections of the glacier's future development are only possible if a calving rate parametrisation suitable for large-scale ice sheet models becomes available. Emergence of such a parametrisation depends on better understanding of the dynamics of Jakobshavn Isbræ's floating ice tongue and its interaction with the ocean, and requires continuous monitoring of the glacier.

We suggest to improve the implementation of the LSM in ISSM by sub-mesh scale application of the boundary conditions at the calving front, and by improving its volume-preservation property by applying a Particle Level-Set Method. The application of automatic remeshing routines will help to cut the computational cost of long prognostic simulations. Finally, since Jakobshavn Isbræ's long-term evolution is controlled by its climatic setting, reliable projections of the glacier's future behaviour will require to couple ISSM to a climate and an ocean circulation model.

Acknowledgements

A rice seedling requires sunlight, soil, space, moisture and warmth as necessary conditions for growth. Likewise, I am very fortunate that numerous precious conditions for my personal development in general and this project in particular have been met, for which I am deeply thankful.

The Three Jewels and my Dharma teachers are the sunlight, who illuminate space, provide orientation and make all existence meaningful. I'd like to express my limitless gratitude in particular to the Karmapa and Lama Ole Nydahl. May I be a worthy vessel for your teachings.

My supervisor Angelika and her team is the soil in which this PhD-project rooted. She allowed me to study the fascinating subject of ice, provided much-needed critical feedback, and enabled me to make this humble contribution to the solution of the challenges of our time. Furthermore, without the invaluable help of Martin and Thomas my transition into the field of glaciology would have never been as smooth as it was. Similarly, many thanks to the members of my PhD-panel for their time and guidance: Peter Lemke, Sergey Danilov, Katharina Klein and again Angelika, Martin and Thomas, as well as to my second thesis reviewer, Prof. Dr. Gerrit Lohmann.

The ISSM team is the space in which this project thrived. Without question, Hélène and Mathieu deserve special mention for their untiring and patient support basically from day one onwards. Many thanks to Eric L. for inviting me for an crucial internship to the Jet Propulsion Laboratory in spring 2014, as well as to Mathieu for funding the last year of writing my thesis. Without you guys this project would have never taken off as swiftly as it did.

The moisture was provided by my many friends and colleagues from all over the world, too many to be named here individually. However, Lesley, Karin, Michael, the Diamond Way Sangha, the AWI and UCI glaciology teams and many others: rest assured that I deeply appreciate our inspiring connection. Moreover, I'd like to thank my peers in the 2014/2015 AWI DokTeam for their patience with me, as well as the Claudias from AWI's POLMAR program, who are instrumental in order to make the life of PhD students at AWI as rewarding as it is.

The ice sheets prove it: without warmth there is no growth. Therefore, last but not least, I'd like to express my deepest love and gratitude towards my family: My radiant mother, Petra, whose love and joy illuminates space like the sun on a clear sky. My late father, Hans-Peter, who through love and warmth taught me to value hard work and respect for all living beings. My brothers, each one unique, and each whom I love just beyond words.

Countless thanks to all of you, and those that I forgot: without you this project and I wouldn't be as fortunate as they are today.

Bibliography

1. Alley, R., Horgan, H., Joughin, I., Cuffey, K., Dupont, T., Parizek, B., Anandakrishnan, S. & Bassis, J. A Simple Law for Ice-Shelf Calving. *Science* **322**, 1344 (2008).
2. Amestoy, P. R., Duff, I. S., Koster, J. & L'Excellent, J.-Y. A Fully Asynchronous Multifrontal Solver Using Distributed Dynamic Scheduling. *SIAM J. Matrix Anal. Appl.* **23**, 15–41 (2001).
3. Amestoy, P. R., Guermouche, A., L'Excellent, J.-Y. & Pralet, S. Hybrid scheduling for the parallel solution of linear systems. *Parallel Computing* **32**, 136–156 (2006).
4. Amundson, J. M., Fahnestock, M., Truffer, M., Brown, J., Lüthi, M. P. & Motyka, R. J. Ice mélange dynamics and implications for terminus stability, Jakobshavn Isbræ, Greenland. *J. Geophys. Res. - Earth Surface* **115**. F01005. ISSN: 2156-2202. doi:10.1029/2009JF001405. <http://dx.doi.org/10.1029/2009JF001405> (2010).
5. Aschwanden, A. & Blatter, H. Mathematical modeling and numerical simulation of polythermal glaciers. English. *J. Geophys. Res.* **114**, 1–10. ISSN: 0148-0227 (2009).
6. Aschwanden, A., Bueler, E., Khroulev, C. & Blatter, H. An enthalpy formulation for glaciers and ice sheets. *J. Glaciol.* **58**, 441–457 (2012).
7. Astrom, J. A., Vallot, D., Schafer, M., Welty, E. Z., O'Neel, S., Bartholomaeus, T. C., Liu, Y., Riikila, T. I., Zwinger, T., Timonen, J. & Moore, J. C. Termini of calving glaciers as self-organized critical systems. *Nat. Geosci.* **7**, 874–878. ISSN: 1752-0894 (2014).
8. Babuška, I. & Guo, B. The h, p and h-p version of the finite element method; basis theory and applications. *Adv. Eng. Software* **15**, 159–174. ISSN: 0965-9978 (1992).
9. Balay, S., Gropp, W. D., McInnes, L. C. & Smith, B. F. *Efficient Management of Parallelism in Object Oriented Numerical Software Libraries in Modern Software Tools in Scientific Computing* (eds Arge, E., Bruaset, A. M. & Langtangen, H. P.) (Birkhäuser Press, 1997), 163–202.
10. Balay, S., Buschelman, K., Eijkhout, V., Gropp, W. D., Kaushik, D., Knepley, M. G., McInnes, L. C., Smith, B. F. & Zhang, H. *PETSc Users Manual* tech. rep. ANL-95/11 - Revision 3.0.0 (Argonne National Laboratory, 2008).
11. Balay, S., Buschelman, K., Gropp, W. D., Kaushik, D., Knepley, M. G., McInnes, L. C., Smith, B. F. & Zhang, H. *PETSc Website* <http://www.mcs.anl.gov/petsc>. 2009.
12. Bamber, J. L., Griggs, J. A., Hurkmans, R. T.W. L., Dowdeswell, J. A., Gogineni, S. P., Howat, I., Mouginot, J., Paden, J., Palmer, S., Rignot, E. & Steinhage, D. A new bed elevation dataset for Greenland. *Cryosphere* **7**, 499–510 (2013).

13. Bassis, J. N. The statistical physics of iceberg calving and the emergence of universal calving laws. English. *J. Glaciol.* **57**, 3–16. ISSN: 0022-1430 (2011).
14. Bauer, A. Missions aeriennes de reconnaissance au Groenland 1957-1958; observations aeriennes et terrestres, exploitation des photographies aeriennes, determination des vitesses des glaciers velant dans Disko Bugt et Umanak Fjord. *Medd. om Grønland* **173** (1968).
15. Benn, D. I., Warren, C. R. & Mottram, R. H. Calving processes and the dynamics of calving glaciers. English. *Earth Sci. Rev.* **82**, 143–179. ISSN: 0012-8252 (2007).
16. Bindschadler, R. Actively surging West Antarctic ice streams and their response characteristics. *Ann. Glaciol. ANNALS OF GLACIOLOGY* **24** (ed Whillans, IM) International Symposium on Changing Glaciers, Fjaerland, Norway, Jun 24-27, 1996, 409–414. ISSN: 0260-3055 (1997).
17. Bindschadler, R. A. Jakobshavn Glacier Drainage Basin: A Balance Assessment. *J. Geophys. Res.* **89**, 2066–2072 (1984).
18. Blatter, H. Velocity And Stress-Fields In Grounded Glaciers: A Simple Algorithm For Including Deviatoric Stress Gradients. English. *J. Glaciol.* **41**, 333–344. ISSN: 0022-1430 (1995).
19. Blatter, H & Hutter, K. Polythermal Conditions in Arctic Glaciers. *J. Glaciol.* **37**, 261–269. ISSN: 0022-1430 (1991).
20. Blatter, H. & Greve, R. Comparison and verification of enthalpy schemes for polythermal glaciers and ice sheets with a one-dimensional model. *Polar Science* **9**, 196–207. ISSN: 1873-9652 (2015).
21. Bondzio, J. H., Seroussi, H., Morlighem, M., Kleiner, T., Rückamp, M., Humbert, A. & Larour, E. Modelling calving front dynamics using a level-set method: application to Jakobshavn Isbræ, West Greenland. *The Cryosphere* **10**, 497–510 (2016).
22. Borstad, C. P., Khazendar, A., Larour, E., Morlighem, M., Rignot, E., Schodlok, M. P. & Seroussi, H. A damage mechanics assessment of the Larsen B ice shelf prior to collapse: Toward a physically-based calving law. *Geophys. Res. Lett.* **39**, 1–5. ISSN: 0094-8276 (2012).
23. Bradford, J. & Harper, J. Wave field migration as a tool for estimating spatially continuous radar velocity and water content in glaciers. *Geophys. Res. Lett.* **32**. ISSN: 0094-8276. doi:{10.1029/2004GL021770} (2005).
24. Brenner, S. & Scott, R. *The Mathematical Theory of Finite Element Methods* (Springer Science & Business Media, 2007).
25. Brown, C., Meier, M. & Post, A. Calving speed of Alaska tidewater Glaciers, with application to Columbia Glacier, Alaska. *U.S. Geological Survey Professional Paper*, 1258–C. 13pp. ISSN: 10449612 (1982).
26. Brown, J., Harper, J. & Humphrey, N. Liquid water content in ice estimated through a full-depth ground radar profile and borehole measurements in western Greenland. *The Cryosphere* **11**, 669–679 (2017).
27. Budd, W., Jenssen, D & Smith, I. A three-dimensional time-dependent model of the West Antarctic ice-sheet. English. *Ann. Glaciol.* **5**, 29–36. ISSN: 0260-3055 (1984).

28. Bueler, E. & Brown, J. Shallow shelf approximation as a “sliding law” in a thermomechanically coupled ice sheet model. English. *J. Geophys. Res.* **114**, 1–21. ISSN: 0148-0227 (2009).
29. Bueler, E., Lingle, C., Kallen-Brown, J., Covey, D. & Bowman, L. Exact solutions and verification of numerical models for isothermal ice sheets. English. *J. Glaciol.* **51**, 291–306. ISSN: 0022-1430 (2005).
30. Bueler, E., Brown, J. & Lingle, C. Exact solutions to the thermomechanically coupled shallow-ice approximation: effective tools for verification. English. *J. Glaciol.* **53**, 499–516. ISSN: 0022-1430 (2007).
31. Burger, M. *Mathematische Modellierung* lecture script. 2007. <http://www.math.uni-muenster.de/u/burger/>.
32. Cassotto, R., Fahnestock, M., Amundson, J. M., Truffer, M. & Joughin, I. Seasonal and interannual variations in ice mélange and its impact on terminus stability, Jakobshavn Isbræ, Greenland. *J. Glaciol.* **61**, 76–88. ISSN: 0022-1430 (2015).
33. Chang, Y., Hou, T., Merriman, B. & Osher, S. A level set formulation of eulerian interface capturing methods for incompressible fluid flows. *J. Comput. Phys.* **124**, 449–464. ISSN: 0021-9991 (1996).
34. Courant, R., Friedrichs, K. & Lewy, H. Über die partiellen Differenzengleichungen der mathematischen Physik. *Mathematische Annalen* **100**, 32–74 (1928).
35. Csatho, B., Schenk, T., Van Der Veen, C. J. & Krabill, W. B. Intermittent thinning of Jakobshavn Isbræ, West Greenland, since the Little Ice Age. English. *J. Glaciol.* **54**, 131–144. ISSN: 0022-1430 (2008).
36. Cuffey, K. & Paterson, W. S. B. *The Physics of Glaciers, 4th Edition* (ed Butterworth-Heinemann) (Elsevier, Oxford, 2010).
37. Dietrich, R., Maas, H.-G., Baessler, M., Ruelke, A., Richter, A., Schwalbe, E. & Westfeld, P. Jakobshavn Isbræ, West Greenland: Flow velocities and tidal interaction of the front area from 2004 field observations. English. *J. Geophys. Res.* **112**, 1–16. ISSN: 0148-0227 (2007).
38. Donea, J. & Huerta, A. *Finite Element Methods for Flow Problems* (John Wiley & Sons, Chichester, UK, 2003).
39. Dubin, D. *Numerical and analytical methods for scientists and engineers using Mathematica* (Wiley, Hoboken, New Jersey, 2003).
40. Duval, P. *The role of the water content on the creep rate of poly-crystalline ice in Symposium on Isotopes and Impurities in Snow and Ice* **118** (Grenoble, 1977), 29–33.
41. Echelmeyer, K. & Harrison, W. Jakobshavns Isbræ, West Greenland - Seasonal variations in velocity or lack thereof. English. *J. Glaciol.* **36**, 82–88. ISSN: 0022-1430 (1990).
42. Echelmeyer, K., Clarke, T. & Harrison, W. Surficial glaciology of Jakobshavns Isbræ, West Greenland: Part I. Surface morphology. *J. Glaciol.* **37**, 368–382. ISSN: 0022-1430 (1991).
43. Echelmeyer, K., Harrison, W., Clarke, T. & Benson, C. Surficial glaciology of Jakobshavns Isbræ, West Greenland: Part II. Ablation, accumulation and temperature. *J. Glaciol.* **38**, 169–181. ISSN: 0022-1430 (1992).

44. Enderlin, E. M., Howat, I. M. & Vieli, A. High sensitivity of tidewater outlet glacier dynamics to shape. *Cryosphere* **7**, 1007–1015. ISSN: 1994-0424 (2013).
45. Enderlin, E. M. & Howat, I. M. Submarine melt rate estimates for floating termini of Greenland outlet glaciers (2000–2010). *J. Glaciol.* **59**, 67–75. ISSN: 0022-1430 (2013).
46. Enright, D, Fedkiw, R, Ferziger, J & Mitchell, I. A hybrid particle level set method for improved interface capturing. *Journal of Computational Physics* **183**, 83–116. ISSN: 0021-9991 (2002).
47. Ettema, J., van den Broeke, M. R., van Meijgaard, E., van de Berg, W. J., Bamber, J. L., Box, J. E. & Bales, R. C. Higher surface mass balance of the Greenland Ice Sheet revealed by high-resolution climate modeling. English. *Geophys. Res. Lett.* **36**, 1–5. ISSN: 0094-8276 (2009).
48. Favier, L., Durand, G., Cornford, S. L., Gudmundsson, G. H., Gagliardini, O., Gillet-Chaulet, F., Zwinger, T., Payne, A. J. & Le Brocq, A. Retreat of Pine Island Glacier controlled by marine ice-sheet instability. *Nat. Clim. Change* **4**, 117–121 (2014).
49. Fowler, A. C. On the Transport of Moisture in Polythermal Glaciers. *Geophysical and Astrophysical Fluid Dynamics* **28**, 99–140. ISSN: 0309-1929 (1984).
50. Funk, M, Echelmeyer, K & Iken, A. Mechanisms of fast flow in Jakobshavns Isbræ, West Greenland: Part 2. Modeling of englacial temperatures. *J. Glaciol.* **40**, 569–585. ISSN: 0022-1430 (1994).
51. Gagliardini, O., Zwinger, T., Gillet-Chaulet, F., Durand, G., Favier, L., de Fleurian, B., Greve, R., Malinen, M., Martín, C., Råback, P., Ruokolainen, J., Sacchetti, M., Schäfer, M., Seddik, H. & Thies, J. Capabilities and performance of Emer/Ice, a new-generation ice sheet model. *Geosci. Model Dev.* **6**, 1299–1318 (2013).
52. Georgi, J. Der Rückgang des Jakobshavns Isbrae (Westgrönland 69 N). *Medd. om Grønland* **158**, 55–70 (1959).
53. Gillet-Chaulet, F, Gagliardini, O, Meyssonier, J, Montagnat, M & Castelnau, O. A user-friendly anisotropic flow law for ice-sheet modelling. English. *J. Glaciol.* **51**, 3–14. ISSN: 0022-1430 (2005).
54. Gillet-Chaulet, F., Durand, G., Gagliardini, O., Mosbeux, C., Mouginot, J., Remy, F. & Ritz, C. Assimilation of surface velocities acquired between 1996 and 2010 to constrain the form of the basal friction law under Pine Island Glacier. *Geophys. Res. Lett.* **43**, 10311–10321. ISSN: 0094-8276 (2016).
55. Gladish, C. V., Holland, D. M., Rosing-Asvid, A., Behrens, J. W. & Boje, J. Oceanic Boundary Conditions for Jakobshavn Glacier. Part I: Variability and Renewal of Ilulissat Icefjord Waters, 2001–14. *J. Phys. Oceanogr.* **45**, 3–32. ISSN: 0022-3670 (2015).
56. Glen, J. The creep of polycrystalline ice. English. *Proc. R. Soc. A* **228**, 519–538 (1955).

57. Gogineni, S., Yan, J. B., Paden, J., Leuschen, C., Li, J., Rodriguez-Morales, F., Braaten, D., Purdon, K., Wang, Z., Liu, W. & Gauch, J. Bed topography of Jakobshavn Isbrae, Greenland, and Byrd Glacier, Antarctica. English. *J. Glaciol.* **60**, 813–833. ISSN: 0022-1430 (2014).
58. Greve, R. A continuum-mechanical formulation for shallow polythermal ice sheets. English. *Phil. Trans R. Soc. A* **355**, 921–974 (1997).
59. Greve, R. Application of a polythermal three-dimensional ice sheet model to the Greenland Ice Sheet: Response to steady-state and transient climate scenarios. English. *J. Clim.* **10**, 901–918. ISSN: 0894-8755 (1997).
60. Greve, R. & Blatter, H. *Dynamics of Ice Sheets and Glaciers* 1–287. ISBN: 978-3-642-03414-5. doi:{10.1007/978-3-642-03415-2} (Springer Science & Business Media, 2009).
61. Gropp, W., Lusk, E., Doss, N. & Skjellum, A. A high-performance, portable implementation of the MPI message passing interface standard. *Parallel Computing* **22**, 789–828 (Sept. 1996).
62. Gropp, W. D. & Lusk, E. *User's Guide for mpich, a Portable Implementation of MPI* ANL-96/6. Mathematics and Computer Science Division, Argonne National Laboratory (1996).
63. Groß, S., Reichelt, V. & Reusken, A. A finite element based level set method for two-phase incompressible flows. *Computing and visualization in science, Springer* **9**, 239–257 (2006).
64. Gudmundsson, G. H., Krug, J., Durand, G., Favier, L. & Gagliardini, O. The stability of grounding lines on retrograde slopes. *Cryosphere* **6**, 1497–1505. ISSN: 1994-0424 (2012).
65. Habermann, M., Truffer, M. & Maxwell, D. Changing basal conditions during the speed-up of Jakobshavn Isbræ, Greenland. *Cryosphere* **7**, 1679–1692. ISSN: 1994-0424 (2013).
66. Helm, V., Humbert, A. & Miller, H. Elevation and elevation change of Greenland and Antarctica derived from CryoSat-2. *Cryosphere* **8**, 1539–1559. ISSN: 1994-0424 (2014).
67. Hewitt, I. J. & Schoof, C. Models for polythermal ice sheets and glaciers. *The Cryosphere* **11**, 541–551 (2017).
68. Hindmarsh, A., Brown, P., Grant, K., Lee, S., Serban, R., Shumaker, D. & Woodward, C. SUNDIALS: Suite of nonlinear and differential/algebraic equation solvers. *ACM Transactions of Mathematical Software* **31**, 363–396. ISSN: 0098-3500 (2005).
69. Holland, D. & Jenkins, A. Modeling thermodynamic ice-ocean interactions at the base of an ice shelf. English. *J. Phys. Oceanogr.* **29**, 1787–1800. ISSN: 0022-3670 (1999).
70. Holland, D., Thomas, R., De Young, B., Ribergaard, M. & Lyberth, B. Acceleration of Jakobshavn Isbrae triggered by warm subsurface ocean waters. English. *Nat. Geosci.* **1**, 659–664. ISSN: 1752-0894 (2008).
71. Hooke, R. L. *Principles of Glacier Mechanics* 2nd (ed Press, C. U.) 763 (Cambridge, 2005).

72. Howat, I. M., Negrete, A. & Smith, B. E. The Greenland Ice Mapping Project (GIMP) land classification and surface elevation datasets. English. *Cryosphere* **8**, 1509–1518. ISSN: 1994-0416 (2014).
73. Howat, I. *MEaSURES Greenland Ice Velocity: Selected Glacier Site Velocity Maps from Optical Images, Version 1. Subset W69.10N*. NASA National Snow and Ice Data Center Distributed Active Archive Center, Boulder, Colorado USA. <http://nsidc.org/data/nsidc-0646>.
74. Howat, I. M., Ahn, Y., Joughin, I., van den Broeke, M. R., Lenaerts, J. T. M. & Smith, B. Mass balance of Greenland's three largest outlet glaciers, 2000-2010. English. *Geophys. Res. Lett.* **38**, 1–5. ISSN: 0094-8276 (2011).
75. Humbert, A. Vulnerable ice in the Weddell Sea. *Nat. Geosci.* (2012).
76. Humbert, A. & Steinhage, D. The evolution of the western rift area of the Fimbul Ice Shelf, Antarctica. *Cryosphere* **5**, 931–944. ISSN: 1994-0424 (Oct. 2011).
77. Hurkmans, R. T.W. L., Bamber, J. L., Sorensen, L. S., Joughin, I. R., Davis, C. H. & Krabill, W. B. Spatiotemporal interpolation of elevation changes derived from satellite altimetry for Jakobshavn Isbræ, Greenland. *J. Geophys. Res.* **117**. ISSN: 2169-9003. doi:{10 . 1029 / 2011JF002072} (2012).
78. Hutter, K., Blatter, H & Funk, M. A Model Computation of Moisture-Content in Polythermal Glaciers. *Journal of Geophysical Research* **93**, 12205–12214. ISSN: 0148-0227 (1988).
79. Hutter, K. *Theoretical glaciology: material science of ice and the mechanics of glaciers and ice sheets* (ed Tokyo, T. S.P. C.) 150 (D. Reidel Publishing Co, Dordrecht, The Netherlands, 1983).
80. Huybrechts, P., Payne, A. & the EISMINT Intercomparison Group. The EISMINT benchmarks for testing ice-sheet models. *Ann. Glaciol.* **23**, 1–14 (1996).
81. Huybrechts, P., Letreguilly, A. & Reeh, N. The Greenland ice sheet and greenhouse warming. *Glob. Planet. Change* **3**, 399–412 (1991).
82. Iken, A., Echelmeyer, K., Harrison, W & Funk, M. Mechanisms of fast flow in Jakobshavns-Isbræ, West Greenland: Part I. Measurements of temperature and water-level in deep boreholes. English. *J. Glaciol.* **39**, 15–25. ISSN: 0022-1430 (1993).
83. IPCC-AR4. *Fourth Assessment Report: Climate Change 2007: The AR4 Synthesis Report* <http://www.ipcc.ch/ipccreports/ar4-wg1.htm> (Geneva: IPCC, 2007).
84. IPCC-AR5. *Climate Change 2013: The Physical Science Basis. Contribution of Working Group I to the Fifth Assessment Report of the Intergovernmental Panel on Climate Change* 1535. ISBN: ISBN 978-1-107-66182-0. doi:10 . 1017/CBO9781107415324. www.climatechange2013.org (Cambridge University Press, Cambridge, United Kingdom and New York, NY, USA, 2013).

85. Jenkins, A. Convection-Driven Melting near the Grounding Lines of Ice Shelves and Tidewater Glaciers. *J. Phys. Oceanogr.* doi:10.1175/JPO-D-11-03.1 (2011).
86. Johnson, J., Prescott, P. & Hughes, T. Ice dynamics preceding catastrophic disintegration of the floating part of Jakobshavn Isbræ, Greenland. *J. Glaciol.* **50**, 492–504. ISSN: 0022-1430 (2004).
87. Joughin, I., Smith, B. E., Shean, D. E. & Floricioiu, D. Brief Communication: Further summer speedup of Jakobshavn Isbræ. *The Cryosphere* **8**, 209–214. ISSN: 1994-0416 (2014).
88. Joughin, I., Abdalati, W. & Fahnestock, M. Large fluctuations in speed on Greenland's Jakobshavn Isbrae glacier. English. *Nature* **432**, 608–610. ISSN: 0028-0836 (2004).
89. Joughin, I., Howat, I. M., Fahnestock, M., Smith, B., Krabill, W., Alley, R. B., Stern, H. & Truffer, M. Continued evolution of Jakobshavn Isbrae following its rapid speedup. *J. Geophys. Res.* **113**. ISSN: 0148-0227. doi:{10.1029/2008JF001023} (2008).
90. Joughin, I., Smith, B. E., Howat, I. M., Floricioiu, D., Alley, R. B., Truffer, M. & Fahnestock, M. Seasonal to decadal scale variations in the surface velocity of Jakobshavn Isbrae, Greenland: Observation and model-based analysis. English. *J. Geophys. Res.* **117**, 1–20. ISSN: 0148-0227 (2012).
91. Jouvett, G., Picasso, M., Rappaz, J. & Blatter, H. A new algorithm to simulate the dynamics of a glacier: theory and applications. *J. Glaciol.* **54**, 801–811. ISSN: 0022-1430 (2008).
92. Kernighan, B. W. *The C Programming Language* 2nd (ed Ritchie, D. M.) ISBN: 0131103709 (Prentice Hall Professional Technical Reference, 1988).
93. Kleiner, T., Rückamp, M., Bondzio, J. & Humbert, A. Enthalpy benchmark experiments for numerical ice sheet models. *Cryosphere* **9**, 217–228 (2015).
94. Kleiner, T. & Humbert, A. Numerical simulations of major ice streams in western Dronning Maud Land, Antarctica, under wet and dry basal conditions. *J. Glaciol.* **60**, 215–232. ISSN: 0022-1430 (2014).
95. Korsgaard, N. J., Nuth, C., Khan, S. A., Kjeldsen, K. K., Bjork, A. A., Schomacker, A. & Kjaer, K. H. Data Descriptor: Digital elevation model and orthophotographs of Greenland based on aerial photographs from 1978–1987. *Scientific Data* **3**. ISSN: 2052-4463. doi:{10.1038/sdata.2016.32} (2016).
96. Krabill, W., Hanna, E., Huybrechts, P., Abdalati, W., Cappelen, J., Csatho, B., Frederick, E., Manizade, S., Martin, C., Sonntag, J., Swift, R., Thomas, R. & Yungel, J. Greenland Ice Sheet: Increased coastal thinning. *Geophys. Res. Lett.* **31**, 1–4. ISSN: 0094-8276 (2004).
97. Krug, J., Weiss, J., Gagliardini, O. & Durand, G. Combining damage and fracture mechanics to model calving. *Cryosphere* **8**, 2101–2117. ISSN: 1994-0424 (2014).
98. Krug, J., Durand, G., Gagliardini, O. & Weiss, J. Modelling the impact of submarine frontal melting and ice melange on glacier dynamics. *The Cryosphere* **9**, 989–1003. ISSN: 1994-0416 (2015).

99. Lampkin, D. J., Amador, N., Parizek, B. R., Farness, K. & Jezek, K. Drainage from water-filled crevasses along the margins of Jakobshavn Isbræ: A potential catalyst for catchment expansion. *J. Geophys. Res.* **118**, 795–813. ISSN: 2169-9003 (2013).
100. Larour, E., Seroussi, H., Morlighem, M. & Rignot, E. Continental scale, high order, high spatial resolution, ice sheet modeling using the Ice Sheet System Model (ISSM). *J. Geophys. Res.* **117**, 1–20 (2012).
101. Larour, E., Morlighem, M., Seroussi, H., Schiermeier, J. & Rignot, E. Ice flow sensitivity to geothermal heat flux of Pine Island Glacier, Antarctica. English. *J. Geophys. Res. - Earth Surface* **117**, 1–12. ISSN: 0148-0227 (2012).
102. Larour, E., Utke, J., Csatho, B., Schenk, A., Seroussi, H., Morlighem, M., Rignot, E., Schlegel, N. & Khazendar, A. Inferred basal friction and surface mass balance of the Northeast Greenland Ice Stream using data assimilation of ICESat (Ice Cloud and land Elevation Satellite) surface altimetry and ISSM (Ice Sheet System Model). English. *Cryosphere* **8**, 2335–2351. ISSN: 1994-0416 (2014).
103. Liu, I.-S. *Continuum Mechanics* (Springer- Verlag, 2002).
104. Lliboutry, L. A. & Duval, P. Various isotropic and anisotropic ices found in glaciers and polar ice caps and their corresponding rheologies. *Ann. Geophys.-Italy* **3**, 207–224 (1985).
105. Luckman, A & Murray, T. Seasonal variation in velocity before retreat of Jakobshavn Isbræ, Greenland. *Geophys. Res. Lett.* **32**. ISSN: 0094-8276. doi:{10.1029/2005GL022519} (2005).
106. Lüthi, M, Funk, M, Iken, A, Gogineni, S & Truffer, M. Mechanisms of fast flow in Jakobshavn Isbrae, West Greenland: Part III. Measurements of ice deformation, temperature and cross-borehole conductivity in boreholes to the bedrock. English. *J. Glaciol.* **48**, 369–385. ISSN: 0022-1430 (2002).
107. Lüthi, M. P., Ryser, C., Andrews, L. C., Catania, G. A., Funk, M., Hawley, R. L., Hoffman, M. J. & Neumann, T. A. Heat sources within the Greenland Ice Sheet: dissipation, temperate paleo-firn and cryo-hydrologic warming. *The Cryosphere* **9**, 245–253. ISSN: 1994-0416 (2015).
108. Lüthi, M. P., Fahnestock, M. & Truffer, M. Calving icebergs indicate a thick layer of temperate ice at the base of Jakobshavn Isbræ, Greenland. *J. Glaciol.* **55**, 563–566. ISSN: 0022-1430 (2009).
109. Ma, Y., Gagliardini, O., Ritz, C., Gillet-Chaulet, F., Durand, G. & Montagnat, M. Enhancement factors for grounded ice and ice shelves inferred from an anisotropic ice-flow model. *J. Glaciol.* **56**, 805–812 (2010).
110. MacAyeal, D. Binge/Purge oscillations of the Laurentide ice-sheet as a cause of the North-Atlantic's Heinrich events. English. *Paleoceanography* **8**, 775–784. ISSN: 0883-8305 (1993).
111. MacAyeal, D. Large-scale ice flow over a viscous basal sediment: Theory and application to Ice Stream B, Antarctica. English. *J. Geophys. Res.* **94**, 4071–4087. ISSN: 0148-0227 (1989).

112. Marshall, J., Adcroft, A., Hill, C., Perelman, L. & Heisey, C. A finite-volume, incompressible Navier Stokes model for studies of the ocean on parallel computers. English. *J. Geophys. Res.* **102**, 5753–5766 (1997).
113. Minchew, B., Simons, M., Bjornsson, H., Palsson, F., Morlighem, M., Seroussi, H., Larour, E. & Hensley, S. Plastic bed beneath Hofsjökull Ice Cap, central Iceland, and the sensitivity of ice flow to surface melt-water flux. *J. Glaciol.* **62**, 147–158. ISSN: 1727-5652 (Mar. 2016).
114. Moes, N, Dolbow, J & Belytschko, T. A finite element method for crack growth without remeshing. *Int. J. Numer. Methods Eng.* **46**, 131–150. ISSN: 0029-5981 (1999).
115. Moon, T., Joughin, I., Smith, B. & Howat, I. 21st-Century Evolution of Greenland Outlet Glacier Velocities. English. *Science* **336**, 576–578. ISSN: 0036-8075 (2012).
116. Moon, T., Joughin, I., Smith, B., van den Broeke, M. R., van de Berg, W. J., Noel, B. & Usher, M. Distinct patterns of seasonal Greenland glacier velocity. English. *Geophys. Res. Lett.* **41**, 7209–7216. ISSN: 0094-8276 (2014).
117. Morland, L. & Zainuddin, R. Plane and radial ice-shelf flow with prescribed temperature profile. English. In Veen, C.J. van der, and Oerlemans, J., eds. *Dynamics of the West Antarctica Ice Sheet. Proceedings of a Workshop held in Utrecht, May 6-8, 1985.* Dordrecht, D. Reidel Publishing Company **117**, 117–140 (1987).
118. Morlighem, M., Rignot, E., Seroussi, H., Larour, E., Ben Dhia, H. & Aubry, D. A mass conservation approach for mapping glacier ice thickness. *Geophys. Res. Lett.* **38**, 1–6 (2011).
119. Morlighem, M., Rignot, E., Mouginot, J, Seroussi, H. & Larour, E. Deeply incised submarine glacial valleys beneath the Greenland Ice Sheet. English. *Nat. Geosci.* **7**, 418–422. ISSN: 1752-0894 (2014).
120. Morlighem, M., Rignot, E., Mouginot, J, Seroussi, H. & Larour, E. High-resolution ice thickness mapping in South Greenland. English. *Ann. Glaciol.* **55**, 64–70. ISSN: 0260-3055 (2014).
121. Morlighem, M., Bondzio, J., Seroussi, H., Rignot, E., Larour, E., Humbert, A. & Rebuffi, S.-A. Modeling of Store Gletscher’s calving dynamics, West Greenland, in response to ocean thermal forcing. *Geophys. Res. Lett.* **43**, 2659–2666. ISSN: 1944-8007 (2016).
122. Morlighem, M., Rignot, E., Seroussi, H., Larour, E., Ben Dhia, H. & Aubry, D. Spatial patterns of basal drag inferred using control methods from a full-Stokes and simpler models for Pine Island Glacier, West Antarctica. *Geophys. Res. Lett.* **37**, 1–6 (2010).
123. Motyka, R., L., H., K.A., E. & C., C. Submarine melting at the terminus of a temperate tidewater glacier, LeConte glacier, Alaska, U.S.A. *Ann. Glaciol.* **36**, 57–65 (2003).
124. Motyka, R. J., Truffer, M., Fahnestock, M., Mortensen, J., Rysgaard, S. & Howat, I. Submarine melting of the 1985 Jakobshavn Isbrae floating tongue and the triggering of the current retreat. English. *J. Geophys. Res.* **116**, 1–17. ISSN: 0148-0227 (2011).

125. Motyka, R. J., Fahnestock, M. & Truffer, M. Volume change of Jakobshavn Isbræ, West Greenland: 1985-1997-2007. *J. Glaciol.* **56**, 635–646. ISSN: 0022-1430 (2010).
126. Mouginot, J., Scheuchl, B. & Rignot, E. Mapping of Ice Motion in Antarctica Using Synthetic-Aperture Radar Data. *Remote Sens.* **4**, 2753–2767. ISSN: 2072-4292 (2012).
127. Muresan, I. S., Khan, S. A., Aschwanden, A., Khroulev, C., Van Dam, T., Bamber, J., van den Broeke, M. R., Wouters, B., Munneke, P. K. & Kjaer, K. H. Modelled glacier dynamics over the last quarter of a century at Jakobshavn Isbræ. *The Cryosphere* **10**, 597–611. ISSN: 1994-0416 (2016).
128. Nagler, T., Forsberg, R. & Engdahl, E. *Product User Guide (PUG) for the Greenland_Ice_Sheet_cci project of ESA's Climate Change Initiative, version 2.1* 19 March 2017 (2017).
129. Nick, F. M., van der Veen, C. J., Vieli, A. & Benn, D. I. A physically based calving model applied to marine outlet glaciers and implications for the glacier dynamics. English. *J. Glaciol.* **56**, 781–794. ISSN: 0022-1430 (2010).
130. Nick, F. M., Vieli, A., Andersen, M. L., Joughin, I., Payne, A., Edwards, T. L., Pattyn, F. & van de Wal, R. S. W. Future sea-level rise from Greenland's main outlet glaciers in a warming climate. *Nature* **497**, 235–238. ISSN: 0028-0836 (2013).
131. Nick, F. M., Vieli, A., Howat, I. M. & Joughin, I. Large-scale changes in Greenland outlet glacier dynamics triggered at the terminus. English. *Nat. Geosci.* **2**, 110–114. ISSN: 1752-0894 (2009).
132. Nocedal, J. & Wright, S. J. *Numerical Optimization, Second Edition* 1–664. ISBN: 978-0-387-40065-5. doi:{10.1007/978-0-387-40065-5} (Springer, 2006).
133. Noël, B., van de Berg, W. J., van Meijgaard, E., Munneke, P. K., van de Wal, R. S. W. & van den Broeke, M. R. Evaluation of the updated regional climate model RACMO2.3: summer snowfall impact on the Greenland Ice Sheet. *Cryosphere* **9**, 1831–1844. ISSN: 1994-0416 (2015).
134. Notz, D. & Worster, M. G. A one-dimensional enthalpy model of sea ice. *Annals of Glaciology* **44** (ed Langhorne, P and Squire, V) International Symposium on Sea Ice, Dunedin, New Zealand, Dec 05-09, 2005, 123–128. ISSN: 0260-3055 (2006).
135. Nowicki, S., Bindshadler, R., Abe-Ouchi, A., Aschwanden, A., Bueller, E., Choi, H., Fastook, J., Granzow, G., Greve, R., Gutowski, G., Herzfeld, U., Jackson, C., Johnson, J., Khroulev, C., Larour, E., Levermann, A., Lipscomb, W., Martin, M., Morlighem, M., Parizek, B., Pollard, D., Price, S., Ren, D., Rignot, E., Saito, F., Sato, T., Seddik, H., Seroussi, H., Takahashi, K., Walker, R. & Wang, W. Insights into spatial sensitivities of ice mass response to environmental change from the SeaRISE ice sheet modeling project I: Antarctica. *J. Geophys. Res.* **118**, 1–23 (2013).

136. Nowicki, S., Bindshadler, R., Abe-Ouchi, A., Aschwanden, A., Bueler, E., Choi, H., Fastook, J., Granzow, G., Greve, R., Gutowski, G., Herzfeld, U., Jackson, C., Johnson, J., Khroulev, C., Larour, E., Levermann, A., Lipscomb, W., Martin, M., Morlighem, M., Parizek, B., Pollard, D., Price, S., Ren, D., Rignot, E., Saito, F., Sato, T., Seddik, H., Seroussi, H., Takahashi, K., Walker, R. & Wang, W. Insights into spatial sensitivities of ice mass response to environmental change from the SeaRISE ice sheet modeling project II: Greenland. *J. Geophys. Res.* **118**, 1–20 (2013).
137. Nye, J. Response of a glacier to changes in rate of nourishment and wastage. *Proc. R. Soc. London, Ser. A* **275**, 87–112. ISSN: 0080-4630 (1963).
138. Nye, J. The distribution of stress and velocity in glaciers and ice-sheets. English. *Proc. R. Soc. A* **239**, 113–133 (1957).
139. Oreskes, N., Shraderfrechette, K & Belitz, K. Verification, Validation, and Confirmation of Numerical-Models in the Earth-Sciences. *Science* **263**, 641–646. ISSN: 0036-8075 (1994).
140. Osher, S. & Fedkiw, R. *Level set methods and dynamic implicit surfaces* (Springer Science & Business Media, 2006).
141. Osher, S. & Sethian, J. Fronts Propagating with Curvature-Dependent Speed - Algorithms Based on Hamilton-Jacobi Formulations. English. *J. Comput. Phys.* **79**, 12–49. ISSN: 0021-9991 (1988).
142. Pachauri, R. K., Allen, M. R., Barros, V. R., Broome, J., Cramer, W., Christ, R., Church, J. A., Clarke, L., Dahe, Q., Dasgupta, P., Dubash, N. K., Edenhofer, O., Elgizouli, I., Field, C. B., Forster, P., Friedlingstein, P., Fuglestad, J., Gomez-Echeverri, L., Hallegatte, S., Hegerl, G., Howden, M., Jiang, K., Jimenez Cisneros, B., Kattsov, V., Lee, H., Mach, K. J., Marotzke, J., Mastrandrea, M. D., Meyer, L., Minx, J., Mulugetta, Y., O'Brien, K., Oppenheimer, M., Pereira, J. J., Pichs-Madruga, R., Plattner, G. K., Pörtner, H.-O., Power, S. B., Preston, B., Ravindranath, N. H., Reisinger, A., Riahi, K., Rusticucci, M., Scholes, R., Seyboth, K., Sokona, Y., Stavins, R., Stocker, T. F., Tschakert, P., van Vuuren, D & van Ypserle, J. P. Climate Change 2014: Synthesis Report. Contribution of Working Groups I, II and III to the Fifth Assessment Report of the Intergovernmental Panel on Climate Change. *EPIC3Geneva, Switzerland, IPCC*, 151 p., pp. 151, ISBN: 978-92-9169-143-2. <http://epic.awi.de/37530/> (2014).
143. Patankar, S. *Numerical Heat Transfer and Fluid Flow* (CRC Press, 1980).
144. Pattyn, F. A new three-dimensional higher-order thermomechanical ice sheet model: Basic sensitivity, ice stream development, and ice flow across subglacial lakes. English. *J. Geophys. Res.* **108**, 1–15. ISSN: 0148-0227 (2003).
145. Pattyn, F., Perichon, L., Durand G. and Favier, L., Gagliardini, O., Hindmarsh, R. C. A., Zwinger, T., Albrecht, T., Cornford, S., Docquier, D., Furst, J., Goldberg, D., Gudmundsson, H., Humbert, A., Hutten, M., Huybrecht, P., Jouvett, G., Kleiner, T., Larour, E., Martin, D., Morlighem, M., Payne, A., Pollard, D., Rückamp, M., Rybak, O., Seroussi, H., Thoma, M. & Wilkens, N. Grounding-line migration in plan-view marine ice-sheet models: results of the ice2sea MISIMP3d intercomparison. *J. Glaciol.* **59 (215)**, 410–422 (2013).

146. Pattyn, F., Schoof, C., Perichon, L., Hindmarsh, R. C. A., Bueler, E., de Fleurian, B., Durand, G., Gagliardini, O., Gladstone, R., Goldberg, D., Gudmundsson, G. H., Huybrechts, P., Lee, V., Nick, F. M., Payne, A. J., Pollard, D., Rybak, O., Saito, F. & Vieli, A. Results of the Marine Ice Sheet Model Intercomparison Project, MISIIP. English. *Cryosphere* **6**, 573–588. ISSN: 1994-0416 (2012).
147. Payne, A. & Dongelmans, P. Self-organization in the thermomechanical flow of ice sheets. English. *J. Geophys. Res.* **102**, 12219–12233 (1997).
148. Pelto, M., Hughes, T. & Brecher, H. Equilibrium state of Jakobshavn Isbræ, West Greenland. *Ann. Glaciol.* **12**, 127–131 (1989).
149. Pettersson, R., Jansson, P. & Blatter, H. Spatial variability in water content at the cold-temperate transition surface of the polythermal Storglaciaren, Sweden. *J. Geophys. Res.* **109**. ISSN: 0148-0227. doi: {10.1029/2003JF000110} (2004).
150. Phillips, T., Rajaram, H. & Steffen, K. Cryo-hydrologic warming: A potential mechanism for rapid thermal response of ice sheets. English. *Geophys. Res. Lett.* **7**, 1–5. ISSN: 0094-8276 (2010).
151. Pilato, C. M., Collins-Sussman, B. & Fitzpatrick, B. W. *Version Control with Subversion* 2nd ed. ISBN: 0596510330 (O'Reilly Media, Sept. 2008).
152. Podlech, S. & Weidick, A. Catastrophic break-up of the front of Jakobshavn Isbræ, West Greenland, 2002/03. *J. Glaciol.* **50**, 153–154. ISSN: 0022-1430 (2004).
153. Podrasky, D., Truffer, M., Fahnestock, M., Amundson, J. M., Cassotto, R. & Joughin, I. Outlet glacier response to forcing over hourly to inter-annual timescales, Jakobshavn Isbræ, Greenland. *J. Glaciol.* **58**, 1212–1226. ISSN: 0022-1430 (2012).
154. Pralong, A. & Funk, M. A level-set method for modeling the evolution of glacier geometry. *J. Glaciol.* **50**, 485–491. ISSN: 0022-1430 (2004).
155. Price, S. F., Payne, A. J. & Shepherd, A. A Three-Dimensional, First-Order Model of ice Flow: Numerical Implementation, Validation, and Initial Application to Iceland and Greenland. *AGU Fall Meeting Abstracts* (Dec. 2007).
156. Price, S., Payne, A., Howat, I. & Smith, B. Committed sea-level rise for the next century from Greenland ice sheet dynamics during the past decade. *P. Natl. Acad. Sci. USA* **108**, 8978–8983 (2011).
157. Rack, W. & Rott, H. Pattern of retreat and disintegration of the Larsen B ice shelf, Antarctic Peninsula. *Ann. Glaciol.* **39**, 505–510 (2004).
158. Rignot, E. & Kanagaratnam, P. Changes in the velocity structure of the Greenland ice sheet. English. *Science* **311**, 986–990. ISSN: 0036-8075 (2006).
159. Rignot, E. & Mouginot, J. Ice flow in Greenland for the International Polar Year 2008-2009. *Geophys. Res. Lett.* **39**, L11501, 1–7 (2012).
160. Rignot, E., Jacobs, S., Mouginot, J. & Scheuchl, B. Ice shelf melting around Antarctica. *Science* **341**, 266–270 (2013).
161. Rignot, E., Koppes, M. & Velicogna, I. Rapid submarine melting of the calving faces of West Greenland glaciers. English. *Nat. Geosci.* **3**, 187–191. ISSN: 1752-0894 (2010).

162. Rosenau, R., Schwalbe, E., Maas, H. G., Baessler, M. & Dietrich, R. Grounding line migration and high-resolution calving dynamics of Jakobshavn Isbrae, West Greenland. *J. Geophys. Res.* **118**, 382–395. ISSN: 2169-9003 (2013).
163. Rückamp, M., Blindow, N., Suckro, S., Braun, M. & Humbert, A. Dynamics of the ice cap on King George Island, Antarctica: field measurements and numerical simulations. *Ann. Glaciol.* **51**, 80–90. ISSN: 0260-3055 (2010).
164. Schoof, C. Coulomb Friction And Other Sliding Laws In A Higher-order Glacier Flow Model. English. *Math. Models Methods Appl. Sci.* **20**, 157–189. ISSN: 0218-2025 (2010).
165. Schoof, C. Ice sheet grounding line dynamics: Steady states, stability, and hysteresis. English. *J. Geophys. Res.* **112**, 1–19. ISSN: 0148-0227 (2007).
166. Schoof, C. & Hindmarsh, R. C. A. Thin-Film Flows with Wall Slip: An Asymptotic Analysis of Higher Order Glacier Flow Models. English. *Quart. J. Mech. Appl. Math.* **63**, 73–114. ISSN: 0033-5614 (2010).
167. Seroussi, H., Morlighem, M., Rignot, E., Khazendar, A., Larour, E. & Mouginot, J. Dependence of century-scale projections of the Greenland ice sheet on its thermal regime. English. *J. Glaciol.* **59**, 1024–1034. ISSN: 0022-1430 (2013).
168. Seroussi, H., Morlighem, M., Larour, E., Rignot, E. & Khazendar, A. Hydrostatic grounding line parameterization in ice sheet models. English. *Cryosphere* **8**, 2075–2087. ISSN: 1994-0416 (2014).
169. Seroussi, H., Morlighem, M., Rignot, E., Larour, E., Aubry, D., Ben Dhia, H. & Kristensen, S. S. Ice flux divergence anomalies on 79north Glacier, Greenland. *Geophys. Res. Lett.* **38**, 1–5 (2011).
170. Seroussi, H., Morlighem, M., Rignot, E., Mouginot, J., Larour, E., Schodlok, M. P. & Khazendar, A. Sensitivity of the dynamics of Pine Island Glacier, West Antarctica, to climate forcing for the next 50 years. *Cryosphere* **8**, 1699–1710 (2014).
171. Sethian, J. Evolution, implementation, and application of level set and fast marching methods for advancing fronts. *J. Comput. Phys.* **169**, 503–555. ISSN: 0021-9991 (2001).
172. Shapero, D. R., Joughin, I. R., Poinar, K., Morlighem, M. & Gillet-Chaulet, F. Basal resistance for three of the largest Greenland outlet glaciers. *J. Geophys. Res.* **121**. 2015JF003643, 168–180. ISSN: 2169-9011 (2016).
173. Shapiro, N. & Ritzwoller, M. Inferring surface heat flux distributions guided by a global seismic model: particular application to Antarctica. English. *Earth Planet. Sci. Lett.* **223**, 213–224. ISSN: 0012-821X (2004).
174. Sohn, H., Jezek, K. & van der Veen, C. Jakobshavn Glacier, West Greenland: 30 years of spaceborne observations. English. *Geophys. Res. Lett.* **25**, 2699–2702. ISSN: 0094-8276 (1998).

175. Spalding, D. B. A novel finite difference formulation for differential expressions involving both first and second derivatives. *International Journal for Numerical Methods in Engineering* **4**, 551–559. ISSN: 1097-0207 (1972).
176. Steinemann, S. Results of preliminary experiments on the plasticity of ice crystals. *J. Glaciol.* **2**, 404–412 (1954).
177. Straneo, F. & Heimbach, P. North Atlantic warming and the retreat of Greenland's outlet glaciers. *Nature* **504**, 36–43 (2013).
178. Straneo, F., Curry, R. G., Sutherland, D. A., Hamilton, G. S., Cenedese, C., Vage, K. & Stearns, L. A. Impact of fjord dynamics and glacial runoff on the circulation near Helheim Glacier. *Nat. Geosci.* **4**, 322–327. ISSN: 1752-0894 (2011).
179. Stroustrup, B. *The C++ Programming Language* 3rd. ISBN: 0201889544 (Addison-Wesley Longman Publishing Co., Inc., Boston, MA, USA, 1997).
180. Thomas, R. Force-perturbation analysis of recent thinning and acceleration of Jakobshavn Isbrae, Greenland. English. *J. Glaciol.* **50**, 57–66. ISSN: 0022-1430 (2004).
181. Thomas, R., Abdalati, W., Frederick, E., Krabill, W., Manizade, S. & Steffen, K. Investigation of surface melting and dynamic thinning on Jakobshavn Isbrae, Greenland. *J. Glaciol.* **49**, 231–239. ISSN: 0022-1430 (2003).
182. Thorsteinsson, T. An analytical approach to deformation of anisotropic ice-crystal aggregates. English. *J. Glaciol.* **47**, 507–516. ISSN: 0022-1430 (2001).
183. Truesdell, C. & Noll, W. in *The Non-Linear Field Theories of Mechanics* 1–579 (Springer, 2004).
184. Truffer, M. & Echelmeyer, K. Of isbrae and ice streams. *Ann. Glaciol. ANNALS OF GLACIOLOGY* **36** (ed Raymond, CF) International Symposium on Fast Glacier Flow, Yakutat, Alaska, Jun 10-14, 2002, 66–72. ISSN: 0260-3055 (2003).
185. Vallon, M., Petit, J.-R. & Fabre, B. Study of an ice core to the bedrock in the accumulation zone of an alpine glacier. *J. Glaciol.* **17**, 13–28 (1976).
186. van den Broeke, M. R., Enderlin, E. M., Howat, I. M., Munneke, P. K., Noel, B. P. Y., van de Berg, W. J., van Meijgaard, E. & Wouters, B. On the recent contribution of the Greenland ice sheet to sea level change. *The Cryosphere* **10**, 1933–1946. ISSN: 1994-0416 (2016).
187. van der Veen, C. J., Plummer, J. C. & Stearns, L. A. Controls on the recent speed-up of Jakobshavn Isbrae, West Greenland. *J. Glaciol.* **57**, 770–782. ISSN: 0022-1430 (2011).
188. van der Veen, C. Fracture mechanics approach to penetration of surface crevasses on glaciers. *Cold Reg. Sci. Technol.* **27**, 31–47. ISSN: 0165-232X (1998).
189. Vieli, A. & Nick, F. Understanding and modelling rapid dynamic changes of tidewater outlet glaciers: Issues and implications. *Surv. Geophys.* **32**, 437–458 (2011).

190. Wang, Q., Danilov, S., Sidorenko, D., Timmermann, R., Wekerle, C., Wang, X., Jung, T. & Schroeter, J. The Finite Element Sea Ice-Ocean Model (FESOM) v.1.4: formulation of an ocean general circulation model. *Geosci. Model Dev.* **7**, 663–693. ISSN: 1991-959X (2014).
191. Weertman, J. Deformation of floating ice shelves. *J. Glaciol.* **3**, 38–42 (1957).
192. Weertman, J. Stability of the junction of an ice sheet and an ice shelf. *J. Glaciol.* **13(67)**, 3–11 (1974).
193. Weidick, A. *Observations on some Holocene glacier fluctuations in West Greenland* English. Part of illustrative matter in pocket (Copenhagen : C. A. Reitzel, 1968).
194. Winkelmann, R., Martin, M. A., Haseloff, M., Albrecht, T., Bueller, E., Khroulev, C. & Levermann, A. The Potsdam Parallel Ice Sheet Model (PISM-PIK) - Part 1: Model description. English. *Cryosphere* **5**, 715–726. ISSN: 1994-0416 (2011).
195. Xu, Y., Rignot, E., Menemenlis, D. & Koppes, M. Numerical experiments on subaqueous melting of Greenland tidewater glaciers in response to ocean warming and enhanced subglacial discharge. *Ann. Glaciol.* **53**, 229–234 (2012).
196. Yashayaev, I. Hydrographic changes in the Labrador Sea, 1960-2005. *Prog. Oceanogr.* **73**, 242–276. ISSN: 0079-6611 (2007).
197. Zhao, H.-K., Chan, T., Merriman, B. & Osher, S. A variational level set approach to multiphase motion. *J. Comput. Phys.* **127**, 179–195 (1996).
198. Zienkiewicz, O. C. & Taylor, R. L. *The finite element method* Fourth (ed McGraw-Hill) (New York, London, 1989).
199. Zwally, H. J., Li, J., Brenner, A. C., Beckley, M., Cornejo, H. G., Dimarzio, J., Giovinetto, M. B., Neumann, T. A., Robbins, J., Saba, J. L., Yi, D. & Wang, W. Greenland ice sheet mass balance: distribution of increased mass loss with climate warming; 2003-07 versus 1992-2002. English. *J. Glaciol.* **57**, 88–102. ISSN: 0022-1430 (2011).
200. Zwally, H. J., Abdalati, W., Herring, T., Larson, K., Saba, J. & Steffen, K. Surface Melt-Induced Acceleration of Greenland Ice-Sheet Flow. *Science* **297**, 218–222 (2002).